Die approbierte Originalversion dieser Dissertation ist in der Hauptbibliothek der Technischen Universität Wien aufgestellt und zugänglich.
http://www.ub.tuwien.ac.at

The approved original version of this thesis is available at the main library of the Vienna University of Technology.
http://www.ub.tuwien.ac.at/eng

DISSERTATION

INTERACTION OF IONS WITH 3D AND 2D MATERIALS

Ausgeführt zum Zwecke der Erlangung des akademischen Grades
einer Doktorin der technischen Wissenschaften
unter der Leitung von

Univ.-Prof. Dr. Friedrich AUMAYR
E134
Institut für Angewandte Physik

eingereicht an der Technischen Universität Wien
Fakultät für Physik
von

Dipl.-Ing. Elisabeth GRUBER
Matrikelnummer.: 0625619
Geblergasse 84/14
1170 Wien

Wien, Februar 2017 (Elisabeth Gruber)

Alles, was überhaupt gedacht werden kann,
kann klar gedacht werden.
Alles, was sich aussprechen lässt,
lässt sich klar aussprechen.

- -Ludwig Wittgenstein - -

Zusammenfassung

Ionen-Festkörper Wechselwirkungsuntersuchungen decken ein breites Spektrum von Wechselwirkungsphänomenen und -prozessen ab. Für die vorliegende Arbeit werden Wechselwirkungen von schnellen schweren Ionen (SHI) sowie langsamen hochgeladenen Ionen (HCI) mit drei- und zweidimensionalen Materialien untersucht. Bei der Wechselwirkung mit dreidimensionalen Materialien liegt der Fokus auf der Oberflächen-Nanostrukturbildung in der Endphase des Wechselwirkungsprozesses, während für die zweidimensionalen Materialien der Ladungsaustausch und der Energieverlust von HCIs im Vor-Gleichgewichtsregime untersucht werden. Das Ziel dieser Studien ist es, einen tieferen Einblick in die verschiedenen Stadien des Neutralisationsvorgangs geladener Ionen zu erhalten und das Materialverhalten bei hoher elektrischer Feldstärke und bei Deponierung hoher kinetischer oder potentieller Energie zu untersuchen.

Seit Jahrzehnten ist bekannt, dass die Bestrahlung von Festkörpern mit SHIs zu permanenten Modifikationen im Festkörpe und auf der Oberfläche führen kann. Ähnliche Oberflächen-Nanostrukturen können auch durch langsame HCIs induziert werden. Systematische Studien in diesem Forschungsgebiet wurden in den letzten zehn Jahren in unserer Gruppe durchgeführt. Im Laufe dieser Arbeit wurden verschiedene Materialien mit SHIs unter streifendem Einfallswinkel bestrahlt, da diese besondere Kollisionsgeometrie die Erzeugung von Ionenspuren nahe der Oberfläche erzwingt, die mit den von HCI induzierten Oberflächen-Nanostrukturen vergleichbar sind. Unter Verwendung von hochauflösender Atomkraftmikroskopie konnten wir zeigen, dass die erzeugten Spuren auf den bestrahlten Materialien eine viel komplexere Struktur aufweisen als in früheren Untersuchungen beobachtet. Für den gut untersuchten Isolatorkristall CaF_2 wurde gezeigt, dass

jedes SHI, das auf der Oberfläche auftrifft, zuerst eine Grube öffnet, die von einer Reihe von Nano-Hügelchen auf beiden Seiten begrenzt wird, die schließlich in eine langsam abfallende Erhöhung übergehen. Die Länge der Grube sowie die Länge der gesamten Spur kann durch Variieren des Einfallswinkels bestimmt werden. Die beobachtete Gruben- und Hügelchen-Bildung in einer einzigen Ionenspur konnten erfolgreich mit Sublimations- und Schmelzprozessen verknüpft werden und wurden mit Simulationen einer dreidimensionalen Version des Zwei-Temperatur-Modells verglichen. Eine sehr ähnliche und genauso komplexe Art der Ionenspur wurde auf dem lamellaren Material Glimmer nach SHI-Bestrahlung beobachtet, wohingegen an der Ionenaufprallstelle von $SrTiO_3$ und TiO_2 viel weniger ausgeprägte Grubenbildungen auf den Kristalloberflächen gefunden wurden.

Der zweite Schwerpunkt dieser Arbeit war die Analyse des Ladungsaustausches und des Energieverlustes von langsamen HCIs in Wechselwirkung mit zweidimensionalen Materialien unter Verwendung eines elektrostatischen Analysators. Die bimodale Ladungszustandsverteilung für die Transmissionsmessungen mit 1 nm dicken amorphen Kohlenstoff-Nanomembranen und die Einzelladungszustandsverteilung für freistehendes einlagiges Graphen wurden durch einen Ladungsaustauschprozess erklärt, der stark vom Stoßparameter abhängt. Während für die Kohlenstoff-Nanomembranen, die aus dicht und weniger dicht gepackten Bereichen bestehen, verschiedene Stoßparameter möglich sind, ist dieser für einlagiges Graphen durch den atomare Abstand der gut geordneten hexagonalen Struktur begrenzt. Aus der Anzahl der aufgenommenen und stabilisierten Elektronen der durchgehenden Ionen konnten extrem kurze Ladungsäquilibrierungszeiten von nur wenigen Femtosekunden extrahiert werden. Darüber hinaus haben detaillierte Untersuchungen keine Zerstörung des einlagigen Graphens nach dem Ionenstoß gezeigt, im Gegensatz zur beobachteten Porenbildung in den Kohlenstoff-Nanomembranen aufgrund von HCI-Stößen. In Zusammenarbeit von experimentellen und theoretischen Untersuchungen konnten wir zeigen, dass große Stromdichten von mindestens $10^{12}\,A/cm^2$ von einlagigem Graphen ohne Zerstörung ausgehalten werden. Obwohl dieser Strom nur für wenige Femtosekunden auf einer Fläche von nm^2 aufrechterhalten wird, ist sein Wert etwa 3 Größenordnungen höher als die aus der Literatur bekannten Durchbruchstromdichten für Graphen. Die durchgeführten Untersuchungen liefern nicht nur tiefere Einblicke in die Neutralisations- und Energieverlustprozesse exotischer hochangeregter hohler Atome, sondern eignen sich auch zur Untersuchung von Materialeigenschaften wie dem elektronischen Ansprechen zweidimensionaler Materialien auf extrem hohe elektrische Feldstärken auf einer Femtosekunden Zeitskala.

Abstract

Ion-solid interaction studies cover a broad range of interaction phenomena and processes. For the present thesis swift heavy ion (SHI) as well as slow highly charged ion (HCI) interactions with three- and two-dimensional materials are studied. For the interaction with three-dimensional materials the focus lies on the surface nanostructure formation in the final stage of the interaction scenario, whereas for the two-dimensional materials the charge exchange end energy loss of HCIs in the pre-equilibrium regime are studied. The goal of these studies is to get deeper insight into the different stages of the neutralisation process of charged ions and to investigate the material behaviour in the presence of a high electric field strength and by the deposition of high kinetic or potential energy.

Since decades it is known that the irradiation of solid targets with SHIs can lead to permanent modifications in the bulk and on the surface. Similar surface nanostructures can also be induced by using slow HCIs and systematic studies in this research field were performed over the last decade in our group. In the course of this thesis various materials were irradiated with SHIs under grazing angle of incidence, since this particular collision geometry forces the track to a region close to the surface comparable to the shallow damage induced by slow HCIs. Using high resolution atomic force microscopy we could show that the created tracks on the irradiated materials have a much more complex structure than observed in previous investigations. For the well studied insulating crystal CaF_2 it was demonstrated that each SHI impacting on the surface first opens a groove bordered by a series of nanohillocks on both sides, which eventually merges into a slowly fading single protrusion. The length of the groove as well as the length of the whole

track can be tuned by varying the angle of incidence. The observed groove and hillock formation in a single track could successfully be linked to sublimation and melting processes and checked by comparison to a three-dimensional version of the two temperature model. A very similar and also complex type of track formation was observed on the lamellar material mica after SHI irradiation, whereat much less pronounced groove formation was found at the ion impact site for $SrTiO_3$ and TiO_2 crystal surfaces.

The second focus of this thesis was on the analysis of charge exchange and energy loss of slow HCIs interacting with two-dimensional materials by using an electrostatic analyser. The bimodal charge state distribution for the transmission measurements with 1 nm thick amorphous carbon nanomembranes and the single charge state distribution for freestanding single layer graphene were explained by a charge exchange process which strongly depends on the impact parameter. While for the carbon nanomembranes with a structure of dense and less dense packed areas various impact parameters are possible, the atomic distance of the well ordered hexagonal structure of single layer graphene limits the range of possible impact parameters. From the number of captured and stabilised electrons of the transmitted ions extremely short charge-equilibration times of only a few femtoseconds could be extracted. Moreover, detailed investigations have shown no rapture and destruction of the single layer graphene after ion impact, in contrast to the observed pore formation in the carbon nanomembranes due to HCI impacts. In a joint experimental and theoretical effort we could demonstrate that large current densities of at least $10^{12}\,A/cm^2$ are sustained by single layer graphene without rupture. Even though this current is only active for a few femtoseconds on a nm^2 sized area, its value is about 3 orders of magnitude higher than breakdown current densities for graphene known in the literature. The performed investigations not only give deeper insights into the neutralisation and energy loss processes of exotic highly excited hollow atoms, but are also suitable to study material properties, like the electronic response of two-dimensional materials to extremely high electric field strengths on a femtosecond time scale.

Contents

1 General Introduction 1

1.1 Motivation . . . 1

1.2 Publication list and supervised students . . . 3

2 Basic concepts of ion-solid interaction processes 9

2.1 Slow highly charged ion interaction with solids . . . 10

2.1.1 Electronic and radiative transition . . . 10

2.1.2 Hollow atom formation and scenario of HCI-surface interaction . . . 13

2.1.3 Classical over the barrier model . . . 14

2.1.4 Promotion of energy levels and molecular orbital formation . . . 16

2.1.5 Decay rates of multiply excited states . . . 17

2.1.6 Interatomic Coulombic decay - ICD . . . 18

2.1.7 Nanostructuring . . . 22

2.2 Energy transfer from ions to solids . . . 23

2.2.1 Nuclear stopping . . . 24

2.2.2 Electronic stopping . . . 25

2.2.3 Energy loss of charged particles . . . 27

2.3 Interaction of swift heavy ions with solids . . . 28

2.3.1 Models for damage creation . . . 29

3 Ion Sources and Methods 33

3.1 Ion sources . . . 33

3.1.1 Sources for HCIs . . . 34

3.1.2 Sources for SHIs . . . 37

3.2 Microscopy Techniques . . . 37

3.2.1 Atomic Force Microscopy - AFM . . . 38

3.2.2 Transmission Electron Microscopy - TEM . . . 40

4 Nanostructuring by ion irradiation 43
4.1 State of the art . . . 44
4.1.1 SrTiO3 . . . 45
4.1.2 TiO2 . . . 47
4.1.3 Mica . . . 51
4.1.4 CaF_2 . . . 54
4.2 Experimental Results . . . 57
4.2.1 Pretreatment of CaF_2 . . . 58
4.2.2 HCI irradiation . . . 60
4.2.3 SHI irradiation under grazing angle of incidence . . . 62
4.3 Discussion . . . 76

5 HCI interaction with 2D materials 83
5.1 State of the art . . . 84
5.2 Experimental setup . . . 86
5.2.1 Ion beam facility and electrostatic analyser in Dresden . . . 86
5.2.2 Experimental setup and electrostatic analyser in Vienna . . . 87
5.2.3 Operation of the analyser . . . 90
5.3 Investigated Materials . . . 94
5.3.1 Carbon nanomembranes . . . 94
5.3.2 Graphene . . . 97
5.4 CNM - Experimental results and discussion . . . 100
5.4.1 Charge exchange . . . 101
5.4.2 Energy loss . . . 106
5.4.3 Comparison with previous CNM measurements . . . 109
5.5 Graphene - Experimental results and discussion . . . 110
5.5.1 Multi-electron capture process . . . 110
5.5.2 Transmission electron microscopy results . . . 120
5.5.3 Local breakdown current density . . . 121
5.5.4 Energy loss . . . 123

6 Summary and Outlook 129

Bibliography 133

Abbreviations

HCI	Highly charged ion
SHI	Swift heavy ion
ECRIS	Electron cyclotron resonance ion source
EBIT	Electron beam ion trap
AFM	Atomic force microscopy
TEM	Transmission electron microscopy
STEM	Scanning transmission electron microscopy
RI	Resonant ionisation
QRN	Quasi-resonant neutralisation
AN	Auger neutralisation
AD	Auger de-excitation
AI	Autoionisation
RD	Radiative de-excitation
COB model	Classical over the barrier model
ICD	Interatomic Coulombic decay
i-TS model	Inelastic thermal spike model
TTM	Two temperature model
DFT	Density functional theory
TTDFT	Time dependent density functional theory
CNM	Carbon nanomembrane
SLG	Single layer graphene
3D	Three dimensional
2D	Two dimensional
HZDR	Helmholtz-Zentrum Dresden-Rossendorf
GANIL	Grand Accélérateur National d'Ions Lourds
IRRSUD	French acronym for irradiation toward south
ARIBE	French acronym for accelerator dedicated to research with low energy ions

1

General Introduction

The present thesis was elaborated under supervision of Prof. Friedrich Aumayr at the Institute of Applied Physics at TU Wien in the years from 2013 until 2016. During this time, several students have contributed to this work by means of Master and Bachelor theses or project works. The investigations of ion irradiation of 3D materials were carried out in the framework of the French-Austrian ANR – FWF Project SIISU (2013-2016). A great part of the interaction studies of highly charged ions with 2D materials were conducted in collaboration with the Helmholtz-Zentrum Dresden-Rossendorf (HZDR).

1.1 Motivation

Investigations of interaction processes of energetic particles with solids have attracted great attention in the last century, driven by the interest to acquire profound knowledge of the underlying physical mechanisms and forced by the large number of technological applications, e.g. ion implantation for semiconductor doping, lithographic modifications, analytical methods like Rutherford backscattering spectrometry and secondary ion mass spectrometry.
In the beginning the experimental and theoretical developments in the field of ion-solid interaction [1] were essentially academic and contributed greatly to today's understanding of the

structure of atoms and molecules [2, 3]. While the first scattering experiments were limited to the use of alpha particles [4] and electron beams [5], extracted from radioactive materials and hot cathods, the construction of the first accelerators enabled the formation of monoenergetic particle beams with tunable kinetic energy [1, 6]. The growing interest in nuclear physics provoked the construction of numerous ion accelerator facilities between 1950 and 1990. Although ion-solid interaction studies played a minor role at those times, lots of investigations were done to understand the stopping and associated energy dissipation channels in solid matter [7–10]. With the arise of new fields like microelectronics and nanotechnology in the last 30 years, these accelerator facilities were more and more used for studying radiation damage and modifications due to ion-solid matter interaction processes. The studied interaction processes were thereby dominated by the large ion mass and high kinetic energy of the used particles. These swift heavy ions (SHI) at energies in the MeV and GeV energy regime create severe structural modifications on the surface and hundreds of nanometer deep in the solid [11] (and references therein). Such severe damage deep insight the material limits the usability of SHIs in nanotechnological applications.
With the development of electron cyclotron resonance ion sources (ECRIS) and electron beam ion traps (EBIT) the production of highly charged ions (HCI) became available [12]. Highly charged ions store a lot of potential energy, namely the sum of the binding energy of all missing electrons, which can be transferred during interaction processes to a solid. The potential energy deposition may cause electron emission [13], sputtering [14, 15] and nanostructuring [16, 17], phenomena known and typically associated with kinetic energy deposition. In comparison to SHI evoked modifications, the structural modifications induced by HCIs are limited to the topmost atomic layers.
Besides the use of HCIs as a tool for surface modification, they are also local probes for gaining information about many-body dynamics in exotic (high excited Rydberg) atoms [18].
Charge exchange and de-excitation processes due to HCI-solid matter interaction have been studied for decades [19]. After passing some nanometers in a solid, the ion reaches the equilibrium charge state. Therefore, pre-equilibrium processes, like charge state dependent energy loss, remained experimentally inaccessible for a long time. With the production of ultrathin materials with a thickness of only some nanometer or even less, like in the case of monolayer graphene, the ion remains in the pre-equilibrium regime after transmission of the solid and details of the neutralisation process can be studied [20–23]. A further positive side effect of such investigations is that HCIs produce a high electric field in front of a target and by studying the neutralisation process of the ion, information on the electronic response of the material can be obtained [24].

The presented work deals with several topics of the above mentioned research fields, where the focus lies on nanostructuring of different insulating materials after SHI irradiation under grazing

incidence and on charge state and energy loss analysis of HCIs transmitted through 1 nm thick carbon nanomembranes (CNM) and through the ultrathin 2D material, single layer graphene.

In chapter 2 the basic concepts of HCI- and SHI-solid interaction processes are presented. To perform HCI and SHI irradiations different ion sources at various ion beam facilities were used and their operating modes are explained in chapter 3. High resolution microscopy techniques, like atomic force microscopy (AFM) and transmission electron microscopy (TEM), were used to characterise surface nanostructuring and are also presented in chapter 3. Chapter 4 focuses on surface nanostructuring of various 3D solids by HCI and SHI irradiation under normal and grazing angle of incidence. In chapter 5 transmission measurements of HCIs through 2D materials, i.e. 1 nm thick carbon nanomembranes (CNM) and single layer graphene (SLG), are shown. Charge exchange and energy loss analysis of the transmitted ions are performed. Results and discussion of these two chapters are presented and argued on the basis of publications which were published in the course of this work [22–27]. A summary of the thesis and an outlook for further investigations are given in chapter 6.

1.2 Publication list and supervised students

Publications connected to the PhD thesis

- R. A. Wilhelm, **E. Gruber**, J. Schwestka, R. Kozubek, T. Madeira, J. Marques, J. Kobus, A. V. Krasheninnikov, M. Schleberger, F. Aumayr: *Highly charged ion neutralization and de-excitation driven by multiple interatomic coulombic decay*; submitted (2017)

- **E. Gruber**, R. A. Wilhelm, R. Pétuya, V. Smejkal, R. Kozubek, A. Hierzenberger, B. C. Bayer, I. Aldazabal, A. K. Kazansky, F. Libisch, A. V. Krasheninnikov, M. Schleberger, S. Facsko, A. G. Borisov, A. Arnau, F. Aumayr: *Ultrafast electronic response of graphene to a strong and localized electric field*; Nature Communications **7**, 13948 (2016)

- **E. Gruber**, P. Salou, L. Bergen, M. El Kharrazi, E. Lattouf, C. Grygiel, Y. Wang, A. Benyagoub, D. Levavasseur, J. Rangama, H. Lebius, B. Ban-d'Etat, M. Schleberger, F. Aumayr: *Swift heavy ion irradiation of CaF_2 - from grooves to hillocks in a single ion track*; Journal of Physics: Condensed Matter **28**, 4050011 (2016)

- R. A. Wilhelm, **E. Gruber**, V. Smejkal, S. Facsko, F. Aumayr: *Charge-state-dependent energy loss of slow ions. I. Experimental results on the transmission of highly charged ions*; Physical Review A **93**, 0527081 (2016)

- V. Smejkal, **E. Gruber**, R. A. Wilhelm, L. Brandl, R. Heller, S. Facsko, and F. Aumayr: *A setup for transmission measurements of low energy multiply charged ions through free-standing few atomic layer films*; Nuclear Instruments & Methods in Physics Section B **382**, 119 (2016)

- **E. Gruber**, R. A. Wilhelm, V. Smejkal, R. Heller, S. Facsko, F. Aumayr: *Interaction of highly charged ions with carbon nano membranes*; Journal of Physics: Conference Series **635**, 0120271 (2015)

- R. A. Wilhelm, A. S. El-Said, F. Krok, R. Heller, **E. Gruber**, F. Aumayr, S. Facsko: *Highly charged ion induced nanostructures at surfaces by strong electronic excitations*; Progress in Surface Science **90**, 377 (2015)

- R. A. Wilhelm, **E. Gruber**, R. Ritter, R. Heller, A. Beyer, A. Turchanin, N. Klingner, R. Hübner, M. Stöger-Pollach, H. Vieker, G. Hlawacek, A. Gölzhäuser, S. Facsko, F. Aumayr: *Threshold and efficiency for perforation of 1 nm thick carbon nanomembranes with slow highly charged ions*; 2D Materials **2**, 0350091 (2015)

- R. A. Wilhelm, **E. Gruber**, R. Ritter, R. Heller, S. Facsko, F. Aumayr: *Charge Exchange and Energy Loss of Slow Highly Charged Ions in 1 nm Thick Carbon Nanomembranes*; Physical Review Letters **112**, 1532011 (2014)

Publications not directly connected to the PhD thesis

- B. M. Berger, R. Stadlmayr, D. Blöch, **E.Gruber**, K. Sugiyama, T. Schwarz-Selinger, F. Aumayr: *Erosion of Fe-W model system under normal and oblige D ion irradiation*; Nuclear Materials and Energy, submitted (2016)

- N. Stolterfoht, **E. Gruber**, P. Allinger, S. Wampl, Y. Wang, M. Simon, F. Aumayr: *Experiments and simulations of 4.5 keV Ar^{7+} ion guiding through a conical glass macrocapillary*; Physical Review A **91**, 0327051 (2015)

- **E. Gruber**, N. Stolterfoht, P. Allinger, S. Wampl, Y. Wang, M. Simon, F. Aumayr: *Temperature control of ion guiding through tapered capillaries*; Nuclear Instruments & Methods in Physics Research Section B **340**, 1 (2014)

- Y. Wang, C. Grygiel, C. Dufour, J. Sun, Z. Wang, Y. Zhao, G. Xiao, R. Cheng, X. Zhou, J. Ren, S. Liu, Y. Lei, Y. Sun, R. Ritter, **E. Gruber**, A. Cassimi, I. Monnet, S. Bouffard, F. Aumayr,

M. Toulemonde: *Energy deposition by heavy ions: Additivity of kinetic and potential energy contributions in hillock formation on CaF_2*; Scientific Reports **4**, 57421 (2014)

- **E. Gruber**, G. Kowarik, F. Ladinig, Johannes Waclawek, D. Schrempf, F. Aumayr, R. Bereczky, K. Tökési, P. Gunacker, T. Schweigler, C. Lemell, J. Burgdörfer: *Temperature control of ion guiding through insulating capillaries*; Physical Review A **86**, 0629011 (2012)

- G. Kowarik, **E. Gruber**, K. Iskratsch, F. Aumayr: *Using a current method for measuring ion-induced electron emission from LiF*; Nuclear Instruments & Methods in Physics Research Section B **269**, 964 (2011)

Talks

- Invited Talk: "Slow highly charged ion interaction with freestanding single layer graphene"; 18th International Conference on the Physics of Highly Charged Ions (HCI-2016), Kielce/Poland; 16.09.2016

- Short Oral: "Interaction of slow highly charged ions with single layer graphene: charge exchange and energy loss studies"; European Materials Research Society (EMRS), Spring Meeting 2016, Lille/Frankreich; 03.05.2016.

- Invited Talk: "Interaction of highly charged ions with graphene and carbon nano membranes; 29th International Conference on Photonic, Electronic and Atomic Collisions (XXIX ICPEAC), Toledo/Spain; 27.07.2015.

- Short Oral: "Ion-induced nanostructures on surfaces: Comparing the effect of slow highly charged ions to grazing incidence swift heavy ions"; 26th International Conference on Atomic Collisions in Solids (ICACS-26), Debrecen/Hungary; 17.07.2014.

- Invited Talk: "Transmission of slow highly charged ions through 1 nm thick carbon nanomembranes"; 6th International Conference on Elementary Processes in Atomic Systems-CEPAS 2014, Hotel Sorea, Bratislava/Slovakia; 11.07.2014.

- Invited Talk: "Controlling ion guiding through capillaries by temperature"; 20th International Workshop on Inelastic Ion Surface Collision (IISC-20), Wirrina Cove/Australia; 20.02.2014.

- Short Oral: "Slow Highly Charged Ions as a Tool for the Fabrication of Nanopores in 1 nm Thick Carbon Nanomembranes"; 22th International Conference on Ion Surface Interactions (ISI-2013), Yaroslavl/Russia; 25.08.2013.

- Short Oral: "Temperature control of ion guiding through straight insulating macro - capillaries"; 19th International Workshop on Inelastic Ion-Surface Collisions (IISC-19), Frauenchiemsee/Germany; 17.09.2012.

- Talk: "Ion induced nanostructures on 3D and 2D materials - recent results"; Seminar, Universität Duisburg-Essen, Duisburg-Essen/Germany; 15.09.2014.

- Talk: "Interaction of slow highly charged ions with single layer graphene"; Seminar, Institut für Angewandte Physik (IAP), TU Wien; 24.05.2016.

Poster presentations at international conferences

- **E. Gruber**, V. Smejkal, M. Kralik, R. A. Wilhelm, R. Heller, S. Facsko, F. Aumayr: "Interaction of Multiply Charged Ions with Single Layer Graphene: Charge Exchange and Energy Loss Studies"; 21th International Workshop on Inelastic Ion-Surface Collisions (IISC-21), Donostia-San Sebastián/Spain; 20.10.2015.

- **E. Gruber**, E. Lattouf, L. Bergen, P. Salou, C. Grygiel, Y. Wang, O. Ochedowski, A. Benyagoub, D. Lavavasseur, J. Rangama, H. Lebius, B. Ban-d'Etat, M. Schleberger, F. Aumayr: "Studies of surface nanostructure formation due to swift heavy ion irradiation under grazing incidence"; 29th International Conference on Photonic, Electronic and Atomic Collisions (XXIX ICPEAC), Toledo/Spain; 23.07.2015.

- **E. Gruber**, V. Smejkal, M. Kralik, R. A. Wilhelm, R. Heller, S. Facsko, F. Aumayr: "Interaction of multiply charged ions with single layer graphene - Part I: charge exchange and energy loss"; 29th International Conference on Photonic, Electronic and Atomic Collisions (XXIX ICPEAC), Toledo/Spain; 23.07.2015.

- **E. Gruber**, E. Lattouf, L. Bergen, H. Lebius, C. Grygiel, Y. Wang, A. Benyagoub, D. Levavasseur, O. Ochedowski, B. Ban-d'Etat, M. Schleberger, F. Aumayr: "Ion induced nanostructures by swift heavy ion irradiation under grazing incidence"; 9th International Symposium of Swift Heavy Ions in Matter (SHIM 2015), Darmstadtium, Darmstadt/Germany; 18.05.2015.

- **E. Gruber**, R. A. Wilhelm, R. Heller, S. Facsko, F. Aumayr: "Exploring the interaction of slow highly charged ions with 2D materials"; 1st Erwin Schrödinger Symposium 2014 of the Erwin Schrödinger Society for Nanosciences "Two Dimensional Nanostructures", Naturhistorische Museum, Wien; 26.11.2014 - 28.11.2014.

- **E. Gruber**, R. A. Wilhelm, R. Heller, R. Ritter, S. Facsko, F. Aumayr: "Charge state dependent energy loss and charge exchange of slow highly charged ions passing through carbon nano membranes"; 26th International Conference on Atomic Collisions in Solids (ICACS-26), Debrecen/Hungary; 15.07.2014.

- **E. Gruber**, P. Allinger, S. Wampl, P Hischenhuber, M. Simon, F. Aumayr: "The effect of conductivity on ion guiding through tapered insulating capillaries"; 11th European Conference on Atoms, Molecules and Photons 2013 (ECAMP-11), Aarhus University/Denmark; 26.06.2013.

- **E. Gruber**, P Hischenhuber, S. Wampl, M. Simon, F. Aumayr: "Controlling ion guiding through tapered glass - capillaries with temperature"; 19th International Workshop on Inelastic Ion-Surface Collisions (IISC-19), Frauenchiemsee/Germany; 18.09.2012.

Supervised Master students

Valerie Smejkal

Master thesis: ELEKTRA - Electrostatic analyser measurements of ion transmission through thin free-standing foils, 2016

Project work: Design of an electrostatic analyser setup for ion charge state and energy loss analysis after transmission through thin membranes, 2015

Lorenz Bergen

Master thesis: Nanostructuring of surfaces by swift heavy ion impacts under grazing incidence, 2016

Project work: Atomic force microscope imaging of ion induced nanostructures on mica surface, 2015

Laurids Prandl

Project work: Design of a heatable sampleholder for transmission measurements with graphene, 2016

Project work: HCI transmission measurements through thin freestanding foils, pending

Supervised Bachelor students

Peter Allinger

Bachelor thesis: Temperature Influence on the Guiding Effect of Taperd Glass Capillaries, 2013

Lukas Leonhartsberger

Bachelor thesis: Konstruktion eines Targethalters für gekrümmte Glasfaserkapillaren, 2013

Stefan Wampl

Bachelor thesis: Ion Guiding Through Tapered Glass Capillaries, 2012

Peter Hischenhuber

Bachelor thesis: Konstruktion und Entwicklung eines Targethalters für Messungen mit verjüngten Glaskapilleren, 2011

2

Basic concepts of ion-solid interaction processes

The bombardment of solids with neutral or ionised atoms, molecules and clusters are studied since decades. Thereby it can be distinguished between processes induced by the kinetic energy of the projectiles and ion-induced phenomena dependent on the internal potential energy of the ions. Here we restrict ourselves to interaction processes of two special kinds of ions, namely highly charged ions (HCI) and swift heavy ions (SHI). While SHIs transfer their kinetic energy via ionisation and electronic excitation processes to the target material and may cause kinetic electron emission, ion scattering and electronic sputtering on the surface and in the bulk, HCIs deposit their potential energy at the topmost surface layers causing potential electron emission and potential sputtering. Despite the differences in the primary excitation processes, both can lead to similar target modifications (for a review see [11]).

The first part of the chapter deals with HCI-solid interaction processes. Charge exchange and de-excitation processes of HCIs interacting with solids are presented. Besides the well known concept of the classical over the barrier model, less established theories, from the promotion of energy levels and molecular orbital formation to the interatomic Coulombic decay (ICD) process of HCIs, are presented. Additionally, surface nanostructuring phenomena due to HCI irradiation

are discussed.
The basic concept of energy loss, for historical reasons divided into nuclear and electronic energy loss, concerns both ion types. In the low energy regime the energy loss is dominated by nuclear stopping, in the high energy regime by electronic stopping. This simple subdivision in nuclear and electronic stopping may be not longer justified for charged particles. In this case the interaction of the projectile with the electronic system of the target due to charge exchange processes has to be considered.
The last part is dedicated to SHI-solid interaction processes. Several theoretical models for damage production, developed during the last decades, are presented. Among them the Coulomb explosion and the thermal spike model are the most prominent ones.

2.1 Slow highly charged ion interaction with solids

The term *slow highly charged* points to the two determining features of the ions. The term *slow* counts for ion impact velocities below 1 a.u. ($2.18 \cdot 10^6$ m/s), at which the electronic transition between the projectile and the target is much faster than significant changes of the projectile distance to the surface during this time.
The term *highly charged* underlines the lack of q electrons which were removed from the originally neutral atom and stored as potential energy (sum of the binding energy of all missing electrons) in the ion. The potential energy can reach tens to hundreds of keV and exceed the kinetic energy. In fig. 2.1 the potential energy for different types of ions is plotted as a function of their charge state. The interaction process for these ions is dominated by potential effects.
Upon surface impact the HCI will regain its q missing electrons inducing thereby various inelastic processes. A transfer of such large energy onto a very small area (typically less than 1 nm^2) within a rather short time of tens of femtoseconds corresponds to the immense power flux of $\geq 10^{14}$ W/cm^2.

2.1.1 Electronic and radiative transition

Pioneering work on slow ion-solid interaction processes was performed by H.D. Hagstrum *et al.* [28, 29] and U. A. Arifov *et al.* [30] in the 1950s and 1960s. They studied the yield and energy distribution of ejected electrons due to the impact of slow singly, doubly and multiply charged ions on metal surfaces. Their studies showed that electron emission arises from fast electron transitions from the surface into empty projectile ion states and starts already before the ion hits the surface. This phenomenon is called potential electron emission (PE) and results from ion-

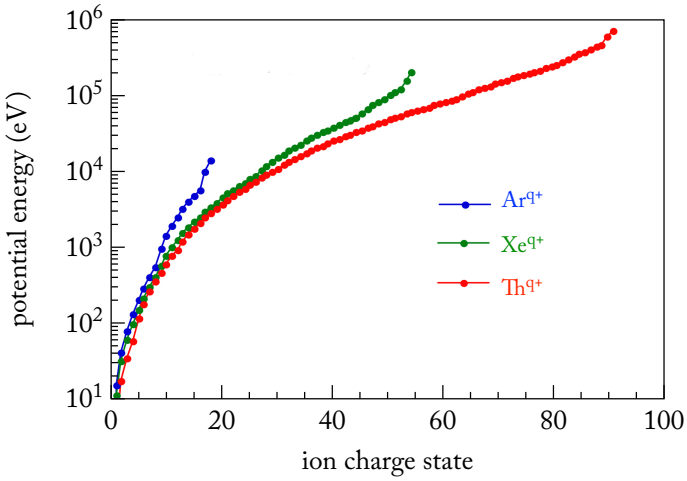

Figure 2.1: Potential energy as a function of the ion charge state
Potential energy of Ar^{q+}, Xe^{q+} and Th^{q+} ions as a function of the charge state. The potential energy reaches values of some ten to hundred of keV and can exceed the kinetic energy. The figure is adapted from [16].

neutralisation and de-excitation in front and at the surface [13]. The PE yield strongly increases with the charge state of the incident projectile and is superimposed and eventually dominated at higher impact velocity by kinetic electron emission (KE) [31].
Various electronic transition channels between the metal surface and the projectile exist and the different channels can be divided into one-electron and two-electron processes [19]. The resonant one-electron transfer, to which the resonant neutralisation (RN) and resonant ionisation (RI) belong, is dominant in the early state of the ion-surface interaction and can start some nanometer above the surface. These processes fill the outer-shells of the projectile with electrons and the inner- shells are left empty. Also the so called quasi-resonant neutralisation (QRN) process belongs to the one-electron transition channel, but arises only at sufficiently close distance between the target and the ion and refills primarily inner-shells. The subsequent electron emitting processes i.e., Auger neutralisation (AN), Auger de-excitation (AD) and auto-ionisation (AI) lead to refilling of the inner-shells by emitting electrons. These processes are characterised by time scales in the order of 10^{-13}–10^{-16} s [19].
In the following list the mentioned processes are described in more detail. A schematic overview is given in fig 2.2.

Resonant neutralisation RN An electron from the surface valence band is transferred into an unoccupied electronic state of the projectile, if the initially unoccupied final state becomes energetically degenerated with the electrons in the valence band.

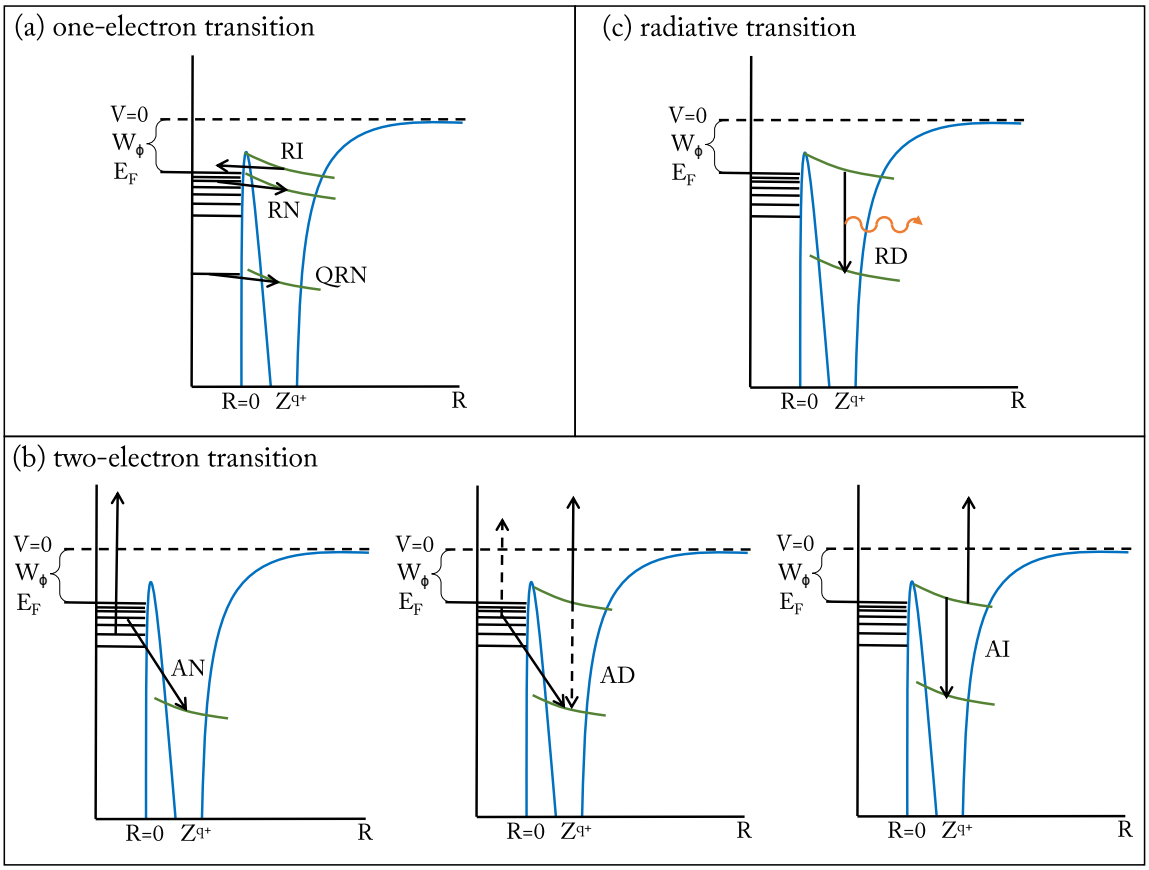

Figure 2.2: Schematic overview of electronic and radiative transition processes *Possible charge exchange- and relaxation channels in ion-surface interaction processes (for details cf. text). The one-electron (a) and two-electron (b) transitions belong to the 'radiationless' processes, (c) shows the electron energy diagram for radiative de-excitation. The arrows indicate the direction of the transitions. The figure is adapted from [19].*

Resonant ionisation RI The inverse process to RN takes place if levels in the conduction band of the solid are empty and the bonding energy of occupied exited states of the projectile become smaller than the surface work function W_ϕ.

Quasi-resonant neutralisation QRN In sufficiently close collisions, when the involved inner electronic orbitals are overlapping, electrons from tightly bound target states are transferred into projectile states.

Auger neutralisation AN Two electrons of the surface conduction band are involved, one is neutralising the ion and the other is ejected from the surface gaining the energy of the

electron-electron interaction. The process is only possible if a projectile state with a binding energy of at least twice the work function is unoccupied.

Auger de-excitation AD This process can proceed in a direct or indirect way. In the direct AD an excited projectile electron is de-excited into a lower state and an electron from the solid is ejected into vacuum. In the indirect way an electron from the solid is transferred to a lower state of the projectile and the projectile excited electron is emitted via electron emission.

Autoionisation AI In initially doubly or multiply excited projectiles, one or more electrons are ejected into vacuum while other electrons are demoted to lower states.

Besides electronic transitions, de-excitation of the projectile can also proceed by photon emission. Since the radiative transition rates are usually several orders of magnitude smaller than Auger transition rates, radiative processes are rather improbable. However, radiative de-excitation become competitive to Auger processes for inner-shell transitions in highly charged ions since the related transition rates increase approximately with the fourth power of the effective ion charge [19].
The de-excitation process by emission of soft X-rays was first demonstrated by Donets [32] and investigated in detail with high-resolution X-ray spectroscopy by Briand *et al.* [33]. In the latter investigation the term *hollow atom* was mentioned for the first time. In the following section a qualitative description of hollow atom formation and a scenario of HCI-solid interaction is given. This scenario was later successfully modelled in a quantitative way by the classical over the barrier model, first for metals and then extended to insulators.

2.1.2 Hollow atom formation and scenario of HCI-surface interaction

The term *hollow atom* describes a short-lived-multiply-excited neutral atom which carries a large part of the electrons in high n shells while inner-shells remain empty [18]. These hollow atoms are created when a highly charged ion interacts with a solid. The different steps of this process are depicted in fig. 2.3. At a relatively large distance above the surface (see next section) the ion captures electrons from the solid via resonant charge transition and because of energy matching, the electrons are captured in high Rydberg states. A hollow atom of the first generation is formed. In the following the hollow atom undergoes de-excitation processes and lower projectile shells are populated with electrons. These de-excitation process rates are generally too small, so that the ion is not relaxed but still excited when hitting the surface. This is reinforced by the image charge force which accelerates the ion towards the surface and sets an upper limit for the interaction

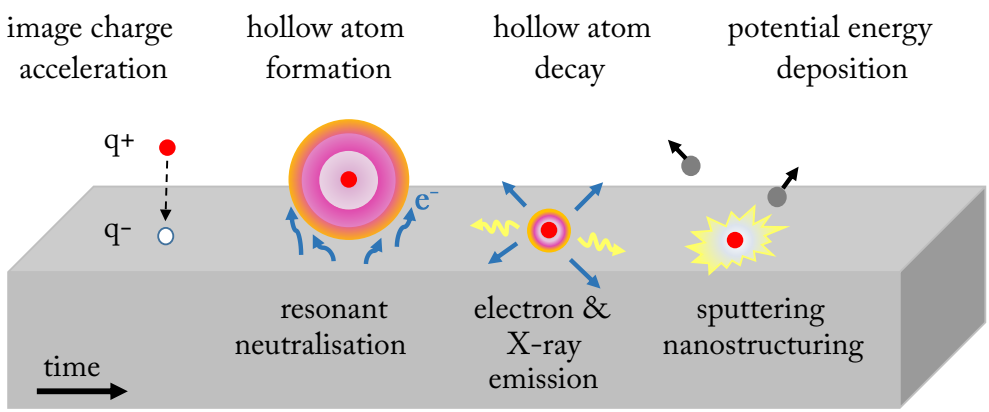

Figure 2.3: Scenario for HCI impact on a metal surface
The approaching HCI is accelerated by the image charge towards the surface. Electrons from the target are captured by the ion and the hollow atom of first generation is formed. De-excitation processes start but are not completed before the ion hits the surface. The electrons in the outer shells are peeled of and a more compact electron cloud is formed; a hollow atom of second generation is created. Ongoing de-excitation processes lead to a refilling of the inner-shells by emitting electrons and X-rays.

time of the HCI above the surface. Apart from that, the interaction time of the ion before hitting the solid is determined by the projectile velocity and the projectile-surface distance at which the electron capture process starts. This distance in turn depends on the projectile charge state and work function of the target material. As the ion hits the surface, the loosely bounded electrons in the outer-shells are peeled off and ejected either into the bulk or into vacuum. The ion becomes screened by a more compact cloud of target electrons, the hollow atom of the second generation is formed below the surface. In the last step the remaining inner-shell vacancies are refilled with electrons by emitting fast Auger electrons or soft X-rays.

2.1.3 Classical over the barrier model

The first theoretical modelling of the interaction of slow multiply charged ions with metals by Hagstrum [29] and Arifov [30] describes a stepwise electronic transition with subsequent autoionisation decay in a so called ladder sequence. This model faces the so called *bottleneck problem*, since the typical Auger rates are not larger than $10^{15}\,\mathrm{s}^{-1}$ and several steps are necessary to complete the whole ladder sequence. Since the interaction time between the first electron capture and the impact to the surface is much less than $10^{-13}\,\mathrm{s}$, the projectile will hit the surface long before the relaxation into the ground state is completed. This bottleneck problem was tried to be

circumvented by others by assuming anomalously high Auger rates [34, 35] or assuming larger distances of the first electron capture [36, 37].

The most convincing model was the classical over the barrier model (COB), which was first developed for a single electron capture during a HCI-atom collision [38], then enhanced to describe a multiple electron capture by Barany [39] and Niehaus [40] and later adapted by Burgdörfer [41] for HCI-surface interaction processes. In this model the target material plays an important role. In metals the conduction band includes occupied and unoccupied states which are separated by the Fermi level and the work function lies typically between 4 and 6 eV. In an insulator the occupied states in the valence band are separated from the unoccupied states in the conduction band by a band gap of several eV and the electron binding energies lie typically between 6 and 12 eV. In addition the dielectric response of an insulator depends on the dielectric function $\varepsilon(\omega)$ and differs from the one of metals. In the case of metals, the approach of a HCI causes a collective response of the electrons which can be described at large distance by the classical image potential. The active electron, which will be transferred from the surface to a high n-shell of the projectile, sees the electronic potential barrier between the HCI and the surface, which is a superposition of its own image potential, the interaction potential with the ion and the interaction potential with the image of the ion. At the critical distance of the projectile above the surface of

$$R_c \simeq \frac{\sqrt{8q+2}}{2W_\phi} \tag{2.1}$$

the potential barrier drops below the work function W_ϕ of the target and electrons are transferred to the projectile [41]. Resonant transitions are favoured and the COB model gives also a prediction of the principal quantum number n into which the first electron will be captured, namely

$$n \approx \frac{q}{\sqrt{2W_\phi}} \frac{1}{\sqrt{1+\frac{q-0.5}{\sqrt{8q}}}}. \tag{2.2}$$

During further approach of the projectile towards the surface, electrons from the higher n-shells will gradually move via electronic transitions to lower n-levels emitting Auger electrons into vacuum. Ongoing resonant neutralisation keeps the projectile neutral above the surface with electrons distributed among highly excited levels. The projectile underlies image charge acceleration until its complete neutralisation and therefore the greatest part of the acceleration is gained far

away until the distance of the first electron capture is reached. The kinetic energy gain of the projectile depends on its charge state and the work function of the target and is given by [42]

$$\Delta E \approx \frac{W_\phi q^{3/2}}{3\sqrt{2}} \tag{2.3}$$

Extending the COB model to insulating materials means to consider the different electronic structure and the dielectric response to a rapidly varying external electric field, characterised by a frequency dependent dielectric response function $\varepsilon(\omega)$. In comparison to metals for insulators the capture of electrons from the target leads to a charging of the surface, since the refilling of the holes needs more time than the electron transfer process. This can be taken into account by adapting the image potential energy of the active electron and the ion with the dielectric response function [43]. Further correction of the potential energy were performed by adding a polarisation energy, the Madelung potential energy[1] for ionic crystals and the screening potential term [44].

2.1.4 Promotion of energy levels and molecular orbital formation

Besides resonant transition of electrons from the target into high n-shells of the projectile at larger distances, with further approach the projectile energy levels are promoted and a direct and efficient filling of inner-shells by quasi-resonant charge transfer becomes possible [45]. This process is known in the literature as side-feeding. In fig. 2.4 the shifting of the binding energy of the outermost electron of O^{q+} ions for the electron configurations K^1L^k with k=1,...,8 in front of a gold surface is shown. The strong upwards shift even of the lowest lying state brings this level in resonance with the 5s and 5p level of gold [45]. Electrons from the 5s and 5p levels can directly be captured into inner-shell vacancies of the projectile.

A further attempt to describe inner-shell vacancy exchange in ion-atom collision was done with molecular orbital (MO) diagrams. The MO diagrams show the energy of electronic orbitals during the development of the collision system from separated atoms to an united atom. The first model calculating the molecular orbitals in atomic collisions between neutral atoms and ions by Fano and Lichten [46] was later extended by Arnau *et al.* [47] and Stolterfoht *et al.* [48] to describe hollow atoms colliding with solids. The investigated collision partners were on the one side hollow Ne ions with the configurations K^1L^k with k=1,...,5 and on the other side neutral Al atoms. The energy levels and screening were obtained by calculations based on the density functional theory (DFT). The calculations showed two characteristic features of the screening of the hollow atom

[1] The Madelung potential energy considers effects coming from the crystal structure of the insulator.

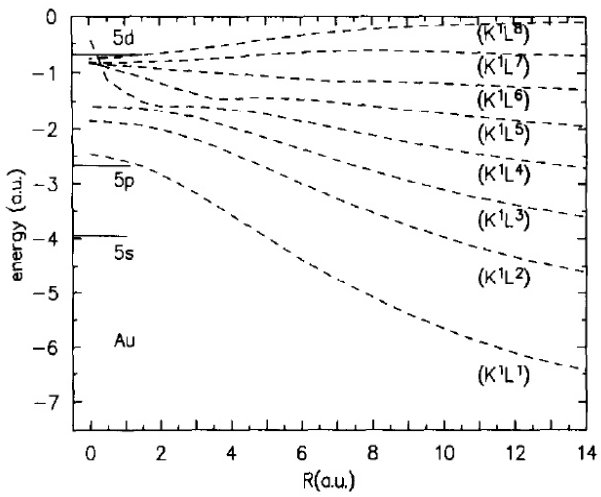

Figure 2.4: Promotion of energy levels
Upwards shifting of energy levels of outermost electrons of O^{q+} ions in the electronic configuration K^1L^k with k=1,...,8 as a function of the distance to a gold surface. The figure is taken from [45].

in the solid, on the one side the hollow character with a strong positive charge within the first few atomic units and on the other side an overscreening at about the size of the hollow atom (M-shell radius). For the presented Ne and Al system the L-shell vacancy transfer may take place via level crossing and level promotion as a consequence of the strong interaction between molecular orbitals, which correlate with the atomic L-shell levels of Ne and Al (see fig. 2.5).

2.1.5 Decay rates of multiply excited states

While the above mentioned decay processes concentrate on the lifetime of single excited states, Veack *et al.* [35, 49, 50] made the first attempt to investigate the lifetime of double and triple-excited states of hollow N atoms with many inner-shell vacancies. They calculated upper limits for the lifetimes of N atoms with the configuration $1s^M np^N$ with M=0-2, n=2-7, 10 and N=2-6. For each n value the lifetimes decrease with the increase of N. The shortest lifetimes (largest rates) were found for the neutral system in the order of $3-6\cdot10^{-16}$ s. However, the lifetimes increase with higher n. In N for n=8 the lifetimes are nearly one order of magnitude larger than for n=7 [35].

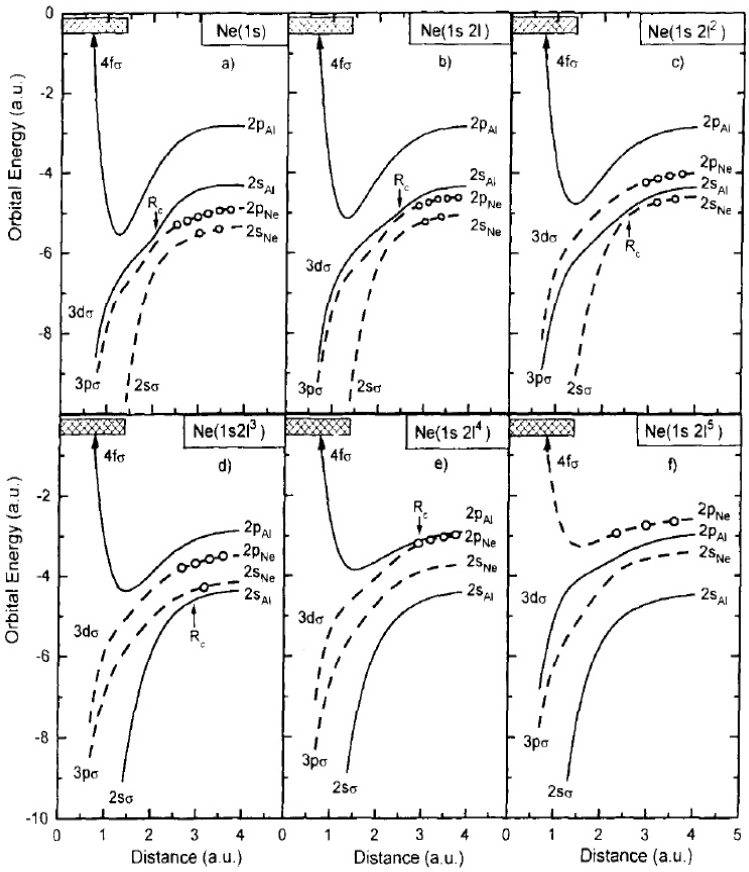

Figure 2.5: Molecular orbital diagrams
Molecular orbital energies for the hollow Ne and Al system. The open circles represent the missing electrons from 0 to 5 in the Ne L-shell. Charge transfer into the hollow atom take place via level crossing at the radius R_c and via level promotion. The figure is taken from [48].

2.1.6 Interatomic Coulombic decay - ICD

The general understanding of an electronic de-excitation process is that the quantum states of an electronic system typically decay by electron and/or photon emission. Highly excited states decay more efficiently by Auger processes emitting electrons and energetically low lying states decay more efficiently radiatively. The lifetime of these two processes depends only weakly on whether the atom is free or integrated in a molecular system. The decay rate is determined by the atomic electrons.

In case of clusters Cederbaum *et al.* [51] proposed in 1997 a novel type of an electronic decay mechanism, the interatomic or intermolecular Coulombic decay (ICD). This process describes a radiationless relaxation in which an inner-shell vacancy is filled by an outer-valence electron and

the released energy is transferred to one or several neighbouring atom(s) from which an electron is emitted into vacuum. The central difference between the ICD and the Auger decay process is therefore that the Auger process is an *intra-atomic* mechanism, whereas the ICD is *inter-atomic*. In the case of ICD the ions are embedded in an environment or have neighbours like in a cluster and the excess energy of the inner-shell vacancies are used to ionise neutral neighbours. The process is ultrafast, in the time order of femtoseconds, and the emitted electrons have kinetic energies of some eV. Some years after the theoretical description of this process, ICD could be confirmed experimentally. While initially ICD was found as an exotic feature of Van der Waals [Ne_n, NeAr] [52, 53] or hydrogen bonded systems [$(H_2O)_n$, $(HF)_n$)] [52], in the meantime this process has been established as a very general and common feature occurring after a manifold of excitation schemes and is in some systems more efficient than local Auger decay processes [54]. In the following section an elementary theoretical description of the ICD process will be given. For a detailed description see [55].

The system, which we are looking at, consists of an atom with an inner-shell vacancy and a neighbouring monomer (see fig. 2.6). The electronic decay process will refill the inner-shell vacancy by emitting an electron. We are dealing with an inner-shell vacancy in the orbital $|\varphi_{\mathrm{iv}}\rangle$ and an outer-valence electron in the orbital $|\varphi_{\mathrm{ov1}}\rangle$ of the atom. The state of the outer-valence electron of the neighbouring monomer is described with $|\varphi_{\mathrm{ov2}}\rangle$ and electrons of the continuum with $|\varphi_{\mathrm{k}}\rangle$. Two different physical mechanisms can induce the electronic decay process, associated with the exchange and the direct term. The exchange term describes the filling of the inner-shell vacancy of the atom with an outer-valence electron of the monomer and emission of the outer-valence electron of the atom. The direct term, however, describes the filling of the inner-shell vacancy with the outer valence electron of the atom and energy is transferred by a virtual photon to the outer valence electron of the monomer which is then emitted into vacuum. The latter one describes the ICD process. It should be stressed that no electron but only an energy transfer between the ion and the neighbouring monomer proceeds.

Looking once more to the electronic transition processes described by Hagsturm *et al.* [28, 29], it can be recognised that there the exchange and direct term were already mentioned and described with the indirect and direct Auger de-excitation process, respectively. For some years now the latter mentioned process experiences a renaissance under the name of ICD thanks to its importance in photoionisation processes of molecules in liquid environments.
The electronic decay width Γ_{iv} is given with

$$\Gamma_{\mathrm{iv}} = 2\pi \sum_{\mathrm{k}} \sum_{\mathrm{ov1}} \sum_{\mathrm{ov2>ov1}} |V_{\mathrm{ov1,ov2[iv,k]}}|^2 \delta(\varepsilon_{\mathrm{iv}} - \varepsilon_{\mathrm{ov1}} - \varepsilon_{\mathrm{ov2}} + V_{\mathrm{ov1,ov2[ov1,ov2]}} + \varepsilon_{\mathrm{k}} - V_{\mathrm{k,ov1[k,ov1]}} - V_{\mathrm{k,ov2[k,ov2]}}) \quad (2.4)$$

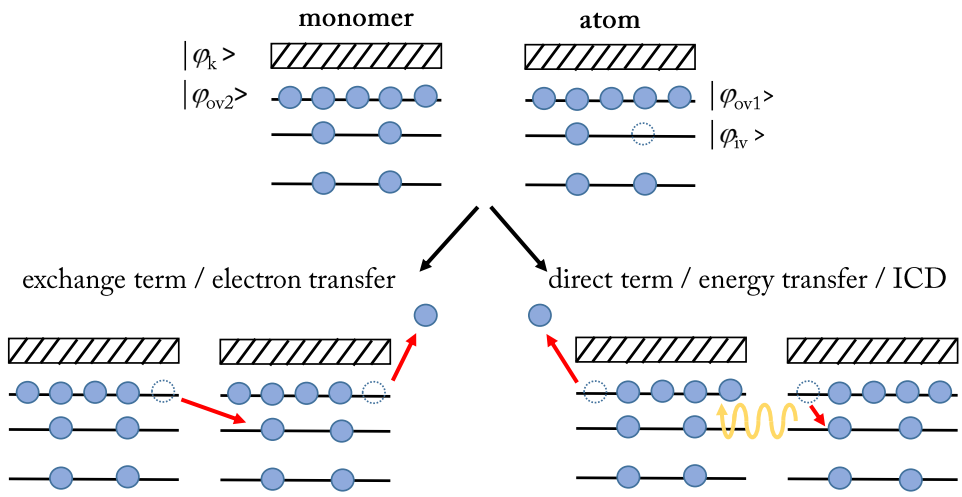

Figure 2.6: Schematic of the ICD process
The system consists of an atom with an inner-shell vacancy and a neighbouring monomer. The orbital of the inner-shell vacancy in the atom is described with $|\varphi_{\mathrm{iv}}\rangle$, the orbital of the outer valence electron in the atom with $|\varphi_{\mathrm{ov1}}\rangle$, the orbital of the valence electron of the neighbouring monomer with $|\varphi_{\mathrm{ov2}}\rangle$ and the electrons of the continuum with $|\varphi_{\mathrm{k}}\rangle$. Two physical mechanisms can lead to a refilling of the inner-shell vacancy of the atom, one related to electron and the other to energy transfer between the ion and the neighbouring monomer. The latter one describes the ICD process.

The rate is proportional to $|V_{\mathrm{ov1,ov2[iv,k]}}|^2 = |V_{\mathrm{ov1,ov2,iv,k}} - V_{\mathrm{ov1,ov2,k,iv}}|^2$, where the two electron-electron Coulomb matrix elements

$$V_{\mathrm{ov1,ov2,iv,k}} = \int\int \varphi^*_{\mathrm{ov1}}(x_1)\varphi_{\mathrm{iv}}(x_1)\frac{e^2}{|x_1 - x_2|}\varphi^*_{\mathrm{ov2}}(x_2)\varphi_{\mathrm{k}}(x_2) \tag{2.5}$$

and

$$V_{\mathrm{ov1,ov2,k,iv}} = \int\int \varphi^*_{\mathrm{ov1}}(x_1)\varphi_{\mathrm{k}}(x_2)\frac{e^2}{|x_1 - x_2|}\varphi^*_{\mathrm{ov2}}(x_2)\varphi_{\mathrm{iv}}(x_1) \tag{2.6}$$

are the direct and exchange contributions to the refilling process of the inner-shell vacancy, respectively. The δ function specifies the decay channels for the inner-shell vacancy with the ionisation potential $-\varepsilon_{\mathrm{iv}}$. The energy of the dicationic state with the holes in $|\varphi_{\mathrm{ov1}}\rangle$ and $|\varphi_{\mathrm{ov2}}\rangle$ is given as the the sum of the ionisation potentials of the two outer valence holes $-\varepsilon_{\mathrm{ov1}}$ and $-\varepsilon_{\mathrm{ov2}}$, and the Coulomb interaction between them $V_{\mathrm{ov1,ov2[ov1,ov2]}}$. The energy of the emitted electron is given by ε_{k} and the interaction of this electron with the two holes is given by $-V_{\mathrm{k,ov1[k,ov1]}} - V_{\mathrm{k,ov2[k,ov2]}}$. By going back to the coupling matrix element $V_{\mathrm{ov1,ov2,iv,k}}$ and $V_{\mathrm{ov1,ov2,k,iv}}$ and looking at the compactness of the orbitals, we see hardly any overlap between $|\varphi_{\mathrm{iv}}\rangle$ and $|\varphi_{\mathrm{ov2}}\rangle$. Therefore, the de-excitation process is dominated by the direct term. Comparing it again with normal Auger

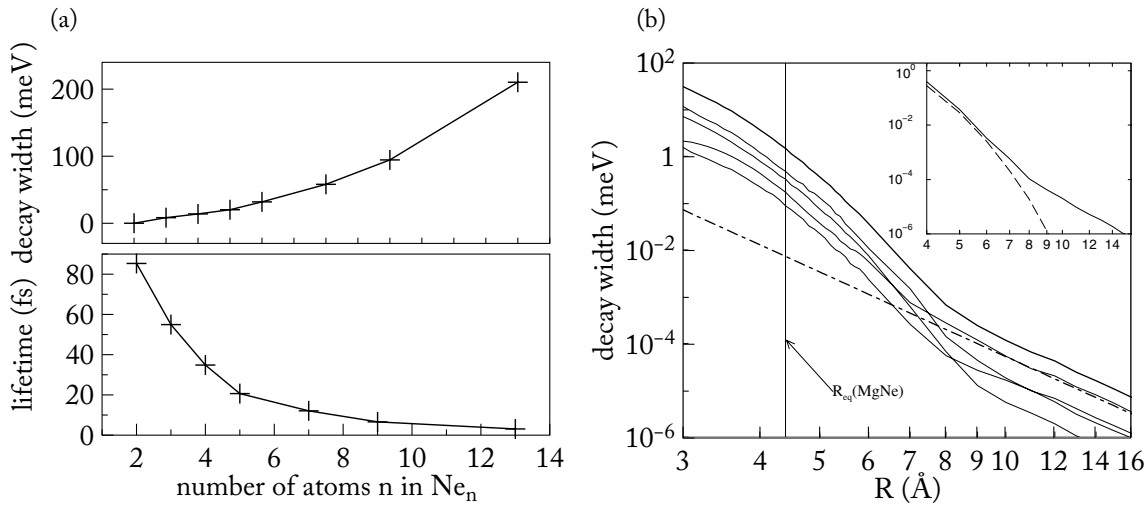

Figure 2.7: ICD width in dependence of cluster size and distance
(a) The electronic decay width and the corresponding lifetime of an inner-shell vacancy for Ne clusters of different sizes. An appreciable decrease of the lifetime of the inner-shell vacancy can be observed by increasing the cluster size. The data points were taken from [55]. (b) A strong increase of the decay rate at closer distances is visible. The figure is taken from [56].

decay processes with the core orbital $|\varphi_{\mathrm{iv}}\rangle$ very localised at its nucleus, the decay process is only efficient if the resulting valence orbital vacancies $|\varphi_{\mathrm{ov1}}\rangle$ and $|\varphi_{\mathrm{ov2}}\rangle$ are also localised or possess localised components at the same nucleus. In the case of ICD, only the orbitals $|\varphi_{\mathrm{iv}}\rangle$ and $|\varphi_{\mathrm{ov1}}\rangle$ have to overlap. $|\varphi_{\mathrm{ov2}}\rangle$ is on a neighbouring monomer and overlaps with the wave function of the emitted electron, which has a relatively long wavelength, in contrast to the Auger electron, which is fast and its wave function oscillates rapidly.

From calculations it is predicted that the ICD process becomes more effective if more inter-atomic decay channels are accessible [55]. This can be achieved by an increase of the cluster size. The lifetime can thereby decrease from hundreds of femtoseconds down to a few femtoseconds, depending on the cluster size (see fig. 2.7a).
Moreover, while the decay rate shows a $1/R^6$ dependency for larger distances R, a calculations by Averbukh *et al.* [56] revealed an even stronger enhancement of the decay rate for smaller distances (see fig. 2.7b).

2.1.7 Nanostructuring

The neutralisation of a highly charged ion due to interaction with a solid is coming along with the deposition of a large amount of potential energy into the solid. This energy transfer may cause nanostructuring of the material. The kinetic energy of the projectile determines how deep insight the target the potential energy of the HCI is deposited and by sufficient small kinetic energies the creation of defects can be limited to the topmost atomic layers of the target. The deposition of potential energy means the capturing and emission of many electrons above and insight the target. On the way to the solid surface the highly charged ion undergoes a large number of neutralisation and de-excitation processes, as mentioned before, which lead to unbalanced holes in the target and a release of electrons with low kinetic energies and up to a few keV. Thus, in the first step the potential energy is deposited into the electronic system of the target and converted into kinetic energy of primary emitted electrons. This primary created electrons can directly be emitted into vacuum or produce by elastic and inelastic scattering processes secondary electrons. In collisions of electrons with lattice atoms, phonons may be excited and thus energy is transferred from the electronic to the lattice system. The lattice temperature will increase and at enough high energy release melting occurs. First of all low-energy electrons contribute to this process, since high-energy electrons spread their energy over a larger volume. The rearrangement of lattice atoms leads to permanent modifications which were observed for various materials ([11] and citation therein). Based on experimental studies and model calculations [57,58], nanostructure formation with slow highly charged ions may be visualised by the following scenario (see fig. 2.8):

- Singly or low charged ions create individual defects at or below the surface. They might be not detectable as topographical but as frictional modifications [59].

- With increasing the charge state of the ions the density of defects increases leading to defect clusters which can also diffuse to the surface and form pits. They can become also visible after etching [60, 61].

- At higher charge states the heating of the lattice atoms by primary and secondary electrons may exceed the melting temperature of the solid leading to a deformation of the surface. Heat and pressure deform the surface and after cooling hillocks or caldera-like structures are formed [62].

- At considerably higher potential energies a further threshold has been predicted [63], above which sublimation/evaporation of atoms and clusters may occur.

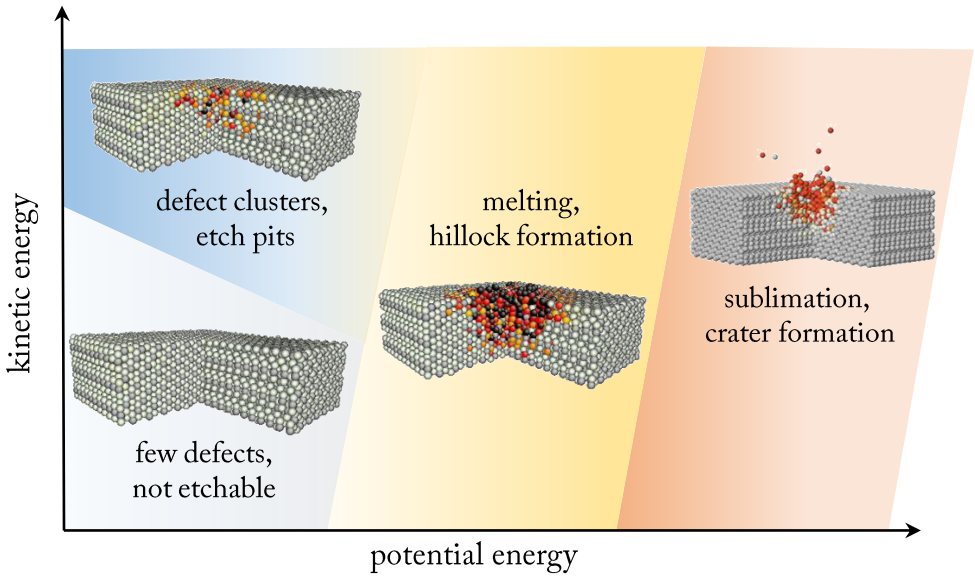

Figure 2.8: Scenario of nanostructuring
Singly or low charged ions create single defects, which might be not detectable, also after etching. An increase of the charge state or the kinetic energy also increases the density of defects, which form pits at the surface or become visible after etching. At higher charge states heating of the lattice exceeds the melting temperature and after rapid quenching hillocks are formed. At considerably higher potential energies evaporation of atoms may occur.

2.2 Energy transfer from ions to solids

Besides the potential energy deposition from charged ions into solids, the particle looses kinetic energy while passing matter, until it is finally stopped. The basis quantity which has to be determined is the energy loss per path-length, given by dE/dx. This quantity is known as *energy loss*, *linear energy transfer* or *stopping power*, whereas the latter expression is not strictly correct, since a power is defined by dE/dt, but nevertheless accepted in the physics community. A better term is stopping force or stopping cross section $S = \frac{1}{N}\mathrm{dE/dx}$. In general the energy loss can be divided into two parts, namely the loss to the target atoms (nuclear stopping) and the loss to the electronic system (electronic stopping) of the target. For slow particles the energy loss is dominated by nuclear stopping, for high energies by electronic stopping. Fig. 2.9 shows the energy loss due to nuclear and electronic stopping as a function of the kinetic projectile energy for the irradiation of a $SrTiO_3$ target with Xe atoms, calculated using the SRIM code [64].

The two mechanism are described in more detail in the following paragraphs and the difficulties arising by considering also charged projectiles will be mentioned. For a more detailed discus-

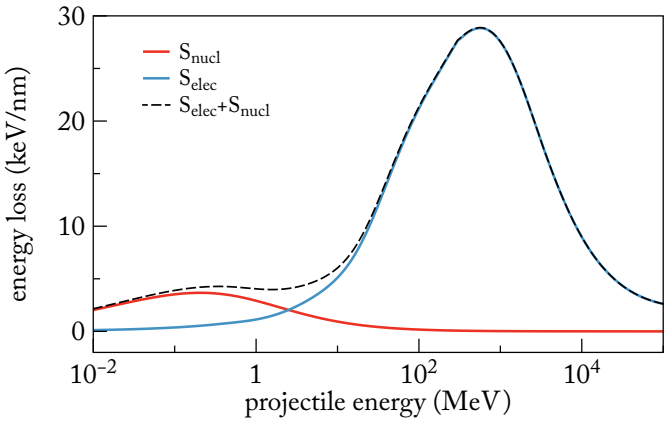

Figure 2.9: Nuclear and electronic energy loss
Energy loss due to nuclear and electronic stopping as a function of the kinetic particle energy for the irradiation of a $SrTiO_3$ target with Xe atoms, calculated using the SRIM code [64].

sion of the energy loss formalism I refer to the PhD thesis of R. A. Wilhelm [65] and references therein.

2.2.1 Nuclear stopping

Nuclear stopping describes elastic collisions between a projectile and a target atom and the established approach to calculate it is to regard it as a sequence of single binary scattering events. Classically the scattering angle of an elastic collision in the centre of mass system is calculated with

$$\Theta(p) = \pi - 2\int_{r_{\min}}^{\infty} \frac{p\mathrm{d}r}{r^2\left[1 - \frac{V(r)}{E_{\mathrm{CMS}}} - \frac{p^2}{r^2}\right]^{1/2}} \tag{2.7}$$

with the impact parameter p, the scattering potential $V(r)$ and the energy of the projectile in the centre of mass system E_{CMS}. The transferred energy is calculated from the energy and momentum conservation law to

$$T(p, E_{\mathrm{CMS}}) = \frac{4m_1}{(m_1 + m_2)} E_{\mathrm{CMS}} \sin^2\left(\frac{\Theta_{\mathrm{CMS}}(p, E_{\mathrm{CMS}})}{2}\right) \tag{2.8}$$

and depends on the scattering angle and the impact parameter. The nuclear stopping cross section is obtained by integrating the transferred energy over all possible impact parameters

$$S_n = \int_0^\infty T(p, E_{\mathrm{CMS}}) 2\pi p \mathrm{d}p. \tag{2.9}$$

The main task to describe and solve the scattering problem between the two scattering partners is to find the appropriate scattering potential $V(r)$. A first attempt for the scattering potential between neutral scattering partners was given by Thomas and Fermi [66, 67] by using a screened Coulomb potential of the form

$$V(r) = \phi(r/a_S)\frac{Z_1 Z_2 e^2}{r} \tag{2.10}$$

with the atomic numbers of the colliding nuclei being Z_1 and Z_2 and the screening potential $\phi(r/a_S)$ with the screening length a_S. In course of time various approaches for the screening potential were developed [68, 69], whereas the most accurate screening function was given by Ziegler, Biersack and Littmark (ZBL) [70] by comparing experimental data. They introduced the so called universal screening function

$$\phi(r/a_U) = 0.1818e^{-3.2r/a_U} + 0.5099e^{-0.9423r/a_U} + 0.2802e^{-0.4028r/a_U} + 0.02817e^{-0.2016r/a_U} \tag{2.11}$$

with $a_U = \frac{0.8853a_0}{(Z_1^{0.23} + Z_2^{0.23})}$. In this description the projectile and the target atoms are assumed to be neutral.

2.2.2 Electronic stopping

Electronic stopping defines inelastic collisions between the projectile and the electrons of the target. The stopping is governed by a number of excitation and ionisation processes of the target electrons, electron capture and projectile excitation and ionisation, and cannot be treated as a classical scattering process between two particles. At high kinetic energies (above several hundred keV/amu) the best known theoretical treatment for electronic stopping is given by the Bethe-Bloch formula [71]

$$-\frac{\mathrm{d}E}{\mathrm{d}x} = \frac{4\pi}{m_\mathrm{e}c^2}\frac{nz^2}{\beta^2}\left(\frac{e^2}{4\pi\varepsilon_0}\right)^2\left[\ln\left(\frac{2m_\mathrm{e}c^2\beta^2}{I(1-\beta^2)}\right) - \beta^2\right] \tag{2.12}$$

with $\beta = v/c$, the vacuum permittivity ε_0, the electron charge e and the electron mass m_e. In this case the interaction of the relativistic particle with matter is described by a point charge z travelling through a target with the electron number density $n = \frac{N_\mathrm{a} Z\rho}{AM_\mathrm{u}}$ (with the Avogadro number N_a, the atomic number Z, the density of the material ρ, the relative atomic mass A and

the molar mass constant M_u) and the excitation potential I. At lower kinetic energies theoretical investigations of electronic stopping become more difficult. In this energy regime the energy loss is dominated by electron capture and loss of projectile electrons and so the screening of the nucleus by the surrounding electrons of the projectile has to be taken into account. At projectile velocities $v \leq v_{\text{Fermi}}$ the Bohr criterion can be used to estimate the equilibrium charge state of the projectile which is reached by subsequent electron capture and loss during the passage of matter. The equilibrium charge state is given by [72]

$$q_{\text{eq}} = \frac{v}{v_0} Z^{1/3} \tag{2.13}$$

with the Bohr velocity $v_0 = 2.19 \cdot 10^6\,\text{m/s}$.
Different theoretical approaches were developed to treat the electronic stopping at low velocities. One of these is the model developed by Firsov [7]. In this model at close impact of the projectile and the target a quasi molecule is formed and electrons from the projectile or the target atom can pass the overlapping intersection of the electron cloud and transfer thereby a netto momentum. The energy loss strongly depends on the impact parameter and on the number of electrons transferred in the collision. By knowing the transferred momentum the acting force on the target atom and projectile is determined. The energy loss is then calculated by the integral of the force along the trajectory of the projectile. The transferred momentum depends on the electrostatic potential of the collision partners since this represents the electron density. The main task is therefore to find the 'right' electrostatic potential.
Another attempt to estimate the electronic stopping was done by Lindhard and Scharff [73]. They used a description independent of the impact parameter since they modelled the momentum transfer to an uniform electron gas where the electrons have a slight drift velocity relative to the ion. During the collision with the ion a net energy is transferred.
Both presented models come to the conclusion that the electronic energy loss is linearly dependent on the projectile velocity $S_e \propto v$.

Besides theoretical studies also several semi-empirical computations of the electronic stopping were developed based on the concept of relating the stopping to the equivalent proton stopping power. This is called the heavy-ion scaling rule [74]. In this case the electronic stopping scales with

$$S_e(Z_p, v_p) = (Z_p^{\text{eff}})^2 S_e(\text{proton}, v_p) \tag{2.14}$$

with the nuclear charge Z_p, the effective charge Z_p^{eff} and the proton stopping power $S_e(\text{proton}, v_p)$, obtained from a large experimental data set. The stopping power problem is transferred to the definition of the effective charge.

In the Brandt and Kitagawa approach [75], only the valence electrons, described by an electron gas, cause electron stopping. The electrons from the projectile only screen the nucleus field. By assuming that the projectile electrons are radially distributed according to a function $e^{-r/\Lambda}/r$ with the screening length Λ, the effective charge is given by

$$\frac{Z_p^{\text{eff}}}{Z_p} = q + C(v_{\text{Fermi}})(1-q)\ln\left(1+(2\Lambda v_{\text{Fermi}})^2\right) \tag{2.15}$$

with the Fermi velocity of the valence electrons v_{Fermi}. The quantity $C(v_{\text{Fermi}})$ depends only weakly on the Fermi velocity and can be taken as 0.5. The first term is the mean charge state of the projectile divided by the projectile nuclear charge and describes the target electrons which do not penetrate the ion's electronic volume. The second term describes the electrons which penetrate the electronic cloud and increase the energy loss. The sum of these two generate the effective charge. Ziegler, Biersack and Littmark (ZBL) [70] used the effective charge model of Brandt and Kitagawa to perform a large compilation and put all the data in a compact routine. Today, ZBL stopping is the by far most used model for electronic stopping.

2.2.3 Energy loss of charged particles

While the existing mathematical and semi-empirical models depict the energy loss for nearly all possible projectile-target combinations [70], the understanding of the role of high charge states on the stopping power is still under discussion. The distinction of nuclear and electronic energy loss is not necessary justified for slow highly charged ions, since the individual processes might be coupled. First order perturbation approaches predict a quadratic dependency of the energy loss on the projectile's nuclear charge state, but are only valid at sufficiently high projectile velocities [76, 77]. For HCIs, charge exchange, excitation and ionisation processes will change the charge state until the equilibrium is reached. The captured electrons will change the Coulomb potential of the nuclear charge and affect the stopping force. A strong enhancement in kinetic energy loss was predicted by Biersack [78] and also experimentally observed by Schenkel *et al.* [20] and by ourselves [22, 23].

At low kinetic energies only the energy loss of medium charged ions in dependence of the number of inner-shell vacancies was calculated, but no universal scaling was deduced from this [79]. A simple model, based on the statistical description of atoms and ions by Thomas and Fermi [66,67] is given in [80]. The formalism for calculating the energy loss depends on the choice of an appropriate electrostatic scattering potential of the incident particle and the electrostatic potential of the scattering partner. By using a modified electrostatic potential which takes the ionic charge

into account, the nuclear and electronic loss were calculated. This model predicts that the nuclear as well as the electronic energy transfer is strongly enhanced for slow, highly charged ions.

2.3 Interaction of swift heavy ions with solids

Swift heavy ions (SHI) are characterised by slowing down in matter predominantly due to electronic excitation and ionisation of target atoms, which is fullfilled for kinetic energies around the maximum of the energy loss curve (see fig. 2.9). Only at the end of the trajectory, for kinetic energies of some keV, nuclear stopping becomes also important [11].
The irradiation of solid targets with SHI leads to modification in the bulk and at the surface. Each individual projectile may induce a continuous or discontinuous trail of defects resulting from a nanometric, dense and shortly created electronic excitation with a hillock or crater-type nanostructure at the impact site. This track formation occurs predominantly in insulators and can be linked to a critical energy loss. Compared to damage results from direct atom-atom interaction, the track resulting from electronic excitation is a four step process [81] (see fig. 2.10):

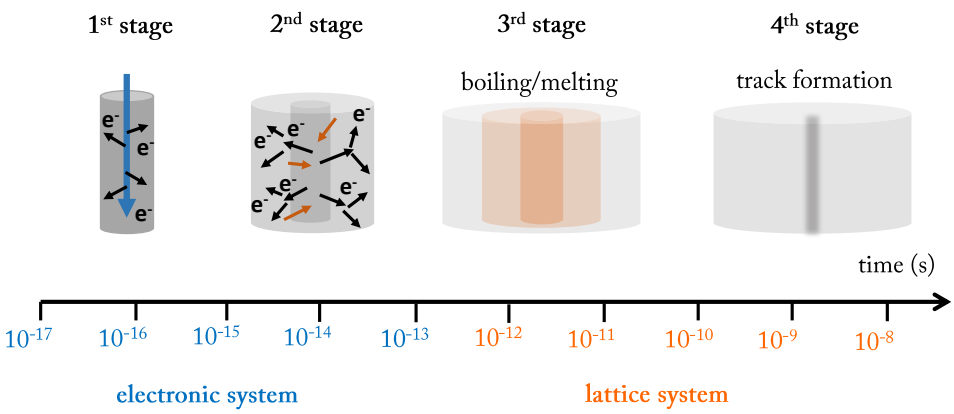

Figure 2.10: Schematic of energy deposition due to SHI irradiation
Schematic of different processes related to the energy deposition to the electrons and its relaxation to the lattice system. In the first stage the ions transfer their energy to target electrons by ionisation and excitation. In the second stage the primary electrons transfer their energy to other electrons and the Coulomb field, created in the first stage, is screened by returning electrons. In the third stage the energy is transferred from the electronic to the lattice system by electron-phonon coupling causing a thermal spike. In the forth stage the energy is dissipated among other atoms and structural modifications might occur. Schematic is adapted from [82].

- first stage: incident ions transfer their energy to the electrons of the target; ion-electron collision causes the ionisation of the target atom which leads to a positive charge along the ion path and the creation of a high electric field

- second stage: energy from the electrons of the first generation is transferred by electron-electron collisions to other electrons; the Coulomb field from the first stage is screened by the returning electrons

- third stage: energy is transferred from the electronic to the lattice system by electron-phonon coupling; the atomic lattice responds to the perturbation with a thermal spike, the atomic temperature increases or shock waves are generated

- forth stage: energy dissipation among the atoms; possible atomic motion and structural modifications

The temporal and radial distribution of energy deposition into the electronic system can be done by performing Monte Carlo calculations. The exact mechanism how the excitation energy is transferred from the electronic to the lattice system is still under discussion and several macroscopic models were proposed to describe this mechanism [82]. Some of them are presented in the following section. The most elaborated model, which can be applied to all kinds of materials, i.e. metals, semiconductors and insulators, is the thermal spike model.

2.3.1 Models for damage creation

Coulomb explosion model

The Coulomb explosion model was developed by Fleischer *et al.* [83] in 1965 as the *ion explosion spike mechanism*. The ion-electron collision leads to the ejection of electrons and the ionisation of the target atoms. A Coulomb field along the ion path in a volume of about $1\,\mathrm{nm}^3$ during a time period of about $10^{-14}\,\mathrm{s}$ is created. The Coulomb repulsion between the ions ejects them from their original place in the surrounding lattice and the periodic structure may be damaged. The model describes under which conditions the repulsive Coulomb forces prevail over the lattice bonding forces. If the electronic stress $\sigma_e = \frac{n^2 e^2}{\varepsilon a_0^4}$ (n is the average ionisation, ε the dielectric constant, a_0 the mean atomic spacing) is larger than the mechanical strength $\sigma_m = \frac{Y}{10}$ (Y is Young's modulus), atomic motion is expected and can lead to track formation.
From this model we can conclude that track formation is more likely in materials with low me-

chanical strength, a small dielectric constant or a small interatomic distance. While the model described by Fleischer *et al.* was applicable for insulators, it couldn't explain the great sensitivity to electronic excitation of metals [84]. Therefore the model was extended by Lesueur and Dunlop [85] and applied to pure metallic materials [86].

Bond weakening (BW) model

Electron excitation affects bonding electrons and may affect interatomic forces, leading to structural modifications and decomposition of chemical bonds. The BW model points to a strong dependence of the crystal structure on the corresponding electronic structure [87]. Primary the model was developed to explain laser annealing of defects in Si [88]. It appeared that the electron-hole pair creation by the laser light absorption was too small to ensure thermal annealing and therefore a transient thermal process was developed to explain such annealing [89]. Recent calculations for Si, Ge and GaAs [90] have shown that excitation and hence valence electron loss by 15% induces instabilities in the lattice within 100 fs. The excitation from bonding valence orbitals to antibonding conduction band orbitals may lead to a rapid structural rearrangement. Extended discussion can be found in [82] and references therein.

Self-trapping exciton (STX) model

SHI irradiation can induce excitation of electrons and holes which polarise the surrounding lattice creating a distortion of a crystal. The electron-hole pair can be trapped by the created distortion and form a so called self-trapped exciton (STX). The trap makes the STXs immobile and unables the energy density to decrease via outward diffusion. The STXs localise energy and decay by radiative and non-radiative mechanism. The non-radiative mechanism transfers energy to phonons, inducing lattice heating, or by forming Frenkel pairs[2]. A quantitative development of this model has been done for crystalline SiO_2 [91]. It could be shown that the lattice order will not be maintained if the exciton density is equal to the number of the SiO units. Clusters of STXs cause then lattice instability and atomic displacements.

Thermal spike model

The most successful model to describe many structural effects in materials due to SHI irradiation is the thermal spike model, or denoted more specifically, inelastic thermal spike (i-TS) model to emphasise the difference to elastic collisions in the nuclear energy loss regime. In the i-TS model

[2] A Frenkel pair is a type of point defect in the lattice of a crystal. An atom leaves its place in the lattice, a vacancy is created and becomes an interstitial in the nearby location.

the solid is considered as a two component system, the electronic and atomic sublattice. The incident ions deposit their energy by ion-electron interactions into the electronic system where the energy diffuses by electron-electron interactions and is then transferred via electron-phonon coupling to the lattice system. The heat diffusion in the electron and lattice subsystem as a function of space r and time t (in cylindrical geometry) is given by two coupled differential equations:

$$C_{\mathrm{e}}(T_{\mathrm{e}})\frac{\partial T_{\mathrm{e}}}{\partial t} = \frac{1}{r}\frac{\partial}{\partial r}\left[rK_{\mathrm{e}}(T_{\mathrm{e}})\frac{\partial T_{\mathrm{e}}}{\partial r}\right] - g(T_{\mathrm{e}} - T_{\mathrm{a}}) + A(r,t) \tag{2.16}$$

$$C_{\mathrm{a}}(T_{\mathrm{a}})\frac{\partial T_{\mathrm{a}}}{\partial t} = \frac{1}{r}\frac{\partial}{\partial r}\left[rK_{\mathrm{a}}(T_{\mathrm{a}})\frac{\partial T_{\mathrm{a}}}{\partial r}\right] + g(T_{\mathrm{e}} - T_{\mathrm{a}}) \tag{2.17}$$

with $T_{\mathrm{e,a}}(r,t), C_{\mathrm{e,a}}(r,t)$ and $K_{\mathrm{e,a}}(r,t)$ being the temperature, the heat capacity per unit volume and the thermal conductivity of the electronic (e) and atomic (a) system, respectively. The input energy is given by the radial and time distribution function $A(r,t)$. The only free parameter is the electron-phonon coupling strength g.

In the course of time different approaches to explore the heat diffusion equations were developed. The analytical thermal spike (a-TS) model [92, 93] provides an analytical solution for the differential equation of the atomic system eq. 2.17, whereas the energy transfer to the atoms is ignored. An analytical solution for the differential equation of the electronic subsystem eq. 2.16 is given in the ionisation diffusion-explosion amorphisation (IDEA) model [94]. A complete numerical solution for both eq. 2.16 and 2.17, taking the coupling into account, is given by the inelastic thermal spike (i-TS) model [95–98]. The common features of this model will be discussed in more detail in the following paragraph.

The mentioned input energy, given by the function $A(r,t)$, is obtained by Monte Carlo calculations for a specific beam energy. The radial distribution of the energy deposited into the electronic system is calculated by the evolution of the kinetic energy in the electron cascade as a function of the radial distance and time. The electronic energy deposition is considered as constant along the trajectory and therefore the eq. 2.16 and 2.17 are given in cylindrical coordinates. The initial boundary conditions are given by the internal energy of the irradiated lattice system and the volume in which the calculations are performed. The latter one should be sufficiently large so that the temperature gradient is negligible far away from the center of the trajectory. The model provides the temperature around the trajectory as a function of time and space, which depends on the efficiency of the coupling between the electronic and atomic subsystem. The coupling is given by the electron-phonon coupling strength g, which is connected with the electron-phonon relaxation time $\tau = C_{\mathrm{e}}(T_{\mathrm{e}})/g$ and the electron-phonon mean free path λ by $\lambda^2 = D_{\mathrm{e}}(T_{\mathrm{e}})\cdot\tau = K_{\mathrm{e}}(T_{\mathrm{e}})/g$ with $C_{\mathrm{e}}(T_{\mathrm{e}})$, $K_{\mathrm{e}}(T_{\mathrm{e}})$ and $D_{\mathrm{e}}(T_{\mathrm{e}})$ being the specific heat, thermal conductivity and diffusion constant for the electronic temperature T_{e}, respectively. The equilibrium melting temperature T_{m} obtained by

the model has not the usual meaning of a temperature but should be seen as an equivalent energy transferred to the atoms. The energy which is necessary to reach the molten phase is defined as the energy to reach the melting temperature plus the latent heat of fusion [95]. This is the so called superheating melting temperature and can reach values up to 500 K above the melting temperature [99]. The same is the case for the boiling temperature and heat of evaporation. The largest radial zone of the atoms, which contains sufficient energy to induce the molten phase, defines the size of the formed track.

3

Ion Sources and Methods

Since the development of accelerators in the last century, it's possible to produce ions with relatively high kinetic energies. With these fast ions the ion-solid interaction processes are dominated by the kinetic energy of the projectiles. With the advent of sources for the production of highly charged ions, the interest of ion-solid interaction field was pushed towards HCI-solid interaction processes. In the presented thesis both types of ions are studied and therefore various types of ion sources were used. The first part of this chapter gives an overview on the working principle of sources for the production of HCIs and SHIs. After the irradiation of the samples high resolution microscopy techniques were used to characterise the materials and investigate topographical changes. The operation modes of the used microscopes are presented in the second part of this chapter.

3.1 Ion sources

In the course of this work various targets have been irradiated with SHIs and HCIs. The irradiations have been conducted partially at the home institute at TU Wien, but mainly during measurement periods at different institutions.

3.1.1 Sources for HCIs

HCIs are ions in high charge states due to the loss of many or most of their bound electrons and are primarily produced by using stripper foils, electron cyclotron resonance ion sources (ECRIS) or electron beam ion traps (EBIT). In all three cases the production of HCIs is based on electron impact ionisation but differs in how the energy is coupled into the atomic system. In the case of stripper foils (most commonly carbon or metal foils) singly or doubly charged ions are accelerated to high kinetic energies and carried through a nm thick stripper foil. By passing this foil, many or all remaining electrons of the ions are stripped off and highly charged or even naked ions according to eq.2.13 are created.
For the performed irradiations discussed in this thesis electron cyclotron ion sources and electron beam ion traps were used and their working principle is described in more detail in the following two paragraphs.

Electron cyclotron ion source - ECRIS

The working principle of an ECRIS is to heat electrons in a magnetically confined plasma by injecting microwaves at the electron cyclotron resonance frequency $\omega_{\text{cycl}} = eB/m_e$ [12] and ionise atoms by electron-atom/ion collisions. The production of HCIs based on electron cyclotron resonance plasma heating was developed by R. Geller and coworkers [100] at the end of the 1960's. At low frequencies (f $<$ 2.45 GHz) intense beams of low charged ions can be created. To produce highly charged ions, higher frequencies ($f > 2.45$ GHz) are favorable which in turn require sufficiently strong magnetic fields to guarantee plasma confinement. This is achieved by normal or superconducting electromagnets. The choice of permanent magnets instead limits the usable frequency to about 14 GHz.
For the presented measurements the HCIs were extracted from the 14.5 GHz ECRIS at the TU Wien [101] and at ARIBE, a low energy ion beam facility of GANIL (Grand Accélérateur National d'Ions Lourds) in Caen, France [102]. Representative for both ion sources, the setup and operating mode of the ECRIS at TU Wien is briefly discussed (see fig. 3.1 and for more details [101]).

The plasma confinement is generated by four permanent magnet rings (two axially and two radially magnetised rings) and a Halbach-type hexapole. The plasma is heated by microwaves, which are created by a thin film oscillator and after amplification they are guided along a travelling wave tube into the plasma chamber, which is separated from the outside by a 2 mm thick PTFE window. The gas inlet system allows the mixing of different gases in the source, what facilitates the production of multiple charged ions. In the case of Ar as working gas a charge state up to $q = 14$ can be achieved due to a step-by-step ionisation. The extraction system consists of three

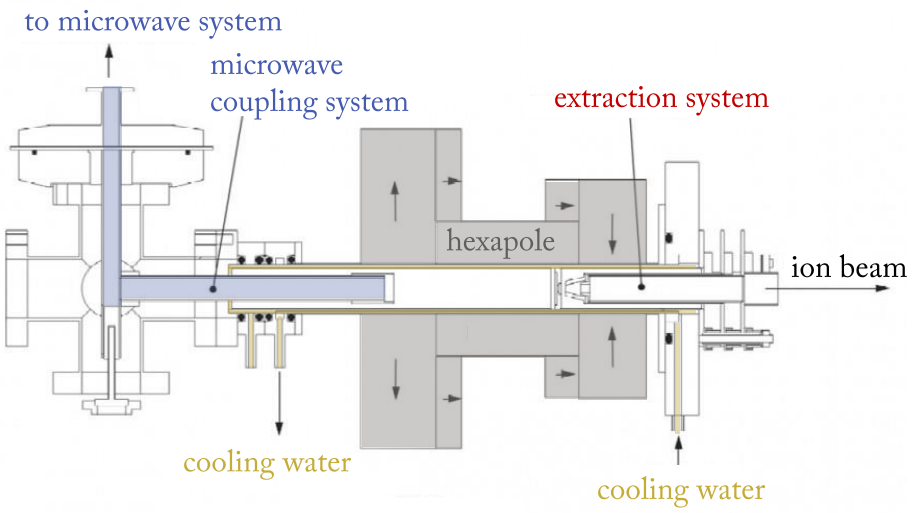

Figure 3.1: Schematic of the ECR ions source SOPHIE at the TU Wien
The 14.5 GHz heated ECR ion source generates due to a step-by-step ionisation in a minimum-B multi mirror magnetic structure slow medium charged ions. The figure is adapted from [101].

cylindrical concentric electrodes. The source can be operated with extraction potentials of up to 6 kV and enables therefore the generation of medium charged ions at kinetic energies of some tens of keV ($E_{\text{kin}} = q \cdot U$, with q being the charge state of the extracted ions and U the extraction potential of the source).

Electron beam ion trap - EBIT

At the same time as Geller and coworkers developed the first ECRIS, another type of a HCI source, namely the electron beam ion trap (EBIT), was evolved by Donets (see [32] for a historical review). The EBIT is an electromagnetic bottle in which highly charged ions are produced and trapped. The HCIs are created due to stepwise ionisation by a dense and focused electron beam. The electron beam is generated by a filament and focused with a strong magnetic field, which is induced by a superconducting magnet (cryogenic EBIT) or a permanent magnet (room-temperature EBIT). The strong negative space charge of the electron beam produces radially a well for the positively charged ions. In axial direction the ions are confined by potentials of cylindrical electrodes around the beam. The trapped ions are ionised until the stripping limit of the electron energy is reached or recombination processes balance the ionisation process or the axial potential distribution is changed and ions are extracted [12].

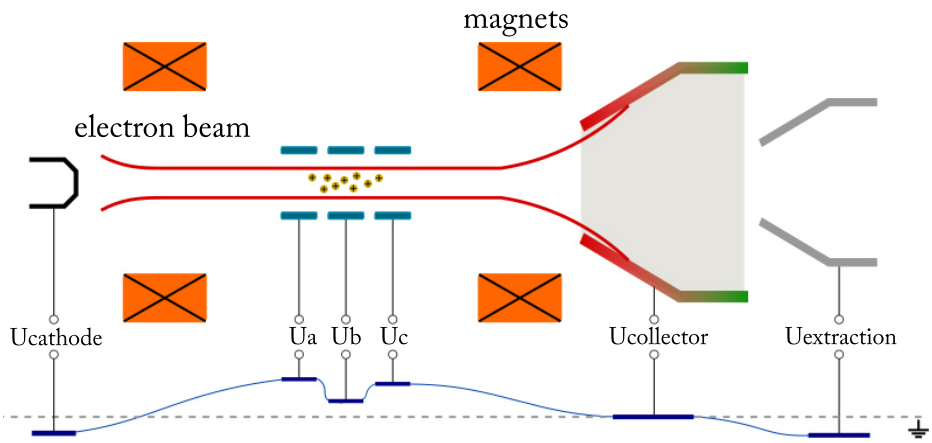

Figure 3.2: Schematic of the EBIT at the HZDR
Drawing of an electron beam ion trap with the cathode for the creation of the electron beam, the magnets and drift tubes for ion trapping. The ions are trapped radially by the space charge of the electron beam and axially by the electrostatic potentials formed by U_a, U_b and U_c. In the leaky mode U_c is decreased in such a way that the potential barrier becomes smaller and ions with thermal energies higher than the potential well can be extracted. In the pulsed mode U_c is alternately raised and lowered with respect to U_b and ions are extracted in pulses. The figure is adapted from [65].

The majority of the presented HCI irradiations, using an EBIT as the ion source, were performed at the two-source facility for HCIs at the HZDR, but one measurement period was done at the ion beam facility at the Universität Duisburg-Essen. Representative for both ion sources, the setup and operating mode of the EBIT at the HZDR is briefly discussed in the following.
The EBIT of the two-source facility is a room-temperature ion source from DREEBIT GmbH and the magnetic field of 250 mT is induced by two SmCo permanent magnetic rings. The magnetic field focuses the electron beam to an electron current density of some 100 A/cm^2. The ions are trapped radially by the space charge potential of the high electron density and axially by an ensemble of three drift tubes. The electrostatic potentials of these drift tubes are adjusted in such a way that a potential well is formed and the ions are trapped and stepwise ionised. A schematic of the ion source is shown in fig. 3.2. The source enables the generation of HCIs, i.e. for Xe ions charge states up to $q = 44$, at kinetic energies of $E_{\text{kin}} \leq 4.4 \cdot q$ keV. For extracting the ions from the source two operating modes are possible, the leaky mode and the pulsed mode. In the leaky mode the confining drift tube (U_c) is lowered such as the potential difference between this tube and the middle tube (U_b) is only some volts and ions with thermal energies higher than the potential well are extracted continuously. In the pulsed mode the potential of the confining drift tube is alternately raised and lowered with respect to the potential of the middle drift tube and ions are extracted in pulses.

3.1.2 Sources for SHIs

Swift heavy ions are produced in large scale facilities where initially slow ions are injected into accelerators and speed up to energies from MeV to GeV. In many facilities stripper foils are used to create low velocity charged ions. In a target the ions strip off all those electrons whose Bohr velocity is smaller as the projectile velocity and this leads to a charge state distribution around the equilibrium charge state $q_{eq} \approx Z^{1/3} \cdot v/v_0$ [72]. Ions at a fixed charge state are then accelerated.
The measurements presented in chapter 4 were performed at the IRRSUD beamline at GANIL (Grand Accélérateur National d'Ions Lourds) in Caen, France. IRRSUD is an irradiation facility which makes use of the low energy (0.5 MeV/amu - 1 MeV/amu) beams from the GANIL IRRSUD injectors. The irradiations were performed during several measurement periods with $^{136}Xe^{23+}$, $^{129}Xe^{23+}$ and $^{208}Pb^{29+}$ ions at kinetic energies of 0.71 MeV/amu and 0.484 MeV/amu, respectively. To perform irradiations also at lower kinetic energies, Al foils of different thickness (1.5, 3 and 6 μm) were used as an energy degrader.
Almost all SHI irradiation were performed under grazing incidence. The zero degree grazing angle was determined by optically aligning the surface parallel to the beam direction by means of a telescope, which was aligned on the optical axis of the beamline. The target was tilted by a stepping motor with a repeatability of about 5/100 of a degree. Considering the good repeatability of the rotation, the main error bar arises from the optical alignment of around 0.2 degree. Before performing the irradiations the optical alignment was proven by comparing the experimentally determined fluence with the nominal one[1] or by making a test irradiation on a well studied target material, like $SrTiO_3$, and comparing the evaluated track length of the corresponding incident angle with data from the literature [103].

3.2 Microscopy Techniques

During the elaboration of this thesis various microscopy techniques at different universities and research facilities were used to investigate different types of materials. For the topographical investigations of irradiated crystals atomic force microscopy (AFM) measurements under ambient conditions were performed with a VEECO NanoScope III atomic force microscope in Caen directly after irradiations. For performing detailed investigations an Asylum Research Cypher Scanning Probe Microscope in Vienna was used. The 2D materials were investigated with transmission electron microscopy (TEM), whereas best images for sample characterisation, regarding the contrast, were obtained with scanning transmission electron microscopy (STEM) measurements with

[1] counted tracks/μm^2=irradiation dose (ions/μm^2)$\cdot \sin(\alpha)$

a Nion UltraSTEM100 at the University of Vienna. The working principle of an AFM, TEM and STEM will be presented in the next paragraphs.

3.2.1 Atomic Force Microscopy - AFM

In 1986 the AFM was proposed by G. Binning, C. Quate and C. Gerber as a new type of microscope to investigate surfaces of conductors and insulators on an atomic scale [104]. Instead of measuring the tunneling current between a probing tip and a sample like with scanning tunneling microscopes (STM), which assumes a conductive sample, this method measures interaction forces typically in the range of some nN between a sharp probing tip and a sample surface.
A typical setup of an AFM is shown in fig. 3.3a. The probing tip is attached to a cantilever-type spring. A laser beam is focused on the backside of the cantilever which is reflected and detected on a four-quadrant photodiode. The sample is scanned in x-, and y-direction and in response to the force between the tip and the sample, the cantilever is deflected. This deflection is detected as a shifting of the laser spot on the detector and is used to track the height profile of the surface. The accurate and precise movement for scanning is ensured by piezoelectric elements.
Different forces are sensed by the AFM. They include Van der Waals and electrostatic forces, capillary forces, ionic repulsion and frictional forces. The interaction between the tip and the sample can be described by a Lennard-Jones potential with an attractive and a repulsive region (see fig. 3.3b). AFM measurements can be performed in both regimes with the basic modes of imaging, the contact (static mode) and the two dynamic modes, the non-contact and the intermittent or tapping mode.

In the contact mode the tip is in close contact with the specimen (separation in the order of some Å) and repulsive forces act on the cantilever. By performing constant height contact AFM the distance between tip and surface is kept constant and the deflection of the reflected laser spot tracks the topography. In the constant force mode the deflection is used as feedback and the mismatch between the measured deflection and a preset value is compensated by variation of the distance between the tip and the sample. The position of the z-piezo creates the topographic image of the surface.
In the dynamic mode the cantilever with the tip is excited to oscillate close to its resonance frequency. In the non-contact mode the tip is held 5-15 nm above the sample surface and the attractive Van der Waals forces are used for topography imaging by detecting changes in amplitude, phase and frequency of the oscillation. Since the measured forces are weak and possible fluid contamination of the surface is thicker than the range of the Van der Waals forces, this mode is inappropriate for AFM measurements under ambient conditions.

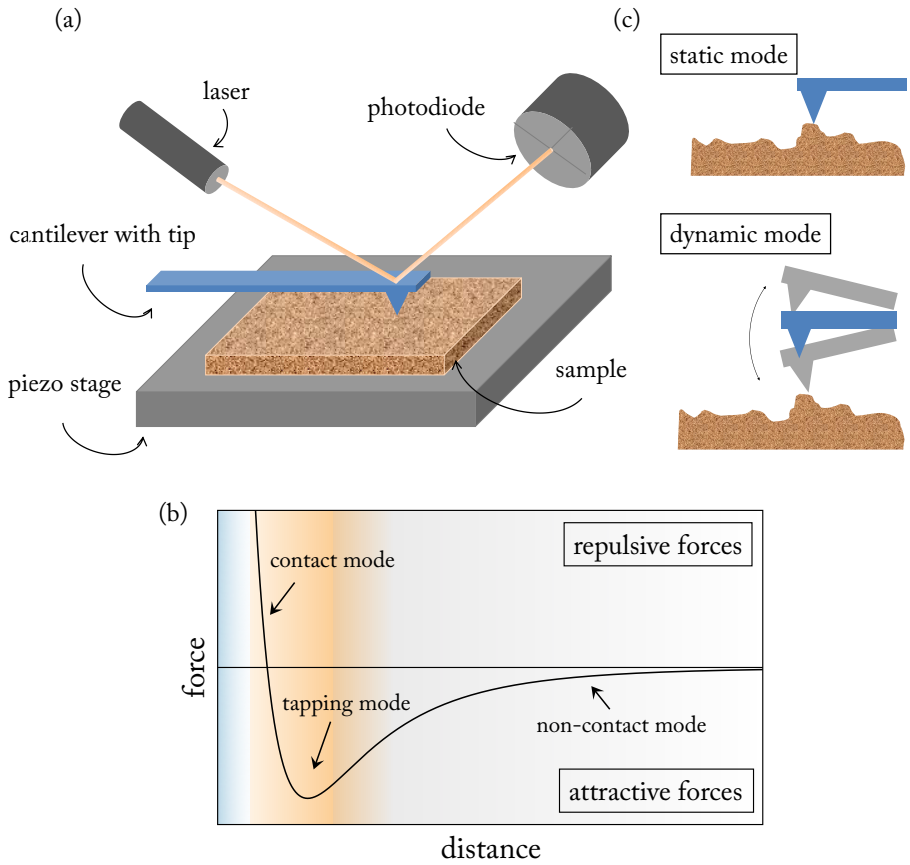

Figure 3.3: Schematic operation principle of an AFM
a) Typical setup of an AFM. A laser beam is focused on the backside of the cantilever and the deflection of the laser spot, due to variation of the force acting between the tip and the sample, is detected. The shifting of the laser spot is used to track the height profile of the surface. b) Different forces are sensed by the AFM which can be described by a Lennard Jones potential with an attractive and a repulsive force region. c) AFM measurements are performed in both regimes in the static (contact) and dynamic (tapping and non-contact) mode.

In tapping mode these problems are prevented by alternately placing the tip in contact with the surface to get high resolution and lifting it off the surface to avoid a dragging of the tip. In the tapping mode the amplitude of the oscillation is used as the feedback signal. The mismatch between the measured amplitude and the preset value is causing the z-piezo to lower or alter the distance between the sample and the surface. The position of the z-piezo is used to track the surface of the sample. Additionally the oscillation phase, the difference between the driven and the actual

oscillation, is recorded and gives information about mechanical properties, e.g. adhesion, friction or elasticity of the investigated sample.

3.2.2 Transmission Electron Microscopy - TEM

The first transmission electron microscope was developed by M. Knoll and E. Ruska in 1931 [105, 106]. This type of microscope uses a high energy electron beam, which interacts with an ultrathin specimen and after transmission a magnified image of the sample is maped on an imaging device. Due to the small de Broglie wavelength of electrons a much higher resolution is possible in comparison to light microscopes. Fig. 3.4 shows the setup of a TEM. The microscope consists of three essential systems, the electron gun and the condenser system to create a focused ion beam on the specimen, the image producing system, to create a magnified and focused image of the sample and the image-recoding system. The obtained quality of the images depends on the mechanical and electrical adjustment of the instrument and the beam alignment.

Initially the measurements of the studied 2D materials were performed with a FEI TITAN 80-300 at the HZDR and a FEI TECNAI F20 at USTEM, TU Wien. Both instruments work at high extraction voltages of the electron beam of 300 keV (TITAN) and 200 keV (TECNAI), respectively, which caused damaging and destruction of the ultrathin graphene sheets. To avoid the destruction of the graphene sheets the TEM measurements were later performed with the Nion UltraSTEM100 at 60 kV extraction voltage at the University of Vienna. Besides standard TEM measurements, high resolution STEM measurements were performed. In this operation mode the electron beam is focused into a narrow spot, scanned over the sample and detected by a high-angle annular dark field detector (HAADF). The advantage in comparison to conventional TEM images is, that the intensity of the obtained signals is proportional, roughly linearly, to the thickness of the sample and proportional, roughly quadratic to the atomic number of the specimen. This allows a facile identification of impurities and an estimate of the thickness of the observed layer (see fig. 3.4). Since atomic resolution with high contrast can be achieved, this method seems also to be suitable for checking possible damage and pore formation of ultrathin layers after ion irradiation.

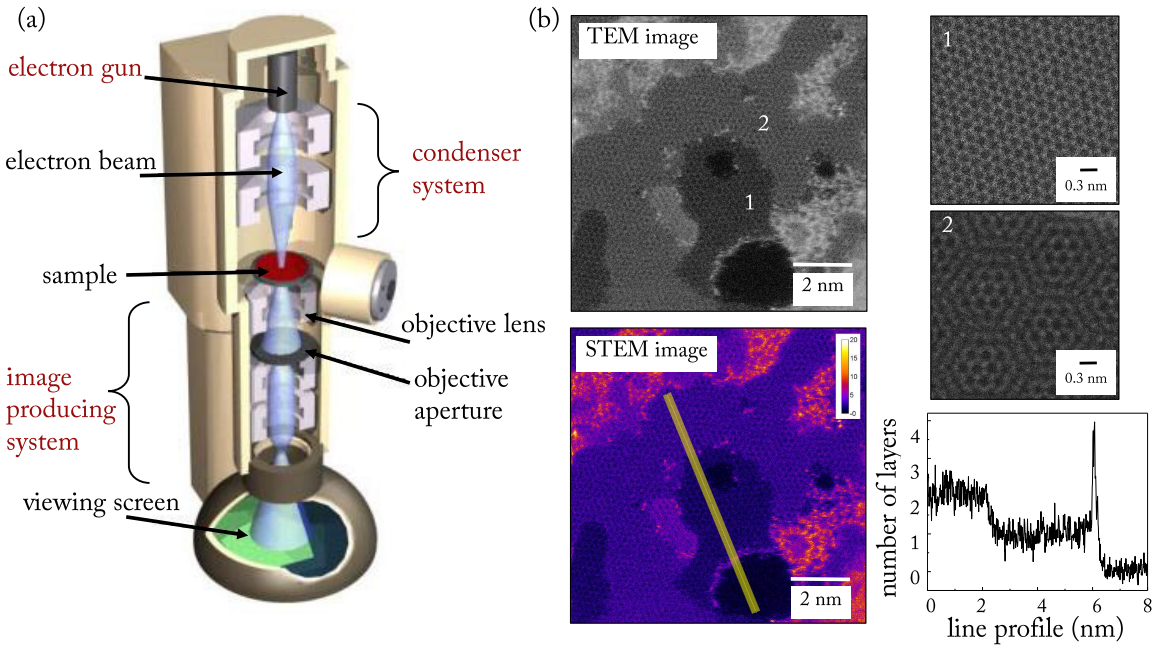

Figure 3.4: Imaging by TEM and STEM
a) The schematic shows the three essential components of the TEM microscope: the beam producing system, the image producing system and the image recording system. The schematic is adapted from [107]. b) High resolution TEM and STEM images are suitable for characterisation studies of thin graphene layers. High resolution between vacuum hole, monolayer patches (1) and bilayer regions (2) are observable. The advantage of STEM imaging is, that the intensity of the obtained signals is proportional, roughly linearly, to the thickness of the sample and proportional, roughly quadratic to the atomic number of the specimen. A facile identification of impurities and an estimate of the thickness of the observed layers is given. The layer analysis is taken from the STEM figure and marked by the yellow line.

4

Nanostructuring by ion irradiation

An intriguing phenomenon in ion-surface interaction is the formation of nanostructures due to single ion impact. Besides the interest on the underlying physical mechanisms, this research field is driven by the interest of using ions as a tool for lithographic modifications. Investigations of various materials have shown that SHI irradiations induce severe structural modifications at the surface and in the bulk [11, 83, 108, 109]. These modifications appear as protrusions and craters on the surface or reveal as phase transitions (e.g. from crystalline to amorphous) and/or create latent tracks of several hundreds of nanometer into the solid. The formation of tracks and surface nanostructures occurs predominantly in insulators (e.g. polymers [110], oxides [103], ionic crystals [109, 111]) and is linked to a critical (electronic) energy loss $\mathrm{d}E/\mathrm{d}x$ of the projectile.

Some years ago, a similar nanometric surface effect has been revealed for the impact of individual, very slow but highly charged ions [60, 62]. In contrast to SHIs, where also deeper layers are involved, for HCIs the energy deposition and consequential nanostructuring is limited to the topmost atomic layers. The nanostructure formation ranges from hillock [61], to crater [112] and pit formation [60] on the surface and becomes visible above a potential energy threshold, which depends on the target material [11]. The terminus visible points to the experimental techniques to investigate the materials after irradiation. Most of the data are obtained by means of scanning probe microscopy, offering the possibility to identify and characterise localised surface modifications. For conductive samples the choice falls on STM to study the electronic density of

states and the connected topography. For insulating materials, AFM is mostly chosen as the ideal imaging instrument. The imaging resolution of an AFM is in general less than for STM, but yields topographic information also for insulators. Thereby the spatial resolution is limited by the geometry of the used tip. By analysing AFM images convolution effects between the nanostructure and the AFM tip have to be considered [113].

In the course of the last decades, nanostructuring due to SHI and HCI irradiations was studied for a large palette of materials. Despite the different primary excitation processes, similarities in the nanostructure formation created by single HCI and SHI impact could be determined (for a review see [11]), which nature, appearance and stability depend heavily on the properties of the target material.

As a continuation of previous investigations, performed by the group of F. Aumayr and coworkers [59,61–63,114–116], comparing studies of HCI and SHI irradiated sample were performed during the elaboration of the thesis in the framework of the French-Austrian ANR – FWF Project SIISU. We focused on SHI irradiations of four different insulators and AFM was choosen as the main technique to study the topography of the SHI induced surface modifications. To enable a direct comparison of the nanostructure formation after single HCI and SHI impact, the SHI irradiations were performed under grazing angle of incidence. This particular collision geometry forces the tracks to a region close to the surface comparable to the shallow damage of slow HCI. The AFM measurements were partially performed during the elaboration of a project work and a diploma thesis and some data, presented in the following, are extracted from these protocol and thesis [117, 118].

A further motivation to study the nanostructure formation on different materials under grazing angle of incidence is the increasing interest of novel nanoscale features on different materials. These new features include chain-like morphology of ion tracks [103], groove formation [119], creation of nanoholes within ion tracks [120], cratering in polymers [110, 121], formation of conductive ion tracks [122] and a folding and unzipping of graphene deposited on a substrate [123–125]. These examples demonstrate the tremendous potential for the nanostructuring of surfaces, also for two-dimensional materials.

4.1 State of the art

Our studies focused on the two oxides $SrTiO_3$ and TiO_2, the lamellar insulator mica and the ionic crystal CaF_2. Before presenting and discussing the results, the properties and previous investigations of these four materials by other research groups are shown.

4.1.1 SrTiO3

The crystal strontium titanate $SrTiO_3$ is an oxide with a cubic unit cell (see fig. 4.1). It exhibits a mixed ionic-covalent chemical bonding with Sr-O being of ionic character and Ti-O is partially covalent. This leads to the unique electronic structure with a band gap of about 3.3 eV [126]. Because of its high dielectric constant, low chemical reactivity and easy growth of ultrathin layers on silicon [127,128], $SrTiO_3$ is discussed as a possible insulator of choice in future microelectronic devices. The ferroelectric oxide is also used as a catalyst [129] and as a substrate material for GaAs solar cells.

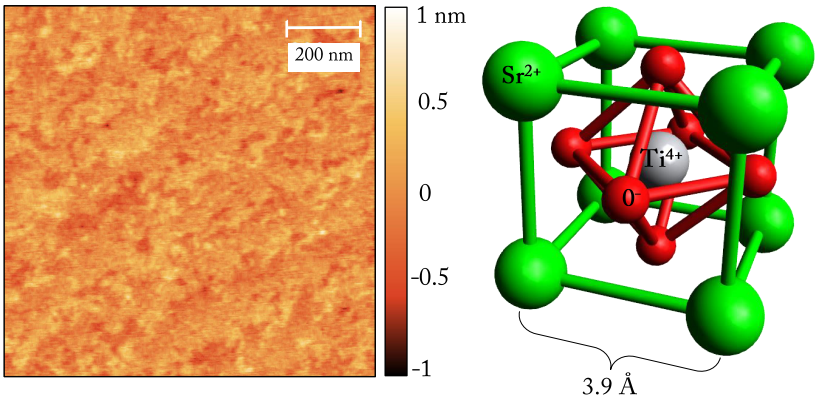

Figure 4.1: Surface topography and crystalline structure of $SrTiO_3$
Topography of an unirradiated $SrTiO_3$ sample, obtained by AFM imaging in tapping mode. The crystalline structure of the ferroelectric oxide shows a cubic unit cell and exhibits a mixed ionic-covalent chemical bonding with Sr-O being of ionic character and Ti-O is partially covalent.

The crystal $SrTiO_3$ is one of the most studied oxides. Surface modifications due to ion irradiation were investigated for SHI [103, 123, 130–132] as well as HCI [133, 134] irradiations. In both cases the creation of nanohillocks with a height of some nm could be observed (see fig. 4.2). The creation of hillocks could be linked to a critical energy loss between 5.3 and 7.2 keV/nm in the case of SHI [131] and between 15.4 keV and 30.4 keV in the case of HCI irradiation [134]. The similarity of the nanostructure formation was interpreted as the fact that for SHI as well as HCI impacts, the projectiles transfer their energy to the electronic system of the target which is then effectively transferred to the target atoms. The energy deposition into the lattice system causes an increase of the lattice temperature. Highly localised melting and rapid quenching leads to the formation of hillocks.

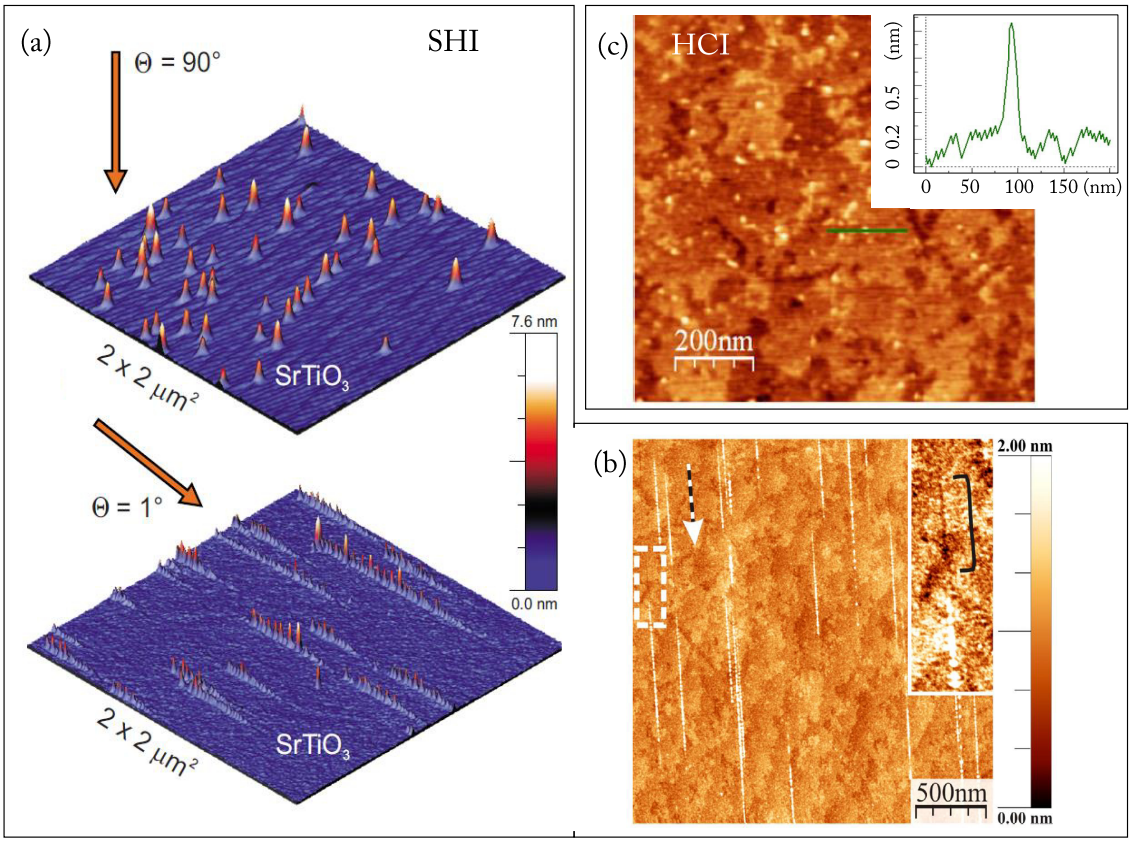

Figure 4.2: SHI and HCI irradiation of $SrTiO_3$
(a) SHI induced nanohillocks on $SrTiO_3$ under perpendicular and grazing angle of incidence. In the case of grazing angle of incidence the formation of a trail of single nanohillocks is visible. Figures are taken from [123]. (b) High resolution AFM imaging shows the formation of a narrow and shallow rift at the impact site of 653 MeV (S_e=29 keV/nm) Xe^{21+} under grazing angle of incidence of θ=1.5°±0.4° [132].
(c) AFM image of a $SrTiO_3$ surface after irradiation with 4.5·q keV Xe^{37+} ions. The bright spots were interpreted as nanohillocks with a height of about 1 nm [134].

Besides SHI irradiation under perpendicular incidence, Akcöltekin *et al.* [103, 130] performed irradiations under grazing angle of incidence and demonstrated the formation of multiple, equally spaced dots, each separated by a few tens of nanometers. The variation of the incident angle controls the number of dots as well as their spacing. The physical origin of these patterns was explained by an anisotropic electron density distribution within the bulk which triggers the energy loss process. The resulting nanodots represent the projection of the three-dimensional electronic density onto the surface. In order to show the relevance of the electron density distribution of the target on the nanostructure formation, the electron density of $SrTiO_3$ was determined by performing density functional theory (DFT) calculations [135]. By considering the electron

density distribution, the electronic stopping power along the trajectory of the primary particle was analysed (see fig. 4.3). The DFT calculations showed that the majority of the electrons are localised around the oxygen atoms and the electron density in the TiO_2 plane exceeds the one in the SrO plane. From these calculations it is obvious that the electron density varies on a sub-nm scale and cannot be treated as a homogeneous electron gas. This results in an oscillation of the stopping power along the track length. A variation of the angle of the incident ion beam results in a variation of the frequency of the oscillating stopping power along the track length (see fig. 4.3). These theoretical results nicely explain the experimentally observed periodic nanodot formation.

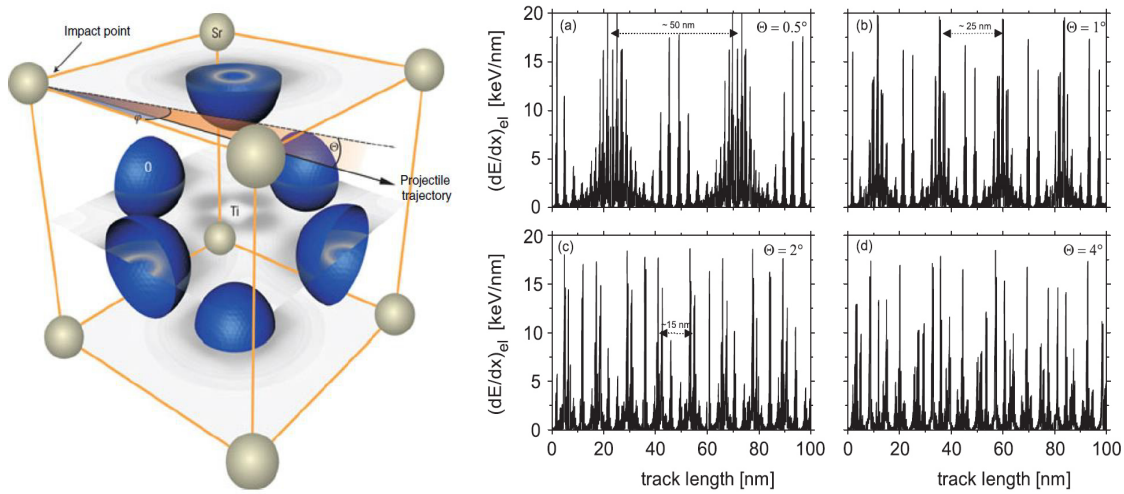

Figure 4.3: Oscillation of the electron density of $SrTiO_3$
The left figure shows the DFT calculations of the electron density of $SrTiO_3$. The grey shading represents the electron density and the arrow indicates a possible projectile trajectory with the azimuthal angle φ and the incident angle θ. The right images show the calculated oscillation of the electronic stopping power along the travelled distance of a Xe^{23+} ion at 93 MeV from the point of impact. The incident angle is varied between (a) θ=0.5°, (b) θ=1°, (c) θ=2° and (d) θ=4°. The figures are taken from [135].

4.1.2 TiO2

TiO_2 is an oxide and appears naturally in three modifications, i.e. rutile, anatase, and brookite. Rutile is the only stable phase, the metastable anatase and brookite phases transform irreversible into rutile upon heating above a temperature between 600° and 800° C [136]. The rutile and anatase crystallise in a tetragonal unit cell with different unit cell parameters (rutile: a=b=4.59 Å, c=2.96 Å; anatase: a=b=3.78 Å, c=9.51 Å) and brookite has an orthorombic unit cell. Since the

presented measurements were performed with rutile TiO_2, only this structure is shown in fig. 4.4. TiO_2, a semiconductor with a band gap of 3.02 eV (rutile) [137], is the most investigated single crystalline system in the surface science of metal oxides and the interest arises from a wide range of technological applications of this versatile material, as, e.g., an opacifier in pigments [138], from its good biocompatibility and its catalytic and photocatalytic properties [139, 140].

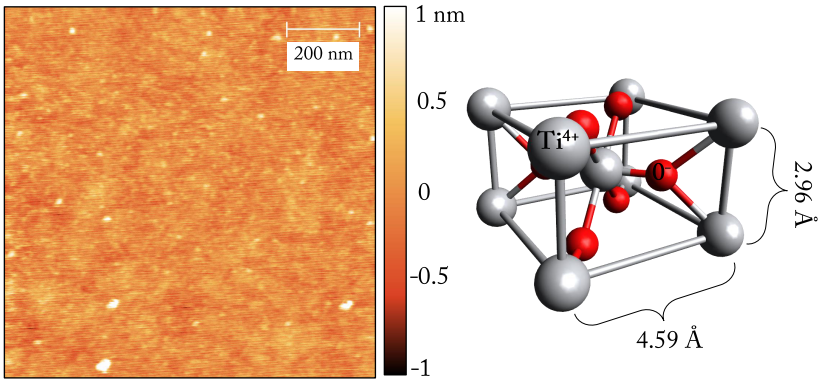

Figure 4.4: Surface topography and crystalline structure of TiO_2
Topography of an unirradiated TiO_2 sample, obtained by AFM imaging in tapping mode. The crystalline structure of rutile TiO_2 with a tetragonal unit cell.

Also for TiO_2 crystals ion track formation and surface modification due to SHI and HCI bombardment were studied and inspected using TEM, AFM and STM (see fig. 4.5). In ref. [112] it is shown that irradiation with 150 keV I^{q+} ions with $25 \leqslant q \leqslant 51$ creates nanometer-sized hillocks or crater structures on rutile TiO_2, which structure size increases with the projectile charge state. Secondary ion emission measurements showed O^+ sputtering, which contribution to the total sputter yield increases with higher charge states. From the size of the craters it could be estimated that a few hundred up to thousand atoms are removed by the impact of one HCI. Since only a few secondary ions are emitted, several hundred of neutral atoms have to be sputtered [112].

The creation of hillocks and craters could also be observed after the impact of keV $Ar^+_{23\pm2}$ cluster ions [141] and MeV multiply charged ions [141]. Performing these measurements it was observed that radiation-damaged TiO_2 has very different water affinity properties in comparison to non-irradiated TiO_2 surfaces. The dangling bonds in the created craters make the impact nanospots highly hydrophilic and favour the adsorption of water molecules. Hence, the observation of craters in the case of 40 MeV I^{9+}, but the appearance of hillocks in the case of 46 MeV I^{10+} were explained by changed adsorption properties and not by true topographical features. Measurements under dry nitrogen atmosphere led to the disappearance of hillocks and only craters were imaged. The disappearance of hillocks was also achieved by heating the sample to 100°C

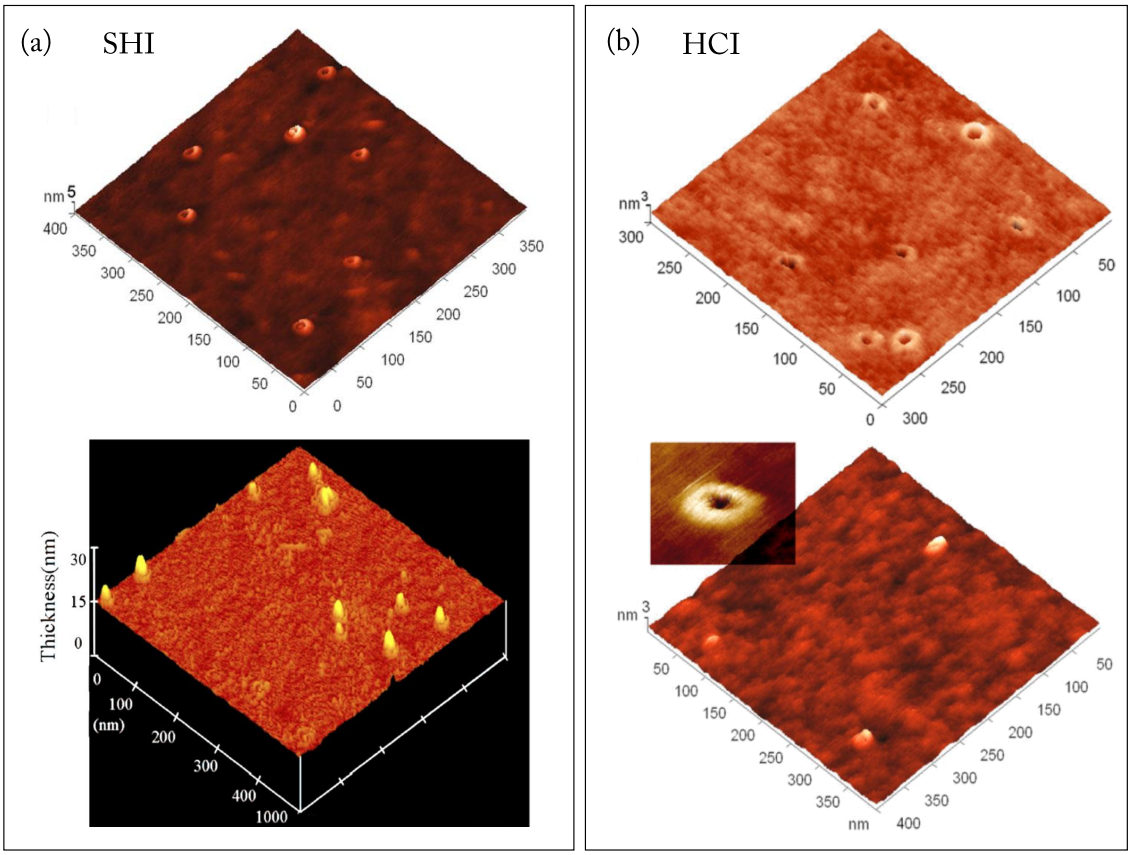

Figure 4.5: SHI and HCI irradiation of TiO_2
SHI as well as HCI irradiation leads to crater or nanohillock structures on TiO_2. The upper figure of (a) shows an AFM image of a TiO_2 surface after irradiation with 40 MeV I^{9+} ions, taken from [141]. The AFM image shows the formation of craters. The lower image represents an AFM image after irradiation with 150 MeV Au^{14+}, taken from [142]. In this case nanohillocks are visible. (b) AFM image of a TiO_2 surface after irradiation with Ar_{23}^{+} cluster ions recorded in dry nitrogen atmosphere (upper image) and under ambient conditions (lower image). The inset shows a magnified image of a crater [141]. The observation of nanohillocks or craters in dependence of the measurement conditions were explained by changed adsorption properties of the irradiated sample and not by true topographical features.

under ambient conditions. Therefore the observation of hillocks and no craters in the case of MeV ions by other groups [142, 143] are explainable.

As shown before for $SrTiO_3$ crystals, also SHI irradiation of TiO_2 under grazing angle of incidence leads to the formation of a chain of single well separated nanodots (fig. 4.6a) [144, 145]. The appearance of distinct and almost equidistant dots was again explained by the fact that the ion

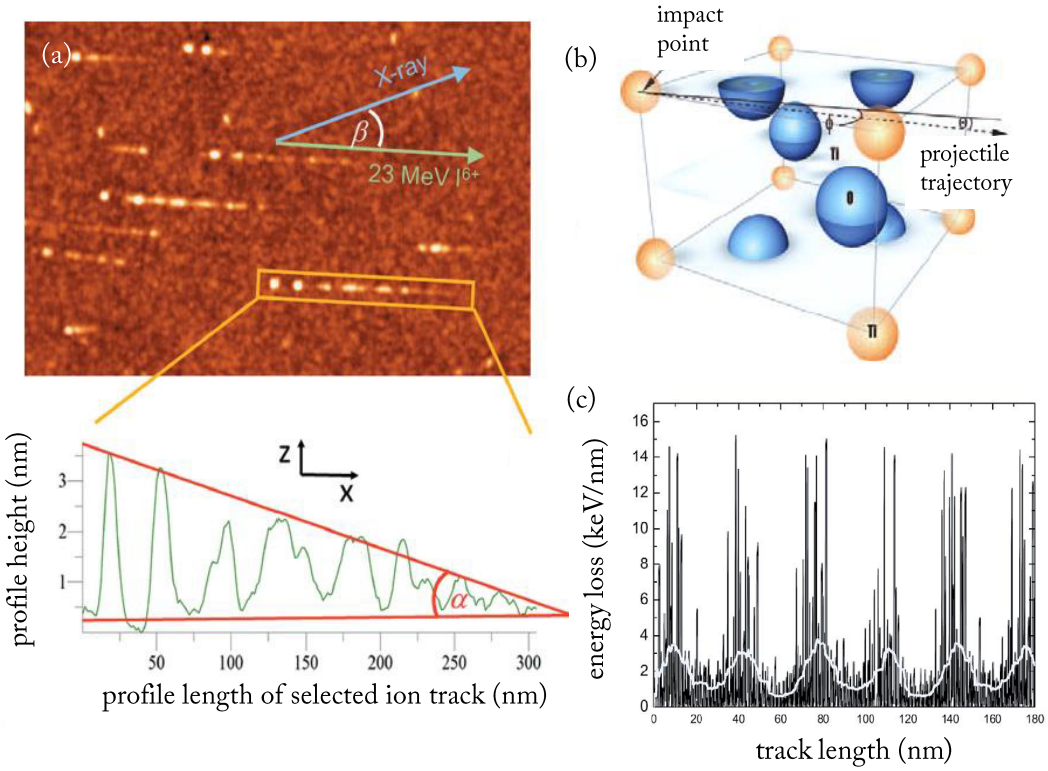

Figure 4.6: Oscillation of the electron density of TiO_2
(a) AFM image of a rutile TiO_2 [001] surface irradiated with 23 MeV I^{6+} ions under grazing angle of incidence, taken from [144]. The profile through one of the formed tracks shows the formation of equidistant single nanodots. (b) DFT calculation of the electronic density of TiO_2 and (c) the calculated energy loss due to electronic stopping for a 92 MeV $^{131}Xe^{23+}$ ion under grazing incidence angle of $\theta = 1°$ and polar angle of $\phi = 7°$ with respect to the [100] direction. Both figures are taken from [145].

crosses regions with varying electron density (fig. 4.6b). Under consideration of the electron density, the energy loss of the incident ions due to electronic stopping was calculated in [145]. Fig. 4.6c shows the energy loss for a 92 MeV $^{131}Xe^{23+}$ ion travelling through a TiO_2 single crystal under grazing incidence angle of $\theta = 1°$ and polar angle of $\phi = 7°$ with respect to the [100] direction. Every 30 nm a maximum of the stopping power appears and results in a nanohillock on the TiO_2 surface.

Recently, also stochiometric changes of TiO_2 during irradiation with 23 MeV I ions by using in situ TOF-ERDA (time of flight elastic recoil analysis) were investigated [144]. The measurements show a pronounced loss of oxygen from the first 10 nm that accompanies the formation of surface tracks on rutile TiO_2. A distinct explanation for the preferential loss of oxygen was not given, but various possible mechanisms, among them vaporisation, promotion of electronic sputtering due

to amorphisation of the TiO_2 surface or sputtering due to Coulomb explosion as a channel of SHI energy dissipation, were mentioned.

4.1.3 Mica

Mica belongs to the sheet silicate minerals and includes several closely related materials with a monoclinic crystal system. The most prominent candidate is thereby muscovite mica with the sum formula $KAl_2(AlSi_3O_{10})(F,OH)_2$. It consists of negatively charged alumino-silicate layers, involving both tetrahedral and octahedral sheets, with intermediate layers of positive potassium ions to provide charge neutrality [146]. The layered structure of mica makes an easy cleaving of the crystal possible, providing smooth and atomically flat surfaces. Fig. 4.7 shows the surface of a freshly cleaved mica sample and the complex structure of the isolator. Mica belongs to the first materials which were studied with respect to ion induced surface modifications because of its radiation sensitivity and its atomically flat surface which is well suited for AFM imaging. Because of its physical properties, particularly its excellent heat isolation and high resistivity against disruptive electrical discharge, mica is used for numerous industrial applications.

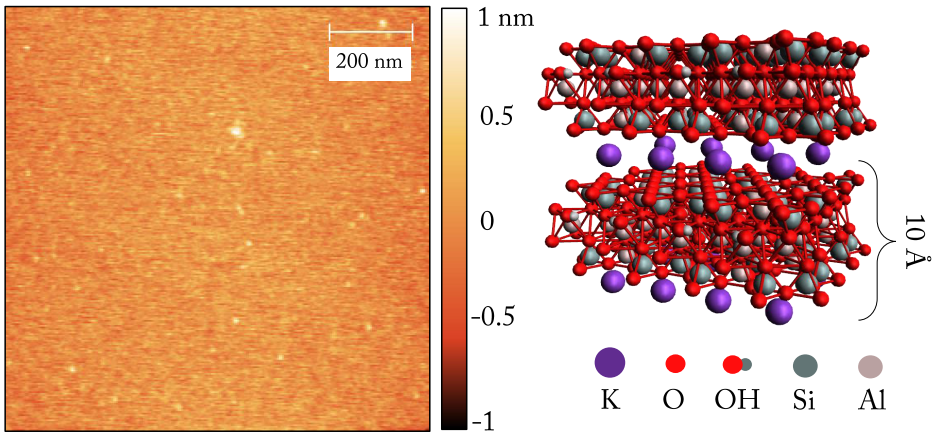

Figure 4.7: Surface topography and crystalline structure of mica
Topography of an unirradiated mica sample, obtained by AFM imaging in tapping mode. The crystalline komplex structure of muscovite mica. It consists of negatively charged alumino-silicate layers with intermediate layers of positive potassium ions to provide charge neutrality.

The first HCI irradiation studies were performed by the group of D. Schneider at Lawrence Livermore National Laboratory [147,148]. They irradiated mica with various slow HCIs ($Xe^{1+,35+,44+,50+}$,

Kr^{35+}, U^{70+} and Th^{74+}) and investigated the surface after irradiation with AFM. They observed blister like structures which through multiple scans of the tip of the AFM over the same area were flattened or completely removed and the primary observed blisters revealed as pits [147]. As there was no change in the appearance of the structures in dependence of the scan direction, the blister and pit formation were ascribed as true topographic surface modification. Comparing the density of created defects with the total ion fluence they concluded that every defect was caused by a single ion impact. An increase of the blister volume with increasing incident charge state and a minimum threshold charge state around $q \sim 35$ for defect formation was pronounced.

Parks *et al.* [149, 150] repeated the measurements and also they observed the formation of circular hillocks with typical dimensions of 10-20 nm in diameter and 0.5-1 nm in height. A lower threshold for observable damage was noted at $q = 30$. Their contact mode microscopy measurements have shown that the features appear as pits or blisters in dependence of the scanning direction and on the force between the tip and the substrate. The apparent topographic inversion was explained by lateral forces of the tip. Lateral forces contribute to the bending torque on the cantilever, hence, mimicking topography. Images are some combination of real topography and lateral forces. To minimise lateral forces and check if the observed structures represent topographic modifications or appear only due to frictional contributions, tapping mode AFM imaging, where lateral forces are minimised, were performed. Since pits were also visible in this mode, the authors proposed that the structures are true topographic modifications.

Similar investigations, but with lower charge states of the incident ions (Xe^{23+} and Xe^{27+}) were performed by Ritter *et al.* [59]. Surprisingly they found HCI-induced nanostructures well below the potential energy threshold, reported in earlier experimental investigations. However, since the observed nanometric features were observed only in contact and not in tapping mode, they may represent not true topographic modifications but rather regions of enhanced friction. True topographic hillocks may appear only above a threshold of $q = 30$, as reported in [147, 149].

The appearance of hollows or hillocks in dependence of the direction of the cantilever movement were also observed after SHI irradiation. This artificial topographic features were explained by frictional forces [154] and changes of the elastic properties due to SHI irradiations [155]. Lateral force mode measurements could also show an increase of the track diameters with an increase of the energy loss [156]. The situation changes by using particles with similar energy loss values (some tens of keV/nm) but much lower kinetic energies (some MeV in comparison to GeV). In this case the formation of true topographic hillocks were reported [151].

True topographic features could also be observed by Daya et al. [152, 153, 157] after 78.2 MeV ^{127}I ions or 20.4 MeV C_{60} irradiations. While for 78.2 MeV ^{127}I irradiation hillocks with a height

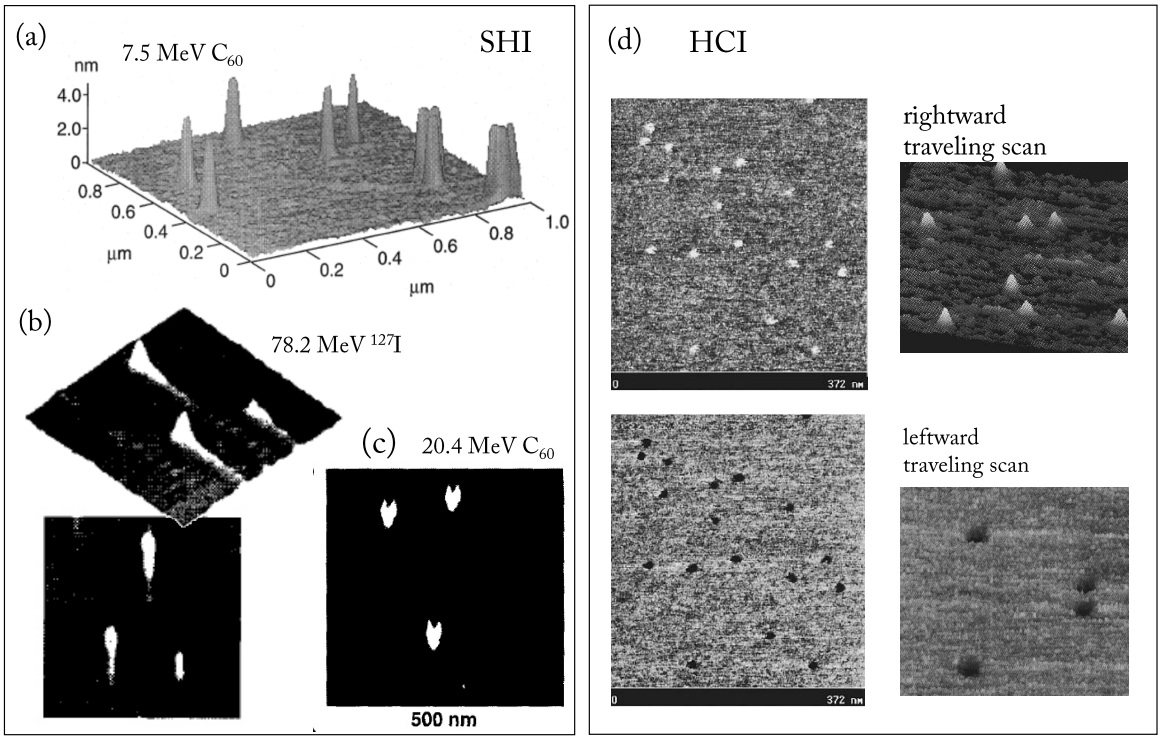

Figure 4.8: SHI and HCI irradiation of mica
SHI and HCI irradiation of mica results in the formation of hillocks or pits on the surface in dependence of the used mode and scanning direction. The images are some combination of real topography and lateral forces. Above a certain threshold of deposited energy the nanostructures are identified as true topographic modifications (a) [151] and (d) [149].
(b) The irradiation under grazing incidence angle of θ=84° [152] showes the formation of a hillock followed by a trail. (c) Better spatial resolution shows the formation of a crater at the impact site of the incident ion [153].

of about 0.5 were created, 'gigantic' (nearly 7 times taller and 2 times broader) conical hillocks were observed after 20.4 MeV C_{60} irradiations. These differences were explained by the much higher total stopping power (3.6 times higher) of C_{60} in comparison to 78.2 MeV ^{127}I.

First SHI irradiations under grazing angle of incidence revealed the creation of conical shaped hillocks accompanied by raised tails (see fig. 4.8b) [152]. At closer look also the formation of topographical craters next to each hillock could be observed [153]. From the first images, due to the poor image quality and poor spatial resolution, details of the nanofeatures are hardly to identify (see fig. 4.8c). Probes with broadened or irregular tip ends result in complete masking of the crater and a broad and blobby image of the hillocks. On some images the creation of a ~0.5 nm deep crater which merges into a quite high (~9 nm) hillock, which is then followed by a

tail is visible. The formation of the crater was linked to sputtering due to pressure pulse or shock wave processes.

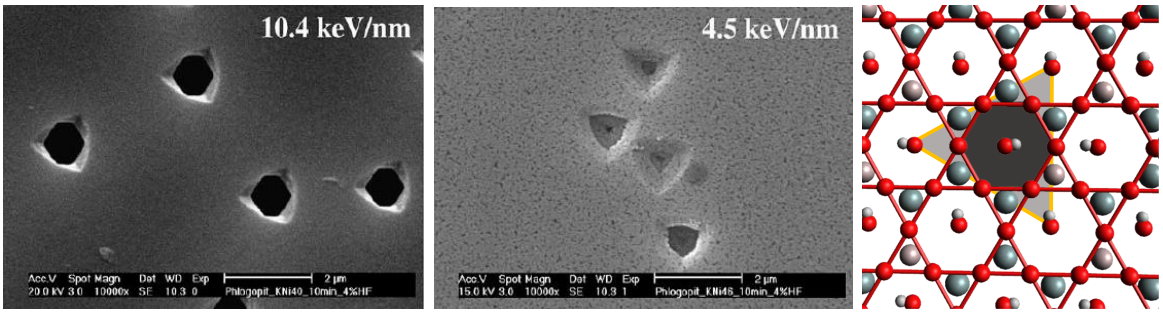

Figure 4.9: Etch pits of irradiated mica
The etching of irradiated mica samples with 4%HF solution shows hexagonal (left image) or triangular (middle image) shaped etch pits. If the energy is high enough the strong bonds of the oxygen anions of the SiO_4 tetrahedron are broken and form a hexagonal etch pit due to the hexagonal symmetry of the plane (see right schematic). For lower energies only the weak bonds between the oxygen and hydroxyl anions of the octahedron are broken and triangular etch pits are formed. The two SEM images are taken from [146].

Another possibility to visualise ion tracks in a solid is chemical etching of an irradiated sample. If an ion is travelling through the solid, energy is deposited and disturbs the crystal. An appropriate etchant (HF in the case of mica) enlarges this latent track and pits are created. The size and the depth of the etch pits grows linearly with time during the etching process. The shape of the pits is controlled by the crystal structure. Lang *et al.* [146] reported the changing from a triangular to a hexagonal shape of etch pits in dark mica when increasing the energy loss from 5.7 to 8.8 keV/nm. If the energy is high enough, the strong bonds of the oxygen anions of the SiO_4 tetrahedron are broken and form a hexagonal etch pit due to the hexagonal symmetry of the plane. For ions with lower energies only the weak bonds between the oxygen and hydroxyl anions of the octahedron are broken and a triangular etch pit is formed (see fig. 4.9). The transition from the triangular to the hexagonal etch pit shape coincides also with the transition from a discontinuous to continuous damage morphology along the tracks.

4.1.4 CaF_2

CaF_2 is an ionic crystal with a cubic crystal system (fig. 4.10). It can be easily cleaved along the (111) plane producing large terraces separated by mono-atomic steps. The isolator has a band gap of 11.8 eV [25] and is interesting for various applications in microelectronic and optoelectronic devices [158, 159].

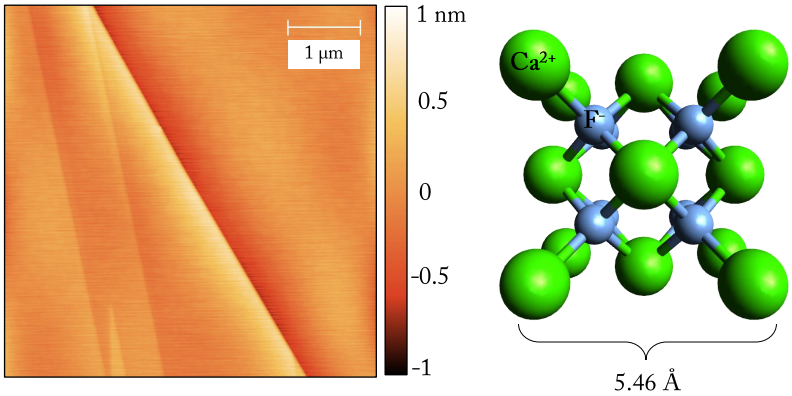

Figure 4.10: Surface topography and crystalline structure of CaF_2
Topography of an unirradiated CaF_2 sample, obtained by AFM imaging in tapping mode. The ionic cubic crystal can easily be cleaved along the (111) plane producing large terraces by mono-atomic steps.

A large data set from different irradiation experiments is available which shows the creation of nanosized hillocks after SHI and HCI irradiation above a certain threshold of deposited energy. The occurrence of nanohillocks induced by SHI under normal incidence angle was first reported in 2002 by Müller *et al.* [160]. An almost linear increase of the hillock height with an increase of the deposited energy loss was shown therein . For an energy loss of 34 keV/nm a hillock height of $\sim$ 5 nm with a diameter of $\sim$ 32 nm was determined. Further systematic studies [109, 161, 162] confirmed these observations and determined a threshold energy loss for hillock creation between S_e=2.3 and 5.8 keV/nm. A similar energy loss threshold was also found when measuring the CaF_2 volume expansion (swelling) [163]. The volume increase is directly linked to a structural disorder.

Besides SHI irradiation, the surface of CaF_2 was also investigated in detail after HCI irradiation [62, 63, 115, 164]. The results can be summarised in a so called phase-diagram (see fig. 4.11d), which shows the defect formation in dependence of the kinetic and potential energy of the incident ions [61]. Three regions can be distinguished. In region A no surface modification after HCI irradiation are observable. Region B is strongly dependent on the kinetic and potential energy. A sufficient number of defects agglomerate in such a way that chemical etchants are able to remove material and triangular pits become visible. Above the potential energy threshold of 12-14 keV, the deposited energy is high enough to lead to melting of a nano-sized region around the impact site, followed by thermal expansion and rapid quenching, which leads in the following to a permanent structural surface modification in the form of small nanohillocks (Region C). At considerably higher potential energies a further threshold has been predicted [63], above which

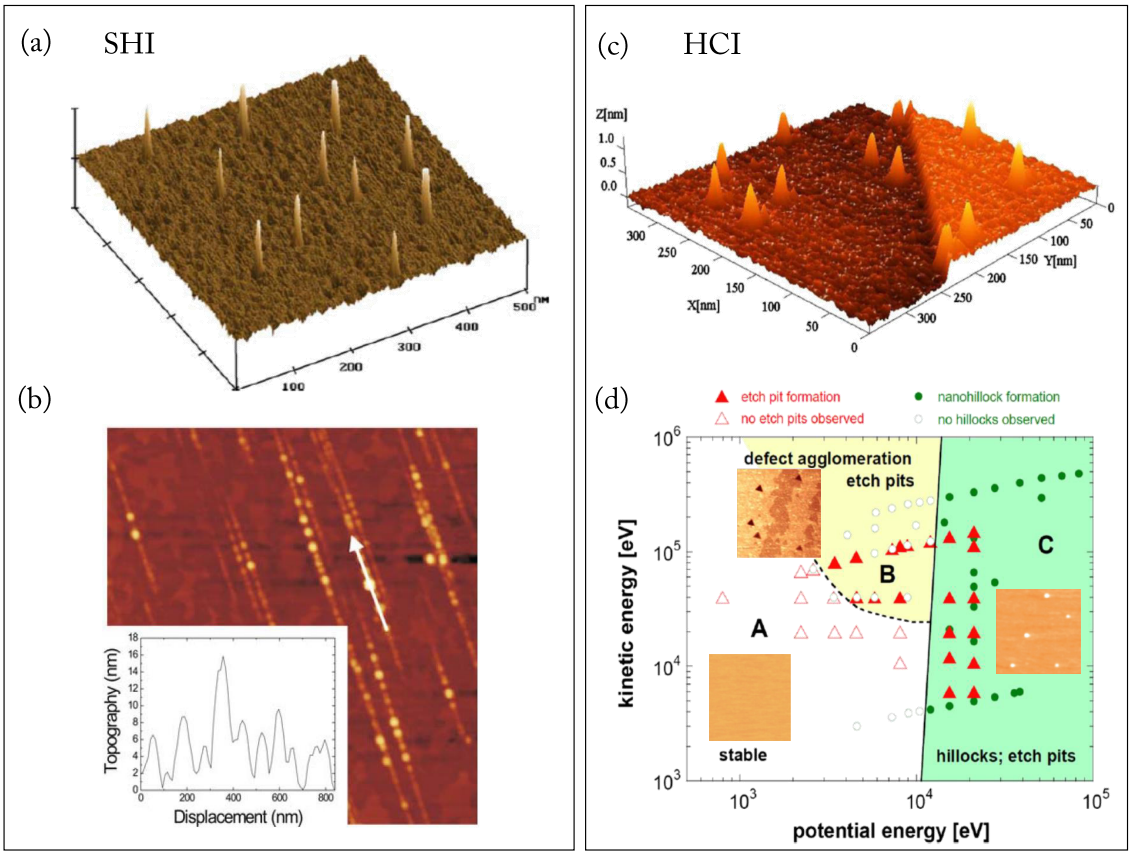

Figure 4.11: SHI and HCI irradiation of CaF_2
SHI and HCI irradiation leads to hillock formation above a certain threshold of deposited energy. (a) shows a CaF_2 surface after exposure to 6.4 MeV/u ^{136}Xe ions, taken from [109] and (c) after exposure to 500 eV/u Xe^{33+}, taken from [62]. (b) Topography image of chains of nanodots after irradiation with 93 MeV Xe^{23+} ions under grazing angle of incidence. The inset shows the formation of a chain of separated single nanodots, taken from [122]. (d) The phase diagram shows three regions of defect formation after HCI exposure in dependence of the kinetic and potential energy of the incident ions. The region A shows pairs of potential and kinetic energies where no defects are observable after HCI exposure, region B where triangular pits become visible after etching and region C where hillocks are produced after irradiation. Figure is taken from [61].

sublimation/evaporation of atoms and clusters should occur. Until now this prediction wasn't verified experimentally.

Irradiation under grazing angle of incidence forces the track formation towards the surface and first SHI irradiations of CaF_2 exploiting this special geometry can be found in [145, 165, 166]. In [165] the formation of grooves with followed humps are reported and explained by evaporation of

atoms and molecules and plastic deformation of subsurface layers and swelling effects. The CaF_2 irradiations performed by Akcöltekin *et al.* showed the creation of chains of single nanodots [145]. Eddy current microscopy (ECM) measurements of the irradiated CaF_2 samples indicated that the produced nanodots predominantly consist of metallic Ca [122]. These observations suggested a depletion of fluorine, resulting in Ca colloids and were in good agreement with earlier TEM measurements that showed the creation of intermittent tracks, consisting of aligned anion voids (or rather Ca inclusions) after irradiation with clusters of ions of a few tens of MeV [167]. The authors of [145] noted the limited spatial resolution of the AFM measurements of the tracks produced on CaF_2 because of the tip radius (convolution) and problems arising from the reactivity of the samples under ambient conditions. This causes the formation of adsorbate islands around the surface tracks, which eventually cover the whole sample and make prolonged measurements difficult.

4.2 Experimental Results

Based on the presented experiences and knowledge about the four insulators collected by others during the last decades, we performed HCI and SHI irradiations for these materials. While for the oxides $SrTiO_3$ and TiO_2 no special pretreatment is necessary, and for mica a simple take off of the topmost layer with a tape is sufficient to get a clean surface, this is not the case for the isolator CaF_2. The pretreatment of CaF_2, which was developed during the elaboration of the thesis and keeps the surface stable under ambient conditions, is described in section 4.2.1.
Besides SHI irradiation under grazing angle of incidence, which has been investigated in the greatest detail during performing this thesis, for comparison reasons also irradiations with HCIs were performed. Apart from using charge states near the predicted thresholds of surface nanostructuring, the main critical and finally also determining issue was the contamination of the surfaces which prohibited to provide unambiguous indications for nanostructures like nanohillocks. To ensure reliable evidence for nanostructuring due to HCI irradiation clean surfaces and in–situ AFM measurements of irradiated samples would be favorable and would require dedicated equipments, which were not available. Nevertheless section 4.2.2 will give a short overview on the performed measurements, pointing also to experimental challenges.
In comparison to HCI irradiations, contaminations are much less problematic in the case of SHI irradiations under grazing angle of incidence. The created special track formation along the surface can clearly be assigned to single ion impacts. The measurement results for the four investigated materials are describe in detail in section 4.2.3. A novel track formation could be observed for the crystal CaF_2 and the lamellar material mica. In the case of CaF_2 a simulation based on a

three-dimensional version of the two-temperature-model (TTM) was performed by coworkers of the group of M. Schleberger and helped us to understand the underlying physical mechanisms.

4.2.1 Pretreatment of CaF_2

In the case of CaF_2 AFM measurements are challenging due to the formation of adorbate islands, as mentioned for example by Akcöltekin *et al.* [145]. The formation of adsorbate islands is enhanced in the vicinity of defects and tracks. Under UHV condition the morphology doesn't change even after days [166]. Hence, in–situ AFM measurements of irradiated samples would be preferable unless they wouldn't be so tedious and wouldn't require dedicated equipment often not available at beamlines.
Initially, also our studies of CaF_2 were performed without any pretreatment of the samples and the surface was affected by adsorbate island formation within a short period of time. AFM measurements had to be performed within the first hours after irradiation. Detailed and repeated AFM investigations were therefore not possible. In fig. 4.12 the growth of the adosorbate islands can be seen. Already some days later the whole surface is covered by adsorbates.

In the course of our investigations we have found a technique, which largely prevents the formation of these adsorbate islands. Heating the cleaved samples to 400°C under high vacuum conditions (10^{-6} mbar) for a prolonged time (several hours), makes the morphology of the surface stable even under subsequent exposition to air. Fig. 4.13 shows that at enough high heating even several months later.

A tentative explanation of the positive effect on the surface morphology of CaF_2 due to heating is given by following considerations. At moderate temperatures up to 240°C, defects like H and F centers diffuse within the bulk towards the surface, which causes in the following the desorption of flourine and F centers aggregate into metallic colloids [168,169]. The metallic colloids progressively oxidise or hydroxilise by oxygen and water and adsorbate islands are formed. Above 250°C the evaporation temperature for calcium is surpassed, the Ca colloids evaporate and an inert and stochiometric CaF_2 surface is formed. On perfect CaF_2 surfaces water molecules do not adsorb at room temperature [170]. Because of the observed positive effect of the sample heating, most of the samples were exposed to this pretreatment procedure before performing irradiations.

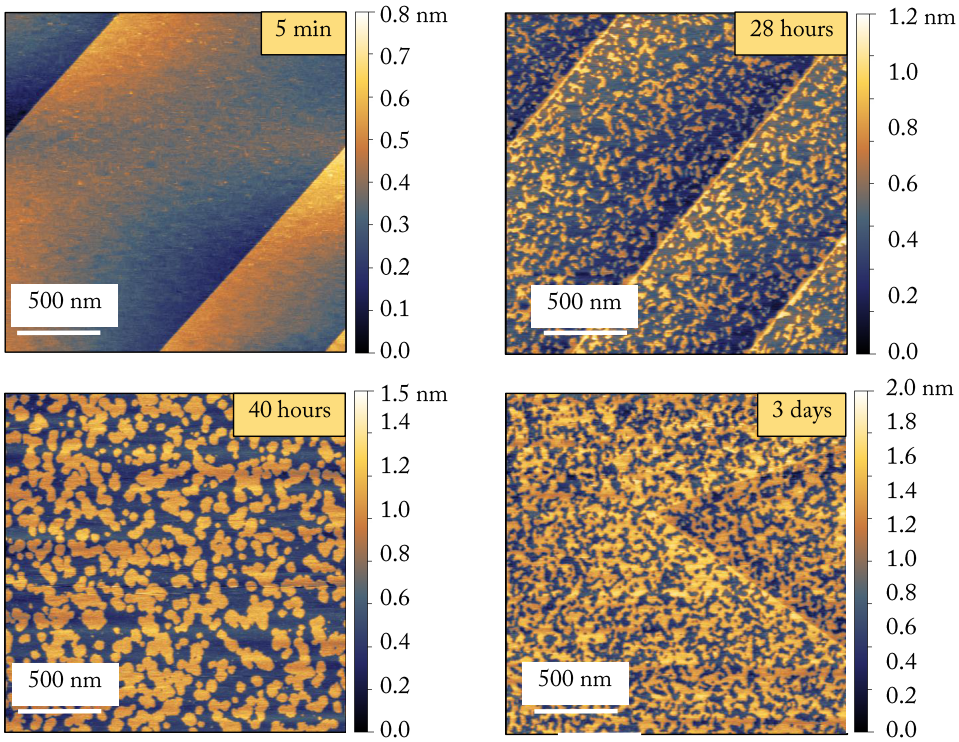

Figure 4.12: Adsorbate island formation on a CaF_2 surface
Within some hours the whole CaF_2 surface is covered by adsorbate islands. The figures show the growth of the islands within 5 min, 28 h, 40 h and 3 days after cleaving.

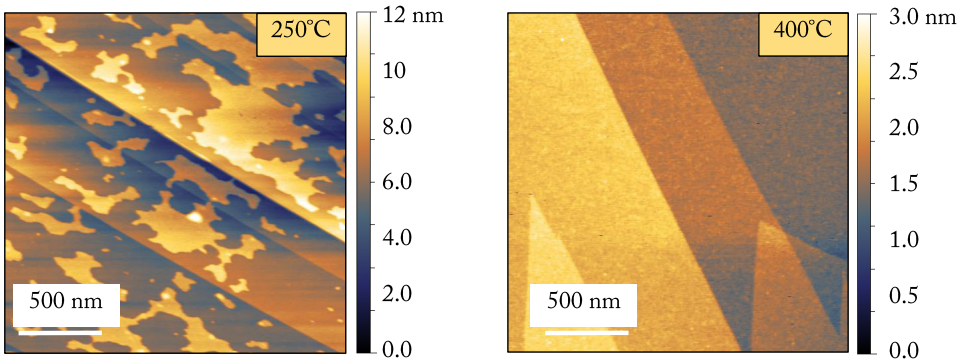

Figure 4.13: Pretreatment of CaF_2
By heating the sample to about 400°C under high vacuum conditions make the morphology of the surface stable even under subsequent exposition to air. The surface doesn't change even after several months.

4.2.2 HCI irradiation

In the case of $SrTiO_3$ a potential energy threshold between 15.4 keV and 30.4 keV for nanostructuring after HCI irradiation was predicted. To determine more accurately the threshold, HCI irradiations of $SrTiO_3$ under perpendicular incidence angle were performed and the samples afterwards investigated with ambient or UHV AFMs. The same irradiation and measurement procedures were also performed with TiO_2 samples, for which similar potential energy threshold values were predicted.

The first irradiations were performed at the ion beam facility ARIBE in Caen with Xe^{29+} at 319 keV and Xe^{31+} at 319 keV and 310 keV. For both sample types no nanostructuring after irradiation could be observed, what is explainable by the low charge state or low potential energy of about 10 keV of the used ions. Due to the limited accessible charge state at the ARIBE facility of Xe^{31+}, the irradiations were repeated with Xe ions at higher charge states, extracted from the two-ion-source facility at the HZDR and from the ion beam facility at the Universität Duisburg-Essen. Also the irradiation with $Xe^{36+,38+,40+}$ at 114 keV at the two-ion-source-facility in Dresden and with Xe^{40+} at 260 keV at the ion beam facility in Duisburg-Essen didn't show definitely nanohillock or crater formation. As mentioned in the introduction of this section the main critical and finally also determining issue was the contamination of the surfaces. It was not possible to clearly assign that the observed hillocks result from HCI irradiations or are simply caused by contaminations. The problem of contamination was tried to be minimised by a cleaning process of the sample before irradiation, including heating, HF etching and snow cleaning as described in [171]. However, since between the irradiation and the AFM measurement process the UHV environment was broken for hours or days, the addition of further contaminations couldn't be eliminated or prevented.
Another attempt to handle the problem with contaminations was to cover the sample with a metallic mesh to irradiate only the uncovered part of the sample, enabling the comparison of the topography of the irradiated and unirradiated surface of the same sample afterwards. But also in this case no distinct differences between the irradiated and non-irradiated area could be stated. To ensure reliable evidence for nanostructuring due to HCI irradiation clean surfaces and in–situ AFM measurements of irradiated samples would be favorable and would require dedicated equipments, which were not available.

Etching of HCI irradiated CaF_2 and mica

The problem of contamination arose also for the CaF_2 and mica samples. These samples were HCI irradiated at the ARIBE facility with ions at charge states around the threshold for hillock

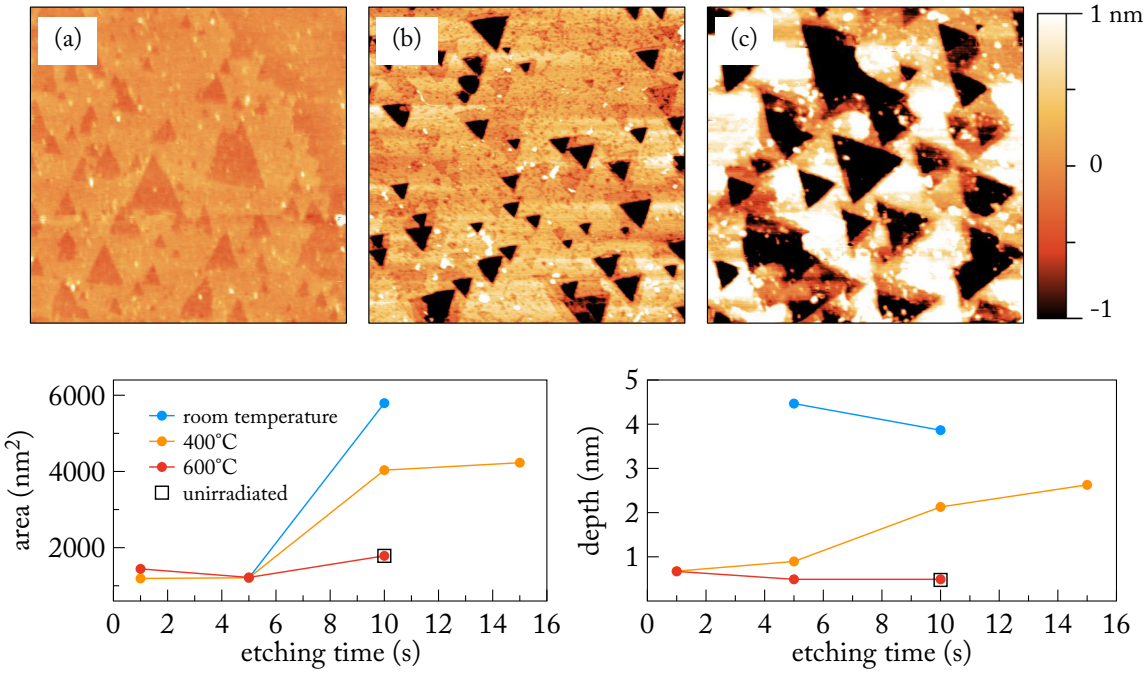

Figure 4.14: Etch pits of HCI irradiated CaF_2
The AFM figures (1 µm×1 µm) show the formation of triangular etch pits after etching unirradiated CaF_2 for 10 sec (a), Xe^{31+} at 155 keV irradiated CaF_2 for 5 sec (b) and for 10 sec (c) in HNO_3 etchant solution. The much deeper etch pit formation of irradiated samples is obvious.
The decrease of etch pit depth and area for samples, which were heated to 400°C and 600°C during irradiation, points to a healing effect due to sample heating.

formation. For the irradiated mica and CaF_2 samples HCI induced defects became only visible as pits after etching.

The Xe^{31+} at 155 keV irradiated CaF_2 samples were chemically etched in a HNO_3 solution (10% vol.) at room temperature for several seconds and subsequently cleaned with deionised water. The irradiated samples exhibit triangular pits, which geometrical shape originates from the (111) crystal lattice orientation of the CaF_2 sample (see fig. 4.14). While unirradiated etched samples show superficially triangular etch pits, arising from randomly occuring atomic-scale dislocations, irradiated samples are much more sensitive to the etching procedure. For the same etching time (10 sec) much deeper etch pits of several nanometers in depth are created (fig. 4.14a and c). An increase of the etching time showed also an increase of the etched area. These observations are not surprising, since the etchability of defect clusters and their appearance as triangular pits in the case of CaF_2 are well known and shown in [61]. Besides the affirmation of these results, we

heated the CaF_2 samples to 400°C and 600°C during the irradiation. The etching of these samples showed a decreased number of created etch pits and a decrease of their depth and area with an increase of the sample temperature. These observations point to healing effects due to sample heating and could be investigated in more detail in future experiments.

The formation of etch pits was also observed for irradiated (Xe^{31+} at 319 keV) mica samples, after etching for 6 min in HF (4% vol.). The number of pits is thereby in good agreement with the applied ion fluence ($\sim$ 50 ions/μm^2). Each pit is created by a single ion impact. Whereas more experimental investigations are necessary to reinforce these first studies, the evolution of HCI induced nanostructures from pits to nanohillocks is possible, like in the case of CaF_2 [61] and LiF_2 [172].

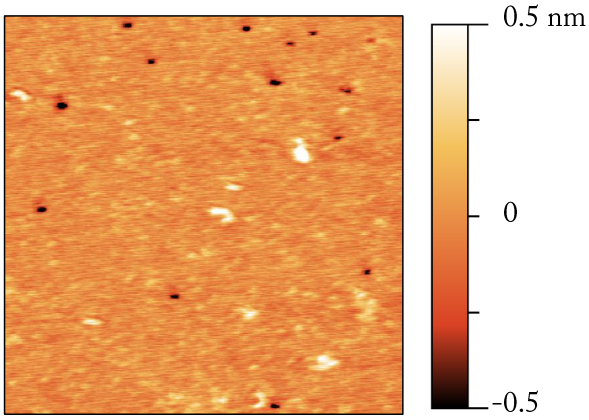

Figure 4.15: Etch pits of HCI irradiated mica
The AFM figure (350 nm×350 nm) shows pit formation after 6 min etching with HF (4% vol.). The number of etch pits is in good agreement with the used ions fluence.

4.2.3 SHI irradiation under grazing angle of incidence

As mentioned above, in the case of SHI irradiation under grazing angle of incidence, contaminations are much less problematic due to the characteristic track formation on the surface. The first SHI irradiations were performed with $SrTiO_3$ and TiO_2, since the large data set already available from the literature makes the two crystals ideal candidates to get familiar with the irradiation and measurement procedure and to use afterwards the gained knowledge to investigate other materials, like CaF_2 and mica in our case. All of the SHI irradiations were performed at the IRRSUD beamline in Caen during various measurement periods and the AFM measurements were partly conducted directly after irradiations while more detailed AFM investigations were performed in

Vienna.
The first part of the following section presents measurements and results obtained with the two oxides $SrTiO_3$ and TiO_2, which confirm earlier investigations performed by Akcöltekin *et al.* [103,130]. The second part focuses on the novel form of ion tracks observed on CaF_2 and mica after SHI irradiation under grazing angle of incidence. The studied structures include groove and hillock formation in a single ion track and are explained by sublimation and melting processes. The results obtained with CaF_2 were largely presented in [25] and parts of the following section are taken from this work.

$SrTiO_3$ and TiO_2

The used parameters for the irradiation of the oxides $SrTiO_3$ and TiO_2 during several measurement periods can be found in table 4.1. The energy loss for the different ions were calculated with the SRIM code [64].

$SrTiO_3/TiO_2$				
ion	energy[MeV]	energy loss[keV/nm]	angle[deg]	temperature[°C]
$^{136}Xe^{23+}$	96	21/20	0.2-2	RT
$^{129}Xe^{23+}$	53	17/16	1,2	RT
$^{208}Pb^{29+}$	100	23/22	1.5	RT, 400

Table 4.1: Parameters of the $SrTiO_3$ and TiO_2 irradiation experiments

The topography of the irradiated $SrTiO_3$ and TiO_2 surfaces are shown in fig. 4.16 and fig. 4.18, respectively. In both cases the formation of tracks consisting of single nanodots with heights up to 3 nm are visible. For longer tracks, like in the case of fig. 4.18a it is clearly visible that the chain of the well separated nanodots is followed by a fading protrusion (see also 3D images in fig. 4.18b). The length of the ion tracks is controlled by the incident angle and follow the relation $L = d/\tan(\theta)$ (see fig. 4.16c and fig. 4.18c). This relation is motivated by a simple geometrical consideration, where L is the track length and d the maximum depth from which the ion induced modification can still be detected at the surface. From the fits through the data points the characteristic depth can be evaluated and is found for $SrTiO_3$ and TiO_2 to be around $d \sim 5$ nm. The determination of the denoted incident angle depends thereby on the alignment of the sample surface relative to the ion beam (see chapter 3, section 3.1.2). To ensure the "correct angle", the incident angle is checked and calculated by the relation tracks/μm^2 = (ions/μm^2)$\cdot \sin\theta$. Most of the time the calculated angle didn't differ from the adjusted one by more than 0.2°. For all the presented results the calculated angle is used.

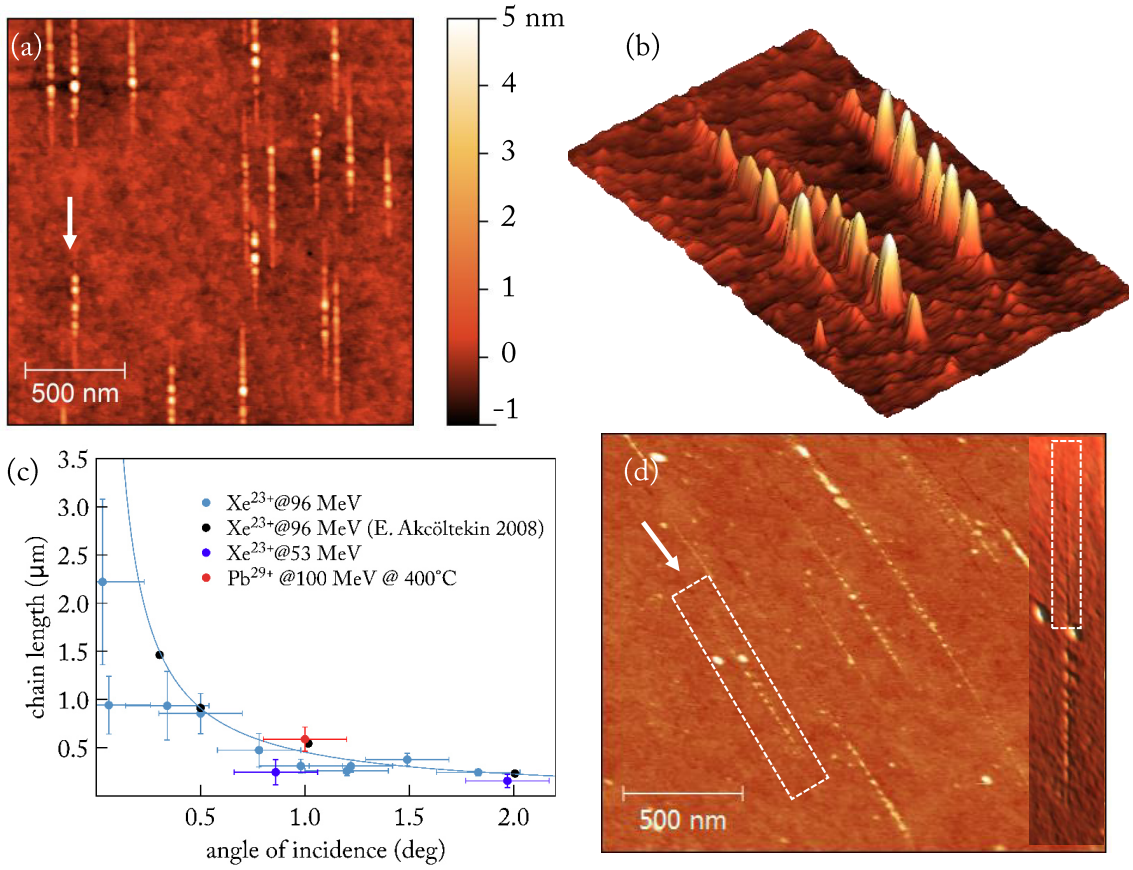

Figure 4.16: SHI irradiation of $SrTiO_3$ under grazing angle of incidence
(a) AFM image of a $SrTiO_3$ surface after irradiation with $^{208}Pb^{29+}$ ions at 100 MeV under grazing incidence angle of 1°. The sample was heated to 400°C during irradiation. Parallel arranged chains of single nanodots are created. The arrow shows the direction of the incident ions. (b) The 3D image shows the formation of chains of single well separated nanodots. (c) The chain length in dependence of the incident angle. The data points can be fitted by the simple relation $L = d/\tan(\theta)$. The tracks induced by particles at lower kinetic energy (53 MeV) tend to smaller lengths. (d) High resolution AFM images show the creation of grooves at the impact site of the particles (highlighted area). Since these grooves are really shallow they can easily be overlooked, like in the case of (a). The white arrow indicates the direction of the incident ions.

Besides the confirmation of the formation of chains of single nanodots and the dependence of the track length on the incident angle, a further observation is confirmed. The tracks show a trend to shorter lengths with decreasing the kinetic energy of the incident ions or the stopping power, respectively. This is in agreement with [131] and shown in fig. 4.16c, 4.18c and 4.17.

Since the measured tracks on the surface represent only a part (which percentage depends on the incident angle, but in our case it ranges from 25 to 30%) of the whole created track (several μm

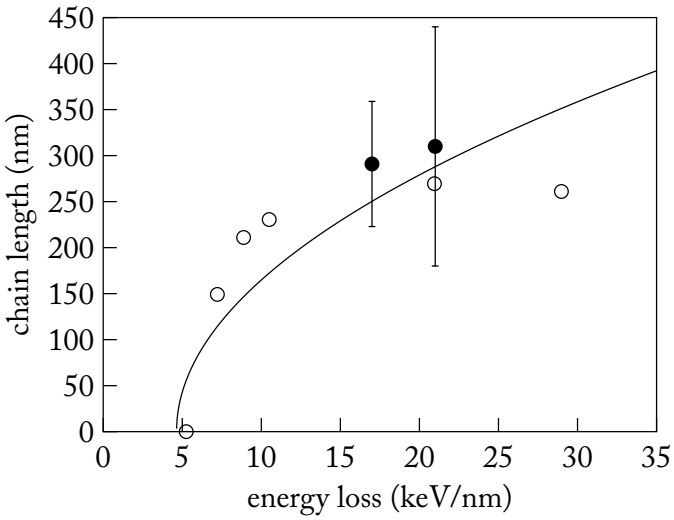

Figure 4.17: Chain length as a function of the stopping power
The open circles show data taken from [131]. The solid points are from irradiations with Xe ions at two different particle kinetic energies and the chain length was corrected to present an incident angle of 1.3°.

in length), naively no differences in the observed track lengths are expected. The observed length differences may arise from the fact that the higher the deposited energy is, the more pronounced nanostructures are created. The determination of the track length depends on the quality of the recorded AFM images and less developed structures, especially the sloping protrusion at the end of the visible tracks, may be missed. This could explain the observation of shorter track lengths with the decrease of stopping power.

A more surprising and unexpected topographical feature become visible by performing high resolution AFM imaging. At the impact site of the track a groove is formed before merging into a chain of single nanohillocks. Since the grooves are really shallow and have depths of only a few tenths of nanometeres, they can easily be overlooked. In fig. 4.16d such shallow grooves can be seen on an irradiated $SrTiO_3$ surface and are marked by arrows. In the case of TiO_2 the formation of pits between hillocks at the impact site became only visible when the target was heated during irradiation to $400°C$ (see fig. 4.18d) and inspected with the AFM directly after irradiation. Recently, the formation of grooves on $SrTiO_3$ at the impact site of the tracks was published in [132]. Also for SiC [119] a groove formation was observed and explained by sublimation of Si atoms along the particle trajectory, resulting in graphitic grooves. In the case of TiO_2 a preferential loss of O from the first layers of the target during grazing angle of incidence SHI irradiation was shown in [144].
Besides the measurements of $SrTiO_3$ and TiO_2 lots of work was done during the elaboration of

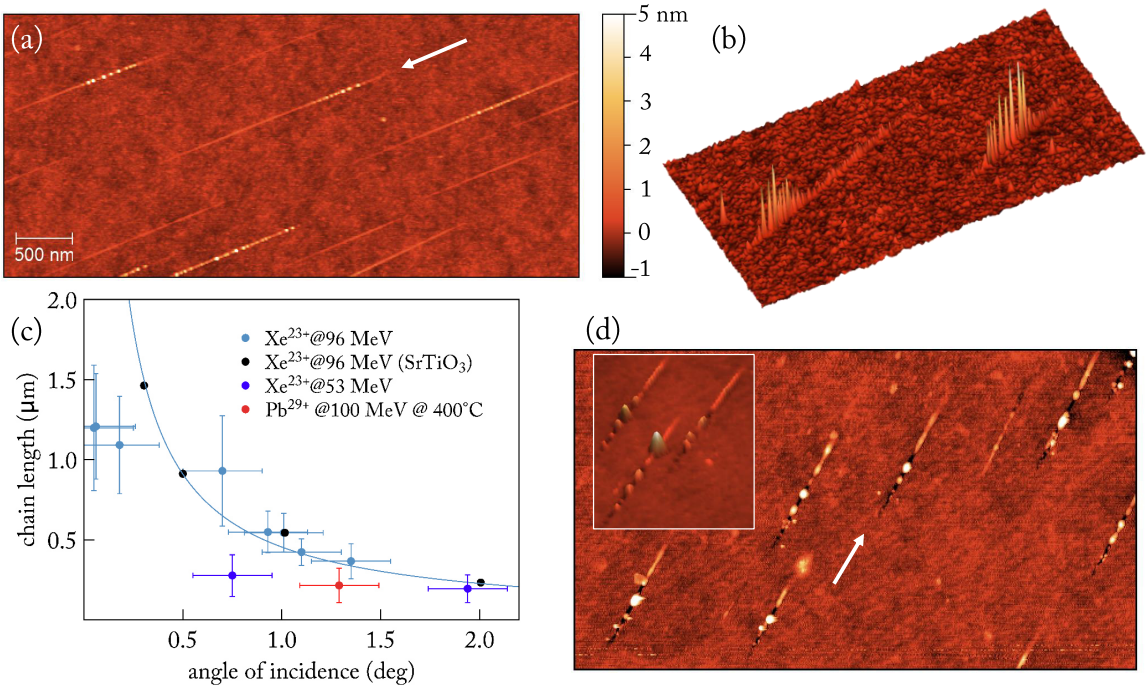

Figure 4.18: SHI irradiation of TiO_2 under grazing angle of incidence
(a) AFM image of a TiO_2 surface after irradiation with $^{136}Xe^{23+}$ ions at 96 MeV under grazing angle of incidence $< 0.2°$. The formation of several 100 nm long tracks can be observed, with chains of single nanohillocks followed by a fading protrusion. The arrow indicates the direction of the incident ions. (b) The 3D image shows the creation of chains of single nanodots followed by a sloping protrusion. (c) Chain length in dependence of the incident angle. The data points for TiO_2 show similar values as measured for $SrTiO_3$. Also for TiO_2 a decrease of the projectile energy leads to a decrease of the chain length. (d) Heating the sample to 400°C during irradiation and AFM measurements directly after irradiation have shown the formation of pits between the creation of hillocks at the impact site. The framed image shows a 3D presentation of the produced tracks with the pits in between.

the thesis by studying nanostructuring on mica and CaF_2. For these two materials a more pronounced groove formation at the impact site could be observed. Before discussing this novel track formations and possible underlying physical mechanisms, the creation of grooves and hillocks in a single track on mica and CaF_2 is discussed.

Novel track formation on CaF_2

High resolution AFM imaging performed during the course of this PhD thesis and partially published in [25] have shown the formation of a much more complex nanostructure on CaF_2 after SHI irradiation under grazing angle of incidence as observed before [145, 166]. In fig. 4.19 the 3D plot shows the typical topography of a CaF_2 surface after SHI irradiation under grazing angle of incidence of 1.3°. The direction of the incoming ion is marked by an arrow and the formation of several parallel arranged tracks induced by single ion impacts can be observed. The groove formation at the impact site, which was difficult to notice in the case of $SrTi_3$ and TiO_2, is clearly visible here. The enlarged figure of a single track shows a detailed picture of the nanostructure. At the impact site a $\sim$ 400 nm long groove is formed, which is bordered on both sites by a series of nanodots. The end of the groove is marked by a single huge hillock, followed by a decaying protrusion of several 100 nm length. Longitudinal and cross profiles show the height, depth and width of the created nanodots and the formed groove in detail. Exemplary, some of them are plotted in fig. 4.19. The longitudinal profile (a) through the center of the track shows the formation of a groove with a depth of 1-2 nm, terminated by a 14 nm high hillock and followed by a decaying protrusion of some nm height. The profile (b) runs through one of the chains of single nanohillocks and shows the formations of a series of equally spaced nanodots with an increasing height up to $\sim$ 5 nm. This nanohillocks eventually merge into the huge single nanohillock at the end of the groove. The straight line of the profile to the right of this hillock shows the flatness of the surface with a RMS-roughness value of 0.15 nm. The cross profiles (c) and (d) through the former part of the track show again the groove formation with the single nanodots on the right and left site with a distance of $\sim$ 15 nm in between.

As shown before for HCI irradiated samples the etching in HNO_3 10% etchant solution for several seconds leads to the formation of triangular etch pits. This is also the case for SHI irradiated samples. In fig. 4.20 a SHI irradiated CaF_2 crystal is shown before and after etching with HNO_3. Since the irradiation was performed under grazing angle of incidence a chain of triangular etch pits is observed.

To analyse the created nanostructures in dependence of the incident angle several irradiations were performed, which parameters are summarised in table 4.2.
The evaluation of the groove and track length (including the groove, the huge hillock and the descreasing protrusion until it vanishes under the surface) has shown that they can be controlled by the incident angle. The length of the groove as well as the whole track follow the relation $L = d/\tan(\theta)$ (see fig. 4.21). From the fits through the data points the characteristic depth for the groove formation is evaluated to be around $d = 4.8$ nm while for the whole track length a

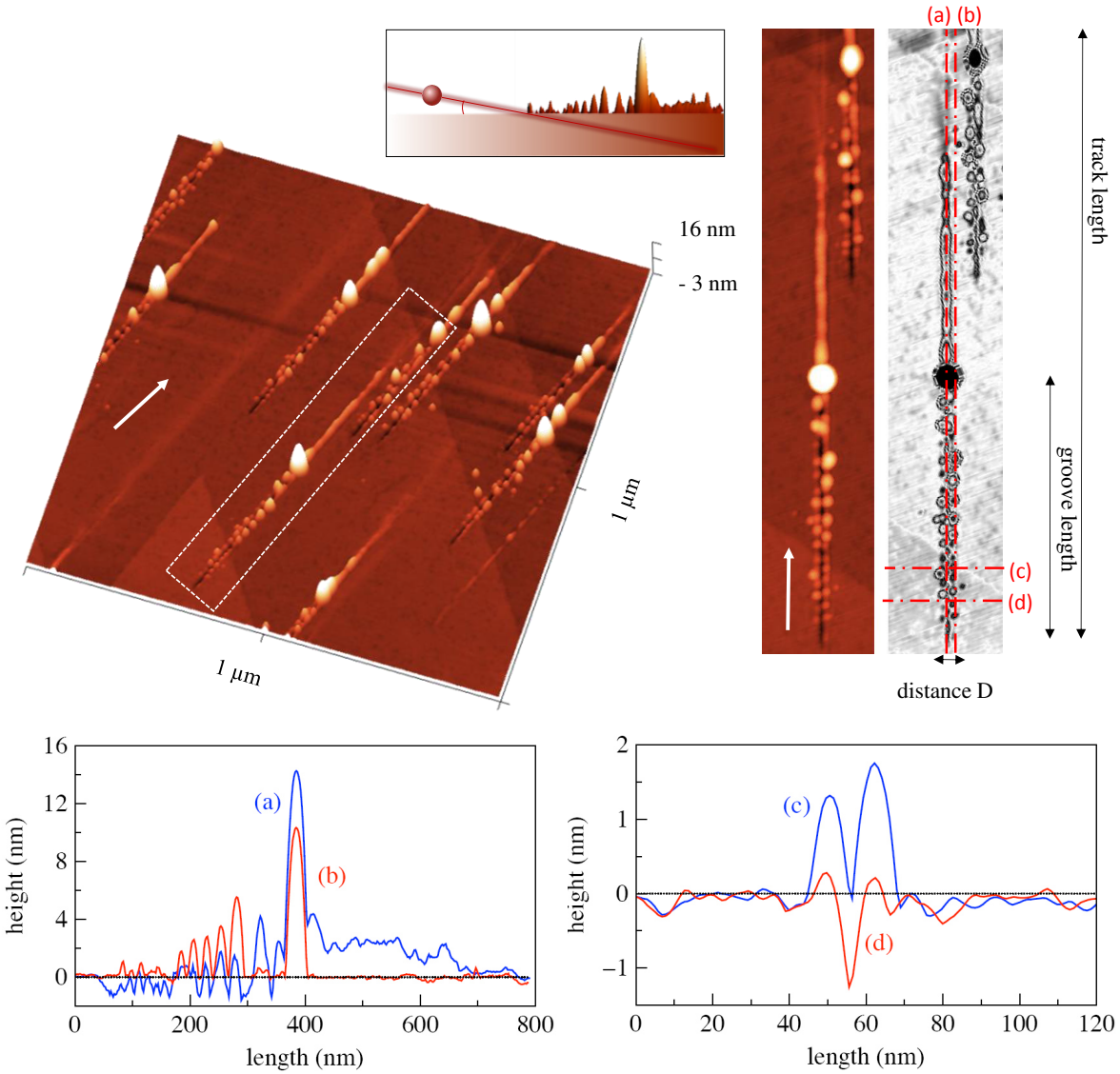

Figure 4.19: SHI irradiation of CaF_2 under grazing angle of incidence
3D plot of an AFM image which shows CaF_2 surface after irradiation with $\sim 100\,MeV$ Pb ions under $1.3°$ angle of incidence. The white arrow indicates the direction of the incident ions. The formation of parallel arranged tracks with a complex structure can be observed. The highlighted track in the 3D plot is shown in more detail in the figure to the right. The formed groove at the impact site is bordered by a chain of single nanodots on the right and left site and merges into a high single nanodot. This one is followed by a decreasing protrusion of several 100 nm length which finally vanishes under the surface. Longitudinal and cross profiles are drawn through the track to analyse the produced structures in more detail. The longitudinal profiles (a) and (b) and cross profiles (c) and (d) show the height, width and depth of the nanohillocks and the groove. The figure is taken from [25].

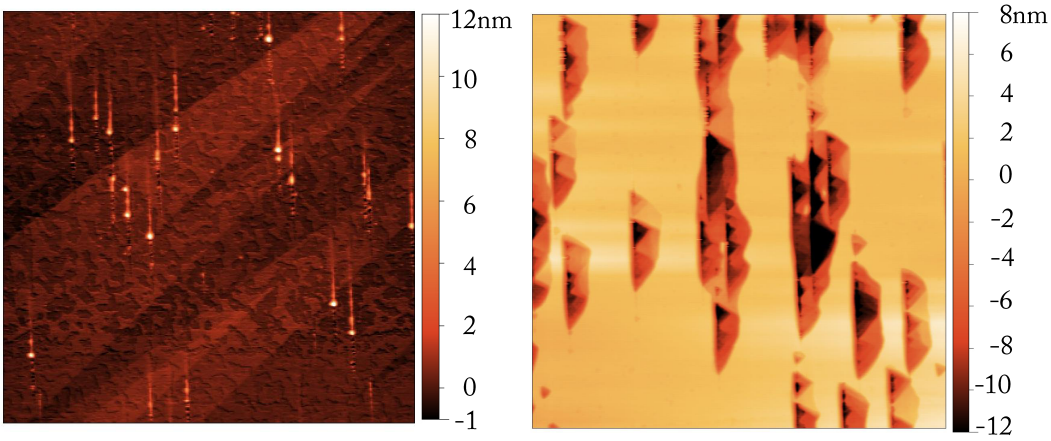

Figure 4.20: Formation of chains of triangular etch pits
The left figure shows an unheated CaF_2 sample irradiated with $^{208}Pb^{29+}$ ions under grazing angle of incidence of 1.3°. The adsorbate islands and parallel arranged tracks are observable. The right figure shows a chain of triangular etch pits. The CaF_2 sample was first irradiated with $^{136}Xe^{23+}$ at grazing angle of incidence of 1.1° and then etched for 10 seconds in HNO_3 10% etchant solution.

value of $d = 10.6$ nm is found. A heating of the sample to 400°C during irradiation seems to have no effects on the groove or track length.

CaF_2				
ion	energy[MeV]	energy loss[keV/nm]	angle[deg]	temperature[°C]
$^{136}Xe^{23+}$	96	16	0.2-3	RT, 400
$^{208}Pb^{29+}$	100	17	0.2,1.3	RT, 400

Table 4.2: Parameters of the CaF_2 irradiation experiments

The evaluation of the distances between the periodically arranged nanodots along the border of the groove shows a similar $a/\tan(\theta)$ relation with the value of a being close to the lattice constant of 5.462 Å (see fig. 4.21). The creation of a chain of nanohillocks may be coupled to the spatially inhomogeneous electron density of the material. As shown for $SrTiO_3$ and TiO_2 (see section 4.1.1 and 4.1.2) every time the projectile travels through a region of high electronic density, which corresponds to the periodicity of the crystal, energy is effectively deposited into the electronic system leading to the creation of equidistant nanodots.

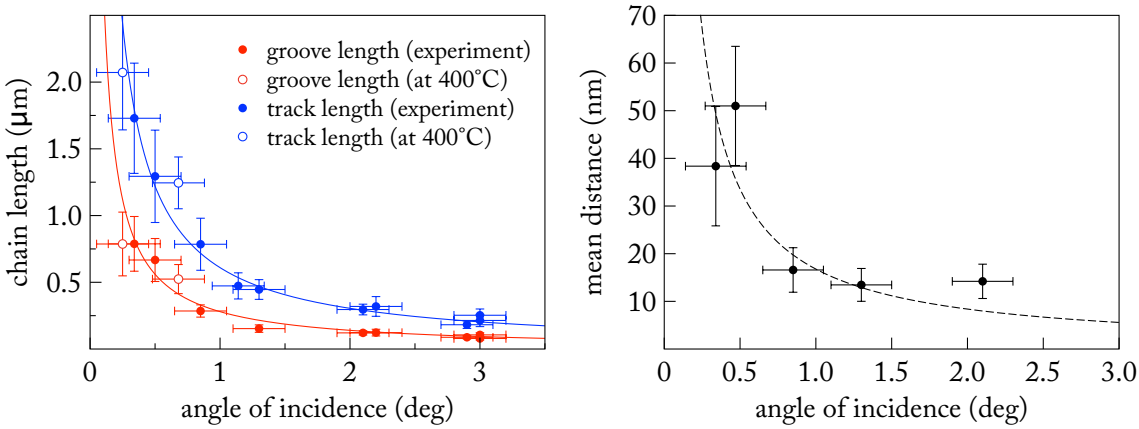

Figure 4.21: Chain length and hillock spacing in dependence of the angle of incidence
The left figure shows the evaluated groove (red data points) and track length (blue data points) as a function of the incident angle for irradiation with $\sim 95\,MeV\,Xe^{23+}$ *ions. The solid lines represent fits through the data points following the equation* $L = d/\tan(\theta)$. *The right figure shows the evaluated distance between the periodically arranged single nanodots of a chain. The experimental data can be fitted with the relation* $a/\tan(\theta)$ *with a being close to the lattice constant* $5.462\,\mathring{A}$.

Novel track formation on mica

Detailed AFM studies were also performed after SHI irradiation of the isolator mica. In this case the formed structures on the surface consist of a double track at the impact site which merges into a single decreasing protrusion and vanishes eventually under the surface (see fig. 4.22). High resolution AFM imaging under UHV conditions[1] show that the double tracks consist of a sequence of single nanohillocks. Remarkable for the mica irradiations are the really long formed tracks along the surface. At small incidence angles of $\sim 0.2°$ chain lengths of several hundreds of nm in length are formed. Systematic irradiations under different incident angles and evaluations of the groove and track lengths yield a characteristic depth for the groove formation of $d = 2.3\,\text{nm}$ and for the whole track length a value of $d = 13\,\text{nm}$.
The etching of HCI irradiated mica samples has shown the formation of single etch pits. By etching mica samples after exposure to SHI ion impact under grazing angle of incidence elongated pit formation becomes visible. In fig. 4.23 a SHI irradiated mica sample is shown before and after etching with HF (4% vol.).

Besides the variation of the incidence angle, the track structures were also studied by varying the kinetic energy of the incident particles and heating the samples to 200°C and 400°C during

[1] UHV-AFM measurements were performed during a measurement stay at the Universität Duisburg-Essen.

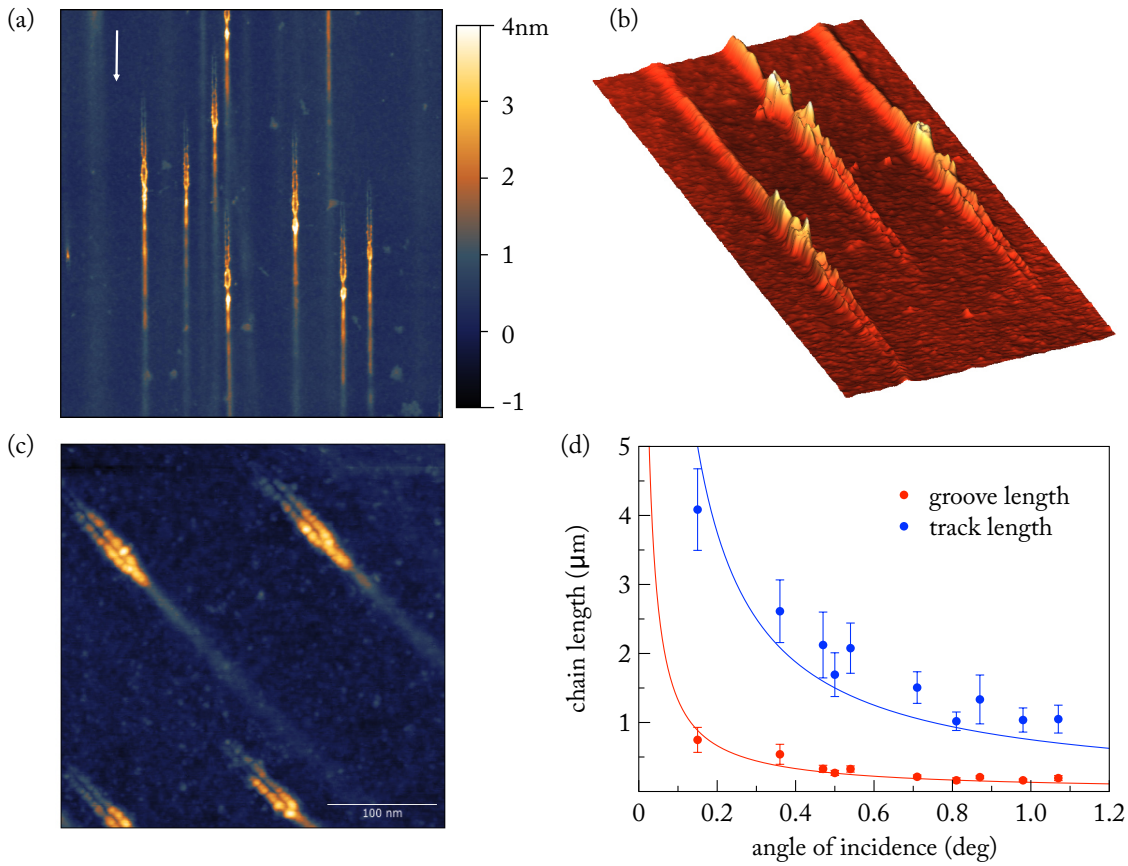

Figure 4.22: SHI irradiation of mica under grazing angle of incidence
2D (a) and 3D (b) AFM image of a mica surface after irradiation with 92 MeV $^{129}Xe^{23+}$ ions under grazing incident angle of 0.7°. The formation of a double track at the impact site which merges into a high hillock, followed by a decreasing protrusion, can be observed. The white arrow shows the direction of the incident ions. (c) High resolution AFM imaging under UHV conditions clearly shows that the double track consists of single nanohillocks. (d) Groove and track lengths for various incident angles follow the relation $L = d/\tan(\theta)$.

irradiation. In addition two different types of mica, which vary in the chemical composition, were investigated and are presented in the following section. An overview of the different irradiation parameters can be found in table 4.3.

The variation of the kinetic energy of the ions results in the deposition of different amounts of energy in the material (fig. 4.24a and b) and shows an effect on the created groove length (fig. 4.24c). Evaluating the groove length as a function of the stopping power S shows that the data can nicely be fitted by the relation $L = k \cdot \sqrt{S - S_{\text{threshold}}}$ with yielding a threshold value of $S_{\text{threshold}} = 4\,\text{keV/nm}$, close to the threshold value of 4.8 keV/nm given by Thibaudau *et al.* [155].

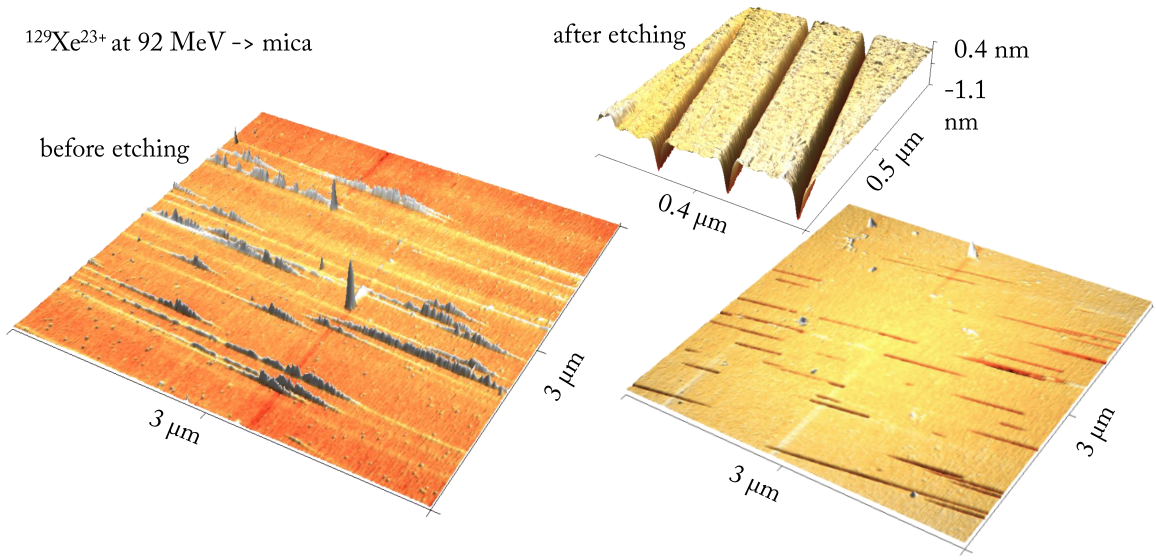

Figure 4.23: Track formation on mica before and after HF etching
The left figure shows the track formation on mica after $^{129}Xe^{23+}$ ions at 92 MeV before etching and the right figure after etching the sample in 4% HF etchant solution for 3 minutes. The chain of hillocks appear after etching as a parallel arranged elongated pit formation. The zoomed 3D image shows the well defined structure of the pit formation with a depth of about 1 nm.

Mica				
ion	energy[MeV]	energy loss[keV/nm]	angle[deg]	temperature[°C]
$^{136}Xe^{23+}$	96	14.4	0.2-1.2	RT, 400
$^{129}Xe^{23+}$	92,72,53,23	14.5, 13, 11.5 ,7	0.2-2, 90	RT
$^{208}Pb^{29+}$	100	15.6	1-2	RT, 200, 400

Table 4.3: Parameters of the mica irradiation experiments

A similar behaviour was shown by Ochedowski *et al.* [119] by calculating the track lengths created on SiC for various kinetic energies of the incident ions (see blue curve in fig. 4.24c).
Besides the groove length the deposited amount of energy determines also the height of the created hillocks of the double tracks at the impact site and the distance between opposite hillocks. An increase of both parameters with an increase of the stopping power were found (fig. 4.24d).

During performing the irradiations the question arose if it would be possible to shift the threshold for track formation by heating the sample during irradiation. A shifting towards lower as well as higher projectile energies was thinkable. By considering the thermal spike model, the projectile energy is converted in the last step into thermal energy and can lead to sublimation or melting processes. A certain amount of energy has to be deposited to achieve a temperature rise.

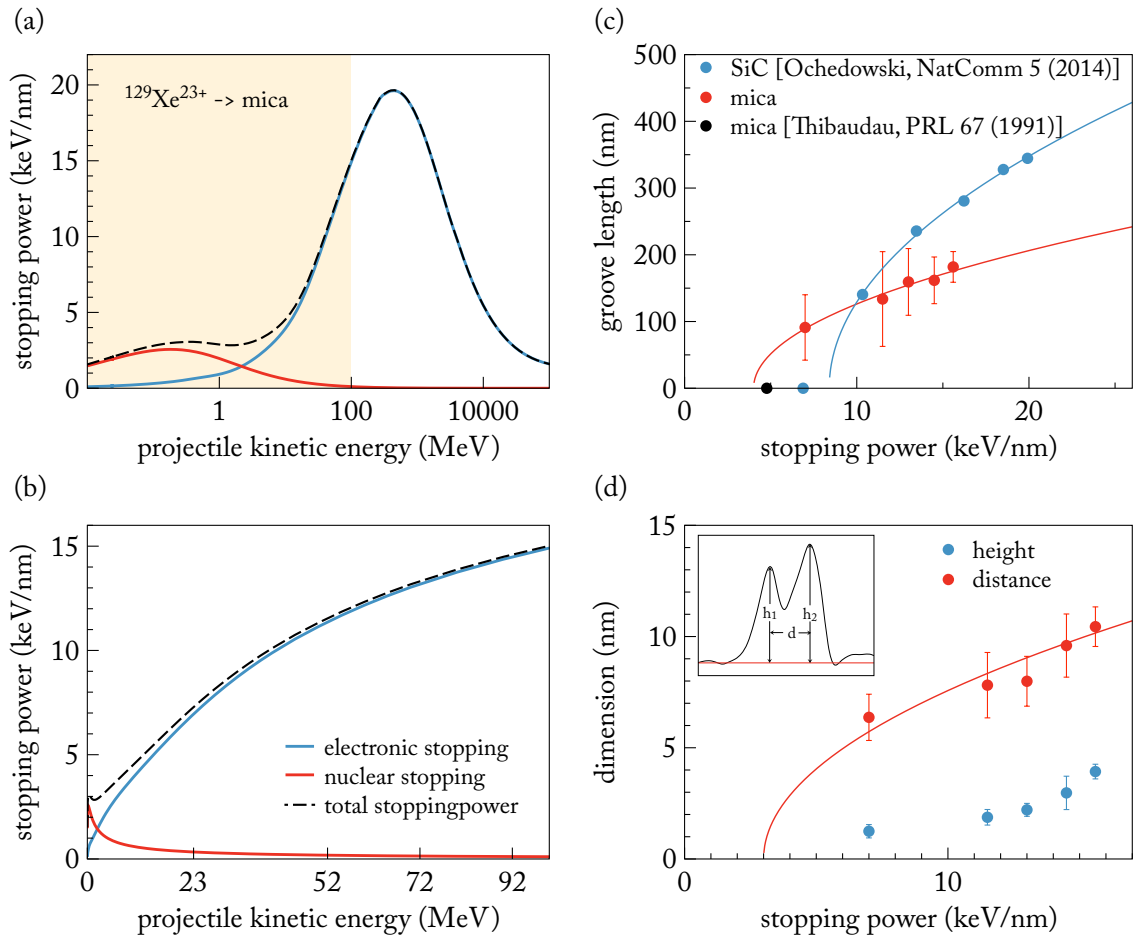

Figure 4.24: Track formation in dependency of the stopping power
(a) Electronic and nuclear stopping power calculated with the SRIM code for a Xe atom impacting on mica with a density of $\rho = 2.82\,g/cm^3$. The highlighted area is zoomed in (b) and includes the projectile energy range of our irradiations, i.e. 23, 52, 72 and 92 MeV. (c) The figure shows the evaluated groove lengths as a function of the stopping power. The black dot shows the predicted threshold for track formation in mica [155]. The solid line represents a square fit through the data points. A similar behaviour was reported for SiC in [119] (blue data points and fit). (d) The mean value of the hillock height of the double tracks and the mean value of the distance between the chains of hillocks show a dependency on the stopping power. The inset illustrates what is meant with the height and the distance.

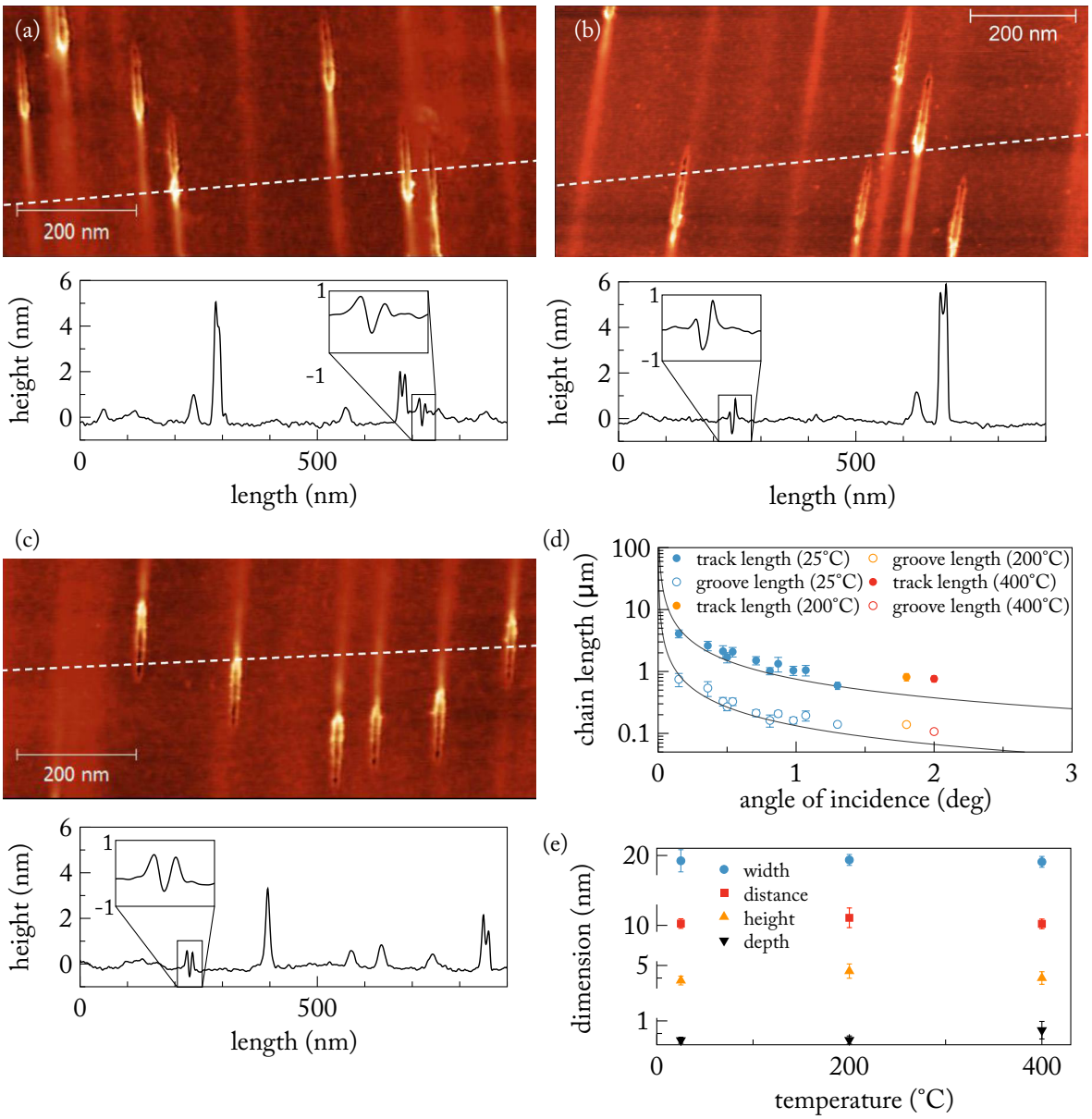

Figure 4.25: Track formation on mica in dependency of the sample temperature *Track formations on mica due to $^{208}Pb^{29+}$ ion impacts at room temperature (a), at 200°C (b) and at 400°C (c). The dashed lines in the images indicate where the line profiles, shown below, are taken from. All three images show the formation of a groove with bordered material at the impact site (zoomed figures), the merging of the double track into a huge $\sim 5-6$ nm high single hillock, followed by a decreasing protrusion with a height of $\sim 1-2$ nm. (d) The groove and track lengths for the heated samples are compared with the results obtained from the unheated samples. A slightly increase of the lengths can be observed. In (e) the width of the hillocks, the distance between opposite hillocks, the height of the hillocks and the depth of the formed grooves are plotted for unheated, 200°C and a 400°C heated mica samples.*

The heating of the sample could enable to get nanostructure formations already for lower deposited energy amounts. On the other side, heating the sample could also lead to annealing and self-healing processes and more energy deposition would be necessary to overcome these processes.

Since the irradiation time was limited and the heating and cooling process of the samples time-consuming, only a small data set of irradiation at higher temperatures is currently available. The results are summarised in fig. 4.25. The irradiations at 200°C and 400°C seem to lead slightly to longer groove and track lengths and the grooves are more pronounced in the AFM images. The parameters like width, distance and height of the hillocks of the chains at the impact site seem unaffected by temperature. A heating of the samples higher then 600°C should be avoided, since at these higher temperatures the surface of mica becomes cracked and is not any more suitable for performing these kinds of measurements.

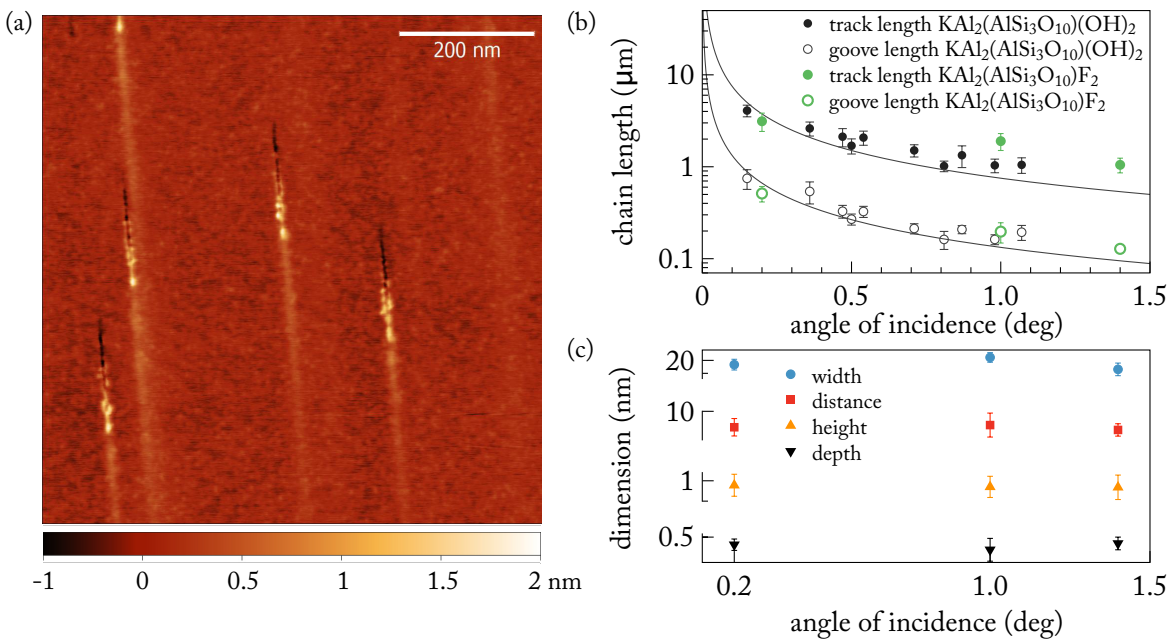

Figure 4.26: Track formation on mica $KAl_2(AlSi_3O_{10})F_2$
(a) The AFM images shows a $KAl_2(AlSi_3O_{10})F_2$ sample irradiated with $^{129}Xe^{23+}$ under grazing angle of incidence of 1.5°. The groove formation at the impact site is clearly visible. (b) Evaluation of the groove and track lengths created on flourine mica $KAl_2(AlSi_3O_{10})F_2$ (green data points) in comparison to natural mica $KAl_2(AlSi_3O_{10})OH_2$ (black data points). (c) Parameters of the double tracks of irradiated flourine mica. The values are similar to those obtained with natural mica, only the height of the double tracks is on the average only a third of the value obtained with natural mica.

A more pronounced groove formation could be observed by performing irradiation at room temperature with Fluorphlogopite mica $KAl_2(AlSi_3O_{10})F_2$. In this synthetic flourine mica the $(OH)^-$ is fully substituted by F^-. Samples of this chemical composition are characterised by superior thermal stability. They can be used up to 1100°C with almost no changes and will decompose gradually only at 1200°C. Natural mica with the $(OH)^-$ group begins to decompose already above 450°C and is almost completely decomposing at 900°C. The melting temperature of natural mica lies between 700 and 1000°C, whereas in the case of flourine mica at about 1350°C. A comparison of AFM images of natural mica $KAl_2(AlSi_3O_{10})OH_2$ and flourine mica $KAl_2(AlSi_3O_{10})F_2$ after irradiations under the same conditions show on both samples parallel arranged tracks with smoothly different topographical characteristics. For natural mica the formation of a double track consisting of single nanodots and a cavity in between is formed. However, in the case of flourine mica a long ditch with no bordered nanodots is notable (fig. 4.26a). The first nanodots appear much later in the modification. In both cases the double track eventually merges into a long decaying protrusion. Looking at the groove and track lengths, the length values for flourine mica lie slightly above the one obtained for natural mica (fig. 4.26b). The other parameters, i.e. the width, distance, height of the created nanodots and the depth of the formed grooves, are independent of the incident angle and show similar values as obtained for natural mica. Only the height of the double tracks is on the average only a third of the value obtained with natural mica.

4.3 Discussion

The irradiation of $SrTiO_3$ and TiO_2 with SHI under grazing angle of incidence could reproduce the formation of chains of single nanodots, reported earlier by Akcöltekin *et al.* [103]. Therein, the formation of chains of nanodots was successfully interpreted as remnants of molten zones from rapidly quenched thermal spikes and the equidistant arrangement of nanodots attributed to the fact that the ions cross regions with varying electron density. High resolution AFM measurements for $SrTiO_3$ or TiO_2 samples, which were heated during irradiation, have shown a shallow rift or hole formation at the impact site of the projectile. Similar observations were reported recently for $SrTiO_3$ in [132]. While the formation of the equidistant hillocks can be attributed to melting processes, the rift at the impact site may be caused by sputtering or sublimation processes.
More pronounced nanostructure formation of similar topography were observed on SHI irradiated CaF_2 and mica samples. The formation of a deep groove with bordered hillocks along the impacting trajectory might result from melting and sublimation processes.

Following the concept of the thermal spike model, the temperature of the system due to energy deposition of the incident projectile with a certain kinetic energy can be evaluated.

A surpassing of the sublimation temperature of the material may lead to groove and hole formation, the surpassing of the melting temperature to the formation of nanodots. To check these assumptions, calculations based on the two temperature model (TTM) were performed for CaF_2 by our coworkers in the group of M. Schleberger at the Universität Duisburg-Essen. Because of the complex structure, no calculations were done so far for mica. The results of the calculations for CaF_2 will be presented in the following in more detail.

As explained in chapter 2, section 2.3.1 the TTM model is based on two coupled heat diffusion equations, one for the electron and one for the phonon system, in which the electron-phonon coupling parameter g controls the energy transfer from the electronic to the lattice system. In the case of irradiation under grazing angle of incidence the cylindrical symmetry of the conventional TTM is broken, and a fully three-dimensional version of the TTM has to be used [119, 131]. To perform simulations comparable to our experimental data, a projectile under an incidence angle of 0.5° and a simulation box with length $x_{\text{box}} = 3000$ nm, width $y_{\text{box}} = 50$ nm and depth $z_{\text{box}} = 50$ nm were chosen. The simulation box is surrounded by a thermal bath with Van Neumann boundary conditions for the surface, and inside the simulation box the two equations 2.16 and 2.17 are solved. The parameters used for solving the two equations can be found in [25].

In fig. 4.27 the temperature profiles of the surface and the bulk of CaF_2, obtained by the calculations, after SHI impact under grazing angle of incidence are shown. The top-view and side-view of the sample show the development of the temperature profile 100 fs and 1 ps after ion impact. The highlighted temperatures of 1691 K and 2806 K mark the region in which the melting and the sublimation temperature of CaF_2 is surpassed.

To compare the results from the calculations with the experimental findings, simulations under different incident angles have been executed. The extension of the surface region, where the sublimation temperature of CaF_2 is surpassed, is compared with the experimentally found groove lengths and where the melting temperature is surpassed with the track length, respectively (see fig. 4.28a). For the total track length the simulations are in good agreement with the experimental values, whereas from the simulation data an overestimation of the groove length evoked. This overestimation could be explained by the omission of the latent heat or the rather asymmetric track formation. At the impact site the atoms gain enough energy to be ejected from the surface and a groove is formed. The deeper the ions penetrate the bulk, the less atoms can leave the target. Deeper layers are molten and push material towards the surface, filling the initial groove with material and forming eventually the huge hillock, which marks the end of the groove. Around the hot zone, where only the melting temperature for CaF_2 is surpassed, melting, thermal expansion and rapid quenching create nanohillocks. The distance between the single nanodots reflects the spatially inhomogeneous electron density of the material under grazing angle of incidence, which

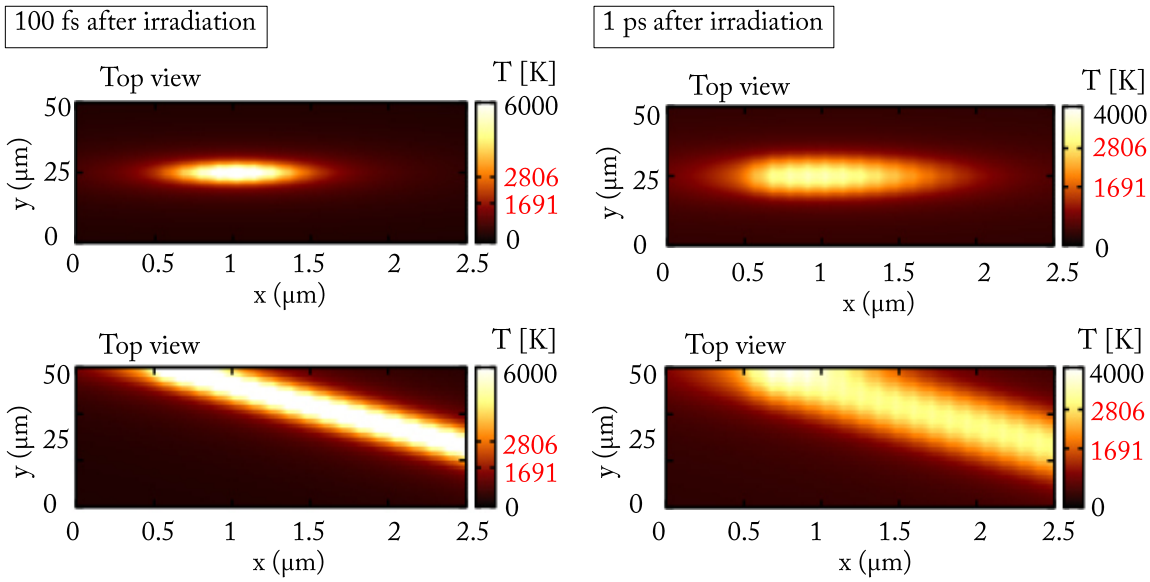

Figure 4.27: Temperature profiles of irradiated CaF_2
Typical results of the 3D-TTM calculation: Top-view and side-view of the lattice temperature profile of a CaF_2 sample 100 fs and 1 ps after ion impact of 95 MeV Xe^{23+} (S_e = 16 keV/nm) under grazing incidence angle of 0.5°. The highlighted temperatures of 1691 K and 2806 K mark the region in which the melting and the sublimation temperature of CaF_2 is surpassed. Figure is taken from [25].

is coupled to the periodicity of the crystal. Every time the projectile travels through a region of high electronic density, energy can effectively be deposited into the electronic system and periodically arranged hillocks are formed. Further penetration of the projectile into deeper layers of the target is accompanied by a single long protrusion from the (quenched) thermal expansion, which slowly fades until the track vanishes.
Besides the good agreement of the groove and track length with the value extracted form the simulations, also the calculated lateral extension of the molten zone of ∼ 10-15 nm corresponds quite well with the observed distance D between the two chains of hillocks (for details see fig. 4.19).

A further accordance between our experimental data and calculations performed by Toulemonde *et al.* [173], based on the thermal spike model, is shown in fig. 4.28b. There the track radii observed by TEM are compared with the inelastic thermal spike model using two criteria, the energy to melt and the energy to boil. The threshold for track formation and the track radii depend thereby on the kinetic energy of the particles. The spreading of the groove and of the melted track of our irradiated CaF_2 samples with particle kinetic energy of 0.7 MeV/u (S_e=16-17 keV/nm) are in good agreement with the predicted values for the track radii.

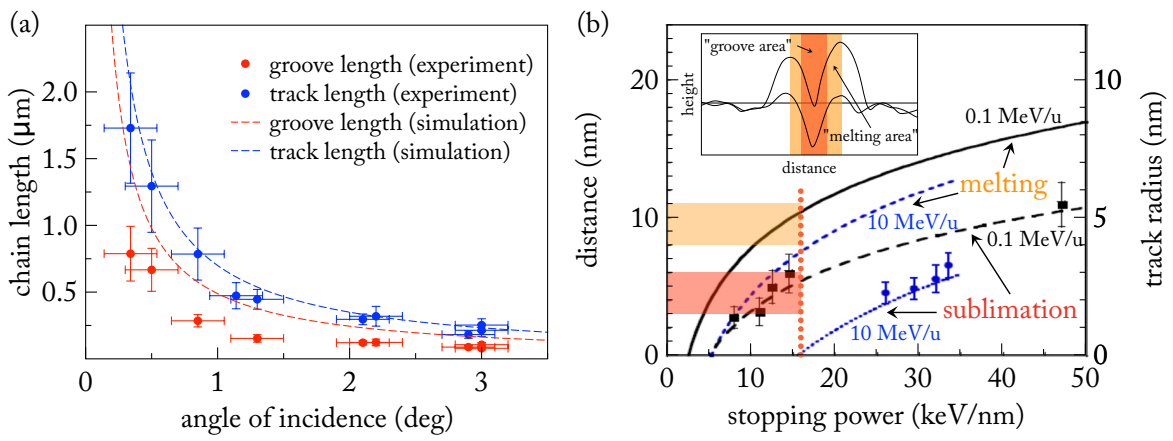

Figure 4.28: Comparison between experimental results and simulations
(a) The figure shows the evaluated groove (red data points) and track length (blue data points) as a function of the incidence angle for irradiation with ∼ 95 MeV Xe^{23+} ions. The dashed lines show the results of the performed 3D-TTM calculations. The experimentally obtained groove lengths are compared to the calculated values of the extension of the surface region where the sublimation temperature is surpassed, while the measured track lengths are compared to the regions where the melting temperature is reached. (b) Tracks observed by TEM in CaF_2 compared with the inelastic thermal spike model using two criteria, the energy to melt and the energy to boil. The data is taken from [173]. The spreading of the groove and of the melted track, indicated by the highlighted area in the subfigure, for 0.7 MeV/u (S_e=16-17 keV/nm) irradiation are in good agreement with the predicted values for the track radii.

As mica has a much more complex atomic structure compared to CaF_2, TTM simulations haven't been done until now for this material. Since we observe similar nanostructures after SHI irradiation on this material, it seems obvious that also for mica sublimation and melting processes are responsible for the complex track formation. Comparing the width of the double track with the track radii in mica after SHI irradiation from the literature [173] (see fig. 4.29), a similar dependency on the stopping power can be determined. The data points are fitted by a square root function with a stopping energy threshold of 2.5 keV/nm. The differences in the absolute values for our estimated track radii and the one from the literature may result from the velocity effect, indicated before for CaF_2 in fig. 4.28b and discussed in more detail in ref. [173]. There it is also mentioned that the track size not only depends on the ion velocity but also on the sample temperature. For Bi it was shown that the track size changes drastically by performing irradiations between 20 and 300 K. Our observation showed that the track length slightly increases and the created grooves are more pronounced for heated samples. This might be caused by the mentioned sample temperature dependency.

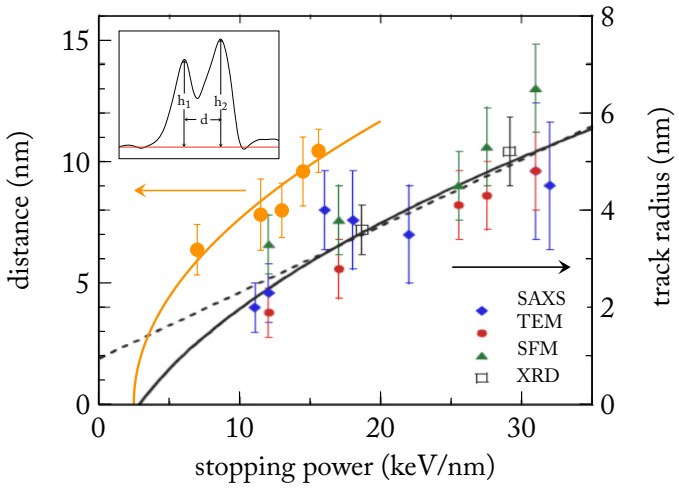

Figure 4.29: Track radii of irradiated mica
Track radii for irradiated mica measured with different methods. The data are extracted from [173]. A linear fit (dotted line) through the data points fails in providing a stopping power threshold, whereas a square root fit (black solid line) yields a threshold above 2 keV/nm. The orange data points represent the width of the double track extracted from our measurements and the square root fit through these data points shows a similar threshold value.

For CaF_2 and mica SHI irradiation leads to a complex form of ion tracks consisting of grooves bordered by chains of equally spaced nanodots merging into a single decaying protrusion. The assumption that the grooves and the hillocks are induced by sublimation and melting processes, respectively and the following chains are created by molten material from deeper layers pushed towards the surface, is supported for CaF_2 by 3D-TTM calculations. The formation of similar structures are expected also for other materials. First evidence is found by considering again the oxides $SrTiO_3$ and TiO_2. For these materials high resolution AFM imaging and heating during irradiation have also shown for these materials a groove or pit formation at the impact site followed by a chain of single nanodots. Since the melting and sublimation temperature of these two samples lie above the one for CaF_2 and mica[2] the formation of less pronounced grooves is comprehensible.

3D-TTM simulations of $SrTiO_3$, performed by Karlusic *et al.* [131], investigated the increase of the surface temperature with the increase of the projectile kinetic energy or stopping power, respectively. For incident Xe ions the melting temperature is achieved for projectiles at energies of around 31 MeV, corresponding to a stopping power of dE/dx =12.7 keV/nm. Similar dependency of the surface temperature on the projectile kinetic energy has to be expected for TiO_2. With our used irradiation parameters the threshold for melting and sublimation is surpassed and not only

[2] CaF_2: T_m=1691 K, T_b=2806 K; mica: T_m ~1000 K, $SrTiO_3$: T_m=2353 K; TiO_2: T_m=2116 K, T_b=3245 K

hillock formation due to melting processes, but also groove formation due to sublimation might occur. The recently presented preferential loss of oxygen [144] during SHI irradiation under grazing angle of incidence might also contribute to groove or pit formation at the impact site of the ions.

5

HCI interaction with 2D materials

Interaction studies of slow HCIs with single atoms, molecules and solids are an active field of basic and applied physics research. Lots of experimental and theoretical studies were performed to understand the neutralisation process above the surface and surface modification due to potential energy deposition in the topmost atomic layers. While the ongoing processes above a surface are well describable with the COB model, the mechanisms, i.e. electron capturing, de-excitation processes and stopping, at work inside the solid after ion impact are still not fully understood. This problem arises from the fact, that ions travelling in a 3D solid will rapidly reach their equilibrium charge state due to charge exchange and ionisation processes independent of the original charge state of the ions [174–177]. Pre-equilibrium effects like a charge state dependent energy loss are therefore very difficult to study even with thin target films and are usually masked by more dominant contributions from interaction processes along the equilibrated part of the projectile trajectories inside the target.

The fabrication of ultrathin films, especially the production of freestanding single layer graphene, opens nowadays the possibility to study ions in the pre-equilibrium regime and to get insight in the neutralisation and de-excitation processes. At projectile velocities $v < v_0$ the equilibrium charge q_{eq} is typically very small and can be estimated by using Bohr's stripping criterion [72] to be $q_{\mathrm{eq}} \approx Z^{1/3} \cdot v/v_0 \leq 1$ with the nuclear charge Z of the projectile and the Bohr velocity $v_0 = 1\,\mathrm{a.u.} = 2.19 \cdot 10^6\,\mathrm{m/s}$. The special combination of slow ($v < v_0$) highly charged projectile

ions with charge states far from equilibrium ($q_{\text{in}} > 10$) and ultrathin membranes is therefore ideally suited to study pre-equilibrium phenomena.
Although experimental investigations with "real" 2D materials are only possible since a few years, first attempts to study HCI interaction processes with thin materials go back more than twenty years and are discussed in the next section in more detail.

5.1 State of the art

In a first attempt to get information on the charge state equilibration length, Herrmann *et al.* [175] investigated the energy loss and final charge state distribution of slow ($v = 0.76\,v_0$) $\text{Ar}^{q_{\text{in}}+}$ ions (q_{in} =8, 12, and 16) after transmission through a freestanding 31 nm thick carbon foil. Within a few percent resolution they could not find any dependence of these data on the projectile's initial charge state and therefore concluded that the ions reach their charge state equilibrium after passing a few atomic layers only. Further transmission measurements through thinner carbon foils (10 nm and 5 nm) performed by Hattass *et al.* [178] could show that HCIs reach their equilibrium charge state after the transmission of a 10 nm thick foil but not after the passage of only a 5 nm thick carbon foil. Evaluating the average exit charge state in dependency of the projectile velocity ($0.25-0.46\,v_0$), the charge equilibration time in the carbon foil could be estimated to be less than 7 fs. Since sequential filling of projectile inner-shell vacancies would probably take much longer than the evaluated equilibration time of only a few fs, the authors concluded that multiple Auger transition cascades must proceed in parallel to facilitate such a rapid equilibration [178].
Besides transmission measurements, similar results were also obtained by performing scattering measurements. Folkerts *et al.* [179] investigated the final charge state distribution of charged O^{q+} ions with $q = 3-8$ scattered under grazing angles of incidence from a gold surface and observed almost complete charge equilibration. With projectile trajectory calculations they could show that the projectiles spend less than 30 fs within 2 Å of the topmost Au layer. They concluded that already at the target interface strong screening effects have to be present which result in a significant upward shift of the projectile energy levels, enabling a direct capture of electrons into the L and M shell. Similar scattering processes were performed by Winecki *et al.* [21] who investigated the final charge state distribution of highly charged $\text{Ar}^{q_{\text{in}}}$ ions ($q_{\text{in}} = 4-17$, $v = 0.15-0.62\,v_0$) scattered under grazing angles of incidence from a smooth highly oriented pyrolytic graphite surface and found that independent of their initial charge state the scattered projectiles leave the surface virtually fully equilibrated. They explained the fast neutralisation process and the measured X-ray spectra in coincidence with grazingly scattered ions with side feeding processes of electrons into the L and K shell.
Apart from transmission measurements and scattering experiments, observation of fast electron

ejection and measurements of the exit projectile charge distribution after frontal collision of Xe^{30+} ions with C_{60} were performed by Martin *et al.* [180] to get a better understanding of the dynamic processes in HCI collisions before and after penetrating the surface. The assumption of greatly enhanced Auger rates was found to be necessary to interpret the observed fast electron ejection during the collision time.

Until neutralisation is incomplete, also charge state effects on the energy loss become experimentally accessible. An enhancement of the average energy loss value as a function of the incident charge state was reported by Schenkel *et al.* [20]. They performed transmission measurements with $Xe^{q_{\text{in}}+}$ and $Au^{q_{\text{in}}+}$ ions ($v \approx 0.3\,v_0$) in high charge states ($q_{\text{in}} \geq 40$) through 10 nm thick carbon foils. In comparison to these measurements, in the scattering measurements performed by Winecki *et al.* [181] a charge dependent energy loss couldn't be observed, which was in turn interpreted as indication for full neutralisation of the projectile before reaching the distance of the closest approach.

In the present work we make a step forward and present transmission measurements with ultrathin membranes. We start with 1 nm thick carbon nanomembranes (CNM) and focus then on the ultimately thin material, a freestanding single layer graphene (SLG). Aside the importance regarding ion-solid interaction processes, by performing these kinds of measurements, HCIs are also used as probes to study the electronic response of the target material. Graphene plays thereby an extraordinary role because of its special properties. Among them its exceptionally high carrier mobility [182] makes graphene a promising material for future electronic applications, for example in the realisation of ultrafast devices in electronics [183], optics [184,185], or even q-bits based on nitrogen-vacancies [186]. Ultrashort time scales of some ps are involved and provide stringent requirements on the material. Moreover, the tuning of the properties of graphene by applying large electric and magnetic fields [187,188] or collisions with energetic particles [125,189–197] have found great interest and would also change the response of the material. A reliable tool to locally probe the timescales of the electronic response of pristine graphene to large fields is thus of great interest. This can be done by irradiation with highly charged ions which means applying an extremely large, local external field, namely the Coulomb field of the approaching ion. To achieve a local electric field strength in the same order of magnitude (10^{11} V/m) with a laser field would require laser power densities above 10^{17} W/cm^2, where non-destructive measurements become challenging. Additionally the interaction area of a HCI is limited to several nanometers in diameter, whereas a laser field interacts with a much larger sample area leading to a spacial averaging. Based on the experimental data a lower bound for the local current densities can be found and the absence of any traces of large-scale lattice deformations, checked by using transmission electron microscopy (TEM) and scanning transmission electron microscopy (STEM), confirms the intrinsic

ability of suspended graphene membrane to locally sustain exceptionally high current densities (see results below).

5.2 Experimental setup

The transmission measurements with CNMs and graphene were mostly performed at the two-source facility at the HZDR. As an extension of the transmission measurements in Dresden, a similar experimental setup with a spherical electrostatic analyser has been built at the TU Wien. The setup of the experiment, the writing of an evaluating program and the first test measurements with CNMs and single layer graphene were developed with support from Master and Project students. In the next paragraphs I will point to the most important aspects of the two setups and evaluating procedures. For more details I refer to the thesis and protocols [65, 198–201].

5.2.1 Ion beam facility and electrostatic analyser in Dresden

The two-source facility at the HZDR is equipped with two ion sources, an ECRIS and an EBIT. Ions used in this work were extracted only from the Dresden EBIT. The working principle of an EBIT is described in chapter 3, section 3.1.1 and a detailed description of the ion source facility can be found in [202]. The EBIT is capable of producing Xe^{q+} ions in charge states up to q=44. After leaving the trap, the HCIs are accelerated by the extraction electrode before reaching the target at ground potential. The charge to mass separation is performed by an analysing magnet and further focusing is done by electrostatic lenses. A big advantage of this facility is that the ion sources and the beamline are located on a platform which is isolated from the target chamber and by applying a negative potential on this platform the ions, which are entering the target chamber, have to overcome a potential wall and lose thereby a part of their kinetic energy. This retarding system enables to reduce the kinetic energies of the ions to some 10 eV·q.

Entering the target chamber, the ion beam first hits the samples on a rotatable target holder and the transmitted ions which pass the cylindrical electrostatic analyser are detected by a Hamamatsu channeltron. The setup is depicted in fig. 5.1. To enable also the measurement of neutral particles, in the course of time a hole was drilled in the electrodes and a further channeltron mounted in forward direction.
Besides the target holder, also the electrostatic analyser can be tilted to enable angle resolved measurements of the transmitted ions. The distance between the target holder and the entrance slit of the electrostatic analyser of 51 mm limits the angular acceptance of the setup to $\sim \pm 0.8°$.

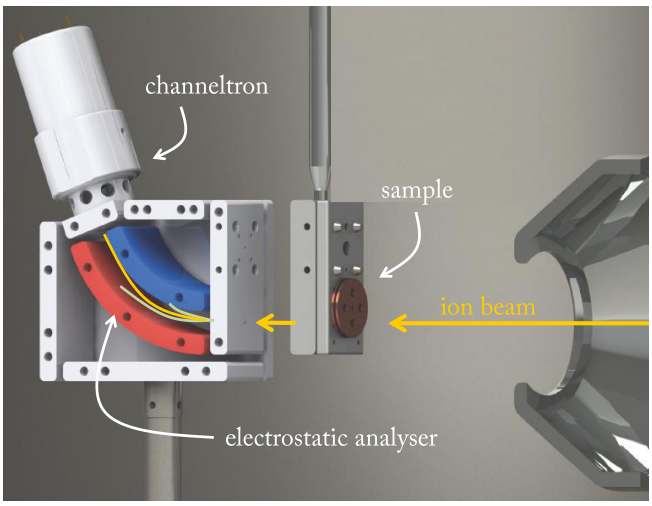

Figure 5.1: Experimental setup at the HZDR
The ions which enter the experimental chamber first hit the target on a rotatable target holder and the transmitted ions, passing the cylindrical electrostatic analyser, are then detected by a channeltron. A sweeping of the potential between the electrodes of the analyser provides the spectrum. The image is adapted from [24].

By sweeping the potential between the electrodes of the analyser, the transmission spectrum is obtained. The maximum voltage difference which can be applied lies around 5 kV. The condition that ions at a kinetic energy of E_{kin} pass the analyser is

$$\frac{\Delta V}{2} = \frac{E_{\text{kin}}}{q_{\text{ion}}} \cdot g \qquad \text{with} \qquad g = \log\frac{r_1}{r_2}$$

with r_1 and r_2 being the inner and outer radii of the analyser. Measurements of the energy resolution of the analyser yielded a resolution of $\Delta E/E \approx 1.5 \cdot 10^{-3}$.

5.2.2 Experimental setup and electrostatic analyser in Vienna

In contrast to the setup in Dresden, in Vienna slow medium charged ions are generated in the 14.5 GHz ECRIS SOPHIE. The working principle of an ECRIS is described in chapter 3, section 3.1.1 and a detailed description of the ion source can be found in [101]. The source is capable of producing Ar^{q+} ions in charge states up to $q = 14$ and can be operated at extraction voltages up to 6 kV. After the extraction from the source, the ion beam is focused by two quadrupole magnets and charge to mass separated by a sector magnet. Entering the beamline, the ions are first collimated by two successive apertures with variable diameters (for the presented measurements apertures with the diameter of 1 mm were used) and then guided by several pairs

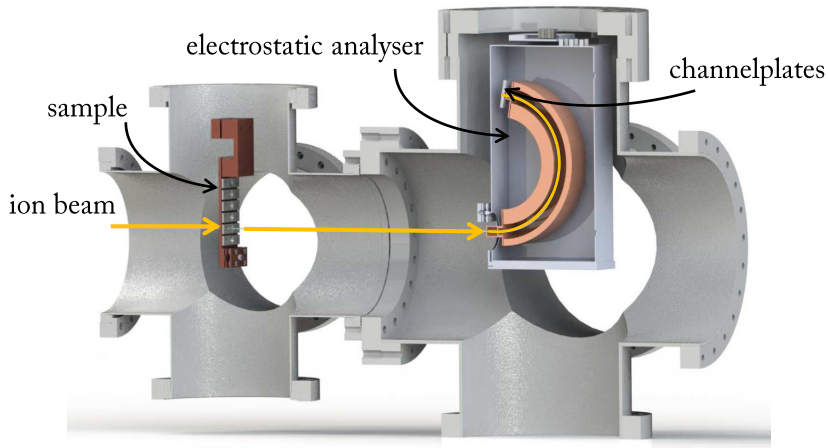

Figure 5.2: Experimental setup in Vienna
The ions hit the target on a rotatable target holder and the transmitted ions, passing the spherical electrostatic analyser are detected by a channelplate detector. The image is adapted from [200].

of deflection plates into the target chamber. Thereby the apertures in the collimator and the target chamber are used for current monitoring. Entering the target chamber, the ion beam hits the samples on a rotatable and heatable holder. Ions, transmitted through the thin membranes, can pass the spherical electrostatic analyser, mounted on a 4-axis-manipulator, and are measured by a channelplate detector. Due to the distance of the target holder to the analyser and the entrance aperture of the analyser the angular acceptance of the setup is limited to $\sim \pm 0.4°$. Fig. 5.2 shows a schematic of the experimental setup.

The Comstock double focusing electrostatic energy analyser is a compact versatile research tool which provides the analysing of the charge state and energy of charged particles incident upon the entrance aperture. Particles at a certain energy are transmitted between the inner and outer spherical sector surfaces and refocused upon the exit aperture. By sweeping the reference potential of the analyser the input energy spectrum is obtained. The high voltage at high stability and low noise is thereby provided by a NIM crate powered modular voltage supply NHS 6060x-K1.

The analyser consists basically of two concentric spherical sector surfaces. The two surfaces are machined from oxygen free copper and then polished and insulated from each other by sapphire balls. For particle detection a channelplate detector Comstock CP-602B, consisting of two channelplates back-to-back and an anode, is used. The detected signal on the anode is sent to a charge sensitive preamplifier ORTEC 142B and further shaping and amplification of the signal is performed by a NIM BIN module amplifier ORTEC 570. A 53131A 225 MHz Universal Frequency Counter/Timer counts the signals above an adjusted threshold and send them via RS232 interface

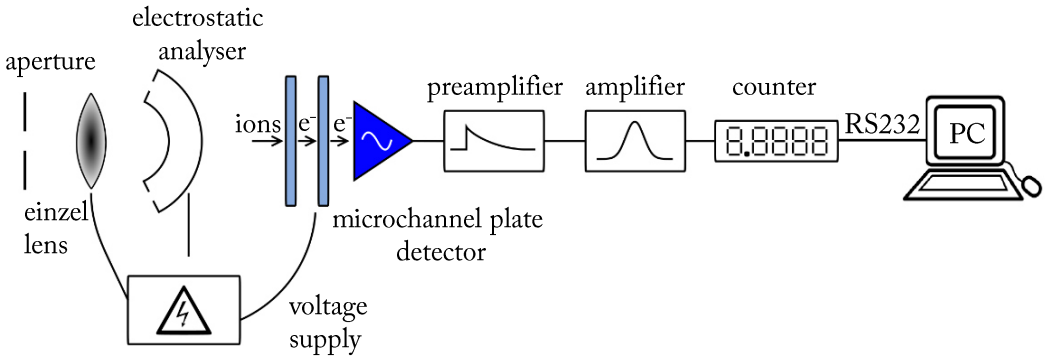

Figure 5.3: Schematic of the electronics of the setup in Vienna
Ions which can pass the electrostatic analyser are detected by a channelplate detector. The signal is first preamplified, then shaped and further amplified and sent to a counter. Signals above an adjusted threshold are then sent to the measuring computer. The schematic is taken from [199].

to the measuring computer. The whole data acquisition of the experiment, from the control of applied voltages to the readout of the counted signal, is controlled by a therefore written LabVIEW program (for details see [199]). A schematic of the electronics is depicted in fig. 5.3.

Single charged ions at a kinetic energy of E_{kin} are transmitted through the constant potential sphere of radii r_1 and r_2 if the potential difference ΔV satisfies

$$\Delta V = \frac{E_{\text{kin}}}{q_{\text{ion}}} \cdot g \qquad \text{with} \qquad g = \frac{r_1 r_2}{r_2^2 - r_1^2}$$

The resolution of the analyser is given by $\Delta E/E$ with ΔE being the energy full width at half maximum signal and E the energy of the passing particle. The energy resolution of the used spherical analyser is $\Delta E/E = 6.8 \cdot 10^{-3}$. The energy spectrum can be obtained by operating the analyser in two different modes:

the constant transmission mode ΔV is set to a constant value and the energy spectrum is obtained by ramping all the potentials on the analyser; the whole range is scanned at constant resolution

the sector field sweeping mode the energy spectrum is obtained by changing ΔV and maintaining the other parts of the analyser on ground potential. In this mode there are no external field changes, but the transmission efficiency and energy resolution will change. For the presented measurements the sector field sweeping mode was used.

5.2.3 Operation of the analyser

In the following three sections some details regarding the operation of the electrostatic analyser in Dresden and in Vienna and the analysis of the obtained spectra are discussed.

Pulse height analysis

The electrostatic analyser selects ions with a certain E_{kin}/q ratio. Therefore the charge state of the detected ions cannot be determined clearly without knowing the kinetic energy. Since the ions, after passing through the analyser, are detected by a channeltron (in Dresden) or two channelplates in Chevron configuration (in Vienna), which working principle is based on electron emission, a second independent method for charge state determination is offered. The secondary electron emission yield of the two detectors namely depends on the charge state of the incident ions and therefore a pulse height analysis provides the charge state of the incident ions. After the calibration of the pulse height spectrum by using ions at a fixed charge state, a simultaneous recording of the pulse height and of the transmission spectrum enables to determine the charge state and energy of the transmitted ions with the electrostatic analyser. In fig. 5.4 the pulse height spectrum obtained with a channel electron multiplier in Dresden is shown. Ions at higher charge states provoke a higher electron emission yield and higher pulses are created, which correspond to the filling of higher channels. All the pulses are well separable from the background noise.

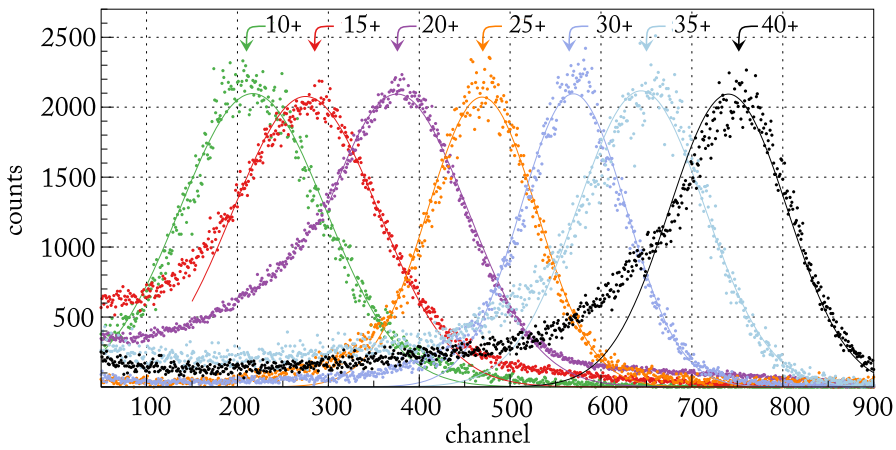

Figure 5.4: Pulse height analysis for charge state determination
Pulse height analysis for different incident charge states of the used Xe ions, extracted at a kinetic energy of $4.4 \cdot q$ *keV. The pulse height analysis was used as a second independent method to determine the charge state of the incident ions. The image is adapted from [65].*

For the measurements performed in Vienna the pulse height analysis was used to define the threshold for signal counting (separation of true signals from the background noise) and looking for the optimal applying voltage at the channelplates (amplification factor). To guarantee an effective counting of all incident ions, the pulse height of ions of all charge states have to be separable from the background. This can be achieved by varying the gaining factor. In fig. 5.5a the shifting of the peaks of 5.8 keV Ar^{9+} ions towards higher channels in dependency of the applied voltage at the channelplates is shown. Each channel corresponds to a pulse height bin of 1.22 mV. The higher distribution at low channels can be attributed to the background noise. By increasing the amplification factor the pulse height peaks induced by the incident ions are separated from the underground and the threshold value for signal counting is determined. In fig. 5.5b the pulse height distribution in dependency of the charge state of the projectiles is shown. The channelplate is operated at 2100 V. A slight shift of the pulse height towards higher channels with the increase of the charge state can be observed due to a higher secondary electron emission upon impact of higher charged particles. By operating the channelplate detector at 2100 V, an effective particle counting for all charge states is possible.

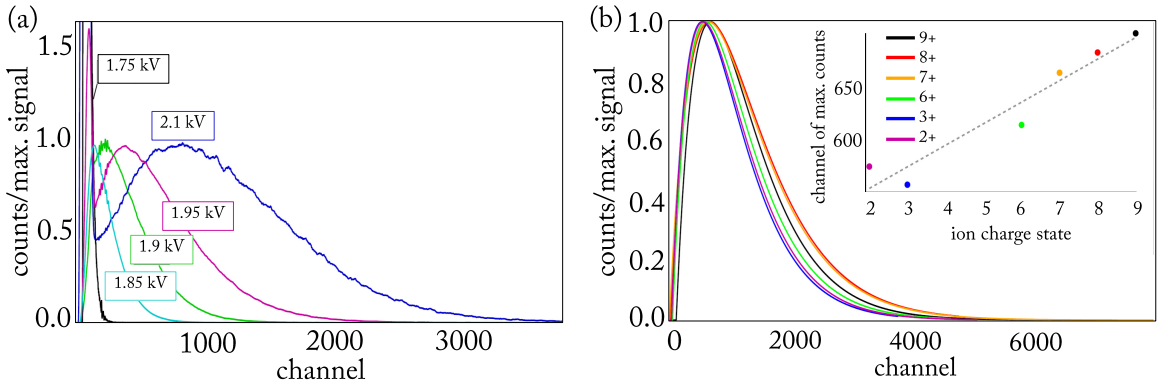

Figure 5.5: Pulse height analysis for threshold and amplification factor determination

(a) Pulse height spectrum for 5.8 keV Ar^{9+} ions for different operating voltages of the channelplate detector. At a operation voltage of 2100 V the pulse height induced by the incident ions can be separated from the background and the threshold value for signal counting is determined. (b) An operation of the channelplate detector at 2100 V enables the detection of ions of all charge states. A slight shift of the pulse height peak maximum for ions with higher charge states towards higher channels due to a higher secondary electron emission upon impact can be observed. Figures adapted from [199].

Calibration of the electrostatic analyser

Before evaluating the obtained transmission spectra, a calibration of the analysing system has to be performed. The pass voltage of a particle is given by

$$\Delta U = \frac{E_{\text{kin}}}{q_{\text{ion}}} \cdot g + U_0 = \frac{U_{\text{Source}} \cdot Q}{q_{\text{ion}}} \cdot g + U_0$$

Here g is the geometry factor defined by the dimensions of the analyser and can deviate from the given value from the manufacturer due to field inhomogenities and imperfect geometry of the analyser. U_0 is an offset voltage and accounts for a voltage difference between the read out voltage and the effective applied voltage between the inner and outer electrode of the analyser and a possible small tilt of the analyser in respect to the incident beam direction. To determine the values for g and U_0, the analyser voltage for measuring an ion peak of a certain kinetic energy is plotted versus the extraction voltage of the ion source (fig. 5.6). The usage of an ECRIS in comparison to an EBIT has the disadvantage that, due to higher electron mobilities, the potential of the plasma relative to the wall will be raised and the value for U_{Source} can slightly differ from the one specified by the source settings. Due to this further unknown variable of the positive plasma potential, which can be limited to +25 V for the used type of ECRIS [203], g and U_0 are determined by making some constrains regarding the energy loss of the transmitted ions (for details see [200]).

The results of the calibration for the electrostatic analysers at the HZDR and at the TU Wien are plotted in fig. 5.6. The values g and U_0 were extracted from the linear fits through the data points and used for the analysis procedure, which will be explained in the next section.

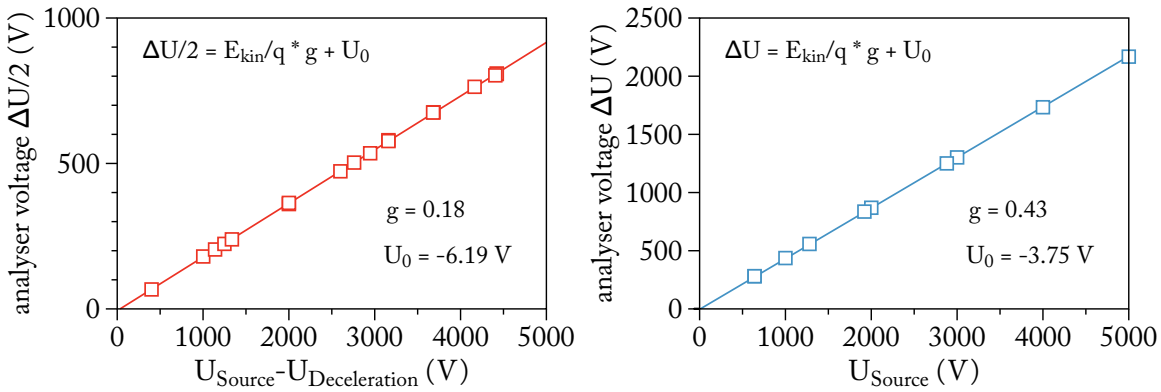

Figure 5.6: Calibration of the electrostatic anlysers
The left graph shows the calibration curve for the HZDR-setup and the right graph for the TU Wien-setup. In both cases the analyser voltage for the ion peak is plotted for various U_{Source} (U_{Source}-$U_{\text{Deceleration}}$ in the case of the HZDR-setup) and the linear fit through the data points yields the geometrical factor g and the voltage offset U_0.

Evaluation procedure

The measured raw data provide a transmission spectrum, which show the counted signals plotted over the analyser voltage. Every single peak of the spectrum represents ions fulfilling a certain E_{kin}/q ratio. The measured spectra are broadened by the design of the analyser since the peaks reflect a convolution of the spectrometer function with the energy distribution of the ions. For the evaluation of the count rate and energy loss for every single peak the knowledge of the energy distribution of the ions is necessary. By choosing an appropriate spectrometer function and energy distribution for the ions and comparing the convolution between them with the measured data, the parameters of the functions can be extracted.
The spectrometer function is defined by the geometry of the entrance and exit aperture of the analyser. At the setup at the HZDR the entrance and exit apertures of the electrostatic analyser are two slits and the spectrometer function can be described with a box function. The width of the box function is thereby the scaling parameter. Since the entrance and exit aperture of the setup in Vienna are two circles, the spectrometer function is more complicated. By geometrical considerations and results obtained by performing Simion simulations (see [199]), a cropped triangle function with two scaling parameters is used for the spectrometer function (see fig. 5.7).
The energy distribution of ions with no or almost no energy loss are describable with a Gaussian distribution. The energy distribution of particles which passed thin films can be described by the Landau distribution. An analytic approximation of the Landau distribution is given by the Moyal distribution

$$f(x) = \frac{1}{\sqrt{2\pi}\sigma}\exp\left(-\frac{1}{2}\exp^{\frac{x-\mu}{\sigma}} + \frac{x-\mu}{2\sigma}\right).$$

The convolution between the spectrometer function and the energy distribution nicely fits the single peaks of the spectra. In fig. 5.7 this is shown exemplary for the setup at the HZDR.
The scaling parameters of the spectrometer function are found by comparing the convolution between the spectrometer function with a Gaussian function, which represents the energy distribution of the incident ions, with the data of the measured primary peak. The spectrometer function width increases with $1/q_{\text{out}}$. The parameters of the Gauss and the Moyal function is varied until the convolution fits the measured data. This parameters provide information about the integral value, the mean[1] and the median of every single peak of the transmission spectrum. It shows that the peak integral is strongly effected by the convolution, since the factor between the measured integral and the deconvolved integral scales with $1/q_{\text{out}}$ and overestimates the count rates with large charge losses. The energy loss of every single peak is determined by subtracting the mean value of the Gauss or Moyal function from the calculated peak position.

[1] the mean of the Moyal distribution is given by $\overline{x} = \mu - \sigma(\gamma + ln(2))$ with $\gamma \approx 0.57721$

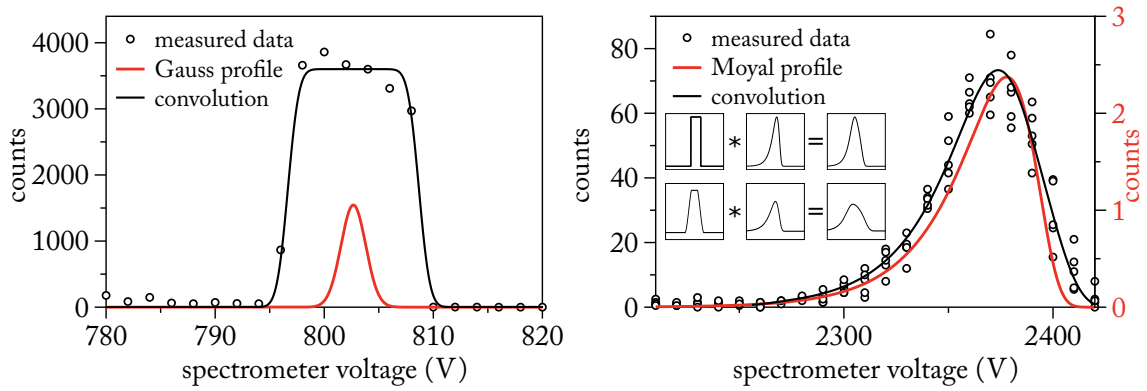

Figure 5.7: Evaluation of the transmission spectra
The convolution between the spectrometer function (a box for the setup at the HZDR and a cropped triangle for the setup at the TU Wien) and assumed profiles (a Gauss function for transmitted ions with no or almost no energy loss and a Moyal function for transmitted ions with energy loss) for the incident ions fits the measured data quite well. The data were obtained with Xe^{30+} ions at 135 keV after transmission through a single layer graphene at the HZDR setup. The left figure shows the data for the 30+ peak, the right figure for the 10+ peak. Note the overestimation of the count rate due to the convolution with the spectrometer function. The inset of the right figure shows the convolution between the spectrometer function and a Moyal function.

5.3 Investigated Materials

The transmission measurements were performed with 1 nm thick carbon nanomembranes and freestanding single layer graphene. Before presenting the results in detail, the preparation and properties of the used membranes are discussed.

5.3.1 Carbon nanomembranes

A carbon nanomembrane (CNM) [204] is a two dimensional object with a thickness of 1 nm and can be seen as a surface without bulk. The used CNMs were fabricated from CNM Technologies Bielefeld and the preparation procedure and characterisation of such films will be described in the following paragraphs. For a detailed review see [205].

Preparation

The starting point for the fabrication of CNMs is a self-assembled monolayer (SAM) of aromatic molecules. Looking at the structure, SAMs consist of three building blocks: the head group,

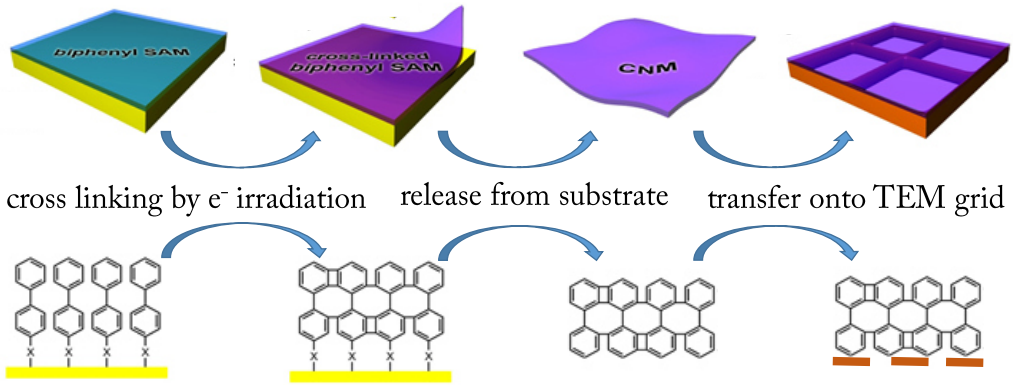

Figure 5.8: Schematic of carbon nanomembrane preparation
The molecules of a self assembled monolayer are crosslinked by electron irradiation. The polymeric film is then released from the substrate and transferred onto a TEM grid. Most of the time an underlying holey- or lacey carbon support film is used for better mechanical stability of the freestanding membrane. Schematic adapted from [114].

which is the bond to a solid surface, the terminal group which constitutes the outer surface and the spacer which connects the head and terminal group. For our CNMs SAMs of 1,1-biphenyl-4-thiol (BPT, H-(C6H4)2-SH) on a gold substrate were used (see fig. 5.8). By electron irradiation of the aromatic SAMs, C–H cleavage occurs which is then followed by crosslinking between neighboring phenyl units and carbon nanosheets with molecular thickness are formed. By combining various techniques like X-ray photoelectron spectroscopy (XPS), near-edge X-ray absorption fine structure spectroscopy (NEXAFS), thermal desorption spectroscopy (TDS), and UV photoelectron spectroscopy and comparing them with quantum chemical calculations, Turchanin *et al.* [206] obtained details about the intermolecular cross-linking process. At room temperature electron irradiation causes a lateral cross-linking via the formation of C-C linked phenyl species as well as a new sulfur species. For BPT SAMs about 650 primary electrons per molecule with an energy of 50 eV are necessary to create the cross-linked molecular network and the thermal stability of the carbon films increases with the electron dose and saturates at $\sim$50 mC/cm^2. By heating the sheets at temperatures above 800 K, all sulfur species are thermally desorbed, while the remaining film reveals an onset of carbonisation. To get a freestanding membrane, the polymeric film is released from the substrate and transferred onto a TEM grid with an underlying holey- or lacey carbon support film for a better mechanical stability. In fig. 5.9a a helium ion microscopy (HIM) image of such a produced CNM is shown. The bars of the TEM grid and the holey carbon support film are visible. The CNM span over micrometer sized holes and is freestanding. At some areas a rapture or folding of the CNM is observable and can be used as a guide for the eye to demonstrate the uniformity of the membrane.

Properties of CNMs

The thickness of the CNMs has been determined by X-ray photoelectron spectroscopy and atomic force microscopy to be ∼1.2 nm, in good agreement with the height of a biphenyl molecule. XP spectra showed also some residual contamination of light elements like O, F, and I from the fabrication and transfer procedure [207]. Additional sulfur contaminations could be observed using Auger electron spectroscopy [22]. Since the contamination concentrations are well below 1 at.%, CNM can be considered as pure carbon material. By heating the CNM samples to 600 K and more, the residual contaminations vanish and the samples thickness decreases to 0.7 nm. Heating changes also the sheets resistivity. After annealing at ∼800 K a measurable electrical current can be detected and further heating increases the electrical conductivity. The structural transformation that occur upon annealing could be confirmed by Raman spectroscopy and high resolution TEM measurements. The temperature dependent changes are characteristic of a phase transition from an amorphous to a nanocrystalline carbon network, finally transforming into graphene flakes [207]. The structural modification is also reflected in mechanical properties. A novel type of *in situ* bulge testing using atomic force microscopy [208] was used to study the elastic properties of CNMs. From the obtained pressure-deflection relation the Young's modulus could be determined which shows similar values as the one obtained for multilayer molecule/metallic nanocomposite membranes. Annealing the sheets increases the Young's modulus to values similar to the one of graphite and points again to the graphitisation of CNMs.

To get a deeper understanding of the structure and formation of carbon nanomembranes, classical molecular dynamics simulations have been performed [209]. The results of the simulations base on a energy minimising procedure. Fig. 5.9b shows a local energy minimum state configuration of the CNM with holes or voids, respectively. The porous structure of the CNM show dense and loosely packed areas.

Besides chemical functionalisation of CNMs [205], the controlled perforation with pores of uniform size is a promising area of application for CNMs. In 2013 Ritter *et al.* [116] could show that HCIs are a versatile drilling tool for CNMs. Impacts of Xe^{q+} ions with $q \geq 25$ induced nanopores in the membrane. The diameters of the pores, ranging from 30 nm down to only 3 nm, can thereby be tuned by the potential energy of the ions. In fig. 5.9c a HIM image of a CNM is shown after exposure to Xe^{40+} ions. The formation of nanometer sized pores is clearly visible. In comparison to other lithographic techniques like extreme UV-interference lithography, for HCI irradiation the membranes do not have to lay on a supporting substrate. A further advantage is the high pore formation efficiency in comparison to focused ion beam lithography [210].

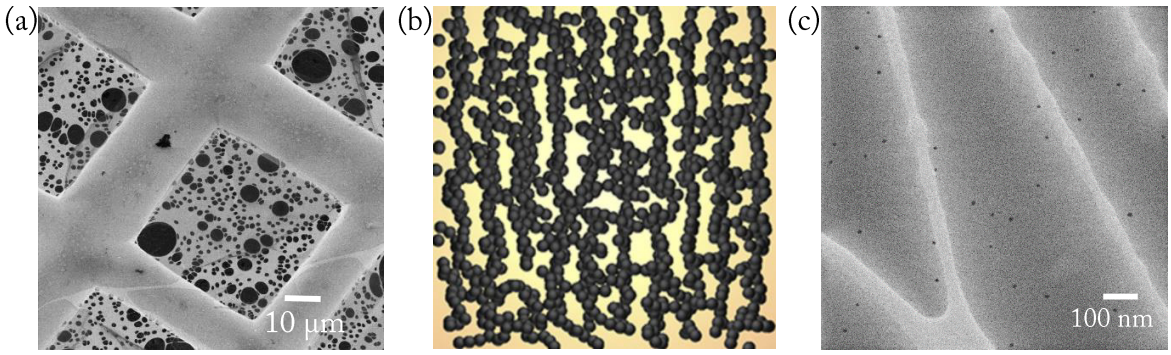

Figure 5.9: Structure and tailoring of CNMs
(a) HIM image of a CNM layer on a TEM grid with a holey carbon support film for a better mechanical stability. At some areas a rapture or a folding of the CNM foil is visible. (b) A local energy minimum state configuration of a CNM obtained by performing classical molecular dynamics simulations. The image is taken from [209]. The porous structure of the CNM show dense and loosely packed areas. (c) HIM image of an irradiated CNM sample with Xe^{40+} at 180 keV. The formation of nanosized pores can be observed.

5.3.2 Graphene

Graphene is the ultimately thin membrane consisting of sp^2 hybridised carbon atoms arranged in a honeycomb structure. Each C atom is connected with three neighbouring C atoms by a σ bond, constituted by the s, p_x and p_y orbitals. The electrons in the p_z orbital forms the Π bond, which is oriented out of the plane. The orbital hybridisation of the Π bonds forms the Π and Π^* bands or the valence and conduction band, respectively. With one p_z electron per atom the valence band is fully occupied, whereas the conduction band is vacant. The valence and conduction band touch each other at the Dirac point and make graphene to be a semiconductor with no band gap. This special band structure which permits a free-moving of electrons, grants the extraordinary properties of graphene in terms of strength, electricity and heat conduction [211].

A very challenging task and the keypoint of the transmission measurements was the preparation of a clean, freestanding single layer of high quality graphene. The used graphene sheets were fabricated at the Universität Duisburg-Essen in the working group of M. Schleberger. The preparation procedure and characterisation of such samples are described in the following two sections.

Preparation

The standard approach is to grow graphene on a copper foil via chemical vapour deposition (CVD) and transfer it then onto a TEM grid with the help of a thin layer of polymethylmethacrylat (PMMA) for mechanical stabilisation [212]. Later this PMMA layer has to be removed. Since

residues of PMMA constitute a source of severe contamination, for our sample preparation the use of PMMA was avoided entirely. Instead of it, the sample preparation procedure was adapted from [213].

A 300-mesh gold TEM grid with a quantifoil (1.2 μm hole diameter) on top was placed onto commercially available CVD graphene (Graphenea). To increase the adhesion between the quantifoil and the graphene layer isopropyl alcohol was used. The stack was placed onto the surface of an ammonium persulphate solution and after approximately 24 h the etchant was substituted by deionised water. During this procedure the copper foil on the graphene layer was removed and the TEM grid with only graphene on it was carefully lifted out of the fluid. To remove contaminations the TEM grid with the graphene is embedded into active carbon within a ceramic dish and then heated in an oven. The samples were heated to a maximum temperature of 260°C with a heating rate of $\sim$ 300°C/h. The sampels were heated for 30 min at maximum temperature. Afterwards they were cooled down and when reaching $\sim$ 70°C the samples were taken out of the active carbon. Active carbon remnants were removed with a smooth nitrogen stream.

Characterisation

After processing, the quality of the transferred graphene was checked by Raman spectroscopy. A typical Raman spectrum is shown in fig. 5.10. The FWHM of the 2D mode peak provide the number of layers of the graphene sample and the ratio of the integral of the D and G mode peak is a measure for the amount of defects. From the obtained Raman spectrum a FWHM of the 2D peak between 26-40 cm^{-1} was extracted. This values point to a single layer graphene, since bilayer graphene would have a FWHM of $>$50 cm^{-1}. On the basis of the Raman data it was determined that the amount of defects was negligibly small and that typically 80-90% of the quantifoil holes are covered with graphene.

To make a rough estimate of the contamination of the graphene sheets, STEM measurements were performed. The STEM measurements were done using a Nion UltraSTEM 100 at 60 kV under ultra high vacuum conditions ($\sim 10^{-8}$ mbar). Before loading the samples into the STEM, they were annealed at 150°C in $\sim 10^{-5}$ mbar for $\sim$8 h to remove light adsorbed water films. The images were taken with a high-angle annular dark field detector (HAADF) (see fig. 5.11a). They show clean monolayer regions of up to hundreds of nm (area A), surrounded by a meandering network of thin hydrocarbon adsorbates (area B and C) and a view heavier residues like Cu and Fe (area D), presumably from the CVD and transfer processes. This information about the composition of the samples can be determined since the HAADF intensity is proportional roughly linearly to the thickness and proportional roughly to squared atomic number Z ($\sim Z^{1.7}$). So heavy impurities

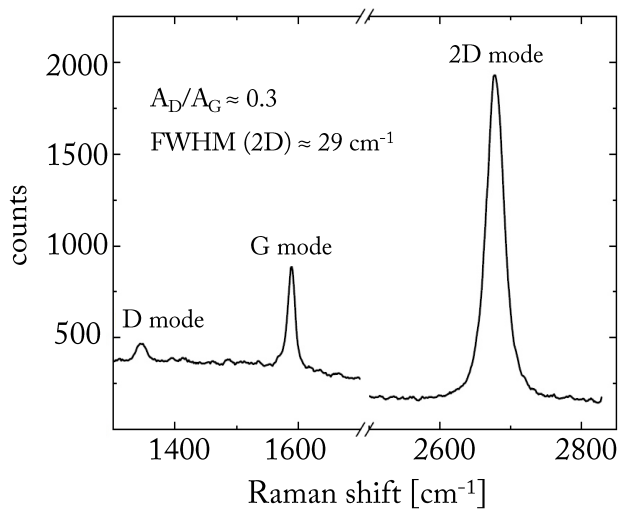

Figure 5.10: Raman spectrum of a graphene sample
The FWHW of ∼30 cm^{-1} of the 2D mode peak ensures single layer graphene and the ratio of the integral of the D and G mode peak points to a negligible amount of defects. Image adapted from Supplemental material of [24].

like Cu or Fe strongly light up in the STEM HAADF images (see fig. 5.11b). Assuming that the hydrocarbon adsorbates have a similar density as graphene, the STEM HAADF images allow direct recalculation of the adsorbate levels to graphene monolayer equivalent thickness. The image intensity (pixel counts) is normalised so that monolayer graphene yields areas equivalent to one monolayer. The monolayer graphene was confirmed via atomic resolution imaging (see fig. 5.11c) and the signal corrected by subtracting the HAADF signal of holes in the film. The obtained histogram over the entire image confirms the visual impression of the hydrocarbon adsorbate thickness distribution (see fig. 5.11d). Despite the careful PMMA-free sample preparation and the activated carbon dry cleaning, the residual hydrocarbon adsorbates can result from air exposure of samples between fabrication and measurements and is typical for the state-of-the-art of suspended graphene membrane [213–215].

Since STEM imaging leaves surfaces not undisturbed, some of these adsorbates may be produced by the electron beam, e.g. by electron beam assisted adsorption of residual hydrocarbon from the STEM vacuum. Fig. 5.12 shows the development (i.e. adsorbate receeding in area A and adsorbate increasing in area B) during a measurement period of 13 min. Effects of electron beam exposure on the contamination morphology was minimised in our STEM measurements via acquisition of fast snapshot images and the use of a very low base pressure in the STEM system (∼10^{-9} mbar).

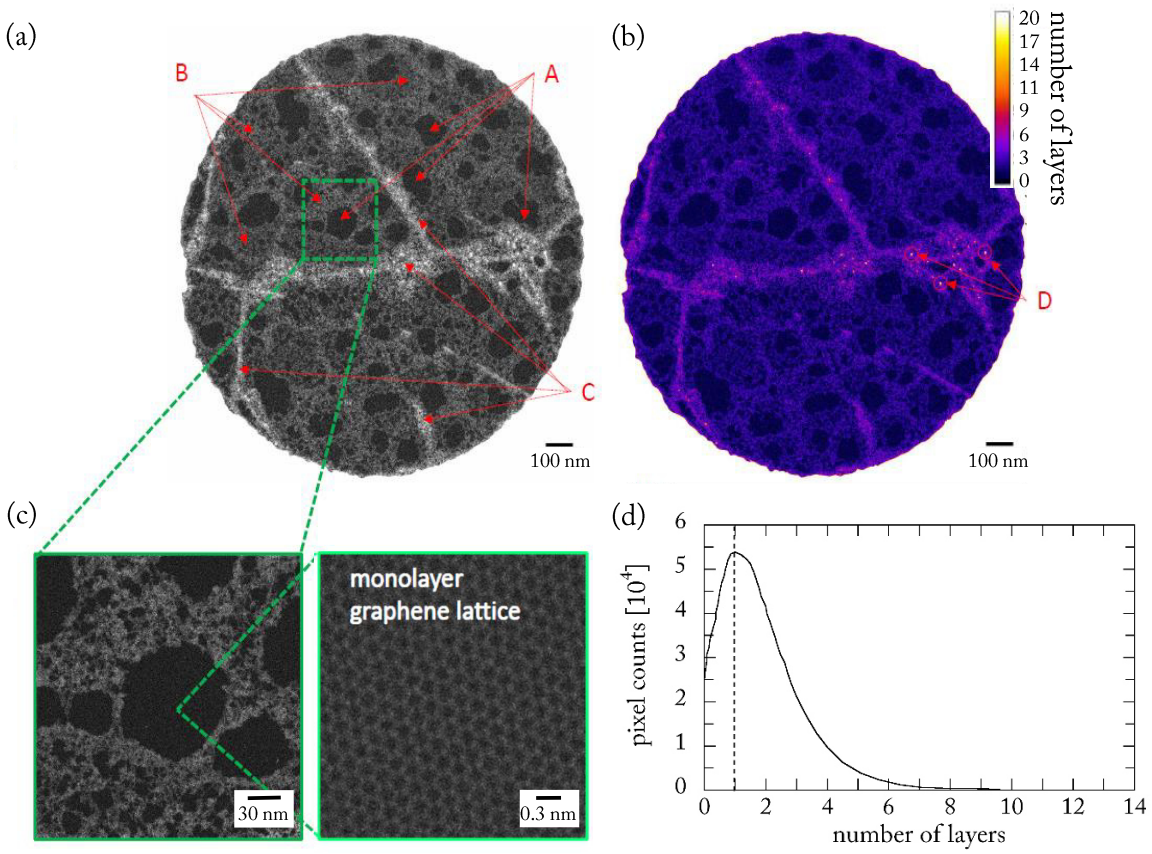

Figure 5.11: STEM measurements of single layer graphene
(a) STEM measurements show clean monolayer regions of up to hundreds of nm (area A), surrounded by a meandering network of thin hydrocarbon adsorbates (area B and C) and a view heavier residues like Cu and Fe (area D). (b) Using the roughly linear intensity scaling of the HAADF STEM signal with specimen thickness, and assuming as an upper limit the same density for the hydrocarbon adsorbates as for graphene, a thickness estimated for the hydrocarbon contamination was calculated as equivalent thickness in number of graphene layers. (c) The monolayer nature of the clean graphene regions was confirmed using atomic-resolution STEM imaging. (d) The obtained histogram over the entire image confirms the visual impression of the hydrocarbon adsorbate thickness distribution.

5.4 CNM - Experimental results and discussion

Our first approach to study the HCI interaction with 2D materials by performing transmission measurements was done by using CNMs. Since the results were presented partially in the PhD thesis of Wilhelm [65] and largely published in [22, 23, 26, 27], the following subchapter is a summary of these publications.

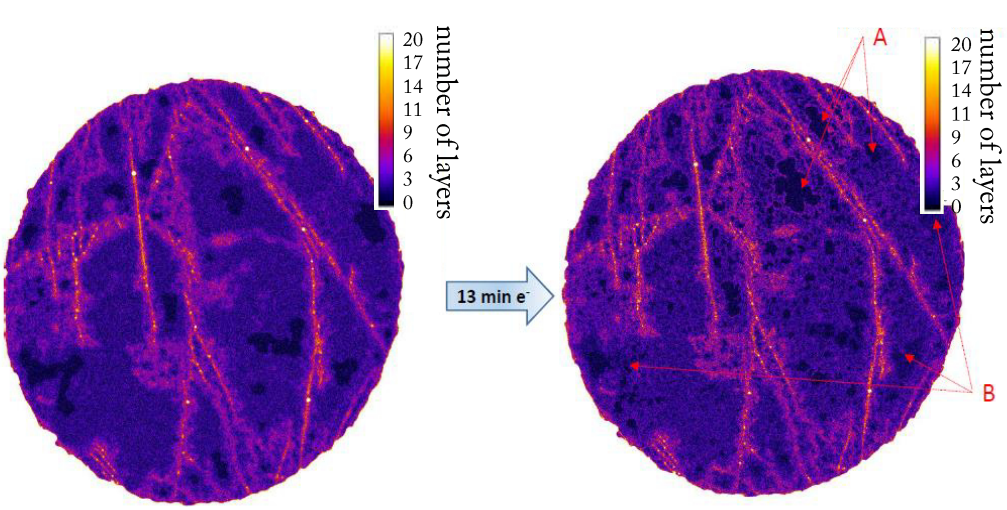

Figure 5.12: Effects of the electron beam exposure to graphene
The exposure to an electron beam during the performance of STEM measurements over a longer period of time (several minutes) shows an electron beam assisted adsorbate receeding and increasing, respectively.

5.4.1 Charge exchange

For slow highly charged Xe ions transmitted through a 1 nm thick CNM a bimodal charge state distribution can be observed. Figure 5.13 shows a typical measured spectrum with two distinct exit charge state distributions. The exit charge states q_{out} are calculated from the spectrometer voltage of the electrostatic analyser and some of them are marked in the figure by arrows. For the plotted spectrum, Xe^{30+} ions at a kinetic energy of E_{kin}=135 keV are used. The first distribution ranges from q_{out}=29 to q_{out}=12 and shows an intensity maximum at q_{out}=28. At first sight these peaks show no energy loss and no straggling. The second distribution goes from q_{out}=12 to q_{out}=5, since the range of the measurable charge states is limited by the analyser's maximum operation voltage of 5000 V. The broadening of these peaks point to an energy loss and energy straggling. Projectiles transmitted with the initial charge state presumably pass through cracks and bigger holes of the CNM sheet or uncovered parts and do not interact with the CNM.

Since all peaks are artificially broadened due to the geometry of the electrostatic analyser, the raw data have to be corrected to obtain the correct abundances and widths of every single peak. Every peak represents a convolution between the spectrometer function, a rectangular function, and a Gauss function, representing the transmitted ions with no or almost no energy loss, or a Moyal function, describing the transmitted ions with energy loss. The data evaluation procedure provides the parameters of the Gauss and Moyal function and the corrected abundances and widths of every single peak are determined. A detail discussion on the data evaluation can be

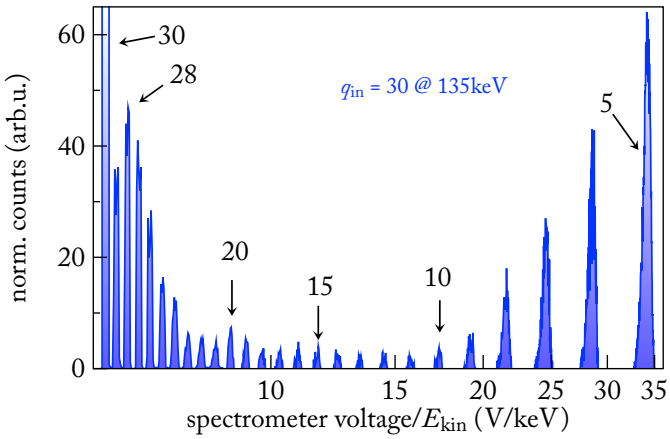

Figure 5.13: Transmission spectrum of Xe ions after passing a CNM
The graph shows the transmission spectrum of a 135 keV Xe^{30+} ion beam after transmission through a 1 nm thick CNM. The exit charge states are calculated from the spectrometer voltage and marked by arrows. Two distinct charge state distributions can be observed, a high charge state distribution with almost no energy loss and a low charge state distribution with high energy loss. Projectiles with the initial charge states pass through cracks and bigger holes of the CNM.

found in section 5.2.3.
In fig. 5.14 the integral value of the measured peaks and of the corrected (deconvolved) peaks are presented exemplary for Xe^{25+} ions at 47.5 keV. Since the factor between the integral value of the measured peak and the corrected peak scales with $1/q$, the raw data overestimate the integral values of the peaks with large charge loss the most.

Looking at the high charge state distribution (low charge exchange) of the transmission spectra a mean exit charge state for various combinations of q_{in} and E_{kin} can be evaluated. The limitation of the maximum operation voltage of the analyser doesn't allow this for the low charge state distribution (high charge exchange). Although, it is obvious from the obtained spectra (see fig. 5.13 and fig. 5.14) that the transmitted ions of this distribution are almost neutral and have captured and stabilised $\sim 20-30$ electrons due to the interaction with the CNM.
The observation of such an effective capture and stabilisation of many electrons within a short period of time agrees with previous measurements performed by Hattass *et al.* [178] with slow HCIs ($33+ \leq q \leq 75+$) through $5-10$ nm thick carbon foils. In fig. 5.15 the results of the transmission measurements with the CNMs are compared with those of the 5 nm thick carbon foils [178]. In fig. 5.15a the mean exit charge state of the high charge state distribution is plotted as a function of the incident ion velocity for various ion charge states. Since no distinct values for the mean exit charge state of the low charge state distribution can be given, only the range, where the mean

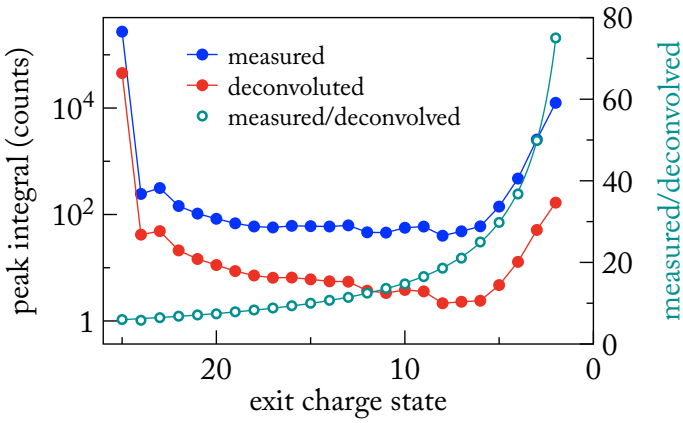

Figure 5.14: Evaluation of the peak integrals
Measured and deconvolved peak integrals of Xe^{25+} at 47.5 keV after transmission through a 1 nm thick CNM. The raw data overestimate the integral values of the peak with large charge loss the most. The open symbols show the ratio of the measured to the deconvolved value, which follow a $1/q$ relation.

exit charge state has to be expected, is highlighted. It corresponds with the mean exit charge state of ions after the passage of a 5 nm thick carbon foil.
In fig. 5.15b the mean number of captured electrons ($q_{\text{in}} - \overline{q}_{\text{out}}$) is plotted as a function of the interaction time for the incident charge state $q_{\text{in}} = 20$ and 30. Again the expected values for the low charge state distribution are marked by the shaded area.

The data points in fig. 5.15a are fitted by the relation

$$\overline{q}_{\text{out}}(q_{\text{in}}, x, v) = q_{\text{eq}} + (q_{\text{in}} - q_{\text{eq}})e^{-\alpha x/v} \tag{5.1}$$

with $q_{\text{eq}} = Z^{1/3}v/v_0$ (v_0 is the Bohr velocity) and x being the thickness of the membrane, following the ansatz of [178]. The variable α yields the relaxation rate. While for the high charge state distribution relaxation rates in the order of $\alpha = 10^{13}\,\text{s}^{-1}$ are extracted, two orders of magnitude larger rates have to be expected for the low charge state distribution, as they are comparable with the data from [178]. The found rates of the high charge state distribution correlate with typical Auger capture rates in solids or radiative decay rates. However, the low charge state distribution seems to relay on a more effective process which enables a neutralisation of HCIs within some fs.

A further hint that the observed bimodal charge state distribution results from two different interaction processes is encouraged by studying angle resolved transmission spectra and the energy

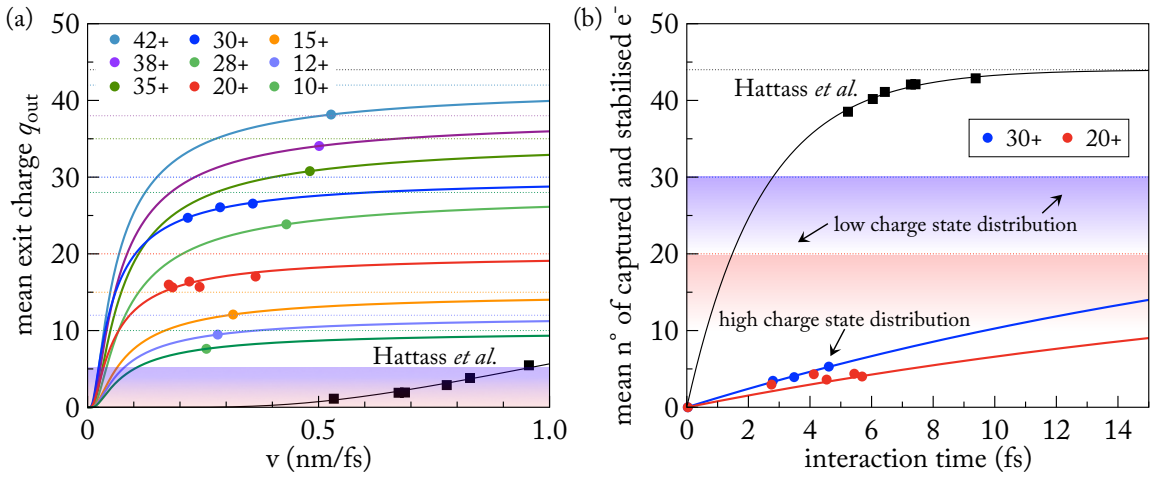

Figure 5.15: Charge exchange process of HCIs with CNMs
(a) Mean exit charge state for the high charge state distribution for various combinations of q_{in} and E_{kin}. Because of the limitation of the maximum operation voltage of the analyser and since the transmitted ions of the low charge state distribution are almost neutral, no distinct values for the mean exit charge state of this distribution can be given. The area where the values are expected are highlighted. For comparison the results of transmission measurements through 5 nm thick carbon foils with Xe^{44+} [178] are presented. All the data are fitted by the eq. 5.1. (b) Mean number of captured electrons as a function of the interaction time for $q_{in} = 20$ and 30.

loss of the single peaks of the bimodal charge state distribution, respectively. Fig. 5.16a shows three transmission spectra analysed under 0°, 2° and 4° projectile exit angle. All transmission spectra were obtained with Xe^{25+} ions at $E_{kin} = 47.5$ keV. Obviously the distribution of high charge states is only visible in forward direction and vanishes with tilting angle (see fig. 5.16b). However, ions at low charge states are transmitted up to 4°, even though with a large decrease of intensity. The evaluation of the energy loss of every single peak shows that only ions with large charge exchange experience an appreciable energy loss. The value of the energy loss increases with the tilting angle (see fig. 5.16c).

The facts, that i) the two distributions are well separated from each other, ii) the high charge state distribution can only be measured in forward direction with no or almost no energy loss and iii) the low charge state ion peaks with high energy loss are transmitted up to 4°, point to an impact parameter dependent charge exchange process. Looking at the structure of the CNM (see fig. 5.9b) the bimodal charge state distribution is comprehensible. An ion impinging on the membrane can either traverse a region of low or high atomic density. At large impact parameter, the charge of the carbon atom is screened and no nuclear stopping occurs. Electrons from the carbon atoms may be transferred via resonant transition to high Rydberg states of the ion and after

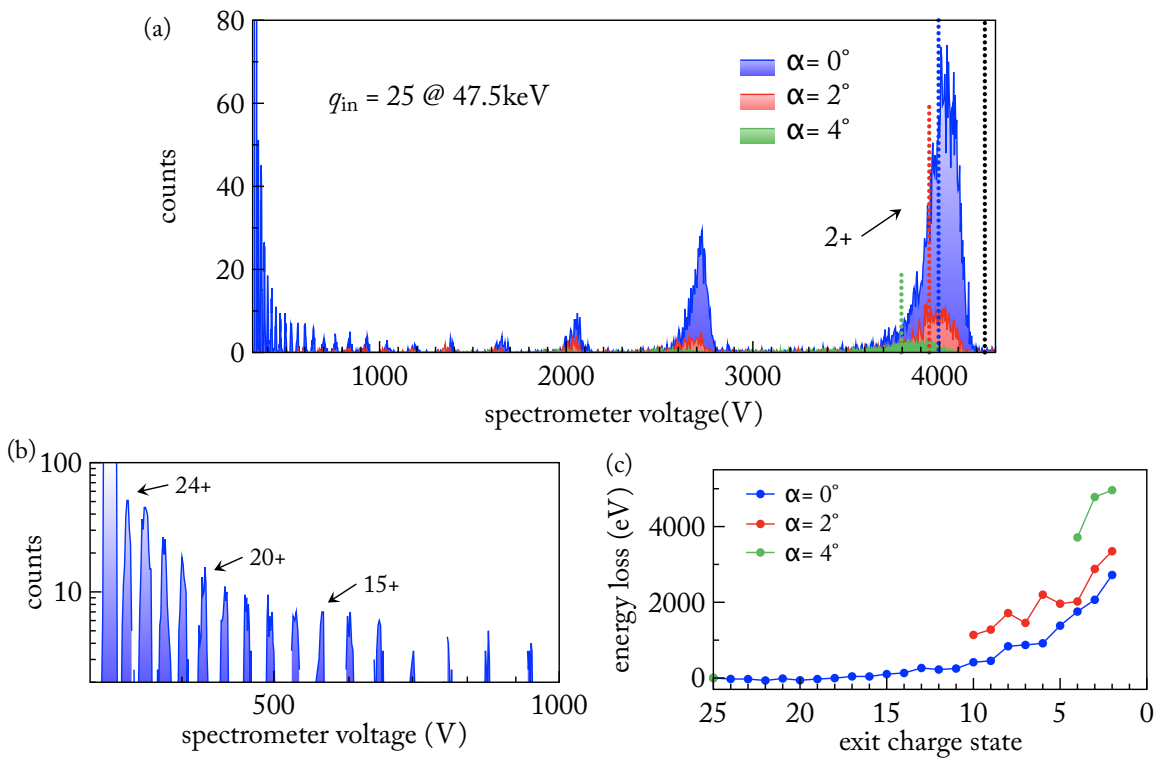

Figure 5.16: Angle resolved transmission spectra
(a) Transmission spectra for Xe^{25+} ions at $E_{kin} = 47.5$ keV analysed under 0° (blue), 2° (red) and 4° (green) projectile exit angle. The black dotted line marks the position of the 2+ peak with no energy loss, the colored dotted lines the mean values of the peak distributions. (b) High charge state distribution of the transmission spectrum. The high charge states are only visible in forward direction and vanish with tilting angle.
(c) Energy loss of the single peaks of the transmission spectrum. An increase of the energy loss with an increase of the charge loss and the tilting angle is observed.

de-excitation processes a few electrons are stabilised. For close collision elastic scattering with high charge transfer and huge energy transfer may occur. Which particular process is responsible for such an effective charge capture and stabilisation of so many electrons within a short period of time will be discussed in section 5.5 in detail.

Apart from the measurements in Dresden, ion transmission measurements were also performed in Vienna with a similar experimental setup (see chapter 5, section 5.2.2). Thereby ions at lower charge states and lower kinetic energies were used and from geometrical considerations the acceptance angle of the analyser was limited to ±0.4°. In fig. 5.17 a typical transmission spectrum is recorded, which was taken with Ar^{9+} ions at $E_{kin} = 17.3$ keV after transmission through a CNM target. A clear decrease of the amount of ions with the increase of the charge loss is observable and at the first view it looks different to the bimodal exit charge state distribution presented

before. Considering the following facts the missing of the low charge state distribution is not astonishing; on the one hand the limitation of the analyser maximum voltage doesn't allow to measure the transmitted ions at very low charge states which dominate the low charge state distribution for low incident charge states like $q_{\text{in}} = 9$ and low kinetic energies. On the other hand the spectrum shows the transmitted ions within an angular field of $0° \pm 0.4°$. The small sector limits the detection range of ions transmitted at close impact. Fig. 5.18 shows the scattering angle as a function of the impact parameter for elastic collisions of Ar and Xe with C assuming the screened Coulomb potential with the universal screening function (see eq. 2.11 in chapter 2) as the interaction potential. The interaction of Xe with C presents the measurements performed with the experimental setup in Dresden which detects the transmitted ions in an angular field of $0° \pm 0.8°$ (blue marked range) in comparison to the setup in Vienna where the measurements were performed with Ar ions in an angular field of only $0° \pm 0.4°$ (red marked area). The blue marked area around $4° \pm 0.8°$ and the associated impact parameters are applicable for the performed transmission measurement by tilting the electrostatic analyser for 4°. In all cases the increase of the kinetic energy of the particles leads to smaller scattering angles for the same impact parameter. A tilting of the analyser or an increase of the projectile kinetic energy makes ions which were transmitted at close impact detectable.

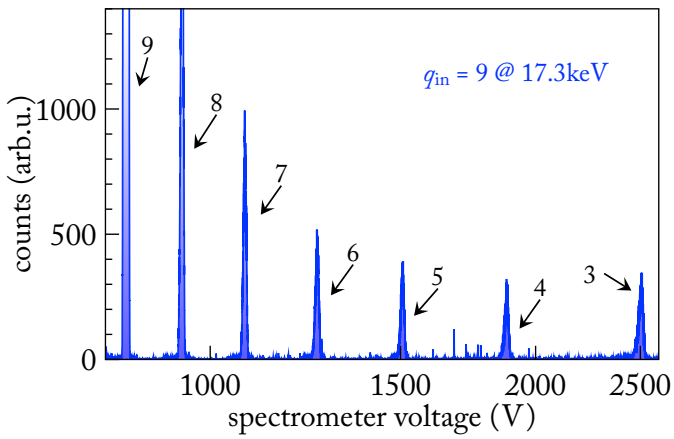

Figure 5.17: Transmission spectrum from the setup in Vienna
Typical transmission spectrum obtained with the setup in Vienna. For the measurements Ar^{9+} ions at $E_{\text{kin}} = 17.3\,keV$ were used. A decrease of the peak height with the increase of the charge exchange can be observed.

5.4.2 Energy loss

The energy loss of a HCI after transmission through a CNM depends on several parameters with different weightings. Theses various parameters and their dependencies are discussed in the

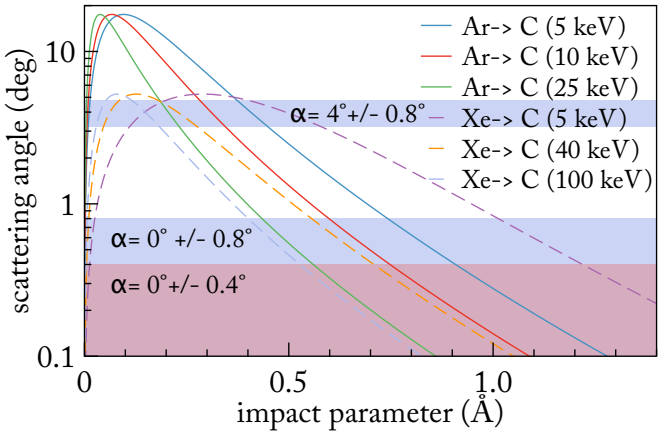

Figure 5.18: Scattering angle of elastic collision
Calculated scattering angle as a function of the impact parameter for Xe and Ar with C assuming the screened Coulomb potential as the interaction potential. The setup in Dresden detects ions in an angular field of ±0.8° *(blue marked area) and the setup in Vienna of only* ±0.4° *(red marked area).*

following paragraph and the attempt to find an "universal scaling" of the energy loss is presented. The results were mostly described in [23].

Looking at the transmission spectra a broadening of the peaks with an increase of the charge loss is obvious and points to a strong dependency of the energy loss on the exit charge state or the charge exchange. An accurate investigation of the energy loss shows, besides the dependency on the charge exchange, an almost quadratic dependency on the incident charge state, which is commonly assumed in the literature [78]. Fig. 5.19a-c show the energy loss for highly charged Xe ions at a constant kinetic energy of 40 keV as a function of the exit charge state for various incident charge states, as a function of the incident charge state for various exit charge states and as a function of the charge loss for various incident charge states, respectively. In all cases the data points can nicely be fitted by the relation

$$\Delta E = q_{\text{in}} e^{\gamma(q_{\text{in}} - q_{\text{out}})/q_{\text{in}}} = q_{\text{in}} e^{\gamma \Delta q / q_{\text{in}}}. \tag{5.2}$$

A Taylor expansion of this formula shows the quadratic increase of the energy loss with the incident charge state, observable in fig. 5.19b. This figure shows also that the mean energy loss reaches values much higher as predicted by TRIM calculations.

The TRIM results consider the nuclear and electronic stopping of a neutral Xe atom if one considers a carbon density of $5.54 \cdot 10^{22}$ at/cm^3 and an angular acceptance of ≤1.6° for the analyser. The simulations predict a value of 237 eV, which is close to the energy loss expected from an ex-

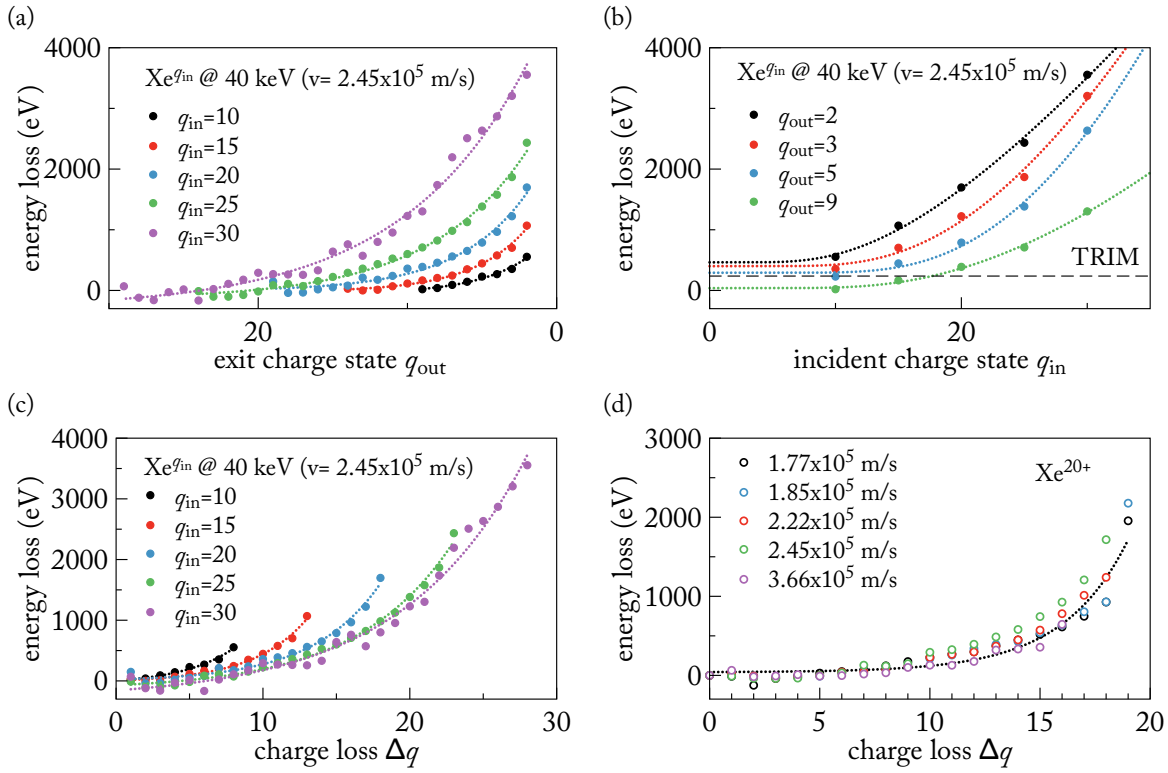

Figure 5.19: Ion energy loss due to interaction with CNM
The energy loss for highly charged Xe ions at a constant kinetic energy of $E_{\text{kin}} = 40\,keV$ as a function of (a) the exit charge state, (b) the incident charge state and (c) the charge exchange. All the data are fitted by eq. 5.2, whose Taylor expansion shows the quadratic dependency on the incident charge state. The mean energy loss reaches values much higher as predicted by TRIM calculations, marked by the dashed line in (b). (d) Energy loss as a function of the charge exchange for different ion energies. The energy loss seems to depend only weakly on the incident velocity.

trapolation of the quadratic fit through the experimental data. Since the low exit charge states may result from close impacts with the CNM (elastic collision), the increase of the energy loss with the incident charge state confirms the increase in nuclear stopping with the charge state as predicted in [78], even though much smaller values for the energy loss are observed.

From the literature a linear dependency of the stopping on the velocity for slow ions is expected [7, 73]. Evaluating the energy loss as a function of the charge exchange for q_{in}=20 for different velocities couldn't clearly confirm this prediction. The dependency on the velocity is by far weaker than the dependency on the charge exchange (see fig. 5.19d).

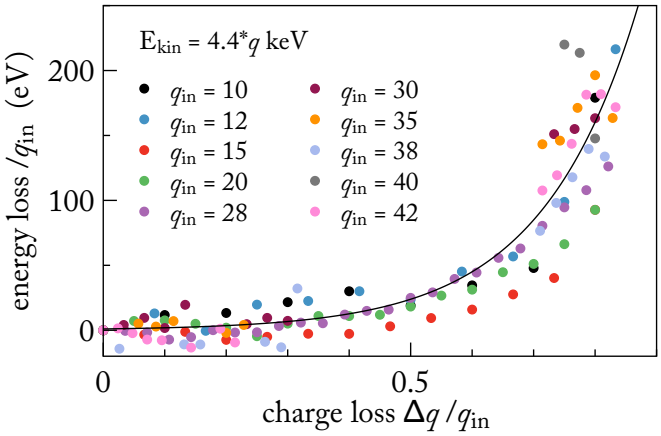

Figure 5.20: "Universal scaling" of the energy loss
The energy loss as a function of the relative charge loss for different incident charge states and kinetic energies. The data points follow eq. 5.2.

By plotting the normalised energy loss as a function of the normalised charge loss an "universal" scaling was found [23]. In fig. 5.20 the energy loss of Xe ions at different incident charge states ($10 \leqslant q_{in} \leqslant 42$) and different kinetic energies ($4.4 \cdot q_{in}$ keV) are plotted. All the data points can nicely be fitted by the eq. 5.2.

5.4.3 Comparison with previous CNM measurements

The observed bimodal charge state distribution displays a clear separation of two impact parameter regimes: large impact parameter collisions result in low charge and energy losses and small impact parameter collisions in large charge and energy losses. Another access to the exit charge state distribution was investigated by Ritter and Wilhelm by irradiating stacks of CNMs and investigating each layer of the stack with high resolution imaging techniques like TEM and HIM [65, 114]. As mentioned before in section 5.3.1 from earlier experiments it is known that HCIs above a certain potential energy threshold can lead to the formation of nanopores [116]. The irradiation of a stack of three CNMs have shown that pores are not only produced in the first, but also in the second and even in the third layer [26, 27]. The size of the pores and the pore density shrinks thereby with the number of the inspecting layer. The pore creation efficiency was evaluated by comparing the pore density (number of counted pores divided by the total area of the image) with the measured incident ion electrical charge. The uncertainties of this method were determined by the inaccuracies of the ion current measurements and the limited number of high resolution images. Taking these uncertainties into account it was evaluated that at least 50% of the incident ions produce a pore upon impact. In comparison to the transmission mea-

surements the inspection of irradiated CNMs makes also highly deflected ions visible, while the measurements with an electrostatic analyser covers only a small solid angle in forward direction. Since the formation of a pore with a diameter in the range of some nm corresponds to a sputter yield of a few 1000 atoms, the potential energy of an incident ion is already consumed after one pore formation, assuming binding energies of a few eV. Therefore the creation of nanopores in the second and third layers appears surprising but can be explained considering the observations from the transmission spectra; some of the projectiles deposit their energy upon pore formation and are transmitted in low charge states, while other still remain in sufficiently high charge states, enabling pore formation in the second or third layer.

5.5 Graphene - Experimental results and discussion

After performing transmission measurements with CNMs, we focused our studies on the ultimately thin material, a freestanding single layer graphene (SLG). The results were largely published in [24] and are discussed in more detail in the next sections.

5.5.1 Multi-electron capture process

In contrast to the bimodal charge state distribution observed for the CNM measurements, the transmission spectra of freestanding SLG show only a single charge state distribution. In fig. 5.21 the transmission spectra of Xe^{30+} ions at two different projectile kinetic energies are shown. The reduction of the kinetic energy shifts the mean exit charge state $\overline{q}_{\mathrm{out}}$ of the transmitted ions towards smaller exit charge states but nevertheless $\overline{q}_{\mathrm{out}}$ remains considerably larger than the equilibrium charge state of $q_{\mathrm{eq}} \sim 1$ [72]. Again, the projectiles transmitted with the initial charge state presumably pass through cracks in the graphene sheet or uncovered parts of the quantifoil support film.

As explained before for the spectra obtained with the CNMs, also for these measurements the raw data were corrected for the artificial broadening caused by the geometry of the electrostatic analyser. The correction of the data enables to extract the correct abundances and widths of every single peak. The evaluation of the transmission spectra for all combinations of q_{in} and E_{kin} showed that the distribution of q_{out} follow a Gaussian function (see fig.5.22a), allowing the determination of the mean exit charge state $\overline{q}_{\mathrm{out}}$, even if very small exit charge states could not be measured with the setup.

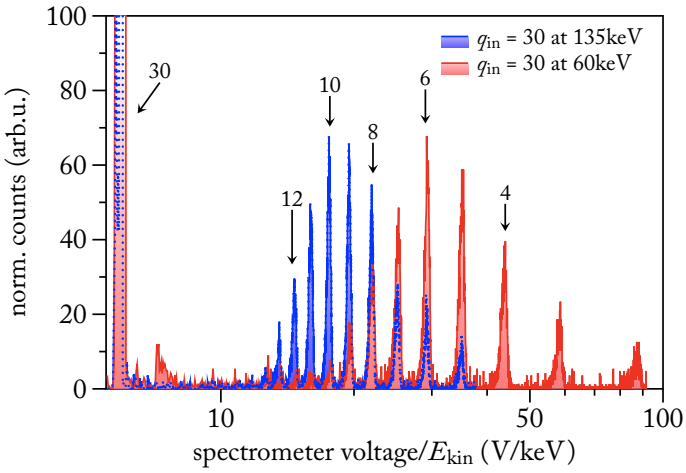

Figure 5.21: Transmission spectrum of Xe ions after passing SLG
Measured spectra of Xe^{30+} ions at an incident kinetic energy of 135 keV and 60 keV transmitted through a freestanding SLG sheet. The exit charge states are calculated from the spectrometer voltage of the electrostatic analyser and are marked by arrows. By increasing the ion kinetic energy, a shifting of the charge state distribution towards higher charge states is observed.

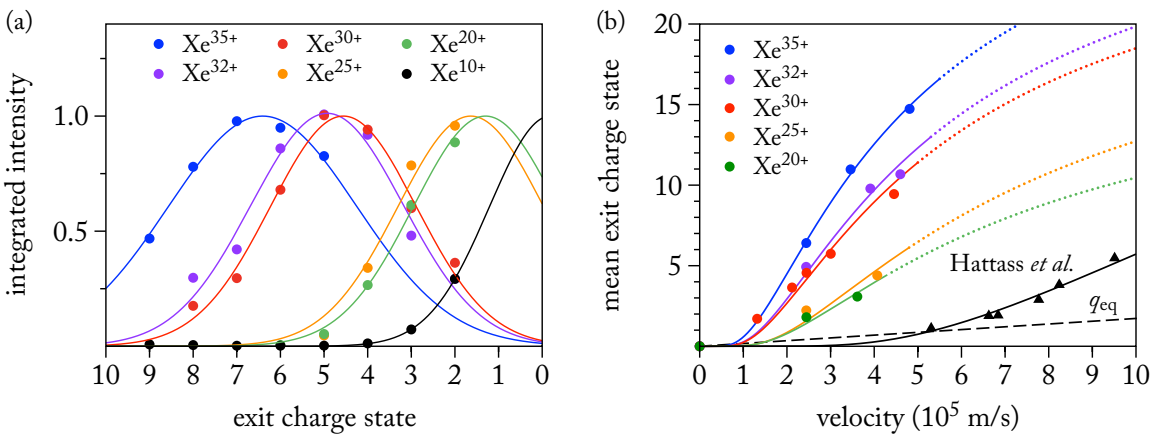

Figure 5.22: Evaluation of the mean exit charge state
(a) Normalised abundance of the exit charge states for different incident charge states from $q_{in} = 10$ to $q_{in} = 35$ at a constant ion kinetic energy of $E_{kin} = 40$ keV. The data points are fitted by a Gaussian function, from which the mean exit charge state $\overline{q}_{out}$ is extracted. (b) Mean exit charge state $\overline{q}_{out}$ after transmission of $Xe^{q_{in}}$ ions through a SLG as a function of the initial ion velocity. The fits follow eq. 5.3. The black triangles represent data points from [178] for the average exit charge state of Xe^{44+} after transmission through a 5 nm thick carbon foil. The dashed line shows the equilibrium charge state for $Z = 54$ according Bohr's stripping criterion.

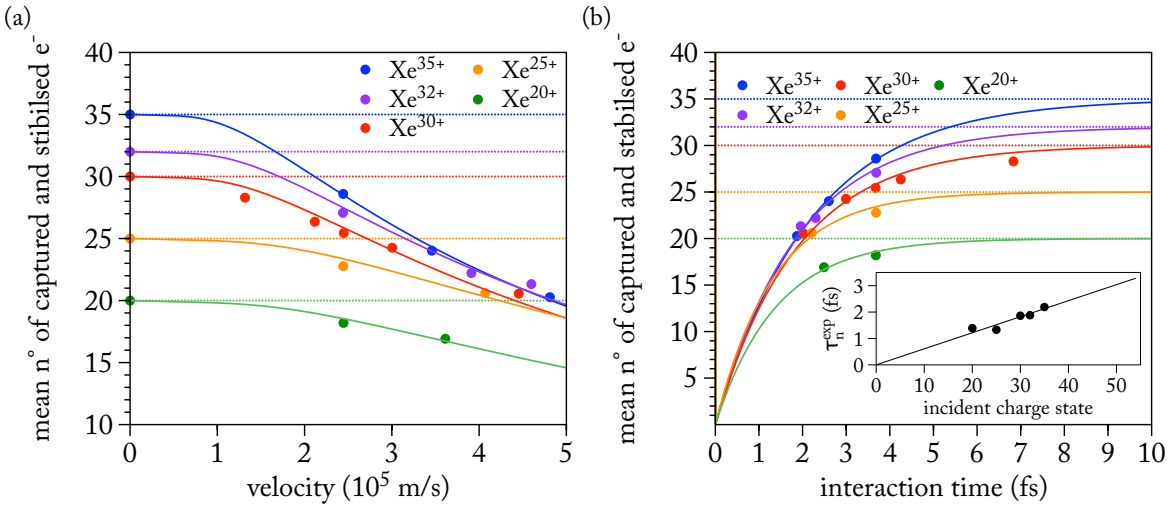

Figure 5.23: Mean number of captured and stabilised electrons
Average number of captured and stabilised electrons ($q_{\text{in}} - \overline{q}_{\text{out}}$) after transmission of $Xe^{q_{in}+}$ ions through a SLG as a function of the velocity (a) and the interaction time (b). The experimental data points are fitted with eq. 5.3 assuming a continuous neutralisation. For the variable d_{eff} in the relation $\tau = d_{\text{eff}}/v$ the critical distance from fig. 5.24 was used. From the fit function a neutralisation time constant τ_n^{exp} of a few fs can be extracted and is plotted in the inset of the right figure.

In fig. 5.22b, the mean exit charge state $\overline{q}_{\text{out}}$ is plotted as a function of the projectile velocity in comparison to the data from [178] for transmission of Xe^{44+} ions through a 5 nm thick carbon foil and the equilibrium charge state calculated using Bohr's stripping criterion for $Z = 54$ [72]. From these data the number of captured and stabilised (e.g. they are not reemitted due to autoionisation processes) electrons ($q_{\text{in}} - \overline{q}_{\text{out}}$) is deduced and plotted as a function of the projectile velocity and interaction time in fig. 5.23.

The data points are fitted by the relation

$$q_{\text{in}} - \overline{q}_{\text{out}} = q_{\text{in}} \left(1 - e^{-\tau/\tau_{\text{n}}^{\text{exp}}}\right) \tag{5.3}$$

assuming an effective neutralisation time constant $\tau_{\text{n}}^{\text{exp}}$. The transmission time τ is thereby defined by $\tau = d_{\text{eff}}/v$ with the ion velocity v and the *effective interaction length* d_{eff} which corresponds to the projectile surface distance where the electron transfer process starts. This distance depends on the projectile charge state and was evaluated by looking at the charge density evolution of incoming ions with various q_{in}, obtained by TDDFT calculation [216]. Figs. 5.24(a-e) show the induced charge density along the direction of the ion motion as a function of time for $q_{\text{in}} = 2, 4, 10, 20$ and 40 as calculated with TDDFT. Already some Å above the graphene layer the

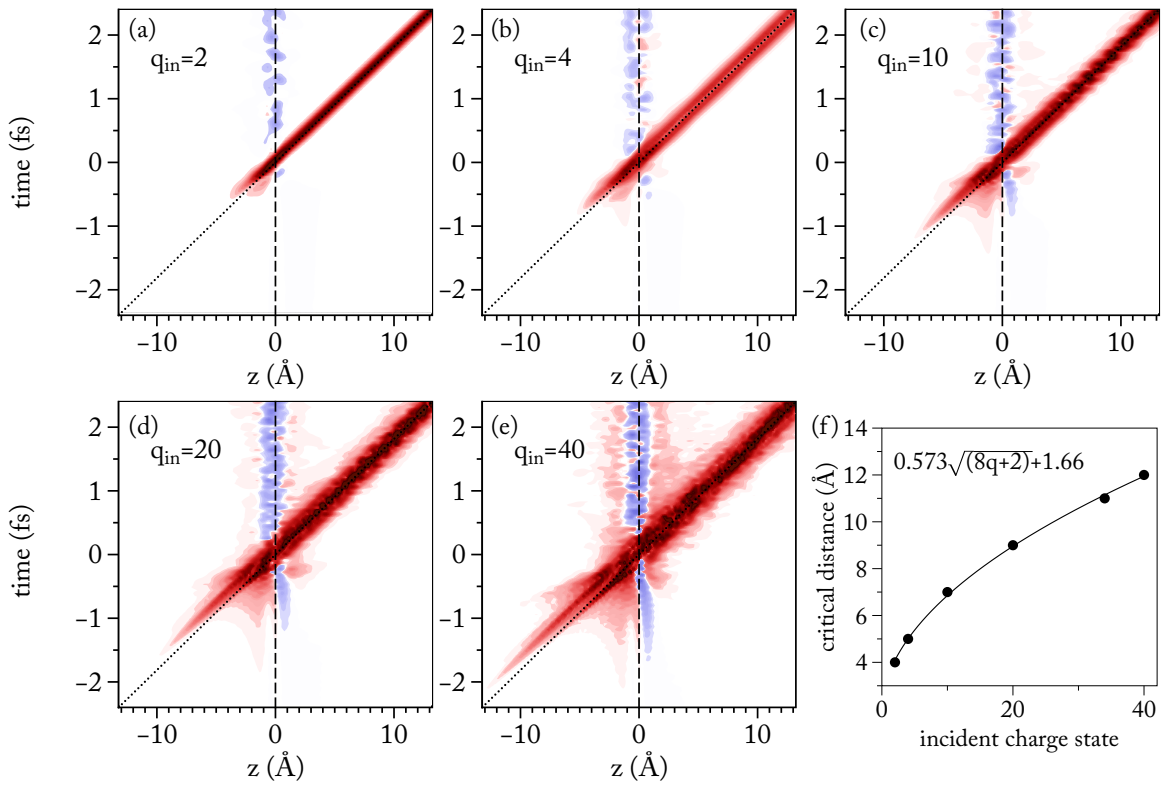

Figure 5.24: Critical distance in dependency of the projectile charge state
(a-e) Charge state density along the direction of the ion motion as a function of time as calculated using TDDFT. Some Å above the graphene layer electrons are captured by the HCI. The critical distance is thereby dependent on the incident charge state of the projectile and is plotted in (f). The fit function through the evaluated data points from the figures follow a square root function as predicted by the COB model.

HCI starts to capture electrons. In fig. 5.24(f) the critical distance is plotted as a function of the ion charge state and is fitted with a square root function as predicted by the COB model (see eq. 2.1 in chapter 2).

By using $d_{\text{eff}} = 0.573\sqrt{8q+2} + 1.66\,\text{Å}$ we obtain $\tau_{\text{n}}^{\text{exp}} = 1.4\,\text{fs}$ for $q_{\text{in}} = 20$ and $\tau_{\text{n}}^{\text{exp}} = 2.2\,\text{fs}$ for $q_{\text{in}} = 35$, respectively (see fig. 5.23). The extrapolated equilibration time for all incident charge states used in the experiment is smaller than 8 fs. The experimentally observed strong reduction of the charge state of the HCI within only some fs could also be confirmed by the TDDFT calculations which showed a multi-electron character of the charge transfer [24]. HCIs with initial charge states $q_{\text{in}} = 10, 20$ and 40 capture ~ 9, ~ 17 and ~ 34 electrons during the passage through the graphene sheet.

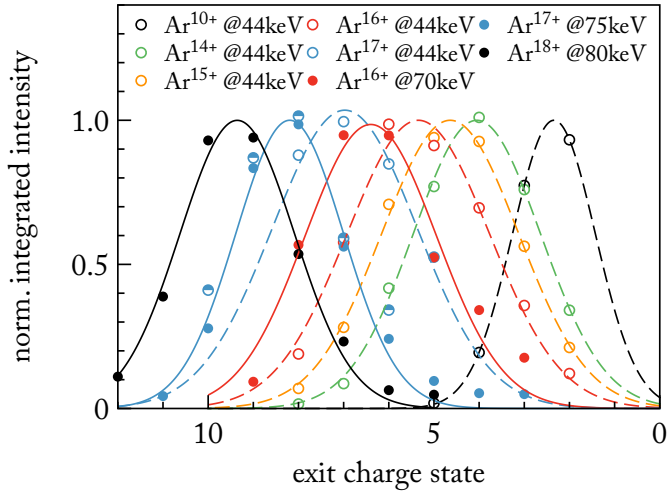

Figure 5.25: Mean exit charge state of Ar transmission spectra
Deconvolved and integrated values of every single peak of Ar transmission spectra for various ion charge states and energies. The data points are fitted by Gaussian functions, which yield the mean exit charge state. The data points were obtained during two measurement periods. In the first period the kinetic energy was kept constant ($E_{\mathrm{kin}} = 44\,keV$) for various incident charge states $q = 10-17$ (open symbols, dashed fit curves). In the second period the extraction voltage of the ion source was kept constant ($U_{\mathrm{Source}} = 4.4\,kV$) in favour of higher count rates. To check the reproducibility transmission measurements with Ar^{17+} at $E_{\mathrm{kin}} = 75\,keV$ were performed during both measurement periods (half-open and full symbols respectively.)

Besides transmission measurements with Xe ions with charge states $10 \leqslant q \leqslant 35$, which correspond to electron holes in the M (n=3) and N (n=4) shell, also first measurements with Ar ions with charge states $10 \leqslant q \leqslant 18$ (electron holes in the K (n=1) and L (n=2) shell) were performed. The Ar transmission spectra show the same behaviour as the Xe spectra. In fig. 5.25 the deconvolved and integrated values of every single peak for various incident charge states and energies are plotted and fitted by a simple Gaussian function. It is evident, that an increase of the incident charge state leads to higher exit charge state values. The data show the results of two measurement series. First the kinetic energy was kept constant ($E_{\mathrm{kin}} = 44\,\mathrm{keV}$) for various ion charge states $q = 10-17$ (open symbols, dashed fit curves). In the second series the extraction voltage of the ion source was kept constant ($U_{\mathrm{Source}} = 4.4\,\mathrm{kV}$) in favour of higher count rates at higher ion charge states up to $q = 18$ (solid points, solid fit curves). To ensure the reproducibility of the measurements, the transmission measurements with Ar^{17+} at $E_{\mathrm{kin}} = 75\,\mathrm{keV}$ were performed during both measurement periods and produced the same results. These data points are marked by the half-open symbol in fig. 5.25.

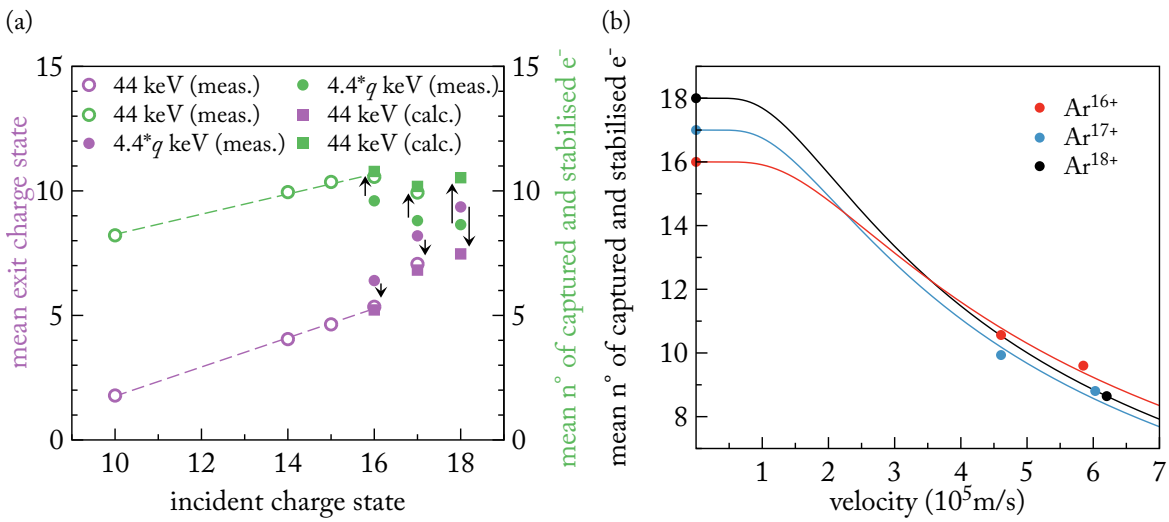

Figure 5.26: Jump of the mean exit charge state
(a) The mean exit charge state and the captured and stabilised electrons are plotted as a function of the incident charge state of Ar ions. To compare the set of experimental data for a fixed kinetic energy (44 keV), the data obtained at higher ion velocities (solid points) are fitted in (b) with eq. 5.3 and from this fit function the number of captured and stabilised electrons for the missing ion velocity (or ion kinetic energy) can be extracted. This calculated values are plotted in (a) as solid squares. A change in slope of the exit charge state or number of captured and stabilised electrons as a function of incident charge state between $q_{\text{in}} = 16+$ and $17+$ can be observed.

By plotting the exit charge state or the number of captured and stabilised electrons as a function of the incident charge state, a jump between the 16+ and 17+ charge state can be observed (see fig. 5.26a). The open symbols show the results of the measurements performed at a fixed ion kinetic energy of 44 keV and the solid symbols at a fixed extraction voltage of the ion source, which leads to different ion kinetic energies ($E_{\text{kin}} = 4.4 \cdot q$ keV). To compare the set of experimental data at a fixed kinetic energy, namely $E_{\text{kin}} = 44$ keV, the data obtained for higher kinetic energies have to be adapted. This is done in fig. 5.26b by plotting the number of captured electrons as a function of the velocity and fitting the data points with the relation 5.3 known from the measurements with Xe ions. This fit function yields the number of captured electrons for the missing kinetic energy.

Beside the transmission measurements, we started recently to also detect emitted X-rays of the HCI-graphene interaction process with a Bruker XFlash silicon drift detector with an energy resolution of 140 eV for getting better insights into the de-excitation processes. For calibration the Mn-K_α and Mn-K_β line of a Fe^{55} source was used. One of the first obtained X-ray spectra for Ar^{q+} with $q = 16, 17$ and 18 is shown in fig. 5.27. Remarkable is thereby the appearance of the additional peaks at $E \sim 3.2$ keV in the case of Ar^{17+} and Ar^{18+}. These peaks are associated to the

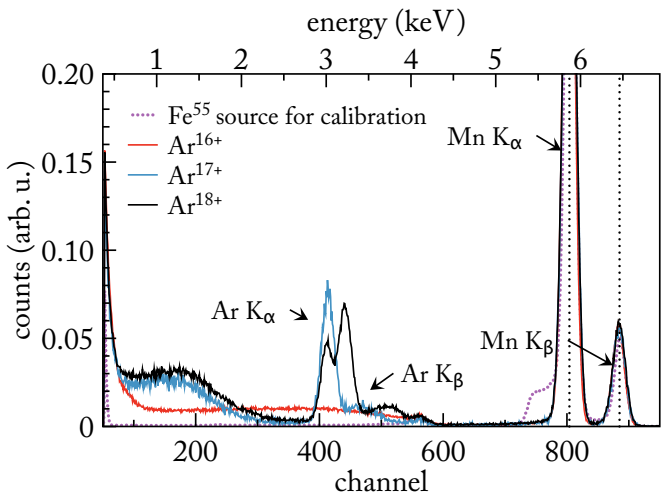

Figure 5.27: X-ray spectrum of Ar interaction with SLG
First X-ray spectra obtained with Ar^{q+} ions due to the interaction with SLG. The additional peak(s) for Ar^{17+} and Ar^{18+} points to the fact that the K-shell holes are refilled by radiative processes. The spectra were calibrated with the Mn-K_α and Mn-K_β line of a Fe^{55} source.

K_α and K_β emission lines. In the case of Ar^{18+} a splitting of the K_α peak is observed. This is due to the energy difference for possible de-excitation into the empty or singly occupied K-shell.

The X-ray spectra point to the fact that a considerable fraction of the vacancies in the K-shell decay via X-ray emission as a competitive de-excitation channel to Auger decay processes, especially for high Z. However, similarly as for Auger decay, the time needed for reaching the ground state is longer than the time needed by the projectile to touch the surface. The persistence of the K-shell holes might explain the observed gap between the 16+ and 17+ charge state distribution in fig. 5.26. The filling of the K shell will occur after the ion has left the graphene layer on the way to the detector. During this time interval ($\sim 1\,\mu$s) electrons from higher levels can decay under emission of an X-ray into the K shell but the hole left-behind can no longer be refilled by an electron from the graphene sheet. Less electrons are captured and stabilised as expected by a naive extrapolation of the data obtained between 10+ and 16+.

Discussion of the neutralisation process

In the case of small impact parameters for the CNMs and for graphene (for intact graphene the impact parameter is $\leq$ half the atomic distance of 1.46 Å) an extraordinary effective charge capture within a few fs could be observed. To find a possible explanation, several transition and

de-excitation processes, which are described in chapter 2, are discussed in the following paragraphs.

Auto ionisation and radiative transition

Within a critical distance from the surface target electrons can be captured by the ion via resonant transitions and populate high Rydberg states of the incident ion. During further approach to the surface auto ionisation processes will start and transfer electrons from higher to lower energy levels emitting Auger electrons, leading to a recharging of the ion. Ongoing resonant transitions keep the projectile neutral. To explain the effective capture and stabilisation of 20-30 electrons the entire auto ionisation sequence must be completed during the interaction time with the SLG, which would require de-excitation rates in the order of $10^{16} - 10^{17}\,\mathrm{s}^{-1}$. Since typical Auger rates for higher quantum numbers $n \sim 13$ are in the order of $10^{8} - 10^{12}\,\mathrm{s}^{-1}$ and only for inner-shell transitions they increase to $10^{14} - 10^{15}\,\mathrm{s}^{-1}$ [19, 35], within the short interaction time of some fs only a few electrons can be stabilised. Due to this large discrepancy resonant transitions followed by auto-ionisation processes cannot explain the observed capture and stabilisation of so many electrons within a few fs. Even more unlikely is a de-excitation due to radiative processes since their transition rates are generally much smaller than those for 'radiationless' Auger processes. However, for higher charged projectiles radiative de-excitation become competitive, since the related transition rates increase approximately with the forth power of the effective ion charge. As soon as inner shell holes are filled with electrons de-excitation by the emission of photons will become important. For K-shell vacancies the 'break-even' for Auger decay versus radiative decay occurs for atoms of nuclear charge around $Z = 30$, for L-vacancies only above $Z = 85$ [19]. In the case of Ar the detection of X-rays showed that also radiative processes may contribute to the neutralisation process.

Quasi-resonant transition

In the case of projectile and target atoms with similar nucleon charges Z, the so called quasi resonant neutralisation (side feeding [218]) may become dominant. In this case at closer distance between the projectile and the target a level shifting or the formation of molecular orbitals enable a resonant transfer of the electrons from closely bound target to closely bound projectile states. The deposited energy in the target may result in the ionisation of the target and emission of an electron or excitation of the electronic system of the target with possible energy transfer to the phononic system. In the case of Ar ions as projectiles and graphene as target material, a direct electron population of the M-shell of the Ar ions is possible at close distance and following Auger and radiative de-excitation processes would bring the electrons into the L- and K-shell of Ar within some fs.

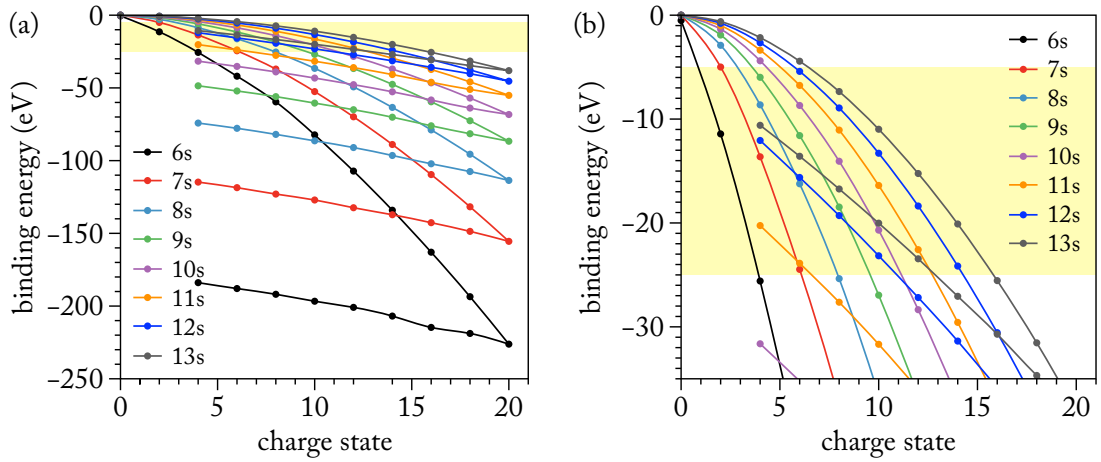

Figure 5.28: Electronic states of a Xe ion
Electronic states of Xe ion as a function of ion charge state when electrons are removed (upper branches of the curves) and injected into higher bound states close to the vacuum (lower branches of the curves). The yellow marked area represents the high energy states which are in resonance with the graphene valence band [217].

Looking at the literature, the side feeding of inner-shells was promoted for example by Winecki *et al.* [21] performing scattering measurements with Ar ions on HOPG and later also calculated by Burgdörfer *et al.* [45].
In the case of very asymmetric projectile and target atoms, like in the case of Xe ions and a graphene sheet as target material, the situation is different. In fig. 5.28 the electronic structure of a Xe ion as calculated by Krasheninnikov [217] shows the shifting towards lower energy levels with the decrease of electrons in the upper atomic shells, since the screening of the nucleus is weaker.

To "simulate" the formation of a hollow atom, upper bound states with large quantum numbers which are in resonance with the graphene valence band (-25 eV<E<-5 eV) are populated with electrons. The single electron levels go up, but remain well below the corresponding values in the neutral atom, as screening of the core levels is still weak. For strongly ionised atoms, only states with large principal quantum numbers are in resonance with graphene.

In this electronic structure calculation the Xe ion is not affected by the presence of the graphene sheet. At small distances the electronic structure of Xe may be better described by a C-Xe molecule. The calculation of the electronic structure of a diatomic molecule, at small separation between the atoms, is a challenging task. The evolution of the atomic structure of the Xe-C pair has been done by using a DFT-based model [217].

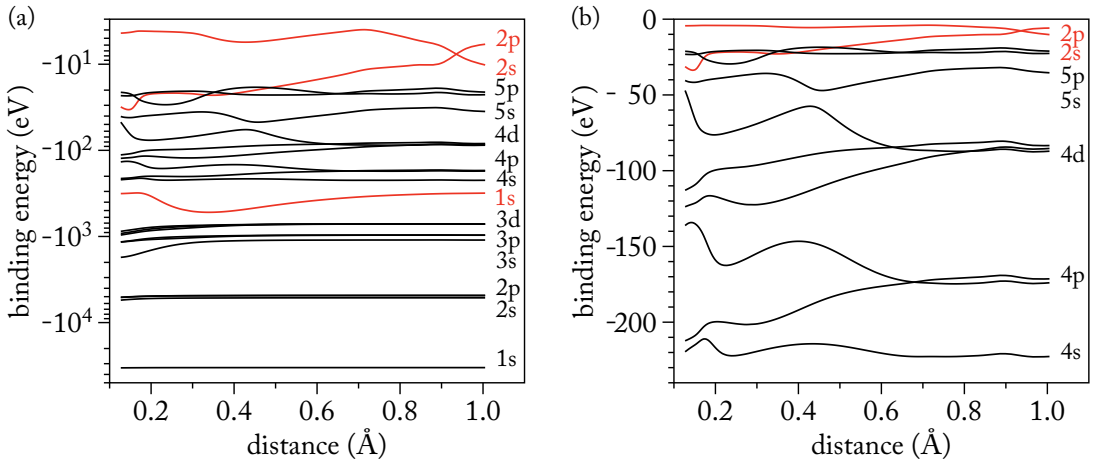

Figure 5.29: Molecular orbital of the Xe-C molecule
Molecular orbital of the Xe-C molecule as a function of separation between the nuclei. A slight shifting of the deeper energy levels of Xe and crossings at close distance are visible but still they appear to lie not high enough for resonant tunneling from the graphene valence band into the molecular orbital [217].

In fig. 5.29 the electronic structure of the Xe-C dimer is plotted as a function of separation between the nuclei. It shows a slight upwards shifting of deeper Xe levels and also crossings at low distances but they appear to lie not high enough for resonant tunneling from the graphene valence band into the molecular orbital. In addition, the calculations were performed with a neutral Xe atom. As shown in fig. 5.28 an increase of the charge state leads to stronger bound shells. From these calculations it seems not convincing to explain the observed short equilibrium time with electron inner-shell side feeding processes.

Auger neutralisation and exchange transition (indirect Auger de-excitation)
In the Auger neutralisation and the exchange transition process electrons are transferred from the projectile directly into deeper shells of the ion and the excess energy leads to the emission of a target or projectile electron. Considering the small overlap between the involved wave functions between the inner-shell of the ion and the outer-valence electron of the target (see chapter 2, section 2.1.6) the electron transfer from the target to an inner-shell hole of the ion is rather unlikely.

Intermolecular Coulombic decay (direct Auger de-excitation)
A much more promising candidate for explaining the experimental observation is the intermolecular Coulombic decay process. Since this process describes the filling of an inner-shell hole by an outer-valence electron of the same atom/ion, leading to the emission of an electron of a neighbouring atom, in contrast to the Auger neutralisation and exchange transition no overlap between

the inner-shell projectile electron state and the outer-valence electron state of the target is necessary. The $1/R^6$ dependency (see chapter 2, section 2.1.6) makes the ICD process only likely at small impact parameters, which is fulfilled for ions transmitted through SLG and through dense packed areas of CNMs. In addition the strong reduction of the lifetime to only some fs with increasing number of neighbouring atoms might even be more dominant in a macromolecule like graphene or CNM. The first electron emission measurements performed by colleagues in our group show that the number of emitted electrons is about 2-3 times the incident ion charge state. Such large number of emitted electrons from HCI impacting on solid surfaces were also measured by others with an energy distribution dominated by low energy electrons ($< 20\,\mathrm{eV}$) [219]). So far the ICD process is the only process which can consistently explain the observed fast neutralisation of HCI interacting with graphene and CNMs. The interaction scenario would then be the following: A HCI is approaching a surface and at a critical distance it starts to capture electrons into high Rydberg states and a hollow atom is formed. As soon as the ion comes close enough to the target, electrons in the high Rydberg states are rapidly quenched into inner-shell holes and the released energy is transferred to several neighbouring target atoms which are multiply ionised almost instantaneously.

5.5.2 Transmission electron microscopy results

In the case of CNMs the capture and stabilisation of ~ 30 electrons within some fs has resulted in the formation of nm sized holes [116]. The failure to sufficiently resupply the missing electrons and to dissipate the absorbed energy on a timescale small in comparison to the lattice vibrations provokes Coulomb repulsion and causes destruction and hole formation in the membrane. In the case of graphene elastic collisions may cause a direct knock out of single C atoms, but less than one C atom is sputtered on average by a 10-100 keV Xe ion [220]. Single localised defects may be recovered by self healing processes like the dissociation of ubiquitous hydrocarbon molecules [215]. Extended structural modifications, provoced by the high potential energy deposition in the mebrane, should be detectable with high resolution imaging techniques like TEM and STEM. Careful investigations of irradiated graphene samples didn't reveal any nm sized defect structures. A typical TEM image of a freestanding SLG after irradiation with Xe^{40+} ions with a kinetic energy of 180 keV is shown in fig. 5.30. The applied fluence of 10^{12} ions/cm^2 corresponds to approximately six ion impacts within this 25 nm x 25 nm frame. No hole formation or rapture could be detected. This means that emitted electrons are resupplied quickly enough along the graphene sheet to the impact region to neutralise all ionised carbon atoms, thus preventing hole formation due to Coulomb repulsion.

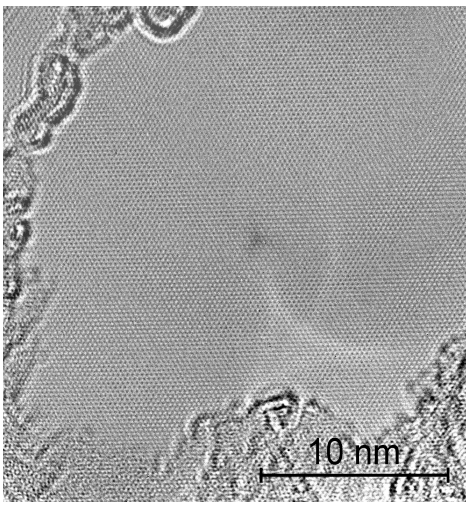

Figure 5.30: TEM image of irradiated freestanding SLG
The irradiation was performed with Xe^{40+} ions at 180 keV with an applied fluence of 10^{12} ions/cm^2 (about six impacts on the shown image). No hole formation or nanosized topographic defects could be observed. The image is adapted from [24].

5.5.3 Local breakdown current density

The loss and fast resupply of electrons in the graphene sheet is connected with an electron flux. From the experimental data a lower bound for the local current density can be estimated. Since at least $q_{\text{in}} - q_{\text{out}}$ electrons are transferred from the graphene sheet to the approaching HCI during the interaction of some fs, a local current of $I > 1.5\,\text{mA}$ can be estimated. From the performed TDDFT calculations it can be seen that the electrons are extracted from a graphene area with a lateral radius of $R = 5\,\text{Å}$ around the impact point and that the electron flow along the graphene layer restores quickly the charge neutrality of the interaction region. This is in accordance with the TEM and STEM measurements which show the absence of nanosized defects or holes after the HCI bombardment, which would result from Coulomb explosion. The electrons cross a surface $S = 2\pi Rh$ with $h = 3.4\,\text{Å}$ being the thickness of the graphene layer, estimated from the interlayer spacing of graphite. Thus, an electron current density of $J = I/S$ in the graphene plane exceeding $6 \cdot 10^{11}\,\text{A/cm}^2$ is kept during the interaction process. The obtained value is only a lower limit of the current density because it only accounts for electrons captured by the projectiles and not for electrons emitted into vacuum. The TDDFT calculations yield that per each captured electron approximately one additional electron is emitted into vacuum. From earlier measurements it is known that the amount of emitted electrons can be as high as $3 \cdot q_{\text{in}}$ if one accounts for Auger processes involving tightly bound electronic shells of the projectile [219].

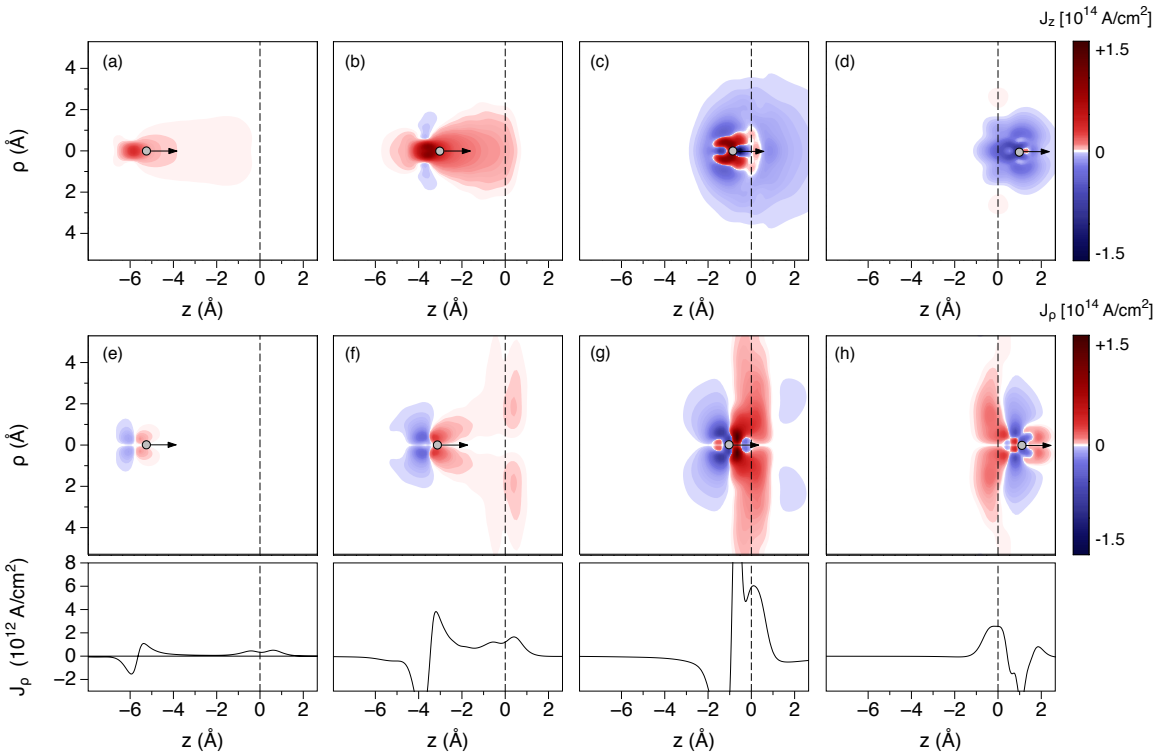

Figure 5.31: Perpendicular and radial current density
Snapshots of the perpendicular J_z (a-d) and radial J_ρ (e-h) components of the current density for $q_{\text{in}} = 20$ at four different HCI-graphene distances obtained from TDDFT calculations. The TDFFT calculations were performed in cylindrical (ρ, z) coordinates with z-axis set along the projectile trajectory perpendicular to the target surface. The position of the HCI is indicated by a small circle, the position of the graphene layer by the vertical dashed line. Already some Å above the surface charge transfer from the graphene layer to the HCI starts and the current density along the direction of motion increases with the approaching HCI. The extracted electrons are restored by the extremely high transverse current density (f-h) along the graphene layer. From the corresponding profiles (lower panels), which show the transverse current density averaged over a disk of 10Å in radius, it is visible that graphene is able to sustain locally extremely high current densities up to $10^{12}\,A/cm^2$. The figure is taken from [24].

In fig. 5.31 the perpendicular and radial components of the current density obtained by TDDFT simulations for $q_{\text{in}} = 20$ at $v = 0.87$ nm/fs for four different HCI-graphene distances are shown. J_z shows the current density along the direction of motion and already some Å before the graphene layer a sizable charge current can be observed which increases with the approaching HCI. Simultaneously a significant transverse current density J_ρ along the graphene layer can be observed which show the fast local response of graphene to the strong HCI perturbation. The corresponding profiles show the averaged transverse current density over a disk of 10 Å in radius and reaches

values exceeding 10^{12} A/cm^2. The absence of any traces of large-scale lattice deformations thus confirms the intrinsic ability of a freestanding SLG to sustain transiently and locally in the fs and nm scale extremely high current densities, exceeding previously measured breakdown currents of supported graphene films by at least three orders of magnitude [221–224].

5.5.4 Energy loss

The energy analysis of transmitted ions in the pre-equilibrium regime enables to make charge state effects on the energy loss experimentally accessible. As shown before for CNMs, the strong (exponential or quadratic) dependency of the energy loss on the incident charge state q_{in} and the exit charge state q_{out} or the charge exchange $q_{\text{in}} - q_{\text{out}}$ is observed also for SLG (see fig. 5.32 and fig. 5.33a). We measure keV energy losses, which are more than an order of magnitude larger than the result from a TRIM simulations for neutral Xe atoms transmitted through a carbon layer with an areal density of $3.82 \cdot 10^{15}$at/cm^2. The simulation predicts an energy loss of 228 eV taking the detector acceptance angle of ±0.8° into account. An extrapolation of the fits of fig. 5.33a through $q_{\text{in}} = 0$ yields a value close to the TRIM value, representing equilibrium stopping.

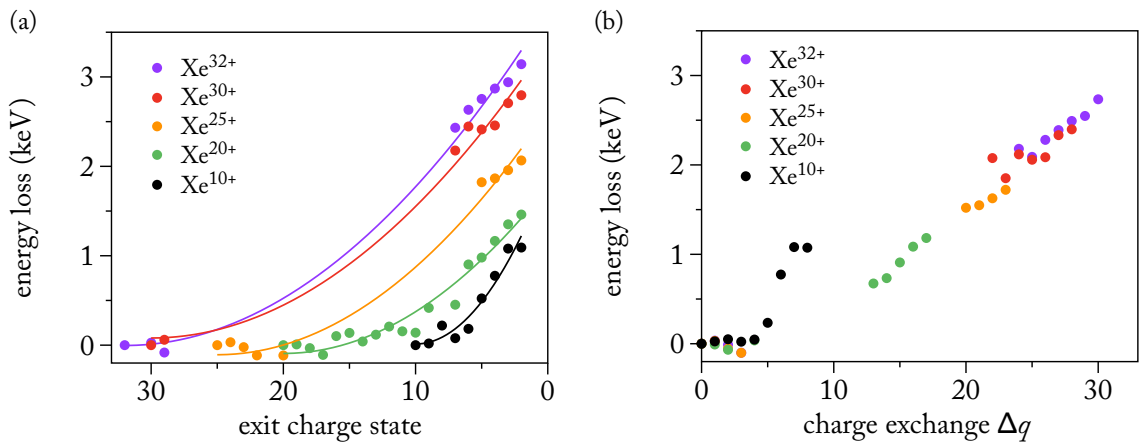

Figure 5.32: Ion energy loss due to interaction of slow HCI with SLG
Energy loss as a function of (a) the exit charge state and (b) the charge exchange for various ion charge states. The fit functions follow the exponential equation 5.2.

The performed TDDFT calculations show energy loss values of similar magnitude as the experimental measurements and reproduce the q_{in}^2 dependency as shown in fig. 5.33a. A detailed view on the neutralisation dynamics is given in fig. 5.33(c-f), where the induced electronic charge density at four different HCI-graphene distances is shown as the HCI approaches the graphene layer. Some Å above the surface the strong attractive potential accelerates electrons towards the HCI.

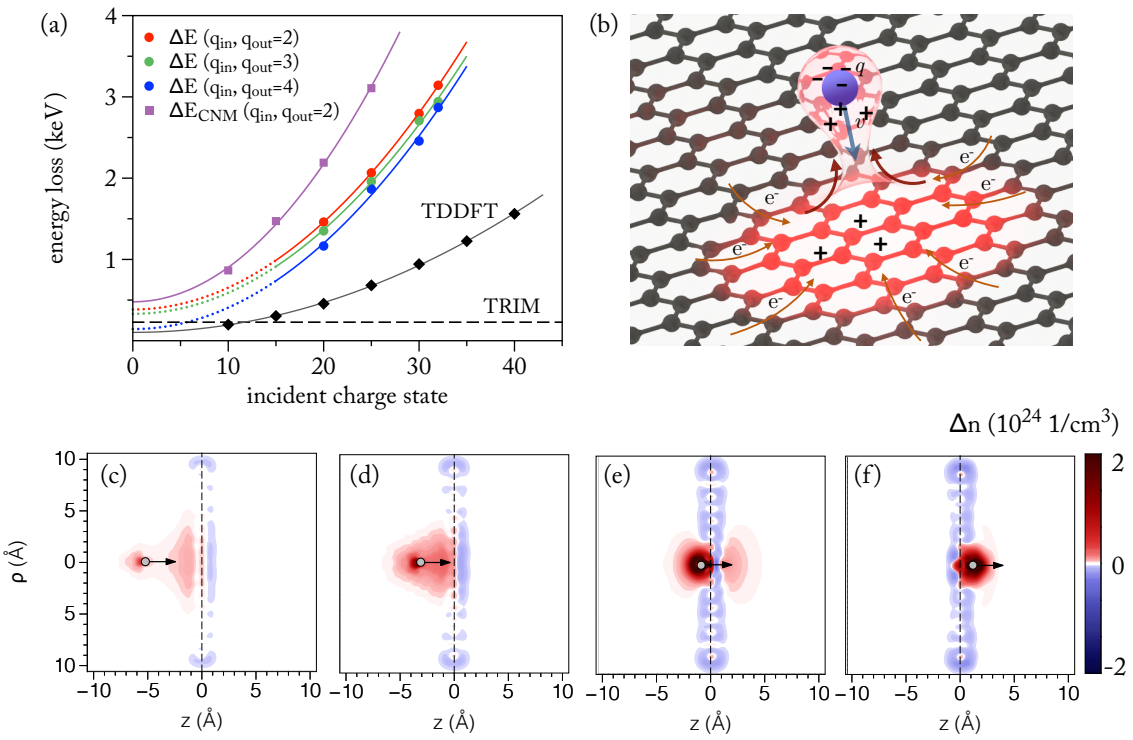

Figure 5.33: Ion energy loss and detailed view of the neutralisation dynamics *(a) Experimentally determined energy loss as a function of the incident charge state for $q_{\text{out}} = 2, 3, 4$ for a fixed kinetic energy of $E_{\text{kin}} = 40\,\text{keV}$. The data points are fitted by a quadratic function and compared with the energy loss for CNM with the same incident particle parameters. The dashed line shows the result from a TRIM simulation which show the nuclear and electronic stopping for neutral Xe ions transmitted through a graphite layer of a thickness of 3 Å. The experimental data are compared with results from TDDFT calculations which reproduce the parabolic dependency with the initial charge state and the order of magnitude of the energy loss. (b) Schematic of the interaction process between a HCI and a freestanding SLG. The approaching HCI captures a lot of electrons from a limited area on the fs time scale leading to a temporary charge-up of the impact region. (c-f) The induced electronic charge density for a Xe^{20+} ion ($v = 0.87\,\text{nm/fs}$) approaching a graphene layer shows two components: the charge density located at the graphene layer due to the target polarisation and the convoy of electrons lagging behind the HCI. As soon as the HCI gets closer to the surface, the two components merge and forward emission of electrons starts. The excitation of the graphene layer while and after the crossing of the ion are clearly visible. The figure is adapted from [24].*

The target is polarised and the capture of lots of electrons from a limited area on the fs time scale leads to a temporary charge-up of the impact region. This scenario is depicted in the schematic

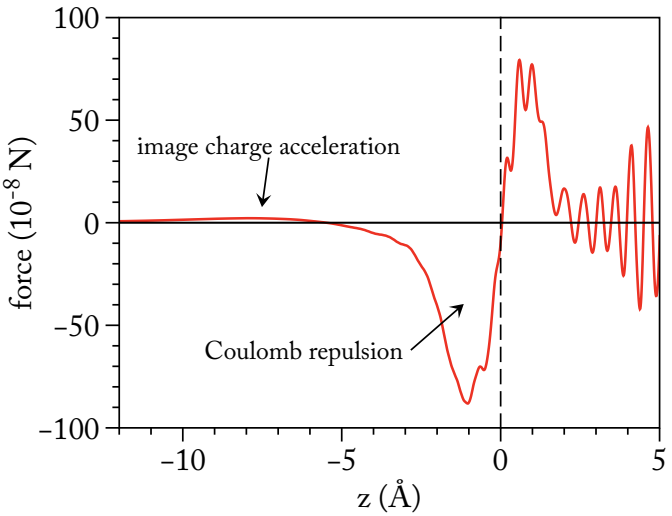

Figure 5.34: Force along the trajectory of the HCI
The Xe^{20+} ion at $E_{\text{kin}} = 40\,keV$ is first accelerated by the image charge towards the surface. After capturing electrons from the target a convoy of electrons is formed around the approaching HCI, which is not centred around the ion but lags behind. The capture of electrons from a limited area on a fs time scale leads to a temporary charge-up of the impact region. A Coulomb repulsion between the approaching ion and the charge patch leads to a netto stopping of the ion and might explain the observed high kinetic energy loss of the ions. The figure is adapted from SI of [24].

in fig. 5.33b. A convoy of electrons is formed around the approaching HCI, but its center is not located at the position of the HCI but "lags behind". This behaviour is also visible in fig. 5.24 where the induced charge density follows the ion trajectory, marked by the black dotted lines.

By looking at the force exerted along the trajectory of the projectile (see fig. 5.34), it becomes visible that the initial image charge acceleration of the projectile is soon counteracted by Coulomb repulsion between the positively charged ion and the locally induced charge patch on the graphene sheet. The integral of the force curve results in a netto stopping of the ion. The underestimation of the energy loss by the TDDFT calculations may result from the fact that the used pseudo potential description of the HCI does not include the full Coulomb singularity at distances smaller than the used cut-off radius. Nevertheless, reproducing the q_{in}^2 dependency and the order of magnitude of the measured energy losses show that the electronic response of the simulated system is well described.

While for CNMs only a weak dependence of the energy loss on the ion velocity could be observed, a linear increase of the energy loss with the ion velocity was found for SLG in the measured velocity regime (see fig. 5.35). An increase of the absolute value of the energy loss, but a de-

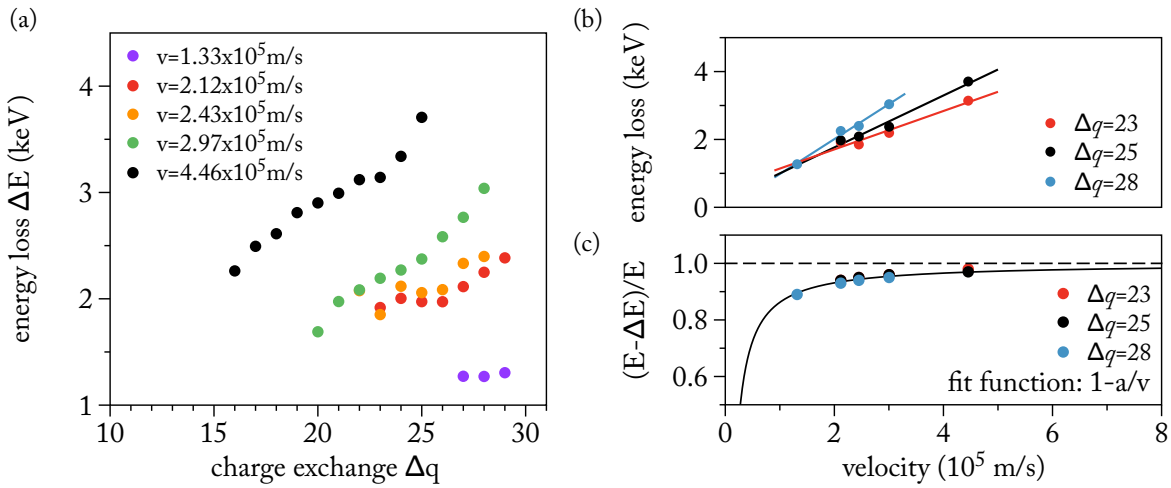

Figure 5.35: Experimental ion energy loss
(a) The energy loss of Xe^{30+} ions as a function of the charge exchange for various particle velocities. (b) A linear increase of the energy loss with the velocity for a fixed Δq can be observed within the measured velocity range. (c) The faster the ion is, the smaller is the relative energy loss $(E - \Delta E)/E$.

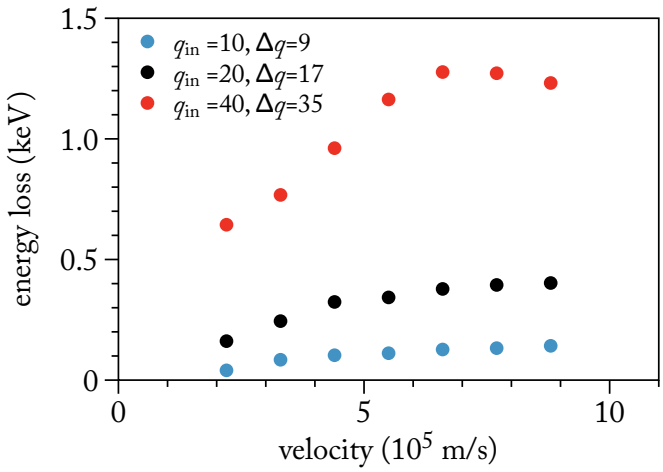

Figure 5.36: Simulated ion energy loss in dependence of the ion velocity
Also the performed TDDFT calculations predict a linear increase of the energy loss within a certain velocity regime. At higher ion velocities the energy loss saturates.

crease of the relative value $(E - \Delta E)/E$ with the velocity was detected. For higher ion energies the TDDFT calculations predict a saturation of the energy loss (see fig. 5.36). This is comprehensible by considering that the induced charge on the graphene layer, which causes Coulomb repulsion, is limited to 2-3·q_{in}. With the decrease of the ion velocity the Coulomb repulsion will

contribute less to the energy exchange term, because the approaching ion will be surrounded by a symmetric electron cloud and the induced charge patch will be neutralised by electrons through the graphene. The observed higher energy loss for CNMs in comparison to SLG for the same irradiation parameters might arise from the different electron mobility of the two materials. The recovery of the neutralisation of the impact area after the electron loss takes longer for CNM, which will lead to larger force acting on the approaching ion. The Coulomb explosion afterwards leads to rapture and hole formation of this material.

6

Summary and Outlook

The presented thesis deals with two main topics in the field of ion-solid interaction. On the one hand possibilities for nanostructuring of 3D materials due to HCI and SHI irradiations were investigated and on the other hand charge exchange and energy loss processes during the transmission of HCIs through 2D materials were studied. From the results it emerged that these studies are also suitable to gain information about the electronic response of the used 2D materials.
The main results obtained are summarised and impulses for further investigations are given in the following paragraphs.

Previous investigations of SHI irradiation of crystals under grazing angle of incidence have shown the formation of chains of single nanodots. Using high resolution imaging in this work it could be demonstrated that the created tracks exhibit a much more complex structure as observed in the previous studies. For the insulating materials CaF_2 and mica the formation of grooves, bordered by chains of single nanodots at the ion impact site which eventually merge into a single slowly fading protrusion, were observed. This particular track formation could successfully be attributed to melting and sublimation processes as checked for CaF_2 by performing 3D-TTM simulations. Similar tracks were also observed for the crystals $SrTiO_3$ and TiO_2, but with much less pronounced groove formation at the ion impact site.
In future experimental investigations the assumption that the observed track formation is induced by melting and sublimation processes can be checked by repeating the irradiation for a larger

range of ion kinetic energies. Besides determining a threshold for hillock formation also a threshold for groove formation should be detectable and linked to the sample melting and sublimation temperatures. An attempt was made to shift the threshold for melting and sublimation processes by heating the samples. These experiments, however, were limited to a small temperature range, since i.e. for CaF_2 and mica cracking and destruction of the surface above a sample temperature of ∼600°-700°C was observed. Besides a variation of ion kinetic energies, also the range of investigated materials can be increased. Further theoretical investigations and simulations are necessary for getting an even more consistent picture. It could be of benefit to think about an experimental setup which enables the measuring of material ejected due to sublimation.
Considering HCI irradiations, the problem of surface contamination would have to be solved to guarantee reliable results. Still, the most secure and reproduceable method would be to perform the cleaning (cleaving, ion sputtering, heating), irradiation and imaging of the different samples without breaking the vacuum conditions in between. The problems with contaminations could maybe be circumvented by performing irradiations under grazing angle of incidence due to the more elongated track formation. Investigations of nanostructures in irradiated samples revealed by etching can be performed without special sample pretreatment, since primary contaminations are thereby also removed.

The interaction studies of HCI with ultrathin materials, i.e. CNMs and SLG, enabled us to investigate charge exchange and energy loss processes in the pre-equilibrium regime. The observed bimodal charge state distribution in the case of CNM was linked to an impact parameter selection of the interaction process. At large impact parameters the ions stabilise only a few (1-5) electrons and experience almost no kinetic energy loss. This is in sharp contrast to close impact processes, where the ions capture and stabilise almost all missing electrons and show a quadratic energy loss dependency on the incident charge state. Considering the structure of the CNMs with dense and less dense packed areas, the impact parameter selection is comprehensible. In the case of SLG only impact parameters ≤ 1.4 Å are available and indeed only a single low charge distribution with high energy loss could be observed. The capture and stabilisation of almost all missing electrons within a time scale of only a few fs cannot be explained sufficiently well with the currently considered and established de-excitation processes like Auger and radiative de-excitation transitions nor with the so called side-feeding processes. In this thesis the interatomic Coulombic decay process is proposed as a very promising candidate to explain the observed ultrafast neutralisation of HCIs.
Besides getting more insights into the de-excitation process of HCIs, the performed investigations enabled us to also get information about the electronic response of a 2D material like graphene in the presence of a high electric filed, induced by the approaching HCI. From the performed experiments and accompanying TTDFT calculations local current densities in the graphene plane

in the order of 10^{12} A/cm^2 could be estimated to be present on a time scale of a few fs. These current densities are at least three orders of magnitude larger than previously established local breakdown currents. Since no nanosized holes or defects could be detected via TEM and STEM after HCI irradiation, it was concluded that the exceptional electronic properties of graphene allow for a resupply of the lost charge and distribution of the deposited (electronic) energy promptly enough to prevent Coulomb explosion in the electron depleted region. This is, however, not the case for the amorphous insulating CNMs, where nanometer sized holes after HCI irradiation have been found. The surprisingly large ion energy loss of a few keV in both graphene and CNMs was explained, at least in the case of SLG, by the formation of positive charge patches in the graphene layer. Coulomb repulsion between the approaching polarised projectile (negative charge lagging behind) and the charge patch causes the high kinetic energy loss. Our studies revealed how graphene responds on a fs time scale to extremely high electric fields and underline the exceptional properties of graphene for ultrafast electronic applications at high current densities.
To verify that the fast observed neutralisation can indeed be explained by the ICD process, further investigations are desirable, wherein the detecting of (a high number of) emitted electrons is the most obvious one. Also the ongoing X-ray measurements should be continued to get complete information about the de-excitation processes. Recently a new experimental setup, based on the time-of-flight technique, was designed and constructed in our group for performing further collision studies between HCI and 2D materials. In the near future an electron statistic detector system will be added to this time of flight setup for enabling the measurement of emitted electrons in coincidence with the transmitted projectiles. Besides performing further studies with CNMs and SLG, investigations of other 2D materials with different electronic properties, e.g. the semiconductor MoS_2 and the insulator h-BN, might yield further insights on the complex de-excitation processes. Moreover, investigations of bi- and trilayer graphene should be continued. The first STEM measurements of purchased bi- and trilayer graphene from the manufacturer Graphenea are shown in fig. 6.1b,c with a sufficient quality. However, also these samples are contaminated with hydrocarbon adsorbates and probably also with PMMA, which is used during the transfer process. First transmission measurements show that the charge distribution of bi- and trilayer graphene lies between those of SLG and CNM (see fig. 6.1d,e).
Another future direction, which is motivated by applications as nanosieves [225] or for DNA sequencing [226], is to investigate nanostructuring of and pore formation in graphene. The irradiation of CNMs with HCIs has shown the formation of nanoholes which pore diameter can be tuned by the potential energy of the ions. In comparison to these results the irradiation of freestanding SLG so far has shown no pore formation after HCI irradiation. Since previous investigations with HOPG show that ion induced surface defects can be made visible as pits after thermal annealing [116], we recently started to apply this method also for freestanding SLG. Further irradiation, etching and STEM measurement periods are planned within the next months.

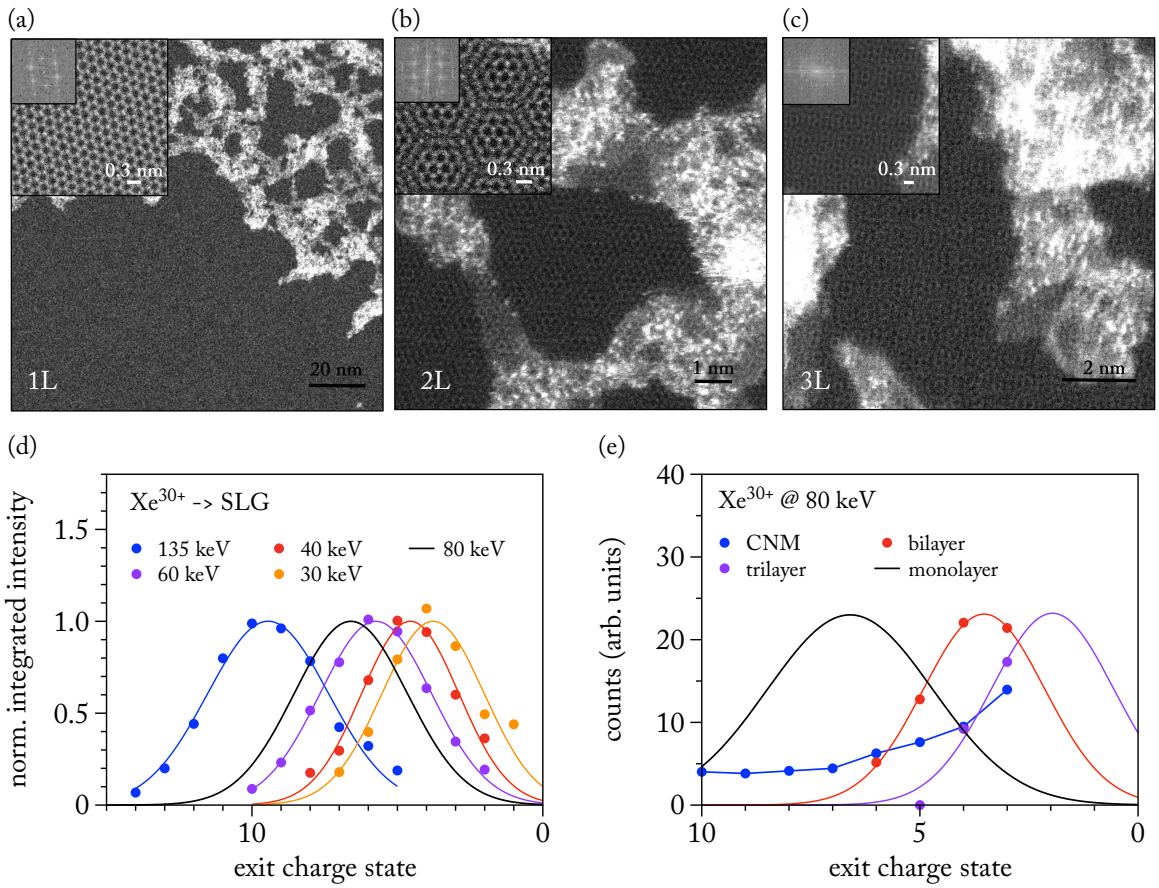

Figure 6.1: Mono-, bi- and trilayer graphene
TEM measurements of single layer (a), double layer (b) and trilayer graphene (c). The insets show atomic resolution and diffraction images. Bi- and trilayer graphene show Moiré patterns due to twisted graphene layers lying on top of each other. (d) Exit charge state distribution for Xe ions after transmission through SLG.
(e) Exit charge state distribution for Xe ions for a fixed kinetic energy after transmitted through CNM, SLG, bi- and trilayer graphene. The curve for SLG at $E_{\mathrm{kin}} = 80\,\mathrm{keV}$ is interpolated from the data shown in (d).

Bibliography

[1] D. Fink and L. T. Chadderton. *Ion–solid interactions: current status, new perspectives*. Radiation Effects & Defects in Solids **160**, 67 (2005).

[2] N. Bohr. *XXXVII. On the constitution of atoms and molecules*. The London, Edinburgh, and Dublin Philosophical Magazine and Journal of Science **26**, 476 (1913).

[3] N. Bohr. *LXXIII. On the constitution of atoms and molecules*. The London, Edinburgh, and Dublin Philosophical Magazine and Journal of Science **26**, 857 (1913).

[4] E. Rutherford. *LXXIX. The scattering of α and β particles by matter and the structure of the atom*. The London, Edinburgh, and Dublin Philosophical Magazine and Journal of Science **21**, 669 (1911).

[5] C. Davisson and L. H. Germer. *Diffraction of electrons by a crystal of nickel*. Physical Review **30**, 705 (1927).

[6] P. Bryant. *A brief history and review of accelerators*. CERN EUROPEAN ORGANIZATION FOR NUCLEAR RESEARCH-REPORTS-CERN pp. 1–1 (1994).

[7] O. Firsov. *A qualitative interpretation of the mean electron excitation energy in atomic collisions*. Zhur. Eksptl'. i Teoret. Fiz. **36**, 1517 (1959).

[8] U. Littmark and P. Sigmund. *Momentum deposition by heavy-ion bombardment and an application to sputtering*. Journal of Physics D: Applied Physics **8**, 241 (1975).

[9] P. Sigmund. *Mechanisms and theory of physical sputtering by particle impact*. Nuclear Instruments and Methods in Physics Research Section B: Beam Interactions with Materials and Atoms **27**, 1 (1987).

[10] U. Littmark and J. Ziegler. *Ranges of energetic ions in matter*. Physical Review A **23**, 64 (1981).

[11] F. Aumayr, S. Facsko, A. S. El-Said, C. Trautmann, and M. Schleberger. *Single Ion Induced Surface Nanostructures: A Comparison between Slow Highly Charged and Swift Heavy Ions*. Journal of Physics: Condensed Matter **23**, 393001 (2011).

[12] B. Wolf (Editor). *Handbook of Ion Sources*. CRC Press, Boca Raton, New York, London, Tokyo (1995).

[13] F. Aumayr and H. Winter. *Potential electron emission from metal and insulator surfaces*. In *Springer Tracts in Modern Physics: Slow Heavy-Particle Induced Electron Emission from Solid Surfaces*, vol. 225, pp. 79–112. Springer (2007).

[14] G. Hayderer, S. Cernusca, M. Schmid, P. Varga, H. Winter, F. Aumayr, D. Niemann, V. Hoffmann, N. Stolterfoht, C. Lemell *et al.* *Kinetically assisted potential sputtering of insulators by highly charged ions*. Physical Review Letters **86**, 3530 (2001).

[15] F. Aumayr and H. Winter. *Potential sputtering*. Philosophical Transactions of the Royal Society of London A: Mathematical, Physical and Engineering Sciences **362**, 77 (2004).

[16] F. Aumayr and H. Winter. *Slow Highly Charged Ions-A New Tool For Surface Nanostructuring?* e-Journal of Surface Science and Nanotechnology **1**, 171 (2003).

[17] F. Aumayr, A. S. El-Said, and W. Meissl. *Nano-sized Surface Modifications Induced by the Impact of Slow Highly Charged Ions - A First Review*. Nuclear Instruments and Methods in Physics Research Section B-Beam Interactions with Materials and Atoms **266**, 2729 (2008).

[18] H. Winter and F. Aumayr. *Hollow atoms*. Journal of Physics B: Atomic, Molecular and Optical Physics **32**, R39 (1999).

[19] A. Arnau, F. Aumayr, P. Echenique, M. Grether, W. Heiland, J. Limburg, R. Morgenstern, P. Roncin, S. Schippers, and R. Schuch. *Interaction of slow multicharged ions with solid surfaces*. Surface Science Reports **27**, 113 (1997).

[20] T. Schenkel, M. A. Briere, A. V. Barnes, A. V. Hamza, K. Bethge, H. Schmidt-Böcking, and D. H. Schneider. *Charge state dependent energy loss of slow heavy ions in solids*. Physical Review Letters **79**, 2030 2033 (1997).

[21] S. Winecki, C. L. Cocke, D. Fry, and M. P. Stöckli. *Neutralization and equilibration of highly charged argon ions at grazing incidence on a graphite surface*. Physical Review A **53**, 4228 (1996).

[22] R. A. Wilhelm, E. Gruber, R. Ritter, R. Heller, S. Facsko, and F. Aumayr. *Charge exchange and energy loss of slow highly charged ions in 1 nm thick carbon nanomembranes*. Physical Review Letters **112**, 153201 (2014).

[23] R. A. Wilhelm, E. Gruber, V. Smejkal, S. Facsko, and F. Aumayr. *Charge-state-dependent energy loss of slow ions. I. Experimental results on the transmission of highly charged ions*. Physical Review A **93**, 052708 (2016).

[24] E. Gruber, R. A. Wilhelm, R. Pétuya, V. Smejkal, R. Kozubek, A. Hierzenberger, B. C. Bayer, I. Aldazabal, A. K. Kazansky, F. Libisch, A. V. Krasheninnikov, M. Schleberger, S. Facsko, A. Borisov, A. Arnau, and F. Aumayr. *Ultrafast electronic response of graphene to a strong and localized electric field*. Nature Communications **7**, 13948 (2016).

[25] E. Gruber, P. Salou, L. Bergen, M. El Kharrazi, E. Lattouf, C. Grygiel, Y. Wang, A. Benyagoub, D. Levavasseur, J. Rangama *et al. Swift heavy ion irradiation of CaF_2–from grooves to hillocks in a single ion track*. Journal of Physics: Condensed Matter **28**, 405001 (2016).

[26] R. A. Wilhelm, E. Gruber, R. Ritter, R. Heller, A. Beyer, A. Turchanin, N. Klingner, R. Hübner, M. Stöger-Pollach, H. Vieker, G. Hlawacek, A. Gölzhäuser, S. Facsko, and F. Aumayr. *Threshold and efficiency for perforation of 1 nm thick carbon nanomembranes with slow highly charged ions*. 2D Materials **2**, 035009 (2015).

[27] E. Gruber, R. A. Wilhelm, V. Smejkal, R. Heller, S. Facsko, and F. Aumayr. *Interaction of highly charged ions with carbon nano membranes*. Journal of Physics: Conference Series **635**, 012027 (2015).

[28] H. D. Hagstrum. *PR I: Auger Ejection of Electrons from Tungsten by Noble Gas Ions*. Physical Review **96**, 325 (1954).

[29] H. D. Hagstrum. *PR II: Theory of Auger Ejection of Electrons from Metals by Ions*. Physical Review **96**, 336 (1954).

[30] U. Arifov, L. Kishinevskii, E. Mukhamadiev, and E. Parilis. *Auger neutralization of highly charged ions at the surface of a metal*. Soviet Physics Technical Physics **18**, 118 (1973).

[31] D. Hasselkamp. *Kinetic electron emission from solid surfaces under ion bombardment*. In *Particle Induced Electron Emission II*, pp. 1–95. Springer (1992).

[32] E. Donets. *The electron beam method of production of highly charged ions and its applications*. Physica Scripta **1983**, 11 (1983).

[33] J. P. Briand, L. de Billy, P. Charles, S. Essabaa, P. Briand, R. Geller, J. P. Desclaux, S. Bliman, and C. Ristori. *Production of Hollow Atoms by the Excitation of Highly Charged Ions in Interaction with a Metallic Surface*. Physical Review Letters **65**, 159 (1990).

[34] H. Andrä and J. Briggs. *NATO Summer School on Fundamental Processes of Atomic Dynamics* (1988).

[35] N. Vaeck and J. Hansen. *Auger decay of hollow nitrogen atoms*. Journal of Physics B: Atomic, Molecular and Optical Physics **28**, 3523 (1995).

[36] P. Apell. *Multiply charged ion-solid interaction*. Nuclear Instruments and Methods in Physics Research Section B: Beam Interactions with Materials and Atoms **23**, 242 (1987).

[37] K. Snowdon. *Charge-transfer and electron emission in the slow ($v<v_0$) multicharged-ion-surface interaction*. Nuclear Instruments and Methods in Physics Research Section B: Beam Interactions with Materials and Atoms **34**, 309 (1988).

[38] H. Ryufuku, K. Sasaki, and T. Watanabe. *Oscillatory behavior of charge transfer cross sections as a function of the charge of projectiles in low-energy collisions*. Physical Review A **21**, 745 (1980).

[39] A. Bárány, G. Astner, H. Cederquist, H. Danared, S. Huldt, P. Hvelplund, A. Johnson, H. Knudsen, L. Liljeby, and K.-G. Rensfelt. *Absolute cross sections for multi-electron processes in low energy Arq+ Ar collisions: comparison with theory*. Nuclear Instruments and Methods in Physics Research Section B: Beam Interactions with Materials and Atoms **9**, 397 (1985).

[40] A. Niehaus. *A classical model for multiple-electron capture in slow collisions of highly charged ions with atoms*. Journal of Physics B: Atomic and Molecular Physics **19**, 2925 (1986).

[41] J. Burgdörfer, P. Lerner, and F. W. Meyer. *Classical Over-the -Barrier Model*. Physical Review A **44**, 5674 (1991).

[42] J. Burgdörfer and F. Meyer. *Image acceleration of multiply charged ions by metallic surfaces*. Physical Review A **47**, R20 (1993).

[43] A. Bárány and C. J. Setterlind. *Interaction of slow highly charged ions with atoms, clusters and solids: a unified classical barrier approach*. Nuclear Instruments and Methods in Physics Research Section B: Beam Interactions with Materials and Atoms **98**, 184 (1995).

[44] L. Hägg, C. O. Reinhold, and J. Burgdörfer. *Above-surface neutralization of slow highly charged ions in front of ionic crystals*. Physical Review A **55**, 2097 (1997).

[45] J. Burgdörfer, C. Reinhold, and F. Meyer. *Fast neutralization of highly charged ions in grazing incidence collisions with surfaces*. Nuclear Instruments and Methods in Physics Research Section B: Beam Interactions with Materials and Atoms **98**, 415 (1995).

[46] U. Fano and W. Lichten. *Interpretation of Ar+-Ar Collisions at 50 KeV*. Physical Review Letters **14**, 627 (1965).

[47] A. Arnau, R. Köhrbrück, M. Grether, A. Spieler, and N. Stolterfoht. *Molecular-orbital model for slow hollow atoms colliding with atoms in a solid*. Physical Review A **51**, R3399 (1995).

[48] N. Stolterfoht, A. Arnau, M. Grether, R. Köhrbrück, A. Spieler, R. Page, A. Saal, J. Thomaschewski, and J. Bleck-Neuhaus. *Multiple-cascade model for the filling of hollow Ne atoms moving below an Al surface*. Physical Review A **52**, 445 (1995).

[49] N. Vaeck and J. Hansen. *Lifetimes of multiply-excited states in nitrogen*. Journal of Physics B: Atomic, Molecular and Optical Physics **24**, 469 (1991).

[50] N. Vaeck and J. E. Hansen. *Calculations of autoionization rates for double-Auger decay of multiply-excited states in nitrogen*. Journal of Physics B: Atomic, Molecular and Optical Physics **25**, 3613 (1992).

[51] L. Cederbaum, J. Zobeley, and F. Tarantelli. *Giant intermolecular decay and fragmentation of clusters*. Physical Review Letters **79**, 4778 (1997).

[52] R. Santra, J. Zobeley, L. S. Cederbaum, and N. Moiseyev. *Interatomic Coulombic decay in van der Waals clusters and impact of nuclear motion*. Physical Review Letters **85**, 4490 (2000).

[53] J. Zobeley, R. Santra, and L. S. Cederbaum. *Electronic decay in weakly bound heteroclusters: Energy transfer versus electron transfer*. The Journal of Chemical Physics **115**, 5076 (2001).

[54] T. Jahnke. *Interatomic and intermolecular Coulombic decay: the coming of age story*. Journal of Physics B: Atomic, Molecular and Optical Physics **48**, 082001 (2015).

[55] R. Santra, J. Zobeley, and L. S. Cederbaum. *Electronic decay of valence holes in clusters and condensed matter*. Physical Review B **64**, 245104 (2001).

[56] V. Averbukh, I. B. Müller, and L. S. Cederbaum. *Mechanism of interatomic Coulombic decay in clusters*. Physical Review Letters **93**, 263002 (2004).

[57] C. Lemell, A. S. El-Said, W. Meissl, I. C. Gebeshuber, C. Trautmann, M. Toulemonde, J. Burgdörfer, and F. Aumayr. *On the nano-hillock formation induced by slow highly charged ions on insulator surfaces*. Solid-State Electronics **51**, 1398 (2007).

[58] G. Wachter, K. Tökési, G. Betz, C. Lemell, and J. Burgdörfer. *Modelling surface restructuring by slow highly charged ions*. Nuclear Instruments and Methods in Physics Research Section B: Beam Interactions with Materials and Atoms **317**, 149 (2013).

[59] R. Ritter, G. Kowarik, W. Meissl, A. S. El-Said, L. Maunoury, H. Lebius, C. Dufour, M. Toulemonde, and F. Aumayr. *Nanostructure Formation due to Impact of Highly Charged Ions on Mica*. Vacuum **84**, 1062 (2010).

[60] R. Heller, S. Facsko, R. Wilhelm, and W. Möller. *Defect mediated desorption of the KBr (001) surface induced by single highly charged ion impact*. Physical Review Letters **101**, 096102 (2008).

[61] A. S. El-Said, R. A. Wilhelm, R. Heller, S. Facsko, C. Lemell, G. Wachter, J. Burgdörfer, R. Ritter, and F. Aumayr. *Phase Diagram for Nanostructuring CaF_2 Surfaces by Slow Highly Charged Ions*. Physical Review Letters **109**, 117602 (2012).

[62] A. S. El-Said, R. Heller, W. Meissl, R. Ritter, S. Facsko, C. Lemell, B. Solleder, I. C. Gebeshuber, G. Betz, M. Toulemonde, W. Möller, J. Burgdörfer, and F. Aumayr. *Creation of Nanohillocks on CaF_2 Surfaces by Single Slow Highly Charged Ions*. Physical Review Letters **100**, 237601 (2008).

[63] A. S. El-Said, W. Meissl, M. C. Simon, J. R. Crespo Lopez-Urrutia, C. Lemell, J. Burgdörfer, I. C. Gebeshuber, H. P. Winter, J. Ullrich, C. Trautmann, M. Toulemonde, and F. Aumayr.

Potential energy threshold for nano-hillock formation by impact of slow highly charged ions on a CaF_2 (111) surface. Nuclear Instruments and Methods in Physics Research Section B-Beam Interactions with Materials and Atoms **258**, 167 (2007).

[64] J. F. Ziegler, J. P. Biersack, and M. D. Ziegler. *The Stopping and Range of Ions in Matter*. SRIM Co. (2008).

[65] R. A. Wilhelm. *Wechselwirkung langsamer hochgeladener Ionen mit Ionenoberflächen und ultradünnen Kohlenstoffmembranen*. PhD thesis, Technische Universität Dresden, unpublished (2014).

[66] L. H. Thomas. *The calculation of atomic fields*. Mathematical Proceedings of the Cambridge Philosophical Society **23**, 542 (1927).

[67] E. Fermi. *A Statistical Method for Determining some Properties of the Atoms and its Application to the Theory of the Periodic Table of Elements*. Z. Phys **48**, 73 (1928).

[68] O. Firsov. *Calculation of atomic interaction potentials*. Zh. Eksp. Teor. Fiz **33**, 696 (1957).

[69] J. Lindhard, V. Nielsen, and M. Scharff. *Approximation method in classical scattering by screened Coulomb fields*. Kgl. Dan. Vidensk. Selsk., Mat.-Fys. Medd. **36**, 31 (1968).

[70] J. F. Ziegler and J. P. Biersack. *The stopping and range of ions in matter*. In *Treatise on Heavy-Ion Science*, pp. 93–129. Springer (1985).

[71] P. Sigmund. *Particle Penetration and Radiation Effects, General Aspects and Stopping of Swift Point Charges*, vol. 151. Springer Berlin Heidelberg (2006).

[72] N. Bohr. *The penetration of atomic particles through matter*. Medd. Dan. Vid. Selsk. **18**, 1 (1948).

[73] J. Lindhard and M. Scharff. *Energy dissipation by ions in the keV region*. Physical Review **124**, 128 (1961).

[74] J. F. Ziegler. *Ion Implantation Science and Technology*. Elsevier (2012).

[75] W. Brandt and M. Kitagawa. *Effective stopping-power charges of swift ions in condensed matter*. Physical Review B **25**, 5631 (1982).

[76] P. Sigmund. *Charge-dependent electronic stopping of swift nonrelativistic heavy ions*. Physical Review A **56**, 3781 (1997).

[77] G. Schiwietz and P. Grande. *A unitary convolution approximation for the impact-parameter dependent electronic energy loss*. Nuclear Instruments and Methods in Physics Research Section B: Beam Interactions with Materials and Atoms **153**, 1 (1999).

[78] J. Biersack. *The effect of high charge states on the stopping and ranges of ions in solids*. Nuclear Instruments and Methods in Physics Research Section B: Beam Interactions with Materials and Atoms **80**, 12 (1993).

[79] J. Juaristi, A. Arnau, P. Echenique, C. Auth, and H. Winter. *Charge state dependence of the energy loss of slow ions in metals*. Physical Review Letters **82**, 1048 (1999).

[80] R. A. Wilhelm and W. Möller. *Charge-state-dependent energy loss of slow ions. II. Statistical atom model*. Physical Review A **93**, 052709 (2016).

[81] J. Zhang, M. Lang, R. C. Ewing, R. Devanathan, W. J. Weber, and M. Toulemonde. *Nanoscale phase transitions under extreme conditions within an ion track*. Journal of Materials Research **25**, 1344 (2010).

[82] C. Dufour and M. Toulemonde. *Models for the Description of Track Formation*. In *Ion Beam Modification of Solids*, pp. 63–104. Springer (2016).

[83] R. Fleischer, P. Price, and R. Walker. *Ion explosion spike mechanism for formation of charged-particle tracks in solids*. Journal of Applied Physics **36**, 3645 (1965).

[84] A. Dunlop and D. Lesueur. *Damage creation via electronic excitations in metallic targets part I: Experimental results*. Radiation Effects and Defects in Solids **126**, 123 (1993).

[85] D. Lesueur and A. Dunlop. *Damage creation via electronic excitations in metallic targets part II: A theoretical model*. Radiation Effects and Defects in Solids **126**, 163 (1993).

[86] A. Dunlop, P. Legrand, D. Lesueur, N. Lorenzelli, J. Morillo, A. Barbu, and S. Bouffard. *Phonon soft modes and damage production by high electronic excitations in pure metals*. EPL (Europhysics Letters) **15**, 765 (1991).

[87] J. Phillips. *Ionicity of the chemical bond in crystals*. Reviews of Modern Physics **42**, 317 (1970).

[88] M. Combescot, J. Bok, and C. B. à la Guillaume. *Instability at the melting threshold of laser-irradiated silicon*. Physical Review B **29**, 6393 (1984).

[89] R. Bell, M. Toulemonde, and P. Siffert. *Calculated temperature distribution during laser annealing in silicon and cadmium telluride*. Applied Physics **19**, 313 (1979).

[90] P. Stampfli and K. Bennemann. *Time dependence of the laser-induced femtosecond lattice instability of Si and GaAs: Role of longitudinal optical distortions*. Physical Review B **49**, 7299 (1994).

[91] N. Itoh. *Self-trapped exciton model of heavy-ion track registration*. Nuclear Instruments and Methods in Physics Research Section B: Beam Interactions with Materials and Atoms **116**, 33 (1996).

[92] G. Szenes. *General features of latent track formation in magnetic insulators irradiated with swift heavy ions*. Physical Review B **51**, 8026 (1995).

[93] G. Szenes. *Ion-velocity-dependent track formation in yttrium iron garnet: A thermal-spike analysis*. Physical Review B **52**, 6154 (1995).

[94] B. Canut and S. Ramos. *The concept of effective electronic stopping power for modelling the damage cross-section in refractory oxides irradiated by GeV ions or MeV clusters*. Radiation Effects and Defects in Solids **145**, 1 (1998).

[95] M. Toulemonde, C. Dufour, A. Meftah, and E. Paumier. *Transient thermal processes in heavy ion irradiation of crystalline inorganic insulators*. Nuclear Instruments and Methods in Physics Research Section B: Beam Interactions with Materials and Atoms **166**, 903 (2000).

[96] C. Trautmann, M. Toulemonde, C. Dufour, and E. Paumier. *Effect of radial energy distribution on ion track etching in amorphous metallic* $Fe_{81}B_{13.5}Si_{3.5}C_2$. Nuclear Instruments and Methods in Physics Research Section B: Beam Interactions with Materials and Atoms **108**, 94 (1996).

[97] A. Meftah, J. Costantini, M. Djebara, N. Khalfaoui, J. Stoquert, F. Studer, and M. Toulemonde. *Thermal spike model applied to the irradiated yttrium iron garnet: Mean diffusion length of the energy deposited on the electrons*. Nuclear Instruments and Methods in Physics Research Section B: Beam Interactions with Materials and Atoms **122**, 470 (1997).

[98] Z. Wang, C. Dufour, E. Paumier, and M. Toulemonde. *The Se sensitivity of metals under swift-heavy-ion irradiation: a transient thermal process*. Journal of Physics: Condensed Matter **6**, 6733 (1994).

[99] S.-N. Luo, T. J. Ahrens, T. Çağın, A. Strachan, W. A. Goddard III, and D. C. Swift. *Maximum superheating and undercooling: Systematics, molecular dynamics simulations, and dynamic experiments*. Physical Review B **68**, 134206 (2003).

[100] S. Bliani, R. Geller, W. Hess, B. Jacquot, and C. Jacquot. *A high intensity ECR stripped ion source*. IEEE Transactions on Nuclear Science **19**, 200 (1972).

[101] E. Galutschek, R. Trassl, E. Salzborn, F. Aumayr, and H. Winter. *Compact 14.5 GHz all-permanent magnet ECRIS for experiments with slow multicharged ions*. Journal of Physics: Conference Series **58**, 395 (2007).

[102] V. Bernigaud, O. Kamalou, A. Lawicki, M. Capron, R. Maisonny, B. Manil, L. Maunoury, J. Rangama, P. Rousseau, and J. Chesnel. *ARIBE: a Low Energy Ion Beam Facility in Caen*. Publications de l'Observatoire Astronomique de Beograd **84**, 83 (2008).

[103] E. Akcöltekin, T. Peters, R. Meyer, A. Duvenbeck, M. Klusmann, I. Monnet, H. Lebius, and M. Schleberger. *Creation of multiple nanodots by single ions*. Nature Nanotechnology **2**, 290 (2007).

[104] G. Binnig, C. F. Quate, and C. Gerber. *Atomic force microscope*. Physical Review Letters **56**, 930 (1986).

[105] M. Knoll and E. Ruska. *Das Elektronenmikroskop*. Zeitschrift für Physik **78**, 318 (1932).

[106] E. Ruska. *The development of the electron microscope and of electron microscopy*. Reviews of Modern Physics **59**, 627 (1987).

[107] http://barrett group.mcgill.ca/tutorials/nanotechnology/nano02.htm .

[108] M. Toulemonde, C. Trautmann, E. Balanzat, K. Hjort, and A. Weidinger. *Track formation and fabrication of nanostructures with MeV-ion beams*. Nuclear Instruments and Methods in Physics Research Section B: Beam Interactions with Materials and Atoms **216**, 1 (2004).

[109] N. Khalfaoui, C. C. Rotaru, S. Bouffard, M. Toulemonde, J. P. Stoquert, F. Haas, C. Trautmann, J. Jensen, and A. Dunlop. *Characterization of swift heavy ion tracks in CaF_2 by*

scanning force and transmission electron microscopy. Nuclear Instruments and Methods in Physics Research Section B: Beam Interactions with Materials and Atoms **240**, 819 (2005).

[110] R. Papaleo, M. Silva, R. Leal, P. Grande, M. Roth, B. Schattat, and G. Schiwietz. *Direct Evidence for Projectile Charge-State Dependent Crater Formation Due to Fast Ions*. Physical Review Letters **101**, 167601 (2008).

[111] C. Trautmann, K. Schwartz, J. Costantini, T. Steckenreiter, and M. Toulemonde. *Radiation defects in lithium fluoride induced by heavy ions*. Nuclear Instruments and Methods in Physics Research Section B: Beam Interactions with Materials and Atoms **146**, 367 (1998).

[112] M. Tona, Y. Fujita, C. Yamada, and S. Ohtani. *Electronic Interaction of Individual Slow Highly Charged Ions with TiO_2(110)*. Physical Review B **77**, 155427 (2008).

[113] P. Markiewicz and M. C. Goh. *Atomic force microscopy probe tip visualization and improvement of images using a simple deconvolution procedure*. Langmuir **10**, 5 (1994).

[114] R. Ritter. *Nanostructures formed on surfaces due to the impact of slow highly charged ions*. PhD thesis, TU Wien, unpublished (2013).

[115] A. S. El-Said, W. Meissl, M. C. Simon, J. R. C. Lopez-Urrutia, I. C. Gebeshuber, M. Lang, H. Winter, J. Ullrich, and F. Aumayr. *Surface nanostructures induced by slow highly charged ions on CaF_2 single crystals*. Nuclear Instruments and Methods in Physics Research Section B-Beam Interactions with Materials and Atoms **256**, 346 (2007).

[116] R. Ritter, R. A. Wilhelm, M. Stöger-Pollach, R. Heller, A. Mücklich, U. Werner, H. Vieker, A. Beyer, S. Facsko, A. Gölzhäuser, and F. Aumayr. *Fabrication of nanopores in 1 nm thick carbon nanomembranes with slow highly charged ions*. Applied Physics Letters **102**, 063112 (2013).

[117] L. Bergen. *Atomic force microscope imaging of ion induced nanostructures on mica surfaces*. Project work, TU Wien, unpublished (2015).

[118] L. Bergen. *Nanostructuring of surfaces by swift heavy ion impacts under grazing incidence*. Master thesis, TU Wien, unpublished (2016).

[119] O. Ochedowski, O. Osmani, M. Schade, B. K. Bussmann, B. Ban d'Etat, H. Lebius, and M. Schleberger. *Graphitic nanostripes in silicon carbide surfaces created by swift heavy ion irradiation*. Nature Communications **5**, 3913 (2014).

[120] M. Karlusić, R. Kozubek, H. Lebius, B. Ban d'Etat, R. A. Wilhelm, M. Buljan, Z. Siketić, F. Scholz, T. Meisch, M. Jakšić, S. Bernstorff, M. Schleberger, and B. Šantić. *Response of GaN to energetic ion irradiation: conditions for ion track formation*. Journal of Physics D: Applied Physics **48**, 325304 (2015).

[121] R. M. Papaleo, R. Thomaz, L. I. Gutierres, V. M. de Menezes, D. Severin, C. Trautmann, D. Tramontina, E. M. Bringa, and P. L. Grande. *Confinement effects of ion tracks in ultrathin polymer films*. Physical Review Letters **114**, 118302 (2015).

[122] T. Roll, M. Meier, S. Akcöltekin, M. Klusmann, H. Lebius, and M. Schleberger. *Conductive nanodots on the surface of irradiated CaF_2*. Physica Status Solidi - Rapid Research Letters **2**, 209 (2008).

[123] S. Akcöltekin, H. Bukowska, T. Peters, O. Osmani, I. Monnet, I. Alzaher, B. Ban d'Etat, H. Lebius, and M. Schleberger. *Unzipping and folding of graphene by swift heavy ions*. Applied Physics Letters **98**, 103103 (2011).

[124] O. Ochedowski, B. Kleine Bussmann, B. Ban d'Etat, H. Lebius, and M. Schleberger. *Manipulation of the graphene surface potential by ion irradiation*. Applied Physics Letters **102**, 153103 (2013).

[125] O. Ochedowski, O. Lehtinen, U. Kaiser, A. Turchanin, B. Ban d'Etat, H. Lebius, M. Karlušić, M. Jakšić, and M. Schleberger. *Nanostructuring graphene by dense electronic excitation*. Nanotechnology **26**, 465302 (2015).

[126] K. van Benthem, C. Elsasser, and R. H. French. *Bulk electronic structure of $SrTiO_3$: Experiment and theory*. Journal of Applied Physics **90**, 6156 (2001).

[127] A. Gentils, O. Copie, G. Herranz, F. Fortuna, M. Bibes, K. Bouzehouane, É. Jacquet, C. Carrétéro, M. Basletić, E. Tafra, A. Hamzić, and A. Barthélémy. *Point defect distribution in high-mobility conductive $SrTiO_3$ crystals*. Physical Review B **81** (2010).

[128] S. Jeon, F. J. Walker, C. A. Billman, R. A. McKee, and H. Hwang. *Electrical characteristics of epitaxially grown $SrTiO_3$ on silicon for metal-insulator-semiconductor gate dielectric applications*. IEEE Electron Device Letters **24**, 218 (2003).

[129] R. Li, Q. Tang, S. Yin, and T. Sato. *Plasma catalysis for CO_2 decomposition by using different dielectric materials*. Fuel Processing Technology **87**, 617 (2006).

[130] E. Akcöltekin, S. Akcöltekin, O. Osmani, A. Duvenbeck, H. Lebius, and M. Schleberger. *Swift heavy ion irradiation of $SrTiO_3$ under grazing incidence*. New Journal of Physics **10**, 053007 (2008).

[131] M. Karlusić, S. Akcöltekin, O. Osmani, I. Monnet, H. Lebius, M. Jaksić, and M. Schleberger. *Energy threshold for the creation of nanodots on $SrTiO_3$ by swift heavy ions*. New Journal of Physics **12**, 043009 (2010).

[132] F. Meinerzhagen, L. Breuer, H. Bukowska, M. Bender, D. Severin, M. Herder, H. Lebius, M. Schleberger, and A. Wucher. *A new setup for the investigation of swift heavy ion induced particle emission and surface modifications*. Review of Scientific Instruments **87**, 013903 (2016).

[133] T. Peters, C. Haake, J. Hopster, V. Sokolovsky, A. Wucher, and M. Schleberger. *HICS: Highly charged ion collisions with surfaces*. Nuclear Instruments and Methods in Physics Research Section B: Beam Interactions with Materials and Atoms **267**, 687 (2009).

[134] A. S. El-Said, R. A. Wilhelm, R. Heller, S. Facsko, C. Trautmann, and F. Aumayr. *Surface nanostructuring of $SrTiO_3$ single crystals by slow highly charged ions and swift heavy ions*. Nuclear Instruments and Methods in Physics Research Section B: Beam Interactions with Materials and Atoms **269**, 1234 (2011).

[135] O. Osmani, A. Duvenbeck, E. Akcöltekin, R. Meyer, H. Lebius, and M. Schleberger. *Calculation of electronic stopping power along glancing swift heavy ion tracks in perovskites using ab initio electron density data*. Journal of Physics: Condensed Matter **20**, 315001 (2008).

[136] N. N. Greenwood and A. Earnshaw. *Chemistry of the Elements* (1984).

[137] M. Grätzel and F. P. Rotzinger. *The influence of the crystal lattice structure on the conduction band energy of oxides of titanium (IV)*. Chemical Physics Letters **118**, 474 (1985).

[138] E. J. Mezey. *Pigments and reinforcing agents*. Wiley, New York (1966).

[139] U. Diebold. *The surface science of titanium dioxide*. Surface Science Reports **48**, 53 (2003).

[140] T. Fujino, M. Katayama, K. Inudzuka, T. Okuno, K. Oura, and T. Hirao. *Surface hydroxyl formation on vacuum-annealed TiO_2(110)*. Applied Physics Letters **79**, 2716 (2001).

[141] V. N. Popok, J. Jensen, S. Vučković, A. Mackova, and C. Trautmann. *Formation of surface nanostructures on rutile (TiO_2): comparative study of low-energy cluster ion and high-energy monoatomic ion impact*. Journal of Physics D: Applied Physics **42**, 205303 (2009).

[142] K. Awazu, X. Wang, M. Fujimaki, T. Komatsubara, T. Ikeda, and Y. Ohki. *Structure of latent tracks in rutile single crystal of titanium dioxide induced by swift heavy ions*. Journal of Applied Physics **100**, 044308 (2006).

[143] M. Thakurdesai, D. Kanjilal, and V. Bhattacharyya. *Formation of nano-hillocks by impact of swift heavy ions on thin films of TiO_2*. Applied Surface Science **254**, 4695 (2008).

[144] M. Karlusić, S. Bernstorff, Z. Siketić, B. Šantić, I. Bogdanovi'c-Radović, M. Jakšić, M. Schleberger, and M. Buljan. *Formation of swift heavy ion tracks on a rutile TiO_2(001) surface*. Journal of Applied Crystallography **49**, 1704 (2016).

[145] S. Akcöltekin, E. Akcöltekin, T. Roll, H. Lebius, and M. Schleberger. *Patterning of insulating surfaces by electronic excitation*. Nuclear Instruments and Methods in Physics Research Section B: Beam Interactions with Materials and Atoms **267**, 1386 (2009).

[146] M. Lang, U. A. Glasmacher, B. Moine, R. Neumann, and G. A. Wagner. *Etch-pit morphology of tracks caused by swift heavy ions in natural dark mica*. Nuclear Instruments and Methods in Physics Research Section B: Beam Interactions with Materials and Atoms **218**, 466 (2004).

[147] D. Schneider, M. A. Briere, M. W. Clark, J. W. Mcdonald, J. P. Biersack, and W. Siekhaus. *Atomic displacement due to the electrostatic potential energy of very highly charged ions at solid surfaces*. Surface Science **294**, 403 (1993).

[148] C. Ruehlicke, M. A. Briere, and D. H. Schneider. *AFM studies of a new type of radiation defect on mica surfaces caused by highly charged ion impact*. Nuclear Instruments and Methods in Physics Research Section B-Beam Interactions with Materials and Atoms **99**, 528 (1995).

[149] D. C. Parks. *Nanometer-size surface features produced by single, low energy, highly charged ions*. Journal of Vacuum Science & Technology B: Microelectronics and Nanometer Structures **13**, 941 (1995).

[150] D. Parks. *Non-kinetic damage on insulating materials by highly charged ion bombardment*. Nuclear Instruments and Methods in Physics Research Section B-Beam Interactions with Materials and Atoms **134**, 46 (1998).

[151] M. Dobeli, F. Ames, C. R. Musil, L. Scandella, M. Suter, and H. A. Synal. *Surface tracks by MeV C_{60} impacts on mica and PMMA*. Nuclear Instruments and Methods in Physics Research Section B-Beam Interactions with Materials and Atoms **143**, 503 (1998).

[152] D. B. Daya, A. Hallén, J. Eriksson, J. Kopniczky, R. Papaléo, C. Reimann, P. Håkansson, B. Sundqvist, A. Brunelle, S. Della-Negra, and B. Y. Le. *Radiation damage features on mica and L-valine probed by scanning force microscopy*. Nuclear Instruments and Methods in Physics Research Section B: Beam Interactions with Materials and Atoms **106**, 38 (1995).

[153] D. B. Daya, C. Reimann, P. Håkansson, B. Sundqvist, A. Brunelle, S. Della-Nagra, and Y. Le Beyec. *Crater formation due to grazing incidence C_{60} cluster ion impacts on mica: a tapping-mode scanning force microscopy study*. Nuclear Instruments and Methods in Physics Research Section B: Beam Interactions with Materials and Atoms **124** (1997).

[154] T. Hagen, S. Grafstrom, J. Ackermann, R. Neumann, C. Trautmann, J. Vetter, and N. Angert. *Friction force microscopy of heavy ion irradiated mica*. Journal of Vacuum Science & Technology B: Microelectronics and Nanometer Structures **12**, 1555 (1994).

[155] F. Thibaudau, J. Cousty, E. Balanzat, and S. Bouffard. *Atomic-force-microscopy observations of tracks induced by swift Kr ions in mica*. Physical Review Letters **67**, 1582 (1991).

[156] J. Ackermann. *Ion track diameters in mica studied with scanning force microscopy*. Nuclear Instruments and Methods in Physics Research Section B-Beam Interactions with Materials and Atoms **107**, 181 (1996).

[157] D. B. Daya, C. Reimann, A. Hallén, B. Sundqvist, and P. Håkansson. *Latent (sub-surface) tracks in mica studied by tapping mode scanning force microscopy*. Nuclear Instruments and Methods in Physics Research Section B: Beam Interactions with Materials and Atoms **111** (1996).

[158] T. Smith III, J. M. Phillips, W. Augustyniak, and P. Stiles. *Fabrication of metal-epitaxial insulator-semiconductor field-effect transistors using molecular beam epitaxy of CaF_2 on Si*. Applied Physics Letters **45**, 907 (1984).

[159] L. Schowalter and R. Fathauer. *Molecular beam epitaxy growth and applications of epitaxial fluoride films*. Journal of Vacuum Science & Technology A **4**, 1026 (1986).

[160] C. Müller, M. Cranney, A. S. El-Said, N. Ishikawa, A. Iwase, M. Lang, and R. Neumann. *Ion tracks on LiF and CaF_2 single crystals characterized by scanning force microscopy*. Nuclear

Instruments and Methods in Physics Research Section B: Beam Interactions with Materials and Atoms **191**, 246 (2002).

[161] N. Khalfaoui, M. Görlich, C. Müller, M. Schleberger, and H. Lebius. *Latent tracks in CaF_2 studied with atomic force microscopy in air and in vacuum*. Nuclear Instruments and Methods in Physics Research Section B: Beam Interactions with Materials and Atoms **245**, 246 (2006).

[162] Y. Y. Wang, C. Grygiel, C. Dufour, J. R. Sun, Z. G. Wang, Y. T. Zhao, G. Q. Xiao, R. Cheng, X. M. Zhou, J. R. Ren, S. D. Liu, Y. Lei, Y. B. Sun, R. Ritter, E. Gruber, A. Cassimi, I. Monnet, S. Bouffard, F. Aumayr, and M. Toulemonde. *Energy deposition by heavy ions: additivity of kinetic and potential energy contributions in hillock formation on CaF_2*. Scientific Reports **4**, 5742 (2014).

[163] M. Boccanfuso, A. Benyagoub, K. Schwartz, C. Trautmann, and M. Toulemonde. *Study of the damage produced in CaF_2 by swift heavy ion irradiation*. Nuclear Instruments and Methods in Physics Research Section B: Beam Interactions with Materials and Atoms **191**, 301 (2002).

[164] S. Facsko, W. Meissl, R. Heller, R. Wilhelm, A. S. El-Said, G. Kowarik, R. Ritter, and F. Aumayr. *Nanostructures induced by highly charged ions on CaF_2 and KBr*. Journal of Physics: Conference Series **194**, 012060 (2009).

[165] I. V. Vorobyova and J. Kopniczky. *MeV-atomic-ion-induced tracks on the surface of CaF_2 single crystal*. Nuclear Instruments and Methods in Physics Research Section B: Beam Interactions with Materials and Atoms **237**, 593 (2005).

[166] S. Akcöltekin, T. Roll, E. Akcöltekin, M. Klusmann, H. Lebius, and M. Schleberger. *Enhanced susceptibility of CaF_2(111) to adsorption due to ion irradiation*. Nuclear Instruments and Methods in Physics Research Section B: Beam Interactions with Materials and Atoms **267**, 683 (2009).

[167] J. Jensen, A. Dunlop, and S. Della-Negra. *Track induced in CaF_2 by MeV cluster irradiation*. Nuclear Instruments and Methods in Physics Research Section B: Beam Interactions with Materials and Atoms **141**, 753 (1998).

[168] R. Bennewitz, C. Günther, M. Reichling, E. Matthias, S. Vijayalakshmi, A. V. Barnes, and N. H. Tolk. *Size evolution of low energy electron generated Ca colloids in CaF_2*. Applied Physics Letters **66**, 320 (1995).

[169] R. Bennewitz, D. Smith, and M. Reichling. *Bulk and surface processes in low-energy-electron-induced decomposition of CaF_2*. Physical Review B **59**, 8237 (1999).

[170] A. Lehmann, G. Konig, and K. H. Rieder. *Water adsorption on perfect CaF_2(111) studied with He scattering: Experimental evidence for ordering of nanoclusters*. Physical Review Letters **73**, 3125 (1994).

[171] G. Koster, B. L. Kropman, G. J. H. M. Rijnders, D. H. A. Blank, and H. Rogalla. *Quasi-ideal strontium titanate crystal surfaces through formation of strontium hydroxide*. Applied Physics Letters **73**, 2920 (1998).

[172] A. S. El-Said, R. A. Wilhelm, R. Heller, M. Sorokin, S. Facsko, and F. Aumayr. *Tuning the Fabrication of Nanostructures by Low-Energy Highly Charged Ions*. Physical Review Letters **117**, 126101 (2016).

[173] M. Toulemonde, W. Assmann, C. Dufour, A. Meftah, and C. Trautmann. *Nanometric transformation of the matter by short and intense electronic excitation: Experimental data versus inelastic thermal spike model*. Nuclear Instruments and Methods in Physics Research Section B: Beam Interactions with Materials and Atoms **277**, 28 (2012).

[174] H.-D. Betz. *Charge States and Charge-Changing Cross Sections of Fast Heavy Ions Penetrating Through Gaseous and Solid Media*. Reviews of Modern Physics **44**, 465 (1972).

[175] R. Herrmann, C. L. Cocke, J. Ullrich, S. Hagmann, M. Stöckli, and H. Schmidt-Böcking. *Charge-state equilibration length of a highly charged ion inside a carbon solid*. Physical Review A **50**, 1435 (1994).

[176] M. Imai, M. Sataka, M. Matsuda, S. Okayasu, K. Kawatsura, K. Takahiro, K. Komaki, H. Shibata, and K. Nishio. *Equilibrium and non-equilibrium charge-state distributions of 2.0MeV/u carbon ions passing through carbon foils*. Nuclear Instruments and Methods in Physics Research Section B: Beam Interactions with Materials and Atoms **354**, 172 (2015).

[177] E. Lamour, P. D. Fainstein, M. Galassi, C. Prigent, C. A. Ramirez, R. D. Rivarola, J. P. Rozet, M. Trassinelli, and D. Vernhet. *Extension of charge-state-distribution calculations for ion-solid collisions towards low velocities and many-electron ions*. Physical Review A **92**, 042703 (2015).

[178] M. Hattass, T. Schenkel, A. V. Hamza, A. V. Barnes, M. W. Newman, J. W. McDonald, T. R. Niedermayr, G. A. Machicoane, and D. H. Schneider. *Charge equilibration time of slow, highly charged ions in solids*. Physical Review Letters **82**, 4795 (1999).

[179] L. Folkerts, S. Schippers, D. Zehner, and F. Meyer. *Time Scales for Charge Equilibration of O q+(3<q<8) Ions during Surface-Channeling Interactions with Au (110)*. Physical Review Letters **74**, 2204 (1995).

[180] S. Martin, R. Brédy, J. Bernard, J. Désesquelles, and L. Chen. *Very Fast Hollow-Atom Decay Processes in Xe^{30+}-C_{60} Collisions*. Physical Review Letters **89**, 183401 (2002).

[181] S. Winecki, M. Stöckli, and C. Cocke. *Energy loss of highly charged Argon ions at grazing incidence on a graphite surface*. Physical Review A **55**, 4310 (1997).

[182] L. Banszerus, M. Schmitz, S. Engels, J. Dauber, M. Oellers, F. Haupt, K. Watanabe, T. Taniguchi, B. Beschoten, and C. Stampfer. *Ultrahigh-mobility graphene devices from chemical vapor deposition on reusable copper*. Science Advances **1** (2015).

[183] E. S. Reich. *Graphene knock-offs probe ultrafast electronics*. Nature **497**, 422 (2013).

[184] K. J. Tielrooij, L. Piatkowski, M. Massicotte, A. Woessner, Q. Ma, Y. Lee, K. S. Myhro, C. N. Lau, P. Jarillo-Herrero, N. F. van Hulst, and F. H. L. Koppens. *Generation of photovoltage in graphene on a femtosecond timescale through efficient carrier heating*. Nature Nanotechnology **10**, 437 (2015).

[185] S. Schuler, D. Schall, D. Neumaier, L. Dobusch, O. Bethge, B. Schwarz, M. Krall, and T. Mueller. *Controlled Generation of ap–n Junction in a Waveguide Integrated Graphene Photodetector*. Nano Letters **16**, 7107 (2016).

[186] A. Brenneis, L. Gaudreau, M. Seifert, H. Karl, S. Brandt, H. Huebl, J. A. Garrido, F. H. L. Koppens, and A. W. Holleitner. *Ultrafast electronic readout of diamond nitrogen–vacancy centres coupled to graphene*. Nature Nanotechnology **10**, 135 (2015).

[187] Y.-J. Yu, Y. Zhao, S. Ryu, L. E. Brus, K. S. Kim, and P. Kim. *Tuning the Graphene Work Function by Electric Field Effect*. Nano Letters **9**, 3430 (2009).

[188] X. Wang, H. Tian, M. A. Mohammad, C. Li, C. Wu, Y. Yang, and T.-L. Ren. *A spectrally tunable all-graphene-based flexible field-effect light-emitting device*. Nature Communications **6**, 7767 (2015).

[189] A. V. Krasheninnikov and K. Nordlund. *Ion and electron irradiation-induced effects in nanostructured materials*. Journal of Applied Physics **107**, 071301 (2010).

[190] M. M. Lucchese, F. Stavale, E. H. M. Ferreira, C. Vilani, M. V. O. Moutinho, R. B. Capaz, C. A. Achete, and A. Jorio. *Quantifying ion-induced defects and Raman relaxation length in graphene*. Carbon **48**, 1592 (2010).

[191] L. G. Cancado, A. Jorio, E. H. Ferreira, F. Stavale, C. A. Achete, R. B. Capaz, M. V. Moutinho, A. Lombardo, T. S. Kulmala, and A. C. Ferrari. *Quantifying defects in graphene via Raman spectroscopy at different excitation energies*. Nano Letters **11**, 3190 (2011).

[192] F. Banhart, J. Kotakoski, and A. V. Krasheninnikov. *Structural Defects in Graphene*. ACS Nano **5**, 26 (2011).

[193] E. H. Ahlgren, J. Kotakoski, and A. V. Krasheninnikov. *Atomistic simulations of the implantation of low-energy boron and nitrogen ions into graphene*. Physical Review B **83**, 115424 (2011).

[194] M. Kalbac, O. Lehtinen, A. V. Krasheninnikov, and J. Keinonen. *Ion-irradiation-induced defects in isotopically-labeled two layered graphene: enhanced in-situ annealing of the damage*. Advanced Materials **25**, 1004 (2013).

[195] J. Hopster, R. Kozubek, B. Ban d'Etat, S. Guillous, H. Lebius, and M. Schleberger. *Damage in graphene due to electronic excitation induced by highly charged ions*. 2D Materials **1**, 011011 (2014).

[196] J. Kotakoski, C. Brand, Y. Lilach, O. Cheshnovsky, C. Mangler, M. Arndt, and J. C. Meyer. *Toward Two-Dimensional All-Carbon Heterostructures via Ion Beam Patterning of Single-Layer Graphene*. Nano Letters **15**, 5944 (2015).

[197] O. Ochedowski, B. Kleine Bussmann, B. Ban d'Etat, H. Lebius, and M. Schleberger. *Manipulation of the graphene surface potential by ion irradiation*. Applied Physics Letters **102**, 153103 (2013).

[198] V. Smejkal. *Design of an electrostatic analyser setup for ion charge state and energy loss analysis after transmission through thin membranes*. Project work, TU Wien, unpublished (2015).

[199] V. Smejkal. *ELEKTRA - Electrostatic analyser measurements of ion transmission through thin free-standing foils*. Master thesis, TU Wien, unpublished (2016).

[200] V. Smejkal, E. Gruber, R. Wilhelm, L. Brandl, R. Heller, S. Facsko, and F. Aumayr. *A setup for transmission measurements of low energy multiply charged ions through free-standing few atomic layer films*. Nuclear Instruments and Methods in Physics Research Section B: Beam Interactions with Materials and Atoms **382**, 119 (2016).

[201] L. Brandl. *Design of a heatable sampleholder for transmission measurements with graphene*. Project work, TU Wien, unpublished (2015).

[202] G. Zschornack, S. Facsko, F. Grossmann, U. Kentsch, D. Kost, S. Landgraf, W. Möller, V. P. Ovsyannikov, M. Schmidt, and H. Tyrroff. *A New Ion Beam Beam Facility for Slow Highly Charged Ions*. Proceedings of EPAC, Lucerne p. 1189 (2004).

[203] N. Bibinov, V. Bratsev, D. Kokh, V. Ochkur, and K. Wiesemann. *Spectroscopic determination of the cold electron population in very low pressure ECR discharges in N_2/He mixtures*. Plasma Sources Science and Technology **14**, 109 (2005).

[204] W. Eck, A. Küller, M. Grunze, B. Völkel, and A. Gölzhäuser. *Freestanding Nanosheets from Crosslinked Biphenyl Self-Assembled Monolayers*. Advanced Materials **17**, 2583 (2005).

[205] A. Turchanin and A. Gölzhäuser. *Carbon Nanomembranes from Self-assembled Monolayers: Functional Surfaces Without Bulk*. Progress in Surface Science **87**, 108 (2012).

[206] A. Turchanin, D. Kafer, M. El-Desawy, C. Woll, G. Witte, and A. Gölzhäuser. *Molecular mechanisms of electron-induced cross-linking in aromatic SAMs*. Langmuir **25**, 7342 (2009).

[207] A. Turchanin, A. Beyer, C. T. Nottbohm, X. Zhang, R. Stosch, A. S. Sologubenko, J. Mayer, P. Hinze, T. Weimann, and A. Gölzhäuser. *One Nanometer Thin Carbon Nanosheets with Tunable Conductivity and Stiffness*. Advanced Materials **21**, 1233 (2009).

[208] X. Zhang, A. Beyer, and A. Gölzhäuser. *Mechanical characterization of carbon nanomembranes from self-assembled monolayers*. Beilstein Journal of Nanotechnology **2**, 826 (2011).

[209] A. Mrugalla and J. Schnack. *Classical molecular dynamics investigations of biphenyl-based carbon nanomembranes*. Beilstein Journal of Nanotechnology **5**, 865 (2014).

[210] D. Emmrich, A. Beyer, A. Nadzeyka, S. Bauerdick, J. C. Meyer, J. Kotakoski, and A. Gölzhäuser. *Nanopore fabrication and characterization by helium ion microscopy*. Applied Physics Letters **108**, 163103 (2016).

[211] K. S. Novoselov, A. K. Geim, S. V. Morozov, D. Jiang, Y. Zhang, S. V. Dubonos, I. V. Grigorieva, and A. A. Firsov. *Electric field effect in atomically thin carbon films*. Science **306**, 666 (2004).

[212] X. Li, Y. Zhu, W. Cai, M. Borysiak, B. Han, D. Chen, R. D. Piner, L. Colombo, and R. S. Ruoff. *Transfer of large-area graphene films for high-performance transparent conductive electrodes*. Nano Letters **9**, 4359 (2009).

[213] G. Algara-Siller, O. Lehtinen, A. Turchanin, and U. Kaiser. *Dry-cleaning of graphene*. Applied Physics Letters **104**, 153115 (2014).

[214] R. S. Pantelic, J. C. Meyer, U. Kaiser, and H. Stahlberg. *The application of graphene as a sample support in transmission electron microscopy*. Solid State Communications **152**, 1375 (2012).

[215] R. Zan, Q. M. Ramasse, U. Bangert, and K. S. Novoselov. *Graphene reknits its holes*. Nano Letters **12**, 3936 (2012).

[216] R. Pétuya[1], A. Arnau[1], and A. Borisov[2]. [1]Donostia International Physics Centre (DIPC), Spain and [2]CNRS-Université Paris Sud, France, private communication (2016).

[217] A. V. Krasheninnikov. Helmholtz-Zentrum Dresden-Rossendorf, Germany, private communication (2016).

[218] H. Andrä, A. Simionovici, T. Lamy, A. Brenac, G. Lamboley, J. Bonnet, A. Fleury, M. Bonnefoy, M. Chassevent, S. Andriamonje *et al.* *X-ray-and Auger-spectra from multi-charged ions interacting with surfaces and solids*. Zeitschrift für Physik D Atoms, Molecules and Clusters **21**, 135 (1991).

[219] F. Aumayr, H. Kurz, D. Schneider, M. Briere, J. McDonald, C. Cunningham, and H. Winter. *Emission of electrons from a clean gold surface induced by slow, very highly charged ions at the image charge acceleration limit*. Physical Review Letters **71**, 1943 (1993).

[220] O. Lehtinen, J. Kotakoski, A. Krasheninnikov, A. Tolvanen, K. Nordlund, and J. Keinonen. *Effects of ion bombardment on a two-dimensional target: atomistic simulations of graphene irradiation*. Physical Review B **81**, 153401 (2010).

[221] R. Murali, Y. Yang, K. Brenner, T. Beck, and J. D. Meindl. *Breakdown current density of graphene nanoribbons*. Applied Physics Letters **94**, 243114 (2009).

[222] A. Behnam, A. S. Lyons, M.-H. Bae, E. K. Chow, S. Islam, C. M. Neumann, and E. Pop. *Transport in Nanoribbon Interconnects Obtained from Graphene Grown by Chemical Vapor Deposition*. Nano Letters **12**, 4424 (2012).

[223] K.-J. Lee, A. P. Chandrakasan, and J. Kong. *Breakdown current density of CVD-grown multilayer graphene interconnects*. IEEE Electron Device Letters **32**, 557 (2011).

[224] L. Su, Y. Zhang, J. O. Klein, Y. Zhang, A. Bournel, A. Fert, and W. Zhao. *Current-limiting challenges for all-spin logic devices*. Scientfic Reports **5**, 14905 (2015).

[225] S. P. Koenig, L. Wang, J. Pellegrino, and J. S. Bunch. *Selective molecular sieving through porous graphene*. Nature Nanotechnology **7**, 728 (2012).

[226] C. A. Merchant, K. Healy, M. Wanunu, V. Ray, N. Peterman, J. Bartel, M. D. Fischbein, K. Venta, Z. Luo, A. C. Johnson *et al.* *DNA translocation through graphene nanopores*. Nano Letters **10**, 2915 (2010).

Danksagung

Da es üblich ist am Ende einer Arbeit, sei es nun die Diplomarbeit oder die Dissertationsschrift, eine Danksagung zu schreiben, möchte auch ich diese Tradition weiterführen. Denn wie es so schön heißt *Es ist ein lobenswerter Brauch: Wer was Gutes bekommt, der bedankt sich auch (Wilhelm Busch)*.

Seit meiner Bachelorarbeit bis hin zu meiner Dissertation gehöre ich der AG Aumayr an und verließ diese Gruppe in all meinen Studienjahren auch nur einmal für eine Projektarbeit. Aus der jahrelangen Zusammenarbeit lässt sich schließen, dass ich mich immer sehr wohl gefühlt habe und mir in dieser Gruppe auch auf wissenschaftlicher Ebene nie langweilig wurde, da ständig neue Aufgaben und Herausforderungen auf mich warteten.

Ein ganz besonders großes Dankeschön dafür möchte ich meinem Doktorvater Prof. Friedrich Aumayr aussprechen, der sich stets väterlich um das Wohlergehen seiner Studenten kümmert und uns im Vorankommen im Studium und in der Wissenschaft unterstützt. Obwohl im Laufe der Jahre sein Aufgabenbereich immer umfangreicher und sein Terminkalender immer ausgelasteter wurde, war es doch möglich jederzeit an der Bürotür anzuklopfen und Gehör für wissenschagftliche als auch private Angelegenheiten zu finden. Besonders bedanken möchte ich mich für die zahlreichen Möglichkeiten, wissenschaftliche und zwischenmenschliche Erfahrungen bei Forschungsaufenthalten und auf Konferenzen im Ausland gemacht zu haben. Diese gehören sicherlich zu den schönsten und bereichernsten Erlebnissen meiner Dissertationszeit. Weiters bedanke ich mich für das große Vertauen, das in mich gesetzt wurde und für die gelassenen und aufbauenden Worte wenn ich wieder einmal mit unerfreulichen Nachrichten in der Bürotür stand. Bewundernsund nachahmenswert fand ich auch immer die positive Einstellung der Jugend gegenüber, das Verständis für Albernheiten und das sichtliche Mitfreuen über wenn auch noch so kleine Erfolgserlebnisse im Labor.

Aber nicht nur ein Chef trägt zum guten Arbeitsklima bei, sondern vor allem die Kollegen, mit denen man doch so einige Stunden täglich verbringt. Da ich mehrere Jahre in der AG Aumayr gearbeitet habe, habe ich viele Arbeitskollegen kennengelernt und darunter auch gute Freunde gefunden. Bereits als Bachelorstudentin, als ich noch das Küken der Gruppe war, habe ich mit

Gregor Kowarik und Katharina Dobes Bekanntschaft gemacht, mit denen mich noch immer eine gute Freundschaft verbindet. Vor allem Kathi war für mich am Anfang meiner Dissertationszeit eine wichtige und große Stütze in der Arbeitsgruppe. Obwohl wir an verschiedenen Experimenten gearbeitet haben, konnten wir uns immer wieder gegenseitig helfen und hatten ein gemeinsames Sorgenkind - Sophie. Zu dieser Zeit war auch bereits Valerie Smejkal Teil unserer Gruppe, die unser *trio infernale* komplett machte. Sie brachte sehr viel Farbe (und damit meine ich nicht nur ihren ausgefallenen farbenfrohen Kleidungsstil) in die Gruppe. Während sich Valerie anfangs noch mit der Quarzkristallmikrowaage beschäftigte, gab sie sich dann später mit Herz und Seele der Tragödie der Elektra hin. Es war ein Vergnügen mit ihr das neue Setup aufzubauen und sehr lang und ausgiebig über technische und physikalische Probleme zu diskutieren. Dabei ergaben sich dann doch so manche Kommunikationsprobleme, die nur noch - wenn überhaupt - mit einem Zettel Papier und Stift bereinigt werden konnten. Nach kurzer Zeit mussten wir feststellen, dass wir in Sachen "Mädchensein" doch ziemlich Konkurrenz bekamen, gab es da noch Florian Laggner. Wir haben ihn gern in unsere Frauengruppe aufgenommen, in glücklicher Runde abgründige Gespräche geführt und auf Selbstbetrug angestoßen. Während er mich als Bürokollege des Öfteren mit seiner für meinen Geschmack unpassenden Auswahl an Musik und seinen Versuchen als Hobbyphsychologe zur Rage brachte, hat er doch immer wieder für gute Stimmung in der Gruppe und Unterhaltung bei den Büropartys gesorgt. Als erfrischende Arbeitsunterbrechung hat sich auch Bernhard Berger erwiesen. Seine verspielte Art ist so manchen schon bei Reperaturen im Labor zu Gute gekommen. Ich war besonders glücklich und dankbar, als er meinen Laptop nach einer ungewollten Taufe durch einen Tastaturaustausch wiederbeleben konnte. Nicht weniger kümmerte sich auch Reinhard Stadlmayer, bekannt als Schmu, um verschiedenste Gebrechen im Labor und zeichnete sich durch große Hilfsbereitschaft aus. Er hat an so manchen Tagen mit einem Stück Schokolade zur besseren Stimmung beigetragen und sich erfolglos darum bemüht, mich zu einem Boot-Camp-Training zu schleppen. Im Kreis der Dissertanten darf seit letztem Jahr auch Janine Schwestka nicht mehr fehlen. Während wir in ihrer Projektarbeit- und Diplomarbeitszeit in unserer AG noch recht wenig miteinandner zu tun hatten, hat sich dies im letzten Jahr geändert. Inzwischen teilen wir uns sogar das Büro. Ich konnte bei Janine meinen *Kleinschwesternschutzinstinkt* voll ausleben und ihr immer wieder klar vor Augen führen welche Fehler sie in der Position als meine Nachfolgerin nicht begehen sollte. Auch Paul Szabo, obwohl er noch zu den Diplomanten gehört, ist inzwischen ein festes Mitglied unserer AG geworden. Er sorgt immer wieder für Ruhe und Ausgeglichenheit in der Gruppe und ist sowohl bei ernsthaften Gesprächen als auch bei jedem Unsinn immer gern dabei. Georg Harrer ist als Mittagessenlieferant ein wichtiges Mitglied der Gruppe geworden und sorgt während der Kaffeepausen mit Youtube-Videos dafür, dass wir auf dem Laufenden bleiben. Bei Lorenz Bergen möchte ich mich für seine Hilfe bei den AFM-Messungen und Auswertungen, die er während seiner Projekt- und Diplomarbeit ausführte, bedanken. Während längerer Messzeiten verstand er es gut, immer wieder neue

Tratschpartner im Labor oder im Malina zu finden und ausgiebig über seine Tutorerfahrungen zu berichten. Die Geduld und Berharrlichkeit, die er sich beim Arbeiten mit dem AFM aneignen konnte und musste, werden ihm hoffentlich bei der Ausführung seiner Dissertation am Festkörperinstitut zu Gute kommen. Ein herzliches Dankeschön geht auch an all die anderen Studenten, die ich im Laufe meiner Zeit in der AG Aumayr kennenlernen durfte und die ich hier nicht alle namentlich nenne.

Da ich während meiner Arbeit immer wieder an ausländischen Forschungseinrichtungen war, habe ich auch dort weitere Kollegen kennengelernt und mir neues Wissen aneignen können. Obwohl ich allen für ihre freundliche und wohlwollende Art danke, möchte ich Richard Wilhelm ganz besonders herausheben. Er machte durch seinen großen Einsatz äußerst produktive und erfolgreiche Messaufenthalte am HZDR möglich. Daher hat es mich besonders gefreut, dass er sich im letzten Jahr dafür entschlossen hat, für acht Monate als PostDoc in unserer AG zu arbeiten. Zahlreiche Diskussionen und seine umfangreiche Literatursammlung haben mir beim Schreiben der Papers und der Dissertationsschrift sehr geholfen. Dafür vielen Dank! Besonders hilfreich waren seine verständnisvollen und aufbauenden Worte, wenn bei mir die Motivation zum Weitermachen und Weiterschreiben fehlte. Es wäre sehr schön, wenn sich in Zukunft die eine oder andere Zusammenarbeit ergeben würde.

Während meiner Dissertationszeit hatte ich auch das Glück, dich Martin, an meiner Seite zu wissen. Du warst für mich der Ruhepol, wenn ich mich zu sehr über die Arbeit oder meine Kollegen aufgeregt habe. Du hast es verstanden, dich in diesen Situationen zurückzunehmen und mir gezeigt, dass doch alles halb so schlimm ist. Du hast es auch immer wieder geschafft, dass ich an vielen Wochenenden von der Arbeit abschalten konnte, um dann erholsamer und besser gelaunt in eine neue Arbeitswoche zu starten. Ich denke sehr gerne an die Ausflüge, Unternehmungen und Reisen während dieser Zeit zurück und freue mich schon auf weitere. Auch mit dir habe ich immer wieder heftigst über physikalische Probleme diskutiert und wurde dadurch öfters dazu angeregt, trotz anfänglicher Überzeugung, meine Aussagen und Überlegungen zu überdenken. Vielen Dank auch dafür.

Mein allerletzter großer Dank geht an meine zwei Schwestern und meine Mama. Sie sind jene Personen, die nicht erst seit den letzten paar Jahren für mich wichtig sind. Obwohl wir vier inzwischen örtlich voneinander getrennt leben, habt ihr doch meine Studienzeit mit all den Hochs und Tiefs miterlebt. Ihr habt mir in meiner gesamten Studienzeit immer sehr großes Vertrauen entgegengebracht und mehr an meine Fähigkeiten geglaubt als ich an mich selbst. Die wenigen Wochen, die ich während meiner Dissertationszeit daheim verbracht habe, waren stets sehr erholsam und ich habe diese “Auszeit” sehr genossen. Dir Verena, danke ich dafür, dass du mich immer wieder daran erinnert hast, dass es auch außerhalb meiner kleinen Disswelt etwas gibt, das nicht weniger wichtig ist. Du, Steffi, hast wohl am meisten von meiner Studienzeit mitbekommen, da du ja auch für einige Jahre in Wien gelebt hast. Dir danke ich für deine Wärme und dein Ver-

ständnis. Unsere Schwesternsamstage bleiben mir in sehr guter Erinnerung, da du mir in dieser Zeit ein guter Gesprächspartner warst. Du Mama, bist mir ein Vorbild, wenn es darum geht, sich von neuen Herausforderungen nicht abschrecken zu lassen und stets bemüht zu sein, das Beste zu geben, um die Arbeit voranzutreiben. Für dich sind der Ehrgeiz und das Streben eine Tugend, der Stillstand unerträglich.

Wir alle leben geistig von dem,
was uns Menschen in bedeutungsvollen Stunden unseres Lebens gegeben haben.
--Albert Schweitzer--

CURRICULUM VITAE

Personal Data

Name	Elisabeth Gruber
Address	Geblergasse 84/14 A-1170 Vienna, Austria, EU
Telephone	+43 (0) 69919295192
Email	egruber@iap.tuwien.ac.at
Date of birth	16.06.1987
Place of birth	Meran, Italy, EU
Nationality	Italian
Languages	German (mother tongue), English, Italian

Education

since January 2013	**PhD Engineering Physics at TU Wien** Project Assistant (2013-2014, 2016-2017) and University Assistant (2014-2016) at the Institute of Applied Physics, TU Wien
October 2009 - November 2012	**Masters Programme Engineering Physics at TU Wien** Master thesis „Ion Guiding Through Insulating Glass Capillaries“ conducted at the Institute of Applied Physics, TU Wien; Graduated with distinction.
October 2006 - September 2009	**Bachelors Programme Engineering Physics at TU Wien** Bachelor thesis „Experimentelle Untersuchung ioneninduzierter Elektronenemission von Isolatoren“ conducted at the Institute of Applied Physics, TU Wien; Graduated with distinction.
2001 -2006	**Gymnasium** „Wissenschaftliches Gymnasium Albert Einstein“ (Meran, Italy), Final diploma „Matura“ (100/100)
1998 –2001	**Middle School** „Mittelschule Simon Ybertracher“ (Naturns, Italy)
1993 –1998	**Elementary School** „Grundschule Anton Lintner“ (Naturns, Italy)

Awards

2010	Proexcellentia II: Honor for academic performance for former proexcellentia prize winners
2006	Proexcellentia I: Honor of the 10 best high-school graduates of South Tyrol of 2006

Research Stays & Collaborations

Helmholtz-Zentrum Dresden-Rossendorf, Germany	2013-2016 7 measurement periods (each for one or two weeks) Transmission measurements with CNM and SLG; X-ray measurements
GANIL, Caen, France	2013-2016 7 measurement periods Irradiations at the ARIBE and IRRSUD facility
Universität Duisburg – Essen, Germany	September 2014 HCI-irradiation (EBIT) and UHV-AFM measurements
Universität Bielefeld, Germany	February 2013 HIM measurements of CNM
Universität Wien	2015-2016 TEM and STEM measurements of SLG
USTEM, TU Wien	2013-2015 TEM measurements of CNM and SLG

Supervised Students

Diploma students	Valerie Smejkal Lorenz Bergen
Project students	Laurids Brandl
Bachelor students	Lukas Leonhartsberger Peter Allinger Stefan Wampl Peter Hischenhuber
Tutor "Grundlagenpraktium"	Winter semester 2015

Publications

R.A. Wilhelm, **E. Gruber**, J. Schwestka, R. Kozubek, T. Madeira, José Marques, J. Kobus, A. V. Krasheninnikov, M. Schleberger, F. Aumayr; submitted (2017)

E. Gruber, R. A. Wilhelm, R. Pétuya, V. Smejkal, R. Kozubek, A. Hierzenberger, B. C. Bayer, I. Aldazabal, A. K. Kazansky, F. Libisch, A. V. Krasheninnikov, M. Schleberger, S. Facsko, A. G. Borisov, A. Arnau, F. Aumayr; Nat. Commun. **7**, 13948 (2016)

E. Gruber, P. Salou, L. Bergen, M. El Kharrazi, E. Lattouf, C. Grygiel, Y. Wang, A. Benyagoub, D. Levavasseur, J. Rangama, H. Lebius, B. Ban-D' Etat, M. Schleberger, F. Aumayr; J. Phys. Condens. Matter **28**, 4050011 (2016)

R. A. Wilhelm, **E. Gruber**, V. Smejkal, S. Facsko, F. Aumayr; Phys. Rev. A **93**, 0527081 (2016)

V. Smejkal, **E. Gruber**, R. A.Wilhelm, L. Brandl, R. Heller, S. Facsko, F. Aumayr; Nucl. Instr. Meth. Phys. Res. **382**, 119 (2016).

B. M. Berger, R. Stadlmayr, D. Blöch, **E. Gruber**, K. Sugiyama, T. Schwarz-Selinger, F.Aumayr; Nuclear Materials and Energy, submitted (2016)

E. Gruber, R. A. Wilhelm, V. Smejkal, R. Heller, S. Facsko, F. Aumayr; J. Phys. Conf. Ser. **635**, 0120271 (2015)

R. A. Wilhelm, A. S. El-Said, F. Krok, R. Heller, **E. Gruber**, F. Aumayr, S. Facsko; Prog. Surf. Sci. **90**, 377 (2015)

R. A.Wilhelm, **E. Gruber**, R. Ritter, R. Heller, A. Beyer, A. Turchanin, N. Klingner, R. Hübner, M. Stöger-Pollach, H. Vieker, G. Hlawacek, A. Gölzhäuser, S. Facsko, F. Aumayr; 2D Materials **2**, 0350091 (2015)

N. Stolterfoht, **E. Gruber**, P. Allinger, S.Wampl, Y.Wang, M. Simon, F. Aumayr; Phys. Rev. A **91**, 0327051 (2015)

R. A. Wilhelm, **E. Gruber**, R. Ritter, R. Heller, S. Facsko, F. Aumayr; Phys. Rev. Lett. **112**, 1532011 (2014)

E. Gruber, N. Stolterfoht, P. Allinger, S. Wampl, Y. Wang, M. Simon, F. Aumayr; Nucl. Instr. Meth. Phys. Res. **340**, 1 (2014)

Y. Wang, C. Grygiel, C. Dufour, J. Sun, Z. Wang, Y. Zhao, G. Xiao, R. Cheng, X. Zhou, J. Ren, S. Liu, Y. Lei, Y. Sun, R. Ritter, **E. Gruber**, A. Cassimi, I. Monnet, S. Bouffard, F. Aumayr, M. Toulemonde; Sci. Rep. **4**, 57421 (2014)

E. Gruber, G. Kowarik, F. Ladinig, J. Waclawek, D. Schrempf, F. Aumayr, R. Bereczky, K. Tökési, P. Gunacker, T. Schweigler, C. Lemell, J. Burgdörfer; Phys. Rev. A **86**, 0629011 (2012)

G. Kowarik, **E. Gruber**, K. Iskratsch, F. Aumayr; Nucl. Instr. Meth. Phys. Res. **269**, 964 (2011)

Talks

Invited Talk: "Slow highly charged ion interaction with freestanding single layer graphene"; 18th International Conference on the Physics of Highly Charged Ions (HCI-2016), Kielce/Poland; 16.09.2016

Short Oral: "Interaction of slow highly charged ions with single layer graphene: charge exchange and energy loss studies"; European Materials Research Society (EMRS), Spring Meeting 2016, Lille/France; 03.05.2016

Invited Talk: "Interaction of highly charged ions with graphene and carbon nano membranes; 29th International Conference on Photonic, Electronic and Atomic Collisions (XXIX ICPEAC), Toledo/Spain; 27.07.2015

Short Oral: "Ion-induced nanostructures on surfaces: Comparing the effect of slow highly charged ions to grazing incidence swift heavy ions"; 26th International Conference on Atomic Collisions in Solids (ICACS-26), Debrecen/Hungary; 17.07.2014

Invited Talk: "Transmission of slow highly charged ions through 1 nm thick carbon nanomembranes";
6th International Conference on Elementary Processes in Atomic Systems-(CEPAS 2014), Hotel Sorea, Bratislava/Slovakia; 11.07.2014

Invited Talk: "Controlling ion guiding through capillaries by temperature"; 20th International Workshop on Inelastic Ion Surface Collision (IISC-20), Wirrina Cove/Australia; 20.02.2014

Short Oral: "Slow Highly Charged Ions as a Tool for the Fabrication of Nanopores in 1 nm Thick Carbon Nanomembranes"; 22th International Conference on Ion Surface Interactions (ISI-2013), Yaroslavl/Russia; 25.08.2013

Short Oral: "Temperature control of ion guiding through straight insulating macro - capillaries"; 19th International Workshop on Inelastic Ion-Surface Collisions (IISC-19), Frauenchiemsee/Germany; 17.09.2012

Talk: "Ion induced nanostructures on 3D and 2D materials - recent results"; Seminar, Universität Duisburg-Essen, Duisburg-Essen/Germany; 15.09.2014

Talk: "Interaction of slow highly charged ions with single layer graphene"; Seminar, Institute of Applied Physics (IAP), TU Wien; 24.05.2016